



**University of
Nottingham**
UK | CHINA | MALAYSIA

**Thesis submitted to University of Nottingham for the degree of
Doctor of Philosophy, March 2024.**

**Rational Design of Functional Covalent Organic Frameworks for the
Oxygen and Carbon Dioxide Reduction Reactions**

Minghao Liu

20416135

DTP Institution:

University of Nottingham, China (UNNC) and Shanghai Academic Research
Institute (SARI, CAS)

Supervisor:

Prof. Jun He (UNNC)

Prof. George Zheng Chen (UNNC)

Prof. Svenja Hanson (UNNC)

Prof. Gaofeng Zeng (SARI, CAS)

Abstract

Porous materials have developed significantly due to their remarkable properties and wide-ranging applications, such as gas capture, gas separation, optoelectronics, ion detection, catalysts, and energy storage. Within the category of porous polymers, covalent organic frameworks (COFs) have garnered increasing attention since their successful synthesis in 2005.

COFs consist of lightweight elements interconnected by covalent bonds, imparting excellent chemical and thermal stability. Furthermore, they possess precisely integrated extended structures with periodic skeletons and ordered pores. COFs exhibit well-defined alignment of π building units in atomic layers and segregated arrays of π columns in their frameworks. These elegant π skeletons form the foundation for structural design, while the 1D channels offer controllable sizes, shapes, and environments. Consequently, the diverse skeleton, ordered porous structure, pre-designable functions, and high chemical stability make COFs highly suitable for applications in gas/molecular adsorption, energy storage, electro-/photo-catalysis, conversion, semiconductors, and Li-ion batteries. Additionally, the pyrolysis of COFs into functional carbons represents a simple and efficient strategy to enhance conductivity.

Nevertheless, direct pyrolysis of COFs often leads to carbons with aggregated skeletons and collapsed pores. Therefore, further exploration is required to synthesize structures of COFs precisely for electrocatalysts in electrocatalysis reactions. Furthermore, the rational design, specific functionalization, and meticulous synthesis of COF structures are crucial for preparing high-crystalline COF materials and improving their application properties.

In this thesis, COF-derived carbons were designed through direct pyrolysis, featuring a unique core-shell framework for constructing high-density active sites. The optimized COF-derived carbons demonstrated exceptional

Abstract

electrocatalysis performance. However, achieving precise control over dimensions, structure, skeleton polarity, pore environments, functional groups, and defects is necessary to explore the elaborate synthesis of COFs and their applications in electrochemical energy storage and conversion systems. Therefore, a class of functional COF material with high crystallinity was successfully prepared through rational structural design and precise regulation, exhibiting excellent performance in electrocatalytic reduction. Specifically, the synthesis strategy involved skeleton engineering, dimension control, and catalytic density modulation to investigate the relationship between structure and electrocatalysis performance.

Scope of this thesis

COFs exhibited many practical applications in sensing, gas adsorption and separation, electro-/photo-catalysis, energy storage, and optoelectronic devices owing to their low density, high porosity, and designable functionality. Notably, the unique structure of COFs provides an ideal platform for small-molecule catalytic conversion, especially in electrochemical catalysis. Compared with traditional semiconductor catalysts, COFs with high crystallinity, 1D channels, and elegant pi-conjugations have superior adsorption, diffusion, and activation behaviours for intermediates due to their large surface area, abundant porosity, and high density of heteroatoms. Compared with other porous polymer materials (e.g., hypercrosslinked and conjugated microporous polymers), COFs have a long-range ordered crystal structure, which is more transparent than other amorphous porous polymer materials, further being conducive to the understanding of the structure-functional relationship and exploring the optimization of properties. Therefore, constructing functional COFs will provide new opportunities for rationally designing efficient electrocatalysts.

Considering the above-mentioned structural characteristics and the requirements of electrocatalytic reactions, COFs and their derivatives can provide a platform for designing highly active and selective electrocatalysts. They offer advantages such as precise control over the spatial arrangement of catalytic centres, extensive conjugated structural frameworks for efficient electron transfer, and designable pore structures and functional groups for effective molecule adsorption, activation, and transfer. These features make COFs highly promising in the field of electrocatalysis. Based on the aforementioned discussions, this thesis focuses on the following seven parts:

(1) In Chapter 1, we summarized the relative backgrounds of COFs and COF-derived carbons, including the design principle, the linkage diversities, the

building blocks and topologies, and the synthesis methods. We also outlined the study's progress and current predicaments of electrochemical conversion, including oxygen reduction reaction (ORR), oxygen evolution reaction (OER), and CO₂ reduction reaction (CO₂RR).

(2) In Chapter 3, a core-shell bifunctional catalyst using COF derivatives for ORR and hydrogen evolution reaction (HER) has been demonstrated. The COF shell prevents the collapse of the MOF core in the pyrolysis process. In addition, the core-shell morphology benefits mass transport, and the COF-derived shell facilitates electron conductivity. The catalyst had Co-N₄ atoms and Co nanoparticles embedded in the carbon, which catalyze ORR and HER with high activity and excellent stability. This work provides a new platform to design multifunctional catalysts from COFs.

(3) Owing to the Co-N₄ atoms and Co nanoparticles belonging to a single metal catalyst, we consider constructing a dual atomic catalyst to improve electrocatalysis performance further. In Chapter 4, we developed a new synergistic dual atomic catalyst for CO₂RR using COF derivatives. The synergistic CoN₄O and ZnN₄ sites significantly improve the electron transport rate and the generation of COOH* intermediate, which is beneficial for the process of CO₂RR. The catalyst showed superior activity selectivity and long-term stability over many other electrocatalysts. This work not only provided new insights for the preparation of carbon-supported bimetallic single atom catalysts but also offered a new method to develop catalytic carbons from COFs.

(4) The COF derivatives cannot realize the precise control for the topology dimensions, further encouraging us to explore the influence of COFs' topologies on electrocatalysis performance. In Chapter 5, we synthesized the 1D catalytic COF using four connected pyrene-based units and the non-linear phenanthroline building blocks to immobilize Fe ions, which showed much higher activity than the controlled 2D COF. The space between the chains was easily expanded owing to weaker interactions, resulting in more exposed catalytic sites. These findings highlight the advantages of 1D COFs as promising candidates for

highly efficient OER catalysis and pave the way for future research in this field.

(5) Considering the synthesis strategy is essential for COFs, we adopted natural units to construct COFs to explore the potential development of COFs' structures. In Chapter 6, we employed the natural building blocks to construct catalytic COFs for ORR and CO₂RR. Incorporating natural units introduced ladder-like conjugation within the frameworks, resulting in enhanced electronic conductivity. This natural-based COF exhibited remarkable catalytic activity, selectivity, and stability in ORR and CO₂RR. Theoretical calculations revealed that the natural linker facilitated the formation of intermediates in the catalytic process, enhancing the overall efficiency. Consequently, this study expands the repertoire of COFs and provides a promising avenue for developing highly efficient energy storage and conversion systems.

(6) Except for space dimensions and building blocks, the density of catalytic sites in COFs to tune the catalytic behaviour for CO₂RR is ignored because it is generally assumed that more metals result in better catalytic activity. Thus, the correlation between the density of metal atoms and catalytic performances has yet to be explored. In Chapter 7, a skeleton engineering strategy based on the multiple-component synthesis to construct the controllable metal density in the skeletons was first reported, which builds the quantitative correlation between the metal density and catalytic performance. By establishing COFs with vacancies and Ni-N sites, the 0.5NiPc-COF catalysed CO₂RR with high selectivity and activity. The design and modulation density of catalytic sites in COFs proposed new insights into electrocatalysis or energy conversion and guidance of constructing COFs with alternate structures of vacancies and metal sites for achieving high catalytic performance.

(7) The skeleton of COFs is also a significant element for the chemical properties and electrocatalysis CO₂RR performance. Specifically, the amine linkages enhance the binding ability of CO₂ molecules, and the ionic frameworks improve the electronic conductivity and the charge transfer along the frameworks. However, direct synthesis of covalent organic frameworks with

amine linkages and ionic frameworks is hardly achieved due to the electrostatic repulsion and predicament for the strength of the linkage. In Chapter 8, a multilevel post-function strategy was demonstrated to modulate the properties of COFs (porosity, crystallinity, and electron states), which can contribute to their tuneable catalytic performance for CO₂RR. This work provides us a more in-depth understanding of COFs and their applications in electrochemical energy storage and conversion systems. Meanwhile, it also guides us in constructing multilevel post-synthetic modification COFs to achieve tailored activity and high stability.

Contents	
Abstract	2
Scope of this thesis	4
Abbreviation summary	8
Chapter 1. Introduction	11
1.1 Introduction of Covalent Organic Frameworks (COFs).....	11
1.1.1 Design principle	12
1.1.2 Topologies	13
1.1.2.1 One-dimensional topology	13
1.1.2.2 Two-dimensional topology	14
1.1.2.3 Three-dimensional topology	15
1.2 Electrochemical Energy Storage and Conversion over the COFs.....	16
1.2.1 Oxygen reduction reaction.....	17
1.2.1.1 ORR over the COFs.....	17
1.2.2 Oxygen evolution reaction.....	20
1.2.2.1 OER over the COFs	20
1.2.3 CO ₂ reduction reaction	22
1.2.3.1 CO ₂ RR over the COFs	22
1.3 COF-derived carbon materials	29
1.3.1 Electrocatalysis application over the COF-derivatives	29
Chapter 2. Methodology and Techniques	34
Abstract	34
2.1 Experimental Reagents and Apparatus.....	34
2.2 Synthesis Methods	35
2.3 Characterization Methods	39
2.3.1 Routine properties.....	39
2.3.2 Pawley refinement	39
2.3.3 X-ray absorption fine structure measurements and data processing	40
2.4 Electrocatalysis testing.....	40
2.4.1 ORR testing.....	40
2.4.2 CO ₂ RR testing	41

2.4.3 OER testing	42
2.4.4 Faradic efficiency calculation	43
2.4.5 Turnover frequency calculation	43
2.4.6 Mass activity calculation	43
2.4.7 Normalization of current density	44
2.4.8 Mott-Schottky curve test	44
Chapter 3. Atomic Co-N₄ and Co nanoparticles confined in COF@ZIF-67 derived core-shell carbon frameworks: Bifunctional non-precious metal catalysts toward ORR and HER	46
3.1 Introduction	46
3.2 Results and discussion	47
3.3 Conclusion	62
Chapter 4. Dual atomic catalysts from COF-derived carbon for CO₂RR by Suppressing HER through Synergistic Effects	64
4.1 Introduction	64
4.2 Results and discussions	65
4.3 Conclusion	80
Chapter 5. Dimensionally Controlled Interlayer Spaces of Covalent Organic Frameworks for the Oxygen Evolution Reaction	83
5.1 Introduction	83
5.2 Results and discussion	85
5.3 Conclusion	107
Chapter 6. Ladder Type Covalent Organic Frameworks Constructed with Natural Units for the Oxygen and Carbon Dioxide Reduction Reactions.....	110
6.1 Introduction	110
6.2 Results and discussion	111
6.3 Conclusion	130
Chapter 7. Modulating Density of Catalytic Sites in Multiple-Component Covalent Organic Frameworks for Electrocatalytic Carbon Dioxide Reduction	132
7.1 Introduction	132
7.2 Results and discussion	133
7.3 Conclusion	150

Chapter 8. Multilevel Post-synthetic Modification of Covalent Organic Frameworks for Electrocatalytic CO₂ Reduction.....	152
8.1 Introduction	152
8.2 Results and discussion	154
8.3 Conclusion	175
Chapter 9. Conclusion and Perspectives.....	177
9.1 Summary of the thesis	177
9.2 Outlook and Future work.....	180
Reference	182
Outputs during the period of PhD	208
Acknowledgement.....	210

Abbreviation summary

Table 1. The summary of abbreviation in the thesis.

Covalent Organic Frameworks	COFs
Zeolitic Imidazolate Frameworks	ZIFs
Metal organic Frameworks	MOFs
Single Atom Catalysts	SACs
Oxygen Reduction reaction	ORR
Hydrogen Evolution Reaction	HER
Oxygen Evolution Reaction	OER
CO ₂ Reduction Reaction	CO ₂ RR
Dynamic covalent chemistry	DCC
Scanning Electron Microscopy	SEM
Transmission Electron Microscopy	TEM
High-Resolution TEM	HR-TEM
Powder X-ray diffraction	PXRD
Brunauer-Emmett-Teller	BET
BET surface areas	S _{BET}
Inductively Coupled Plasma Optical Emission Spectroscopy	ICP-OES
Fourier transform infrared spectroscopy	FT-IR
Energy-dispersive X-ray spectroscopy	EDX
X-ray Photoelectron Spectroscopy	XPS
Thermal Gravimetric Analysis	TGA
Electrostatic Potential Surface	ESP
Lowest Unoccupied Molecular Orbital	LUMO
Highest Occupied Molecular Orbital	HOMO
Gas Chromatography	GC
Ultraviolet–Visible spectrum	UV-Vis
Electron Paramagnetic Resonance	EPR
¹³ C Nuclear Magnetic Resonance	¹³ C NMR
High-Angle Annular Dark-Field Scanning Transmission Electron Microscopy	HAADF-STEM
X-ray Absorption Fine Structure	XAFS
X-ray Absorption Near Edge Structure	XANES
Wavelet Transform	WT
Faraday efficiency of CO	FE _{CO}
Reversible Hydrogen Electrode	RHE
Cyclic Voltammogram	CV
Linear Sweep Voltammetry	LSV
Rotating Disk Electrode	RDE
Chronopotentiometry	i-t
Chronoamperometry	V-t
Rotating Ring Disk Electrode	RRDE
CO partial Current Density	j _{co}
Onset Potential	E ₀

Table 1. The summary of abbreviation in the thesis.

Half-wave Potential	$E_{1/2}$
Limited Current Density	j_{lim}
turnover frequency	TOF
Double Layer Capacitances	C_{dl}
Electrochemically Active Surface Area	ECSA
Free Energy Change	ΔG
Total Density of States	TDOSs
Partitioned Density of States	PDOSs
Electrochemical Impedance Spectroscopy	EIS
Density Functional Theory	DFT
Rate-Determining Step	RDS
Self-Consistent Charge Density Functional Tight Binding	DFTB
Water Contact Angle	WCA

Chapter 1. Introduction

1.1 Introduction of Covalent Organic Frameworks (COFs)

Porous materials have been well developed because of their outstanding character and broad application, including gas capture, gas separation, optoelectronics, ion detection, catalysts, and energy storage.^[1] Among porous polymers, COFs as a unique class of porous polymers, are getting more and more attention since the first examples were successfully synthesized in 2005.^[2] This pioneering work paves the way for developing new, stable, and ordered accessible channels over framework materials. Over the past twenty years, the development of reticular chemistry has dramatically enhanced the exploration of designing and synthesizing COFs and deepened the understanding of exploring functional applications derived from their ordered frameworks and channels.

COFs, as an organic porous material based on the solid covalent bond of C, H, O, B, and other light elements, possess low density, large specific surface area, and excellent stability.^[3] Additionally, they are precisely integrated into extended structures with periodic skeletons and ordered pores, which are different from zeolites, mesoporous silica, MOFs, conjugated microporous polymers, porous carbons, and metal–organic and organic cages. COFs are classified into one- / two- / three-dimensional (1D, 2D, and 3D) COFs controlled by the geometries of the building blocks. The low interaction force between layers endows 1D COFs to expose more active sites, further boosting the catalytic performance compared with 2D and 3D COFs.^[4] In 3D COFs, the building blocks are covalently connected, and covalent bonds maintain the lattice structures. 3D COFs have high surface areas, numerous open sites, and low densities, making them ideal candidates for gas capture.^[5] By contrast, in 2D COFs, the organic units are linked into 2D atomic layers that further stack

via π - π interactions to crystallize layered structures. The frameworks are locked by intralayer covalent bonds and controlled by interlayer non-covalent forces. 2D COFs have a well-defined alignment of π building units in their atomic layers and segregated arrays of π columns in their frameworks. The elegant π skeletons of 2D COFs provide a fundamental basis for structural design.^[6] Meanwhile, the sizes, shapes, and environments of their 1D channels are fully controllable. Thus, the diverse skeleton, order porous structure, pre-designable functions, and high chemical stability endow COFs to apply in the gas / molecular adsorption, energy storage, electro-/photo- catalysis, conversion, semiconductor, and Li-ion batteries.^[7] The rational design, specific functionalization, and elaborate synthesis of COF structure are significant in preparing high-crystalline COF materials and improving their application properties.^[8] In addition, pyrolysis of COFs into functional carbons is a simple and efficient strategy to improve the conductivity. Therefore, exploring COF derivatives as electrocatalysts for electrocatalysis reactions is also significant for developing functional COFs. This chapter first discusses the structure, synthesis method, and properties of COFs and COF derivatives. Meanwhile, we also reviewed various application fields and recent developments in the COFs. Importantly, this thesis focused on the electrocatalysis application of COFs; thus, we summarized and discussed the field of electrocatalytic reactions, including the principle and current development of electrocatalytic oxygen reduction reaction (ORR), hydrogen evolution reaction (HER), oxygen evolution reaction (OER) and CO₂ reduction reaction (CO₂RR).

1.1.1 Design principle

The synthesis of COFs generally depends on kinetically controlled reactions. Dynamic covalent chemistry (DCC) deals with reversible covalent reactions that allow the free exchange of molecular components to achieve the thermodynamic minimum of the system at equilibrium.^[9-15] Different from noncovalent interactions and conventional covalent bond formation utilized in

supramolecular chemistry, DCC enables efficient thermodynamic equilibrium and exhibits “error checking” and “proof-reading” characteristics.^[16-21] Thus, the DCC is favoured for forming ordered, crystalline, and thermodynamic stability structure COFs. From the concept of DCC, those issues must be considered in the design and synthesis of COFs: the first is the linkages, which should be synthesized from reversible reaction; the second is the suitable building blocks.^[22-27]

1.1.2 Topologies

1.1.2.1 One-dimensional topology

Compared with two-dimensional COF, 1D COFs have abundant exposed edge sites owing to weaker pi–pi stacking of 1D chains.^[28] The feature can promote mass transport to the active sites of the framework and improve catalytic efficiency. 1D COFs are constructed from 1D-confined covalent linkages with noncovalent interactions (such as π – π interactions and hydrogen bonding) in the vertical 2D direction.^[29] In 2020, Yaghi and co-workers developed a 1D COF (COF-76) by using excess tris(4-aminophenyl)amine (TAA) and 1,3,6,8-tetrakis(p-formylphenyl)pyrene (TFPPy). More recently, Xu et al. constructed 1D COFs (PYTATPEDH-COF and TPETA-TPEDH-COF), showing an excellent electrocatalysis $2e^-$ pathway with a high H_2O_2 selectivity of 85.8% (Figure 1.1).^[30]

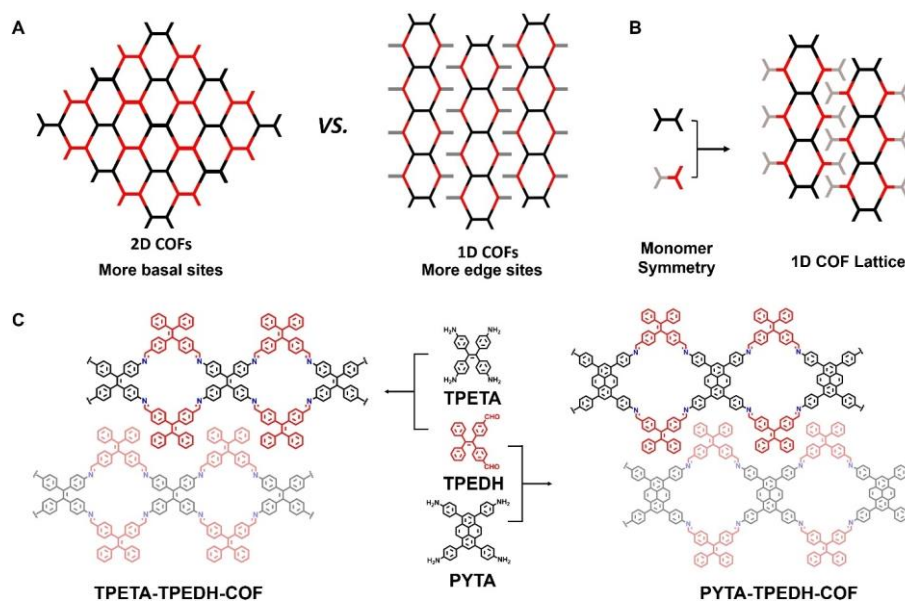


Figure 1.1 The designable principle and structure of 1D COFs for electrocatalytic systems.^[30]

1.1.2.2 Two-dimensional topology

The 2D COFs have regular channel structures and uniform pore size distributions. The symmetry and combination of monomers determine the pore shape, including hexagon, rectangle, diamond, and triangle.^[31]

COFs with hexagonal channels are generally achieved using C₂-symmetric monomer self-aggregation or copolymerization of C₂ and C₃-symmetric monomers. The copolymerization of C₄ and C₂ symmetric monomers or the copolymerization of C₄+C₄ symmetric monomers generally achieves rectangular channels. For example, Jiang et al. constructed COFs with a square pore size of 1.9 nm by copolymerizing phenol phthalocyanine monomers and p-phenyldiboric acid (Figure 1.2).^[32]

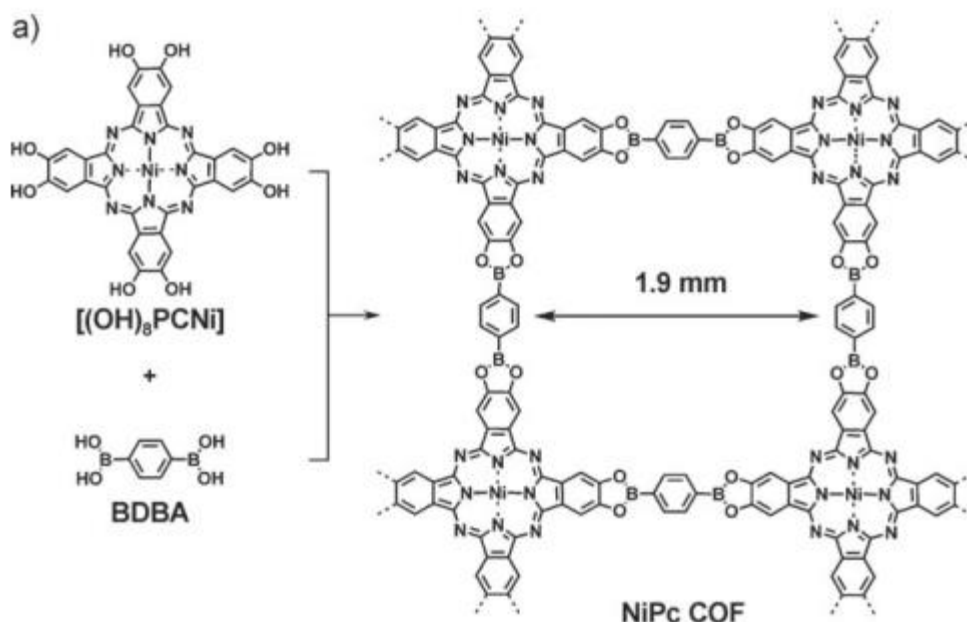


Figure 1.2 The structure of COFs with 2D pores.^[32]

1.1.2.3 Three-dimensional topology

2D COFs are formed by covalent bonds relying on intermolecular pi-pi interaction to layer-by-layer stack in the 3D space.^[33] The construction units of 3D COFs are generally selected modules with 3D spatial configuration, and the most used 3D core modules are tetraphenylmethane and amantadine monomers.^[34] One of the challenges in synthesizing 3D COFs is the unpredictability of spatial interpenetrating structures, which hinders the structure determination of 3D COFs. In 2009, Yaghi et al. first constructed a 3D COF with 5-fold interpenetration and dia topology.^[35] In 2018, Wang et al. created the single crystal structure of 3D COFs for the first time by using aniline as a crystallization regulator (Figure 1.3).^[36]

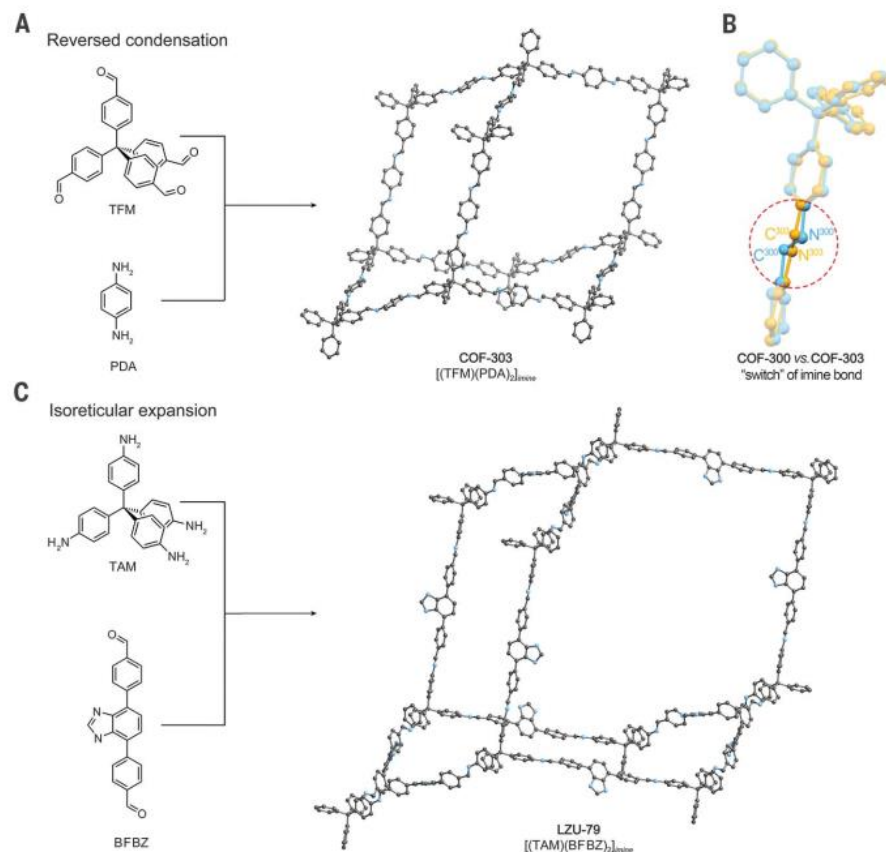


Figure 1.3 Single-crystal structures of 3D COFs.^[36]

1.2 Electrochemical Energy Storage and Conversion over the COFs

As a new energy storage and conversion technology, electrochemistry is considered the key to developing renewable and clean energy.^[37-40] Additionally, as the skeletons and pores of COFs can be systematically designed according to the topological design principle and can be synthetically controlled by judicious choice of building blocks, the functions of COFs could be designed and managed; this designability in both structures and functions is the significant feature of COFs that makes a sharp contrast to other extended porous materials.^[41-43] The design of COFs to create porous structures includes the design and control of pore shape, pore size, and pore environment, which are key parameters that determine sorption, separation, catalysis, and energy conversion and storage applications. Apart from the designable, the other important feature of COFs was pore surface engineer. Different functional groups could modify the pore

channels of COFs for different applications. The designable character and pore surface engineer features endow the frameworks with outstanding physicochemical properties, including optoelectronic, chemical sensors, and catalysts.^[44-45] Especially, various electric functional building blocks, excellent thermal stability, and 1D fast pore channels make COFs show superior performance in electrochemical energy storage and conversion devices, such as ORR, OER, and CO₂RR.^[46-49]

1.2.1 Oxygen reduction reaction

The traditional energy system with fossil energy has brought a double crisis of environmental problems, including carbon cycle imbalance and insufficient energy reserves.^[50] Thus, establishing a new energy system, such as fuel and metal-air cells, is the leading technology for energy and catalytic chemistry in the 21st century.^[51] ORR is a vital reaction involving various energy devices; it can also be used as a green oxidizer hydrogen peroxide synthesis reaction.^[52-58]

1.2.1.1 ORR over the COFs

In 2017, Luo et al. reported a reduced graphene oxide/CoCOF using pyridine-functionalized reduced graphene oxide as the building block. The optimized CoCOF with rGO exhibited high half-wave potential with 0.84 V, close to the commercial Pt/C.^[59] In addition, Tang and his co-workers constructed a 2D porphyrin COFs (M-TP-COF) with different metals for the ORR performance. The ORR catalytic activity of M-TP-COF was tuned by changing the M atom in the centre of the porphyrin backbone. Specifically, Co-TPCOF showed a more positive half-wave potential at about 0.73 V, higher than other M-TP-COF (Figure 1.4). The superior performance originated from the lower free energy change of the O₂-O₂*-OOH*-O*-OH*-OH route.^[60]

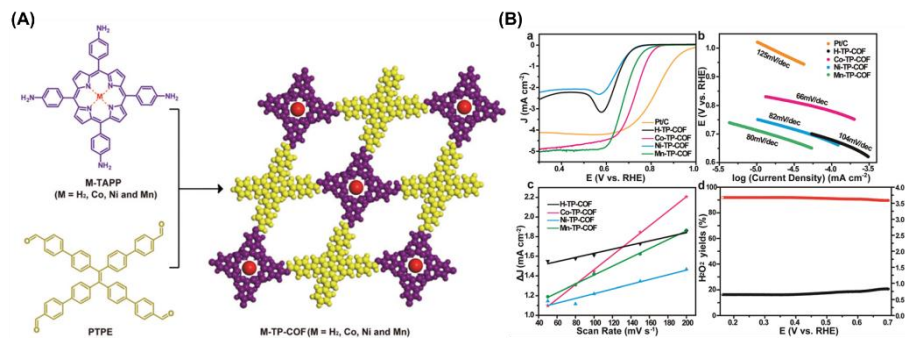


Figure 1.4 (A) The structure and (B) ORR performance of M-TP-COF.^[60]

In addition, the metal-free COFs also exhibited good ORR performance due to the fast mass transport and abundant heteroatoms.^[61-62] For example, the COFs (JUC-527-COF and JUC-528-COF) provided fast mass transport pathway in ORR process. And the JUC-528-COF had the onset potential of 0.83 V, and half-wave potential of 0.7 V (Figure 1.5).^[63]

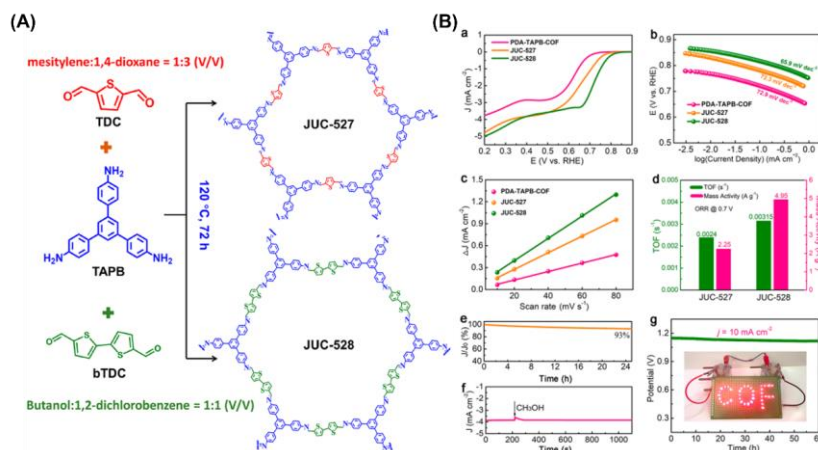


Figure 1.5 (A) The chemical structure and (B) ORR performance of JUC-527 and JUC-528.^[63]

In addition, Wang. et al. had constructed 3D thiophene-based COF as catalysts for ORR. The conjugated 3D COF (BUCT-COF-11) adopted dia topology with 11-fold interpenetration and a narrow band gap of 1.87 eV. The LSV curves showed that the BUCT-COF-11 had a half-wave potential of 0.72 V with a Tafel slope of 47 mV dec⁻¹, indicating a faster kinetic performance. It suggested that the more thiophene units contributed to higher catalytic activity. The DFT

calculation revealed that the introduction of thiophene promoted electronic conductivity along the frameworks and optimized the intermediates' binding ability. (Figure 1.6).^[64]

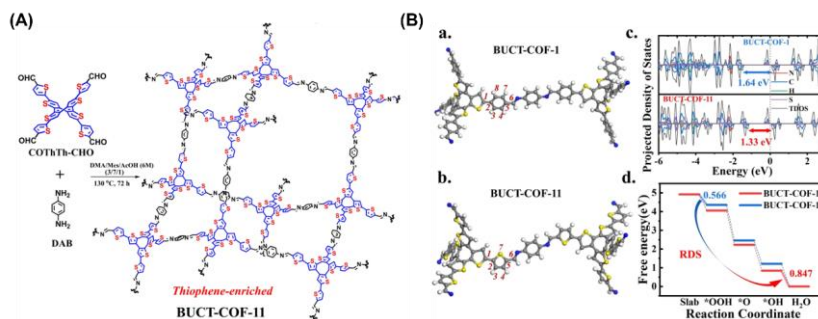


Figure 1.6 (A) The chemical structure and (B) DFT calculation of BUCT-COF-1/11.^[64]

In 2022, Long et al. first demonstrated that unsaturated bonds (UBs) precisely regulate the carbon environment of COFs' strategy to improve the activity. For example, Vinyl-COF and Azo-COF were synthesized by inserting UBs into a molecular framework model. The adsorption strength of Azo-COF is 1.52 eV, which is close to the optimal value of 1.81 to 2.88 eV, indicating that the adsorption capacity of Azo-COF is moderate. In particular, the presence of N=N bonds can generate additional electron distribution in the skeleton so that the catalyst molecules have more robust electron localization, which promotes the activation of the para C=N bond and makes it easier to adsorb OOH* (Figure 1.7).^[65]

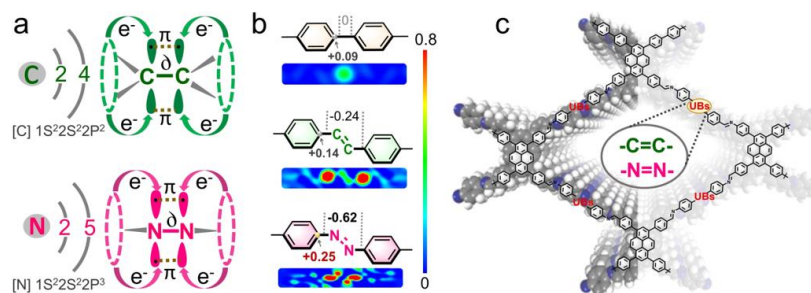


Figure 1.7 (a) The electronic structure of ethylene and azo bonds. (b) Mulliken charges and (c) the unsaturated bond decorated COFs.^[65]

In addition to the unsaturated bonds strategy, regulating the bonding state of methyl groups can also modulate catalytic properties. Solvothermal conditions synthesized the MFMG-COFs (BD-COF, MBD-COF, and DAF-COF). Among them, DAF-COF exhibited the highest ORR activity compared with BD-COF and MBD-COF catalysts; the good adsorption of DAF-COF to oxygen and its intermediates (OOH^*) improved the oxygen reduction kinetics (Figure 1.8).^[66]

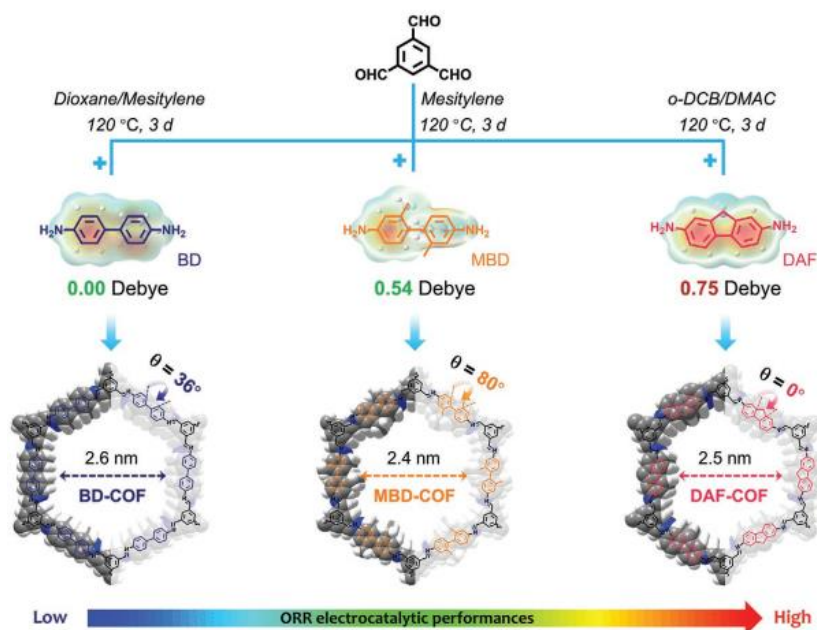


Figure 1.8 The heterocyclic-free biphenyl-based BD-COF, MBD-COF, and DAF-COF.^[66]

1.2.2 Oxygen evolution reaction

OER involves the process of four-electron transfer; thus, the kinetics is slower than that of another half-reaction. Additionally, the pathway of OER is complex.^[67-68] Due to the properties of proton coupling, the specific reaction pathway of the cathode and anode depends on the pH value of the electrolyte when electrolyzing water.

1.2.2.1 OER over the COFs

COFs offer a promising platform to construct electrocatalysts, including carbon dioxide reduction, oxygen reduction, hydrogen evolution, and OER reaction at

the molecular level due to their tunability of the skeletons and porosities. In 2016, Kurungot et al. constructed a Co-TpBpy-COF using bipyridine-containing frameworks as an OER catalyst. Specifically, the OER activity in phosphate buffer under neutral pH conditions exhibited an overpotential of 400 mV at a current density of 1 mA cm^{-2} (Figure 1.9).^[69]

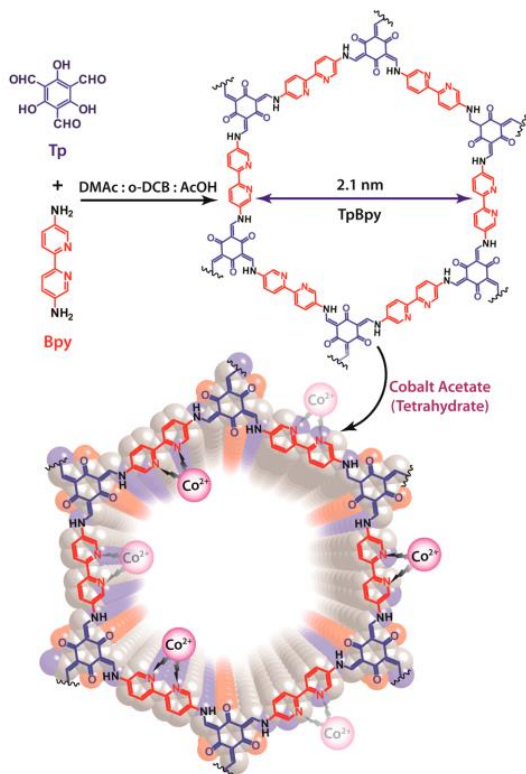


Figure 1.9 The chemical structure of Co-TpBpy-COF.^[69]

In the same year, Thomas et al. reported a COFs with inherent microporosity and template-induced, homogeneously distributed, yet tunable, macroporous structures. The resulting macro-CoCOF showed a high OER activity, which is much improved compared to the purely microporous COF with a competitive overpotential of 380 mV at 10 mA cm^{-2} (Figure 1.10).^[70]

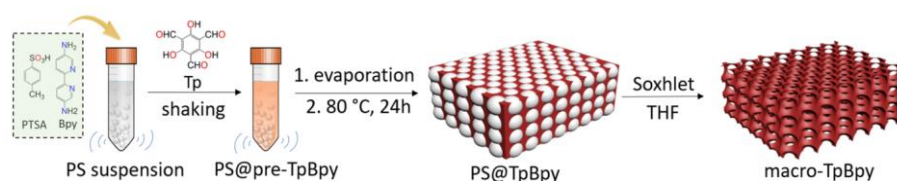


Figure 1.10 The scheme synthesis of macro-COFs.^[70]

In addition, Deng and his co-workers reported a methodology for the design of 3D COFs with different metals for the OER. Meanwhile, DFT calculations showed that Fe–N₃O-1, Fe–N₄, Co–N₂O₂, Ni–N₂O₂, Ni–N₃O-1, Ni–N₂O₂-1, and Fe–N₂O₂ possessed higher OER performances than other units. Among them, the experiments and DFT calculation confirmed the Ni–N₂O₂ sites in 3D COFs. Then, the current density reaches 10 mA cm⁻² at a low overpotential of 335 mV. Moreover, the extended 3D networks lengthen the distance for the electron transport, leading to suboptimal catalytic performance (Figure 1.11).^[46]

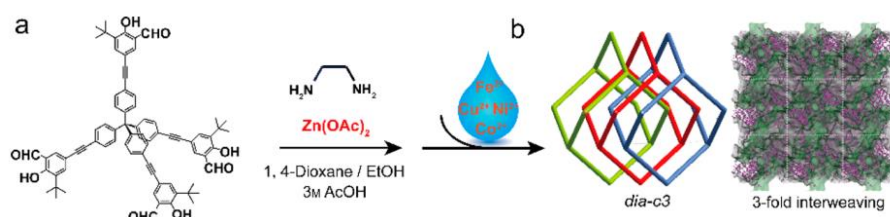


Figure 1.11 The scheme synthesis of 3D COFs with different metals.^[46]

1.2.3 CO₂ reduction reaction

The electrocatalytic CO₂RR process, combined with the utilization of green electricity, can convert CO₂ into high-value fuels and chemicals under mild conditions. This technology provides a sustainable path to maintain carbon balance and alleviate energy shortages. Specifically, CO₂ is reduced to a carbonized chemical substance at the cell's cathode, while oxidation occurs at the cell's anode (e.g., oxidation of water).^[71] Theoretically, the first step of the CO₂RR is forming *CO₂ free radicals after the adsorbed CO₂ molecules. However, this step would be realized when it gained an electron; thus, it is challenging owing to the theoretical potential of -1.9V vs. RHE.^[72] Generally, forming chemical bonds between CO₂ and catalyst can reduce the binding energy of CO₂ molecules and stabilize *CO₂ free radicals or reaction intermediates. Thus, reducing the negative redox potential and the overall activation energy are essential for the CO₂RR.^[73-74]

1.2.3.1 CO₂RR over the COFs

In 2015, Chang et al. reported a strategy of modularization for COFs by connecting cobalt-porphyrin units into frameworks via imine bonds and using them as catalysts for CO₂RR for the first time.^[75] Due to the π -conjugation and short interlayer distances, it exhibits high conductivity. In an aqueous solution with pH=7, the FE_{CO} reached 90% when the overpotential was -0.55V (vs. RHE), which was 26 times than that of the cobalt-porphyrin molecule and had a highly high long-term cycle stability. Homogeneous molecular catalysts are fixed in the frameworks of COFs by reticular chemistry, realizing the hetero-phase of homogeneous molecules, which can significantly increase the stability and activity of the catalyst. Therefore, COFs can regulate electrochemical properties by utilizing pore structures, various building blocks, and precise design functions (Figure 1.12).

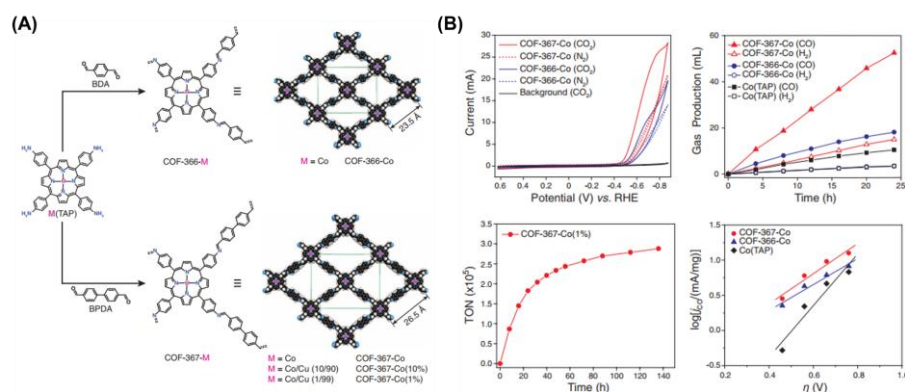


Figure 1.12 (A) Structure of COF-366 and COF-367 and (B) CO₂ electroreduction properties.^[75]

The porous properties of COF can enhance the diffusion efficiency of CO₂ molecules. In addition, rational-designed functional groups in COFs can be used as cocatalysts for other electrodes, further improving the catalytic efficiency.^[76] In 2018, Deng et al. reported 3D and 2D COFs with C-N bonds (COF-300-AR and COF-366-Co-AR) for the CO₂RR.^[77] The selectivity and activity were significantly improved using amine COFs and silver foil electrodes to construct molecularly defined interface (MDI) to cooperatively catalyse the

electrochemical reduction of CO₂ to CO. Specifically, compared with silver electrodes, the FE_{CO} increases from 13% to 53% at 0.70 V (vs. RHE) and from 43% to 80% at 0.85 V. Thus, the porosity of COF is conducive to the diffusion of CO₂ molecules to the surface of the silver electrode. The amine bonds near the surface of the electrode improve the CO₂ conversion efficiency by forming carbamate intermediates (Figure 1.13).

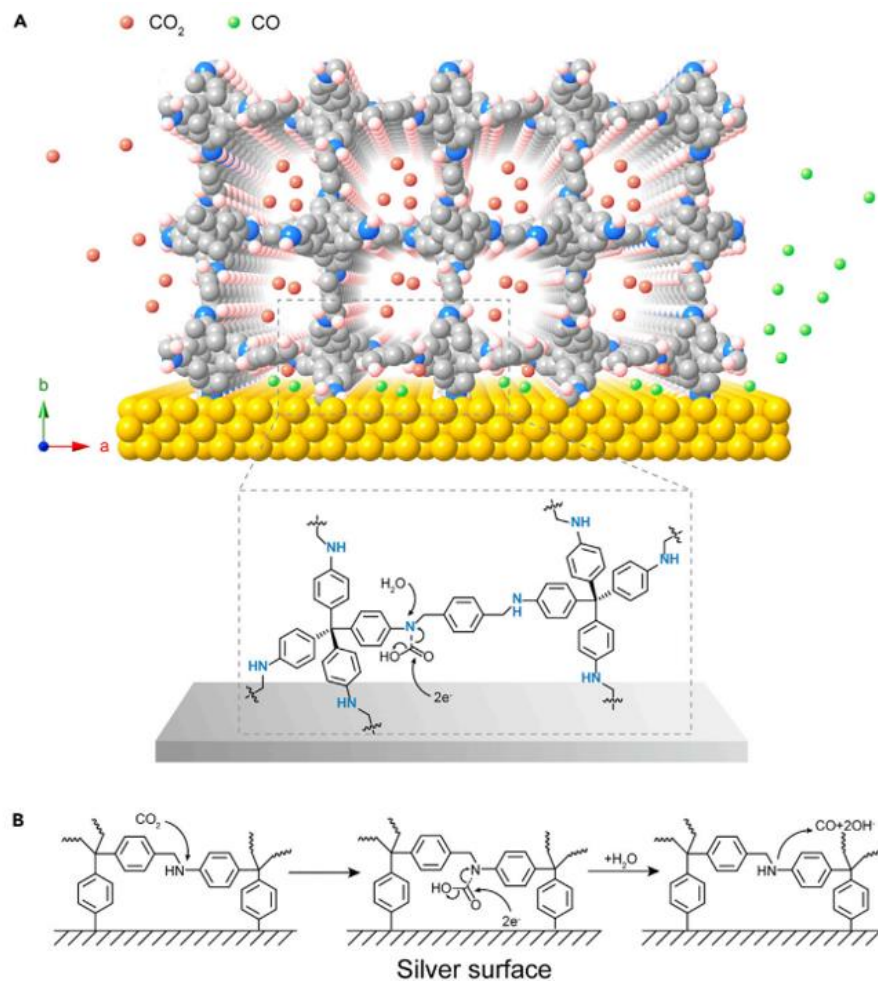


Figure 1.13 (A) Scheme of the molecularly defined interface and (B) the mechanism of concerted CO₂ reduction.^[77]

Furthermore, COFs containing iron (III) porphyrin units also showed high activity on CO₂RR. In 2019, Kubiak et al. investigated the CO₂RR performance of in situ synthesis of iron-porphyrin-containing COF (FeDhaTph-COF) on carbon cloth electrodes.^[78] Electrochemical experiments showed that the high

catalytic activity of FeTAPPCl molecules is retained in COF and showed higher FE_{CO} in acetonitrile and DMF electrolytes than in porphyrin molecules. The LSV curves and gas and liquid chromatography analysis at different potentials suggested that the FeDhaTph-COF electrode has good catalytic activity of CO_2 reduction to CO, with an average FE_{CO} of 80% (Figure 1.14).

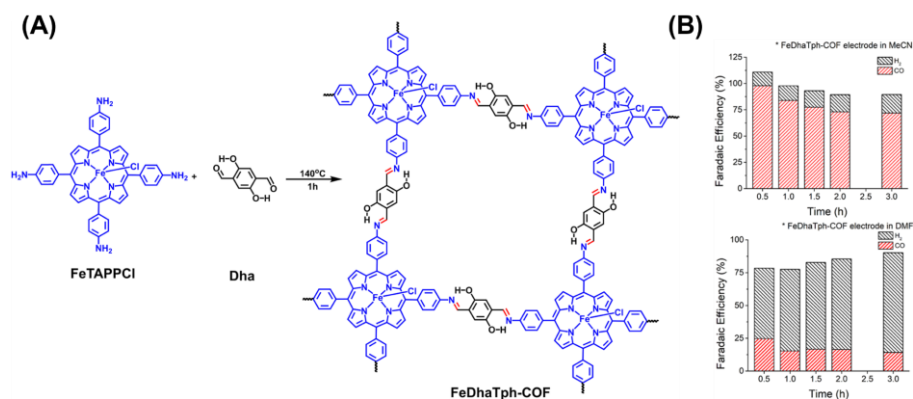


Figure 1.14 (A) The chemical structure and (B) CO_2RR performance of Fe-COF. [78]

It is important to design functional COFs rationally by introducing building units with specific functions.^[79] In 2019, Cao et al. constructed a COF containing donor-acceptor (D-A) heterojunction (TT-Por(Co)-COF) via imine condensation reaction for electrocatalysis CO_2RR . The TTPor(Co)-COF has good electron conductivity ($1.38 \times 10^{-8} \text{ S m}^{-1}$) and carrier mobility ($0.18 \text{ cm}^2 \text{ V}^{-1} \text{ s}^{-1}$).^[80] In addition, the LUMO of TT units has a higher potential (-3.47 eV) than that of Co-TAPP units, which facilitates electron transfer from TT units (donor) to the centre of Co-TAPP units (acceptor). In addition, TT-Por(Co)-COF showed a redshift in the solid-state ultraviolet spectrum compared to COF-366-Co, resulting in the electron transfer behaviour of TT-Por(Co)-COF. The CO_2RR tests showed that the FE_{CO} of TT-Por(Co)-COF is 91.4% at -0.6 V , and the current density is as high as 7.28 mA cm^{-2} at -0.7 V . This work provides a new way to improve CO_2RR performance by introducing D-A heterojunction into COFs to enhance electron transfer capability (Figure 1.15).

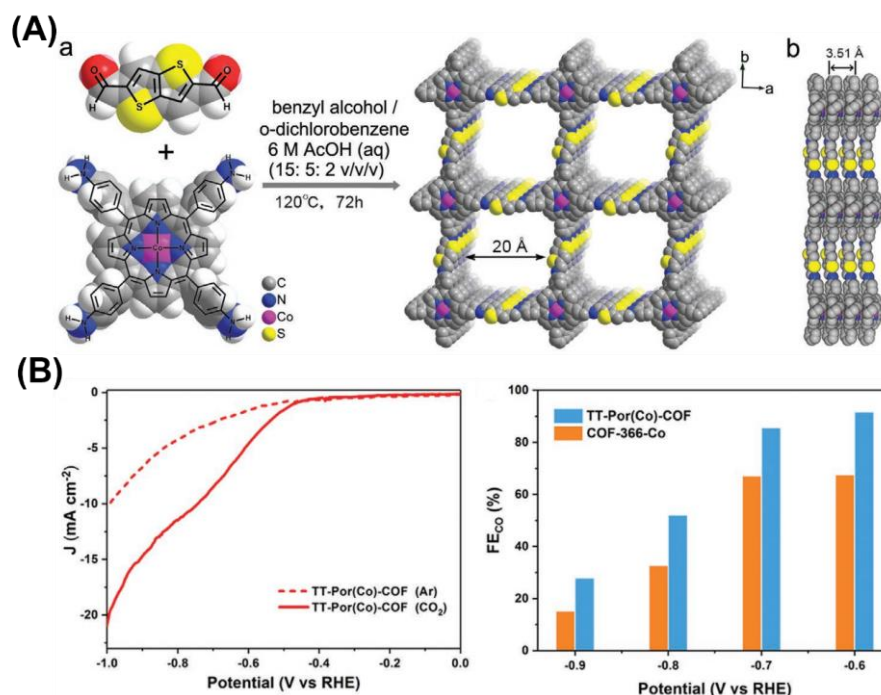


Figure 1.15 (A) Scheme of construction and (B) CO₂RR performance for the TT-CoPor-COF.^[80]

In 2020, Cao and his co-workers developed the 2D NiPc-COF nanosheet for CO₂RR. Due to its highly intrinsic conductivity and accessible active sites, the robust conductive 2D NiPc-COF nanosheets exhibit very high CO selectivity (>93%) in a wide range of the applied potentials and large partial current density of 35 mA cm⁻² at -1.1 V in aqueous solution (Figure 1.16).^[81]

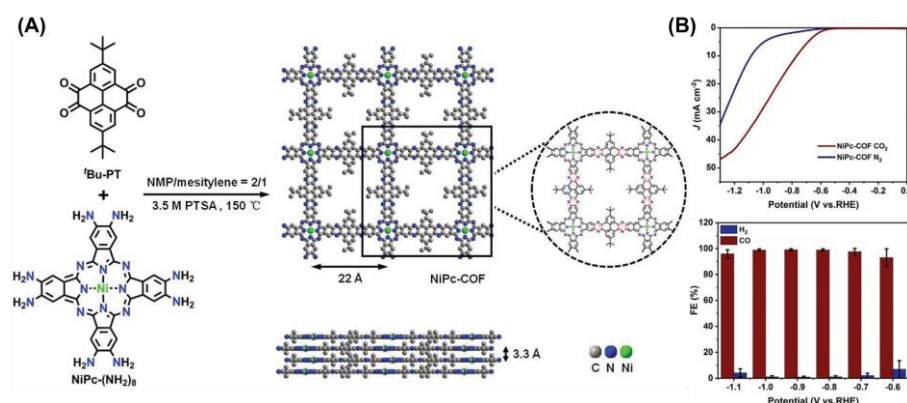


Figure 1.16 (A) Scheme of construction and (B) CO₂RR performance for the NiPc-COF.^[81]

In 2020, Jiang et al. synthesized a stable and electrically conductive CoPc-PDQ-COF as a catalyst for CO₂RR in water. The cobalt phthalocyanine molecules are connected by phenazine to form two-dimensional COFs in a quartet framework. In addition, this structure can be stable in boiling water, acids, and bases. The 2D lattice is completely π -conjugated along the x and y directions, and electrons can be transferred along the π -column along the z -axis. Thus, the FE_{CO} of the electrocatalyst is 96%, which is 32 times higher than that of the cobalt phthalocyanine molecular catalyst (Figure 1.17).^[82]

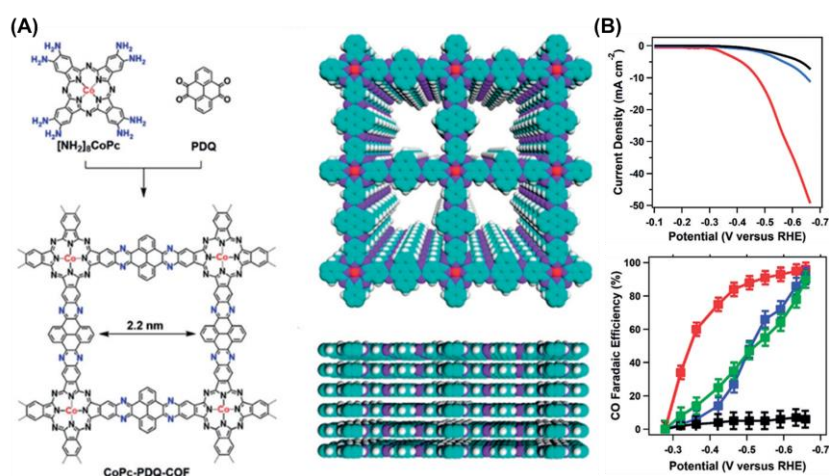


Figure 1.17 (A) Scheme of construction and (B) CO₂RR performance for the CoPc-PDQ-COF.^[82]

Furthermore, the dimensions could influence the densities of exposed catalytic sites, further influencing the performance. In 2022, Jiang et al. constructed two 3D imide-bonded COFs with pts topology via the imidization reaction between phthalocyanine-based tetra anhydride and 1,3,5,7-tetra(4-aminophenyl)adamantine. CoPc-PI-COF-3 doped with carbon black has been employed to fabricate the electrocatalytic cathode towards CO₂ reduction reaction within KHCO₃ aqueous solution, displaying the FE_{CO} of 88–96%. Notably, the unique 3D porous structure of CoPc-PI-COF-3 ensures the electrochemical surface concentration as high as 183 nmol cm⁻² on the electrode, namely 32.7% of total metal phthalocyanine subunits acting as active centres,

further resulting in the high activity and selectivity (Figure 1.18).^[83]

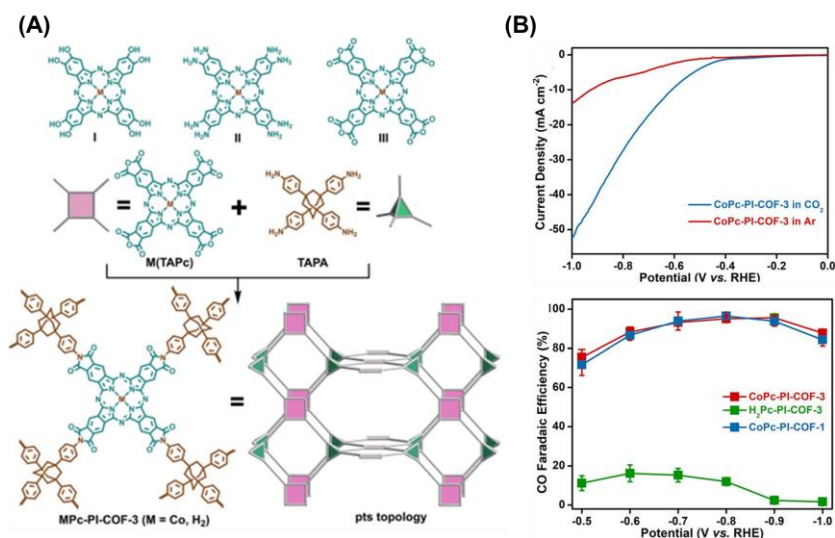


Figure 1.18 (A) Scheme of construction and (B) CO₂RR performance for the CoPc-PI-COF.^[83]

The kinds of catalytic sites also are essential factors in constructing COFs with stable frameworks for the CO₂RR. In 2021, Huang et al. designed and synthesized new kinds of ultrastable bimetallic polyphthalocyanine COFs constructed with the dioxin linkage through nucleophilic aromatic substitution. The bimetallic COFs with dioxin linkages showed an FE_{CO} of 97%. The DFT calculations further revealed that the Cu atoms in bimetallic COFs are supposed to accelerate the protonation process of adsorbed *CO₂ on Co species, further boosting the CO₂RR. This work offered a platform for the tailormade development of bimetallic electrocatalysts for CO₂RR (Figure 1.19).^[27]

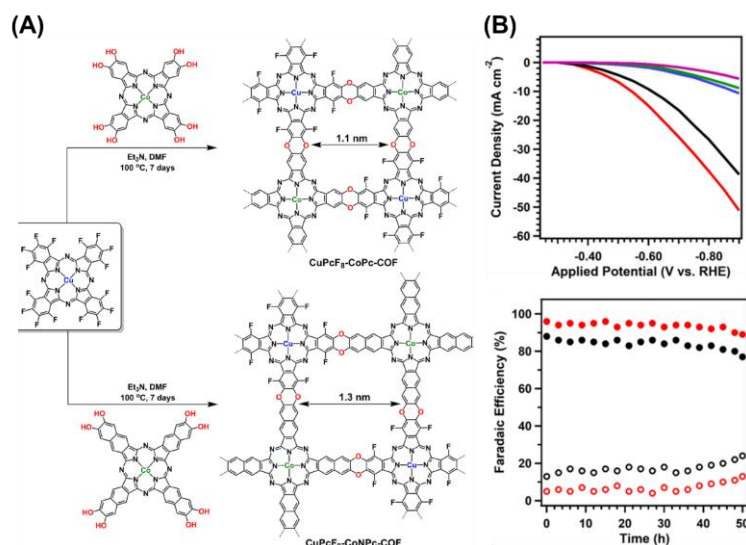


Figure 1.19 (A) Scheme of construction and (B) CO₂RR performance for the CuPcF₈-CoNPc-COF.^[27]

1.3 COF-derived carbon materials

COFs are a class of crystalline porous polymers with broad structural diversity, enabling synthetic control over their topologies, building blocks, and pores. COFs are comprised mainly of carbons and are versatile for integrating heteroatoms such as B, O, and N into the skeletons. The designable structure and abundant composition render COFs useful as precursors for the pyrolytic synthesis of heteroatom-doped carbons. However, the structure and morphology of COFs would collapse, which enhanced the difficulties in preparing functional carbons from COFs.^[84-85]

1.3.1 Electrocatalysis application over the COF-derivatives

In 2019, Sun et al. fabricated a nanostructured COF with preferentially exposed edges and converted it into porous standing carbon (Co@COF₉₀₀). In the Co@COF₉₀₀, the abundant edge sites of nanosized standing carbon layers served as anchoring sites for cobalt single atoms. Specifically, the performance of ORR in alkaline electrolytes is better than that of commercial Pt/C. The half-wave potential of Co@COF₉₀₀ is 0.86 V, and the diffusion current density is 6.2 mA cm⁻². In addition, Co@COF₉₀₀ has a half-wave potential of 0.65 V under acidic

conditions. This study provides reference and design ideas for COF's design of oxygen reduction catalysts (Figure 1.20).^[86]

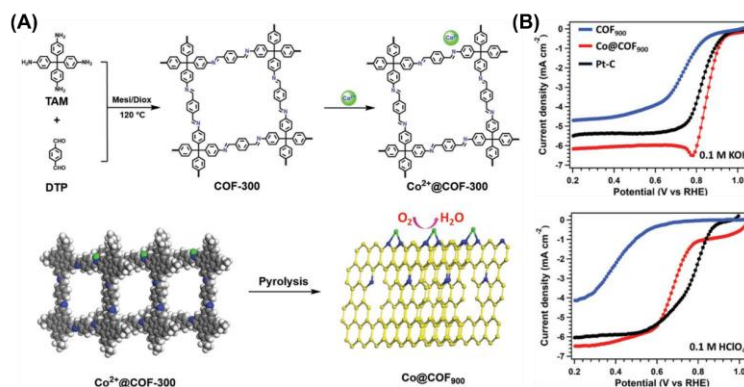


Figure 1.21 (A) Scheme of construction and (B) ORR performance of Co@COF₉₀₀.^[86]

Considering that the fully conjugated skeletons potentially converted into 2D carbons, Jiang et al. fabricated 2D carbon nanorods from a sp^2 carbon-linked COF. The 1D channels confined the Fe ions during pyrolysis, facilitating the formation of ultra-close atomic sites. Thus, this Fe-COF₉₀₀ displayed high catalytic activity towards oxygen reduction reaction, with a half-wave potential of 0.82 V. This work provided a new strategy for constructing a single-atom catalyst (Figure 1.22).^[87]

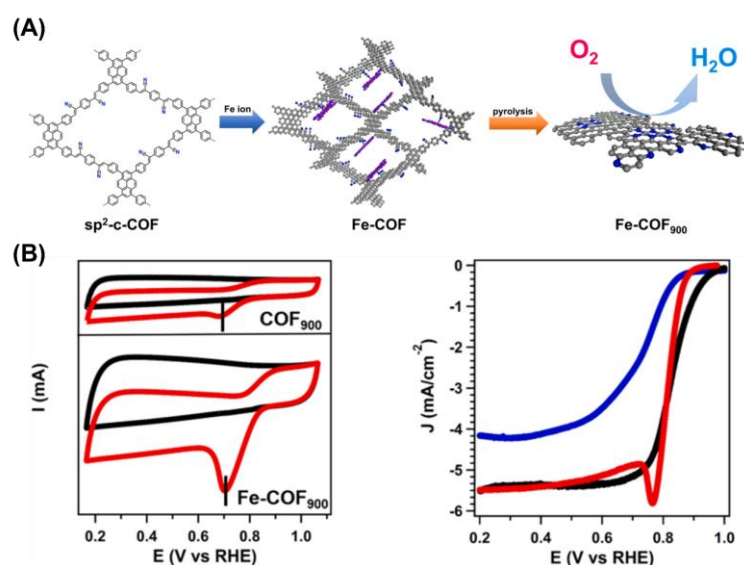


Figure 1.22 (A) Scheme of construction and (B) ORR performance of Fe-COF₉₀₀.^[87]

The low nuclear Pt atoms and nanoparticles are significant for the ORR performance. Generally, catalysts assembled with hierarchical Pt structures can integrate activity, selectivity, and stability for the ORR while balancing the cost of Pt. In 2023, Jiang et al. reported a highly active and stable ORR catalyst using COF-derived functional carbon to support Pt subnano- and nanoparticles (Pt-COF₉₀₀). The COF-derived carbon exhibits a high surface area and abundant N atoms, immobilizing Pt nanoparticles in the ORR process. Specifically, Pt-COF₉₀₀ exhibited a half-wave potential of 0.88 V, which was 30 mV more positive than that of commercial Pt/C in 0.1M KOH (Figure 1.23).^[88]

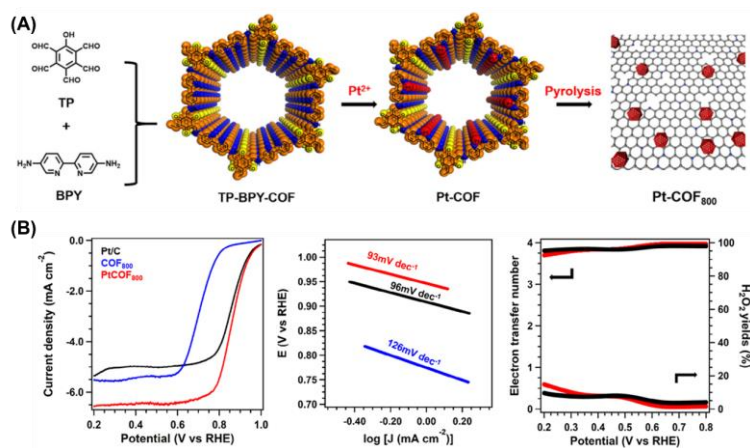


Figure 1.23 (A) Scheme of construction and (B) ORR performance of Pt-COF₉₀₀.^[88]

The construction of dual-metal sites can enhance the electrocatalysis ORR performance. However, developing dual-metal sites coordinating with different atoms in the oxides could quickly form the clusters. In 2023, Zeng et al. synthesized Fe₂@P-HC supported by P-doped hollow carbons (COFs and MOFs) for the ORR. The Fe₂@P-HC has catalytic sites of Fe₂N₅, which exhibited high catalytic activity and selectivity toward the ORR with a half-wave potential of 0.89 or 0.75 V under alkaline or acidic conditions. The theoretical calculations reveal that the P atoms in the Fe₂N₅P sites facilitate the OOH* formation and thus improve the activity (Figure 1.24).^[89]

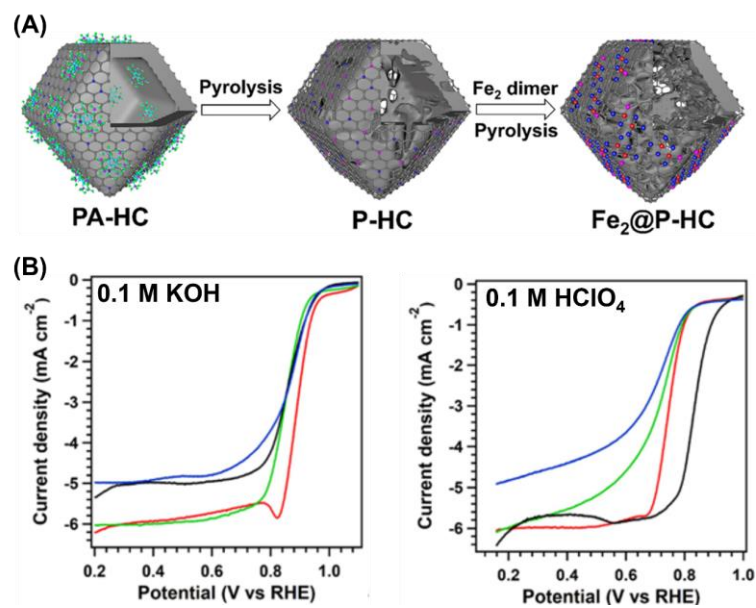


Figure 1.24 (A) Scheme of construction and (B) ORR performance of Fe₂@P-HC.^[89]

Chapter 2. Methodology and Techniques

Abstract

This chapter comprehensively describes the chemicals, experimental apparatus, and research methods utilized throughout this thesis. The research methods can be categorized into three primary classifications: synthesis method, material characterization, and electrochemical testing. These methodological divisions serve as the foundation for the subsequent chapters, forming the basis for the research approaches employed in this study.

2.1 Experimental Reagents and Apparatus

2-Methylimidazole were purchased from Aladdin. 2,4,6-Trihydroxybenzene-1,3,5-tricarbaldehyde (TP) and 2,2'-bipyridine-5,5'-diamine (BPY) were purchased from Alfa. Cobalt nitrate hexahydrate, methanol (MeOH), tetrahydrofuran (THF), ethanol (EtOH) and potassium hydroxide (KOH) were from Sinopharm Chemical Reagent Co.,Ltd. (*Chapter 2 and 3*)

1,10-phenanthroline-2,9-dicarbaldehyde (PTDE) and 4,4',4'',4'''-(pyrene-1,3,6,8-tetraol)tetraaniline (PYTA) and 4,4',4'',4'''-(pyrene-1,3,6,8-tetraol)tetrakis(ethyne-2,1-diyl)tetraaniline (PTTA) were obtained from Alfa.

Acetic acid, o-Dichlorobenzene (o-DCB), tetrahydrofuran (THF), mesitylene, dioxane and ferrous chloride (II) were obtained from Sinopharm Chemical Reagent Co.,Ltd. (*Chapter 4*)

Cohexadecafluorophthalocyanine (CoPc), ellagic acid (EA), [1,1'-biphenyl]-3,3',4,4'-tetraol (BP) were obtained from Alfa. Acetic acid, Mesitylene, 1,4-Dioxane, tetrahydrofuran (THF) and N,N-Dimethylformamide were obtained from Sinopharm Chemical Reagent Co.,Ltd. (*Chapter 5*)

pyromellitic dianhydride, urea, NH_4Cl , $(\text{NH}_4)_6\text{Mo}_2\text{O}_7$ and NiCl_2 were obtained from Alfa. HCl , NaOH and KHCO_3 were obtained from Sinopharm Chemical Reagent Co.,Ltd. (*Chapter 6*)

5,10,15,20-tetrakis(4-aminophenyl)porphinato]-cobalt (TAPP(Co)), 4,4',4'',4'''-(1,4-phenylenebis(azanetriyl))tetrabenzaldehyde (PATA), iodomethane (CH_3I) and NaBH_4 were obtained from Alfa. Acetic acid, o-Dichlorobenzene (o-DCB), tetrahydrofuran (THF), n-Butanol (BuOH) and Dimethylacetamide (DMAC) were obtained from Sinopharm Chemical Reagent Co.,Ltd. (*Chapter 7*)

2.2 Synthesis Methods

The synthesis of ZIF-67

7.17g $\text{Co}(\text{NO}_3)_2 \cdot 6\text{H}_2\text{O}$ was added into 1000 mL anhydrous methanol by stirred for 30 mins. In addition, 16.22 g 2-methylimidazole was dispersed in 1000 mL anhydrous methanol. Mix the above solution and stir magnetically for 24 hours. The ZIF-67 solid was washed with MeOH and THF in sequence and then dried in vacuum.

The synthesis of COF@ZIF-67

63 mg of TP in 50 mL THF and 83.7 mg of BPY in 50 mL THF were added into the mixture of ZIF-67 (500 mg) and THF (200 mL), which were then sonicated for 30 minutes and stirred at 25 °C for 24 hours to obtain ZIF-67-supported TP-BPY-COF (named as COF@ZIF). The collected COF@ZIF was washed with MeOH and THF in sequence and then dried in vacuum with the yield of 81% TP-BPY-COF.

The synthesis of ZIF₈₀₀

The as-prepared ZIF-67 were heated to 800 °C with a rate of 5 °C min⁻¹ and kept for 1 hour in N_2 to yield ZIF₈₀₀.

The synthesis of COF@ZIF₈₀₀

The as-prepared COF@ZIF were heated to 800 °C with a rate of 5 °C min⁻¹ and kept for 1 hour in N_2 to yield COF@ZIF₈₀₀.

The synthesis of PYTA-PTDE-COF

To prepare the PYTA-PTDE-COF, PTDE (0.3 mmol) and PYTA (0.3 mmol) were dispersed in 2 mL mixture solution with 1.0 mL 1,4-dioxane and 1.0 mL mesitylene in a Pyrex tube. After being sonicated for 5 min, 0.2 mL aqueous acetic acid (6 M) was added, and the mixture was sonicated to afford a homogeneous dispersion. Subsequently, the mixture was subjected to three freeze-pump-freeze cycles, then the tube was sealed off and heated at 120 °C for 72 h. The precipitate was collected by centrifugation and washed with THF and acetone. The collected powder was dried at 60 °C under vacuum for 12 h to afford the PYTA-PTDE-COF.

The synthesis of PTTA-PTDE-COF

To prepare the PTTA-PTDE-COF, PTDE (0.3 mmol) and PTTA (0.3 mmol) were dispersed in 1 mL mixture solution with 0.3 mL 1,4-dioxane and 0.7 mL mesitylene in a Pyrex tube. After being sonicated for 5 min, 0.1 mL aqueous acetic acid (6 M) was added, and the mixture was sonicated to afford a homogeneous dispersion. Subsequently, the mixture was subjected to three freeze-pump-freeze cycles, then the tube was sealed off and heated at 120 °C for 72 h. The precipitate was collected by centrifugation and washed with THF and acetone. The collected powder was dried at 60 °C under vacuum for 12 h to afford the PTTA-PTDE-COF.

The synthesis of 2D-COF

To prepare the 2D-COF, BPY (0.3 mmol) and PYTA (0.3 mmol) were dispersed in 3 mL mixture solution with 1.5 mL 1,4-dioxane and 1.5 mL mesitylene in a Pyrex tube. After being sonicated for 5 min, 0.1 mL aqueous acetic acid (6 M) was added, and the mixture was sonicated to afford a homogeneous dispersion. Subsequently, the mixture was subjected to three freeze-pump-freeze cycles, then the tube was sealed off and heated at 120 °C for 72 h. The precipitate was collected by centrifugation and washed with THF and acetone. The collected powder was dried at 60 °C under vacuum for 12 h to afford the 2D-COF.

The synthesis of Fe-COF

In a 50 mL round flask, 50 mg PYTA-PTDE-COF (PTTA-PTDE-COF or 2D-COF) and 2 mg ferrous chloride (II) were dispersed in 20 mL methanol, and the mixture was stirred for 72 h at 50 °C under N₂ atmosphere. The resulting solid was fully washed with THF and methanol. Then, the obtained material was dried at 60 °C for 12 h.

The synthesis of H₂Pc-COF.

A mixture of pyromellitic dianhydride (PMDA) (1.86 mmol), urea (40.10 mmol), NH₄Cl (5.00 mmol) and (NH₄)₆Mo₂O₇ (1.17 mmol) was degassed in a Pyrex tube (20 mL) by three freeze-pump-thaw cycles. The tube was sealed and heated at 180 °C for 3 hours. The precipitate was collected by centrifugation, washed with THF, 1.0 M HCl, 0.5 M NaOH and dried at 120 °C under vacuum overnight to give H₂Pc-COF in a yield of 86.7%.

The synthesis of 0.25NiPc-COF.

A mixture of pyromellitic dianhydride (PMDA) (1.86 mmol), urea (40.10 mmol), NH₄Cl (5.00 mmol), (NH₄)₆Mo₂O₇ (1.17 mmol) and NiCl₃ (0.21 mmol) was degassed in a Pyrex tube (20 mL) by three freeze-pump-thaw cycles. The tube was sealed and heated at 180 °C for 3 hours. The precipitate was collected by centrifugation, washed with THF, 1.0 M HCl, 0.5 M NaOH and dried at 120 °C under vacuum overnight to give 0.25NiPc-COF in a yield of 85.7%.

The synthesis of 0.5NiPc-COF.

A mixture of pyromellitic dianhydride (PMDA) (1.86 mmol), urea (40.10 mmol), NH₄Cl (5.00 mmol), (NH₄)₆Mo₂O₇ (1.17 mmol) and NiCl₃ (0.42 mmol) was degassed in a Pyrex tube (20 mL) by three freeze-pump-thaw cycles. The tube was sealed and heated at 180 °C for 3 hours. The precipitate was collected by centrifugation, washed with THF, 1.0 M HCl, 0.5 M NaOH and dried at 120 °C under vacuum overnight to give 0.5NiPc-COF in a yield of 86.1%.

The synthesis of 0.75NiPc-COF.

A mixture of pyromellitic dianhydride (PMDA) (1.86 mmol), urea (40.10 mmol), NH₄Cl (5.00 mmol), (NH₄)₆Mo₂O₇ (1.17 mmol) and NiCl₃ (0.63 mmol) was

degassed in a Pyrex tube (20 mL) by three freeze-pump-thaw cycles. The tube was sealed and heated at 180 °C for 3 hours. The precipitate was collected by centrifugation, washed with THF, 1.0 M HCl, 0.5 M NaOH and dried at 120 °C under vacuum overnight to give 0.75NiPc-COF in a yield of 86.1%.

The synthesis of NiPc-COF.

A mixture of pyromellitic dianhydride (PMDA) (1.86 mmol), urea (40.10 mmol), NH₄Cl (5.00 mmol), (NH₄)₆Mo₂O₇ (1.17 mmol) and NiCl₃ (0.84 mmol) was degassed in a Pyrex tube (20 mL) by three freeze-pump-thaw cycles. The tube was sealed and heated at 180 °C for 3 hours. The precipitate was collected by centrifugation, washed with THF, 1.0 M HCl, 0.5 M NaOH and dried at 120 °C under vacuum overnight to give 0.75NiPc-COF in a yield of 84.3%.

Synthesis of CoPc-EA-COF

A mixture of N,N-dimethylformamide (DMF, 0.5 mL), mesitylene (0.5 mL), CoPc (18.38 mg, 20 mmol), EA (12.08 mg, 40 mmol), and triethylamine (Et₃N, 0.1 mL) was degassed in a Pyrex tube (10 mL) by three freeze-pump-thaw cycles. The tube was sealed and heated at 100 °C for 7 days by a base-catalyzed nucleophilic substitution to construct the catalytic COFs. The precipitate was collected by centrifugation, washed with THF, and dried under vacuum overnight to give CoPc-EA-COF in a yield of 85%.

Synthesis of CoPc-BP-COF

A mixture of DMF (0.5 mL), mesitylene (0.5 mL), CoPc (18.38 mg, 20 mmol), [1,1'-biphenyl]-3,3',4,4'-tetraol (BP) (8.72 mg, 40 mmol), and Et₃N (0.1 mL) was degassed in a Pyrex tube (10 mL) by three freeze-pump-thaw cycles. The tube was sealed and heated at 100 °C for 7 days by a base-catalyzed nucleophilic substitution to construct the catalytic COFs. The precipitate was collected by centrifugation, washed with THF, and dried under vacuum overnight to give CoPc-BP-COF in a yield of 82%.

2.3 Characterization Methods

2.3.1 Routine properties

PXRD data were recorded on a Rigaku model RINT Ultima III diffractometer by depositing powder on glass substrate, from $2\theta = 2^\circ$ up to 90° with 1° increment. Nitrogen sorption isotherms were measured at 77 K with a Micromeritics Instrument Corporation model 3Flex surface characterization analyzer. The BET method was utilized to calculate the specific surface areas. By using the non-local density functional theory (NLDFE) model, the pore volume was derived from the sorption curve. FE-SEM images were obtained on a FEI Sirion-200 or Hitachi high technologies (SU-6600) field-emission scanning electron microscope at an electric voltage of 5 KV. EDX and elemental mapping were acquired using a HITACHI Miniscope TM3030. High-resolution transmission electron microscope images were obtained by transmission electron microscopy (TEM, FEI Tecnai G2). The metal content of samples was obtained using inductively coupled plasma optical emission spectroscopy on an Optima 8000 spectrometer. FT-IR spectroscopy was measured using KBr pellets on a Perkin Elmer Spectrum 100 spectrometer in the $500\text{-}4000\text{ cm}^{-1}$. UV-vis absorbance spectra were recorded on a Cary 5000 UV-vis spectrophotometer equipped with a mercury lamp. Substrates were mixed with BaSO_4 . Base line correction was done towards BaSO_4 . Spectra were taken over a wavelength range of 200-800 nm with a 5 min collection time and 1 nm resolution.

2.3.2 Pawley refinement

The PXRD pattern simulation was performed using a software package for crystal determination from PXRD pattern, implemented in Reflex module of Materials Studio. We performed Pawley refinement to optimize the lattice parameters iteratively until the R_p and R_{WP} values converge. The pseudo-Voigt profile function was used for whole profile fitting and Finger-Cox-Jephcoat

function was used for asymmetry correction during the refinement processes.

2.3.3 X-ray absorption fine structure measurements and data processing

The Ni / Co XAFS measurement was performed at BL14W1 station in Shanghai Synchrotron Radiation Facility (SSRF). The electron storage ring of SSRF was operated at 3.5 GeV, with a maximum current of 200 mA. Ni / Co K-edge XAFS data was collected using a fixed-exit Si(111) double-crystal monochromator. A Lytle detector was used to collect the fluorescence signal, and the energy was calibrated using metal foil. Utilizing the ATHENA module of the IFEFFIT software packages, the obtained extended XAFS (EXAFS) data were performed according to the standard procedures. The EXAFS contributions were separated from different coordination shells by using a hanning windows ($dk=1.0 \text{ \AA}^{-1}$). Subsequently, the quantitative curve-fittings were carried out in the R-space ($1.0\text{--}3.0 \text{ \AA}$) with a Fourier transform k-space range of ($3\text{--}10.5 \text{ \AA}^{-1}$) using the module ARTEMIS of IFEFFIT. During the curve-fitting, the overall amplitude reduction factor S_0^2 was fixed to the best-fit value of 0.85 determined from fitting the data of metal Ni / Co foil. For Ni / Co, the structural parameters, such as the coordination number N, interatomic distance R, the Debye-Waller factor σ^2 and the edge-energy shift ΔE_0 (eV) were allowed to vary during the fitting process.

2.4 Electrocatalysis testing

2.4.1 ORR testing

Catalyst (5 mg) was ultrasonic dispersed in a Nafion ethanol solution (0.25 wt.%, 500 μL) for 2 h to yield a homogeneous ink. The catalyst ink (12 μL) was pipetted onto a glassy carbon electrode ($d = 5.00 \text{ mm}$, $S = 0.196 \text{ cm}^2$) with a loading amount of 0.6 mg cm^{-2} . The commercial Pt/C catalyst (20 wt.% platinum on carbon black, BASF) was employed as a reference. The Pt/C

catalyst ink and electrode were prepared by the same conditions. All the electrochemical measurements were conducted in a conventional three-electrode cell using the electrochemical workstation (Pine Research Instrumentation, USA) at room temperature. The Ag/AgCl (3 M KCl) and platinum wire were used as reference and counter electrodes, respectively. A rotating ring disk electrode (RRDE) with a Pt ring and a glassy carbon disk served as the substrate for the working electrode for evaluating the ORR activity and selectivity of various catalysts. The electrochemical experiments were conducted in O₂ saturated aqueous solution of KOH (0.1 M) for ORR and in N₂ saturated aqueous solution of KOH (1.0 M) for HER, respectively. The RRDE measurements were conducted at a rotation rate of 1600 rpm with a sweep rate of 10 mV s⁻¹. On the basis of ring and disk currents, the electron-transfer number (*n*) and four-electron selectivity of catalysts based on the H₂O₂ yield (H₂O₂ %) were calculated from the equations of $n = 4 I_D / (I_R/N) + I_D$ and $H_2O_2 \% = 200 (I_R/N) / (I_R/N) + I_D$, where *I_D* and *I_R* are the disk and ring currents, respectively, and the ring collection efficiency *N* is 0.37. The Tafel slope was estimated by linear fitting of the polarization curves according to the Tafel equation ($\ln j = b \times \log j + a$, where *j* is the current density and *b* is the Tafel slope). For the cyclic voltammetry (CV) tests, the potential range was circularly scanned between 0.15 and 1.1 V at a scan rate of 50 mV s⁻¹ after purging O₂ gas for 30 min. To estimate the double layer capacitance, the electrolyte was deaerated by bubbling with nitrogen, and then the voltammogram was evaluated again in the deaerated electrolyte.

2.4.2 CO₂RR testing

The preparation of working electrode 5 mg COFs and 5 mg carbon black was grinded for 10 min and dispersed in mixed solution of 50 μL Nafion solution (5 wt%), ethanol (950 μL) followed with sonication for 120 min. The 320 μL as-prepared catalyst ink was directly spray-coated on a hydrophobic carbon paper

(1 cm × 1 cm) to form a 1 cm² catalyst area with a catalyst loading of 1 mg cm⁻². The deposited carbon paper was further dried at room temperature. All the electrochemical experiments were performed in a H-type cell with two-compartments separated by an anion exchange membrane (Nafion-117). Each compartment contained 70 mL electrolyte (0.5 M KHCO₃). Electrochemical measurements were performed in a three-electrode cell using the Ag/AgCl electrode as the reference electrode and Pt foil as the counter electrode on the electrochemical instrument (CHI760E). Before the electrochemical measurements, the electrolyte solution was purged with CO₂ for 30 min to obtain the CO₂-saturated solution. The pH is 7.2 for CO₂-saturated 0.5 M KHCO₃ and 8.8 Ar-saturated 0.5 M KHCO₃. A mass flow controller was used to set the Ar or CO₂ flow rate at 30. The LSV curves were conducted with scan rate of 10 mV/s. All the potentials were reported with respect to the reversible hydrogen electrode (RHE) and converted using the formula $E(\text{vs. RHE}) = E(\text{vs. Ag/AgCl}) + 0.196 \text{ V} + 0.059 \times \text{pH}$. Gas products were detected by gas chromatograph.

2.4.3 OER testing

Glassy carbon electrode: The catalyst (5 mg) with carbon black (8 mg) were ultrasonic dispersed in a Nafion ethanol solution (0.25 wt.%, 1000 μL) for 2 h to yield a homogeneous ink. The catalyst ink (5 μL) was pipetted onto a glassy carbon electrode (d = 0.25 cm, S = 0.19625 cm²) with a loading amount of 0.025 mg cm⁻².

Ni foam electrode: The working electrode was prepared by coating the catalyst ink onto a Ni foam (NF, 1 × 1 cm). In a typical process to prepare the catalyst ink, 8 mg catalyst (8 mg carbon black) was suspended in 2 mL mixed solvent containing ethanol and 5% Nafion (v/v = 9/1) to form a homogeneous ink. After sonication for 60 min, the catalyst ink was dripped on the two sides of the working electrode. The optimal mass loading is measured to be about 1 mg cm⁻².

For comparison, the commercial ruthenium oxide (RuO₂) catalyst was measured under identical conditions. The RuO₂ catalyst ink and electrode were prepared by the same conditions to that of COFs. All the electrochemical measurements were conducted in a conventional three-electrode cell using the electrochemical workstation (Pine Research Instrumentation, USA) at room temperature. The Ag/AgCl (3 M KCl) and platinum wire were used as reference and counter electrodes, respectively. The electrochemical experiments were conducted in N₂ saturated aqueous solution of KOH (0.1 M and 1.0 M) for OER. The Tafel slope was estimated by linear fitting of the polarization curves according to the Tafel equation ($\eta = b \times \log j + a$, where j is the current density and b is the Tafel slope).

2.4.4 Faradic efficiency calculation

$$FE = \frac{N \times F \times n_{CO}}{I \times 60 \text{ (s/min)}} \times 100\% \text{ (Equation 1)}$$

Where F is the Faraday constant; n_{CO} is the moles of produced CO (mol); I is total steady-state cell current (mA); N is the electron transfer number for product formation.

2.4.5 Turnover frequency calculation

The turnover frequency (TOF, s⁻¹) was evaluated by the following standard equation:

$$TOF = (J \times A) / (4 \times F \times n) \text{ (Equation 2)}$$

Where j (A/cm²) is the partial current for certain product;

A (cm⁻²) is the geometric surface area of the electrode;

F stands for the Faraday constant;

n (mol) is molar amount of Fe loaded on the gas chromatography electrode which was determined by the ICP analysis.

All metal cations in the COFs were assumed to be catalytically active, so the calculated value represents the lower limits of the TOF.

2.4.6 Mass activity calculation

The electrocatalyst metal loading (m) and the measured current density J (A cm⁻²).

mass activity (A mg^{-1}) = J/m (*Equation 3*)

2.4.7 Normalization of current density

The normalization process from current density (j) to the activity per active sites ($j_{\text{real/site}}$) was operated by following:

$j_{\text{real}} (\text{A/cm}^2) = j (\text{A/cm}^2 \text{ geo}) \times (1/\text{catalyst mass loading } (\text{mg}(\text{cat})/\text{cm}^2 \text{ geo}) \times (1/\text{Real active area } (\text{cm}^2 \text{ real} / \text{mg}(\text{cat})))$. (*Equation 4*)

2.4.8 Mott-Schottky curve test

Preparation of working electrode: 2 mg COF powder was mixed with 1.0 mL ethanol and 50 μL Nafion (5%) dispersion, and ultrasonic treatment was performed for 30 min. The resulting mixture slurry is evenly coated on the bottom of the ITO glass plate in the $1 \times 2 \text{ cm}^2$ area and placed in the air to stand for drying naturally.

Electrochemical measurements were performed in a three-electrode cell using the Ag/AgCl electrode as the reference electrode. Using 500 Hz and 1000 Hz to test the curve.

Chapter 3. Atomic Co-N₄ and Co nanoparticles confined in COF@ZIF-67 derived core-shell carbon frameworks: Bifunctional non-precious metal catalysts toward ORR and HER

3.1 Introduction

ORR and HER play vital roles in the electrochemical energy storage and conversion devices, including metal-air batteries, fuel cells, and water splitting. Up to now, Pt-based compounds were most employed as the catalysts for ORR and HER, due to their high activity.^[90-93] However, their high costs and weak durability impede their further applications. Thus, developing robust and highly active catalysts is highly desirable for ORR and HER. Recently, non-previous metal catalysts are getting more attentions owing to the affordable cost.^[94-96] Till now, there are two classes of hosts used to support metal atoms or nanoparticles, carbon-based materials including carbon nanotubes, graphene, and porous carbons, and metal-containing compounds such as oxides, dichalcogenides, carbides, and nitrides.^[97-99] Different from metal-containing support, carbon-based materials not only provide anchoring sites for the single metal atoms, offer good electrical conductance with the graphitic skeletons, but also manipulate the charge density and electronic structure of the metal atoms and nanoparticles.^[100-102]

COFs possess periodic atomic distribution, well-defined skeletons, ordered porous channels, which permits COFs as an ideal platform for catalysing ORR and HER with controlling the active sites of COFs.^[103-105] However, the poor conductivity of COFs limits their electro-catalytic behaviours. To improve the conductivity, pyrolysis COFs into functional carbons is a simple and efficient strategy.^[106] Nevertheless, the direct pyrolysis of COFs always made carbons with aggregated skeletons and collapsed pores. Thus, how to precisely

synthesize COF-derived carbons for bifunctional catalysts for ORR and HER is still under explored.

In this chapter, we have designed and synthesized Co nanoparticles and atomic Co-N₄ embedded carbons for catalyzing ORR and HER from a core-shell hybrid of COF and ZIF-67. The corresponding carbon possessed abundant active sites, multi-level porosity, and high graphitization degree. The COF-derivatives (COF@ZIF₈₀₀) were characterized and demonstrated the successful synthesis of porous carbon materials with Co-N₄ sites and Co clusters. Then, we studied the morphology of the synthesized materials, and found that COF@ZIF₈₀₀ is core-shell carbon frameworks. Electrochemical tests showed that the resultant COF@ZIF₈₀₀ exhibited bifunctional catalytic performance in ORR and HER, in which the excellent ORR performance with half-wave potential of 0.85 V in 0.1 M KOH and the outperformed catalytic behavior for HER with an overpotential of 0.16 V at 10 mA cm⁻² in 1 M KOH were achieved.

3.2 Results and discussion

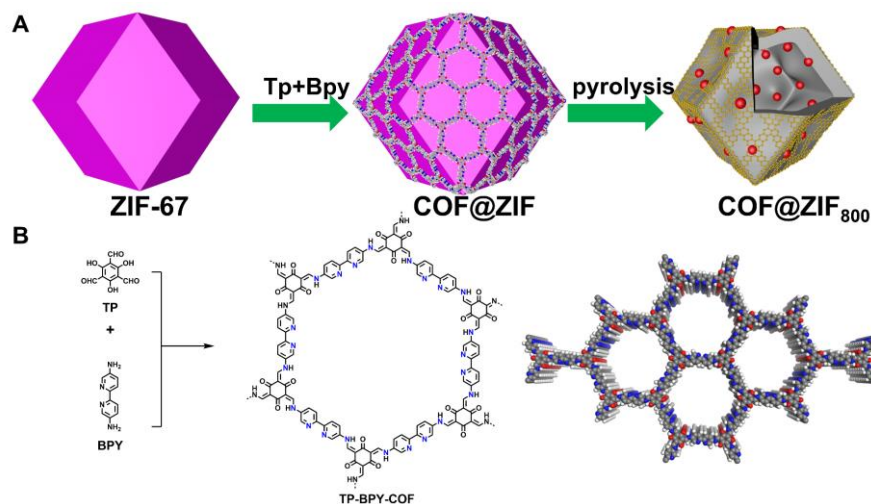


Figure 1. (A) Schematic of the synthesis procedure of COF@ZIF₈₀₀ catalyst by in-suit growing TP-BPY-COF on the surface of ZIF-67. (B) The synthesis and structure of TP-BPY-COF.

As illustrated in Figure 1, the preparation of COF@ZIF₈₀₀ involves creating ZIF-

67 nanocrystals, in-situ encapsulating ZIF-67 crystals with TP-BPY-COF thin layer (COF@ZIF) and controlled-pyrolyzing COF@ZIF in inert atmosphere.^[107]

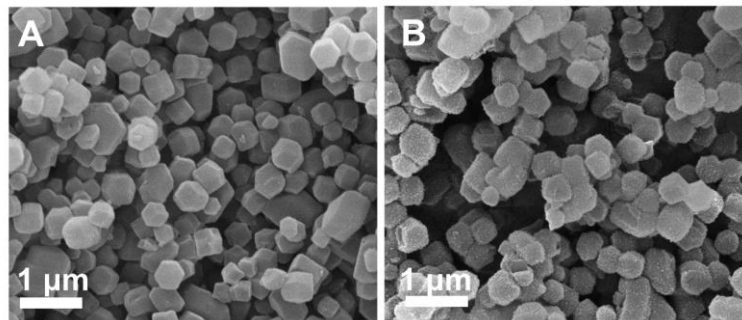


Figure 2. The SEM images of (A) ZIF-67 and (B) COF@ZIF.

The SEM images showed that the as-prepared ZIF-67 crystals presented a dodecahedron morphology with a uniform particle size of ~ 350 nm and smooth surface (Figures 2A). After TP-BPY-COF coating, the COF@ZIF particles were well isolated without visible aggregations, which retained the rhombic dodecahedral morphology and the similar particle size to that of ZIF-67 precursors (Figure 2B). This suggests that the TP-BPY-COF layer is thin. Although the COF@ZIF₈₀₀ particles were shrank in compared to their precursors, the framework morphology was well maintained without collapses. It indicated that the organic components of COF@ZIF were lost while the skeleton was well survived in the pyrolysis (Figure 2C).

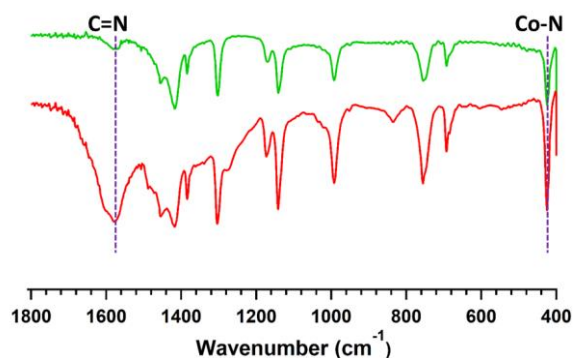


Figure 3. FT IR spectra of ZIF-67 (green) and COF@ZIF (red).

In addition, The FT-IR spectra showed that COF@ZIF posted a new vibration band at 1578 cm^{-1} , ascribed to C=N linkages, suggesting the successful

formation of TP-BPY-COF (Figure 3). At the same time, all bands of ZIF-67 can also be clearly identified from the spectrum of COF@ZIF. It revealed that the framework of ZIF-67 was intact during the coating of COF layer.

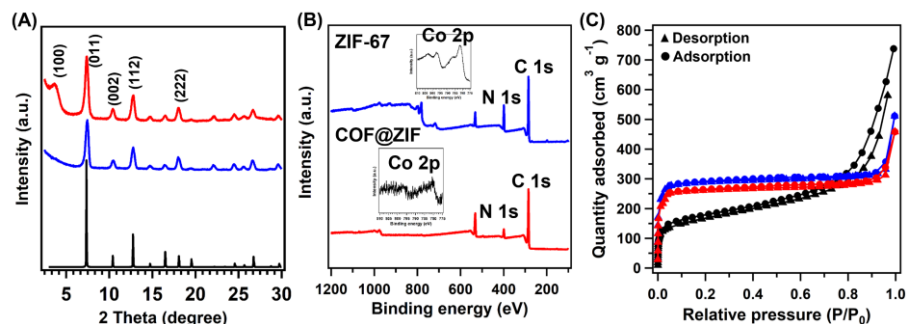


Figure 4. (A) PXRD patterns of ZIF-67 (blue), COF@ZIF (red) and the simulation of ZIF-67 (black). (B) XPS spectra of ZIF-67 (blue) and COF@ZIF (red). (C) Nitrogen sorption isotherm profiles at 77 K of COF (black), ZIF-67 (blue) and COF@ZIF (red).

With coating the COF on the surface of ZIF-67, all the peaks from ZIF-67 were well retained. According to simulated XRD pattern of ZIF-67 (Figure 4A, black curve), the peaks at 7.44°, 10.56°, 12.92° and 18.13° were from (011), (002), (112) and (222) facets (Figure 4A, blue curve), respectively. In addition, a new peak at 3.6° was clearly identified, which was from (100) facet of the COF (Figure 4A, red curve). The interface interaction between the shell layer and the core particle was proved by XPS measurements. The binding energy of Co peak decreased from 781 eV for ZIF-67 to 780 eV of COF@ZIF, suggesting the interaction between the Co ions and bipyridine units (Figure 4B). In addition, the Co content on ZIF-67 surface was 14.7 wt.%, closing to the elemental composition of ZIF-67, while COF@ZIF posted 1.0 wt.% Co, confirming that TP-BPY-COF thin layer was successfully formed. The pore structure of ZIF-67 and COF@ZIF was investigated by N₂ sorption isotherms at 77 K (Figure 4C). Both ZIF-67 and COF@ZIF showed a steep increase in the N₂ adsorption–desorption isotherms at P/P₀ around 0, which was due to the filling of micropores.^[108] The same slope in this region also indicated that both samples

had the similar micro-pore size. This further suggests that the structure of ZIF-67 cores is unchanged, and the outer layer TP-BPY-COF is thin. The S_{BET} for TP-BPY-COF, ZIF-67 and COF@ZIF were 574, 1439 and 1051 $\text{m}^2 \text{g}^{-1}$, with corresponding pore volumes of 1.14, 0.65 and 0.51 $\text{cm}^3 \text{g}^{-1}$, respectively. In addition, the S_{BET} of mesopores for TP-BPY-COF and ZIF-67 in the COF@MOF were 406, 117, 105 $\text{m}^2 \text{g}^{-1}$. According to the S_{BET} of mesopores, the weight of COF was 3.2 wt.% and ZIF-67 was 96.8 wt.% in the COF@MOF. Then, we updated the manuscript (Page 49).

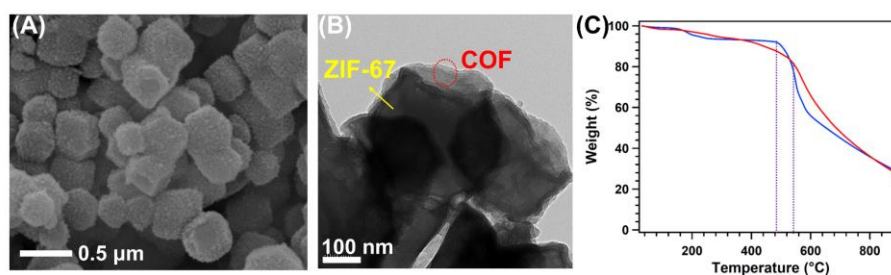


Figure 5. (A) SEM image, (B) HR-TEM image and (C) TGA curves of ZIF-67 (blue) and COF@ZIF (red).

Similar to the SEM observations, the transmission electron microscope (TEM) image of COF@ZIF displayed well separated nanocrystals with rhombic dodecahedral structure (Figure 5A). With higher resolution, it is clear to observe that COF@ZIF nanocrystal was composed by the regular crystal core and the outer shell with a thickness of ~ 30 nm (Figures 5B). Thermal gravimetric analysis (TGA) measurements of ZIF-67 and COF@ZIF samples were conducted under N_2 . ZIF-67 showed obvious decompose at 500 $^\circ\text{C}$, while the beginning decomposition temperature for COF@ZIF was about 550 $^\circ\text{C}$ (Figure 5C). It is reasonable that the interactions between ZIF-67 cores and TP-BPY-COF shell increase the thermal stability of COF@ZIF.

To investigate the effects of core-shell structure on the properties of pyrolysis products, both ZIF-67 and COF@ZIF samples were heated at 800 $^\circ\text{C}$ in N_2 for 1 h to prepare the ZIF₈₀₀ and COF@ZIF₈₀₀, respectively. The PXRD patterns revealed that the peaks at 26.5 $^\circ$, 44.1 $^\circ$, 52.5 $^\circ$ and 76.8 $^\circ$ were ascribed to graphitic

carbon (002), (111), (200) and (220) facets of Co (Figure 6A), respectively. It indicates that the organic groups of precursors were decomposed, and the crystalline structure of ZIF-67 was totally changed, leaving the inorganic graphitic-skeletons and metallic particles.

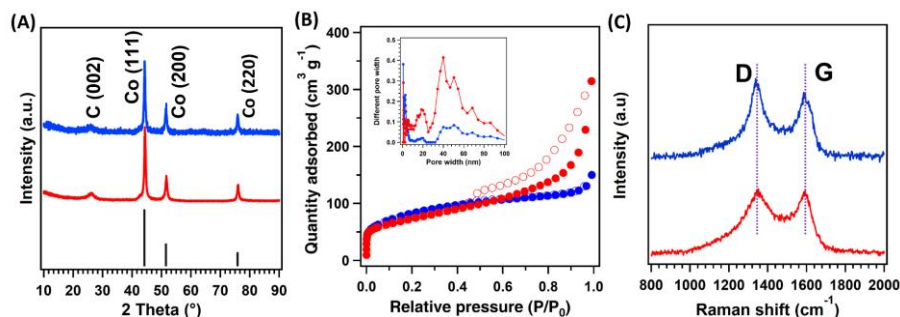


Figure 6. (A) PXRD patterns and (B) Nitrogen sorption isotherm profiles at 77 K (inset: pore size distribution curves) and (C) Raman spectra of ZIF₈₀₀ (blue) and COF@ZIF₈₀₀ (red).

The N₂ sorption curve of COF@ZIF₈₀₀ exhibited the type-IV isotherms with an obviously bigger hysteresis loop than that of ZIF₈₀₀ in the region $0.5 < P/P_0 < 1.0$, suggesting enhanced mesopores in COF@ZIF₈₀₀ (Figure 6B). Correspondingly, COF@ZIF₈₀₀ owned a total pore volume of $0.48 \text{ cm}^3 \text{ g}^{-1}$ and a mesopore volume of $0.26 \text{ cm}^3 \text{ g}^{-1}$ (accounting pore size $> 20 \text{ nm}$), which were much larger than those of ZIF₈₀₀ (total- and meso-pore volumes of 0.23 and $0.04 \text{ cm}^3 \text{ g}^{-1}$, respectively) (Figure 6B, inset). With the increasing of mesopore, the S_{BET} of COF@ZIF₈₀₀ was slightly decreased from $303 \text{ m}^2 \text{ g}^{-1}$ for ZIF₈₀₀ to $244 \text{ m}^2 \text{ g}^{-1}$. Therefore, the core-shell COF@ZIF structure is helpful to form mesopores in the catalyst, which benefits mass transport in the electrochemical processes. The Raman spectra of ZIF₈₀₀ and COF@ZIF₈₀₀ provided the characteristic signals of graphitic carbon, which contained a G band at 1590 cm^{-1} , arising from the first-order scattering of sp² carbon atoms in a 2D hexagonal lattice, and a D band at 1354 cm^{-1} , ascribed to the vibrations of carbon atoms in plane terminations of disordered graphite (Figure 6C).^[109] The intensity ratio of the D and G band (I_D/I_G), which was sensitive to the level of disorders and

defects on the carbon backbone, was decreased from 1.07 of ZIF₈₀₀ to 0.96 of COF@ZIF₈₀₀. It indicates that the COF@ZIF structure is helpful to form more order graphitic carbon in the pyrolysis.

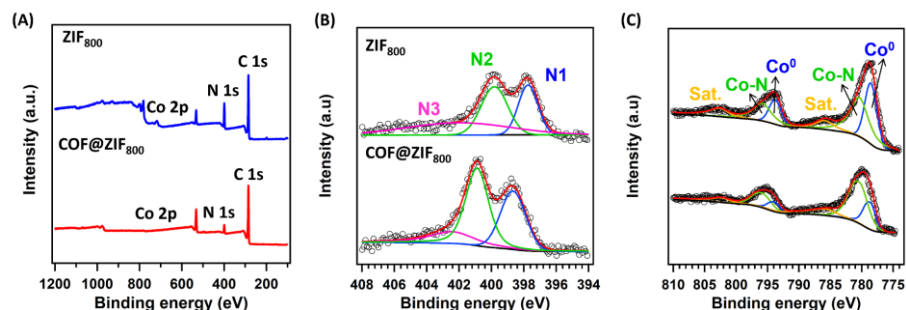


Figure 7. (A) The XPS spectra, (B) high-resolution N 1s spectrum and (C) high-resolution Co 2p spectrum of ZIF₈₀₀ and COF@ZIF₈₀₀.

The XPS measurements unveiled C, Co, N, and O elements on the sample surface. ZIF₈₀₀ contained 9.51 wt.% Co and 5.22 wt.% N while COF@ZIF₈₀₀ had 5.98 wt.% Co and 4.41 wt.% N on surface (Figure 7A). As no Co existed in the precursor of TP-BPY-COF, the enrichment of Co on the surface of COF@ZIF₈₀₀ revealed the migration of Co from core to surface during the pyrolysis. The high-resolution N 1s spectrum of ZIF₈₀₀ can be deconvoluted into three peaks centred at ~397.7, ~399.8, and ~402.0 eV, which can be ascribed to pyridinic N (N1, weighting 27.7%), pyrrolic N (N2, 36.1%), and graphitic N (N3, 36.2%), respectively (Figure 7B). Similarly, the XPS N 1s of COF@ZIF₈₀₀ also displayed these types of nitrogen. However, the binding energies of these peaks were left-shifted by ~0.7 eV. This suggests that the main element Co contributes different interaction strengths with nitrogen in ZIF₈₀₀ and COF@ZIF₈₀₀. In addition, the relative content of pyridinic N in COF@ZIF₈₀₀ increased to 34.5%. It has been reported that the carbon atoms next to the pyridinic N were active sites in catalyzing ORR.^[110] Therefore, the increased ratio of pyridinic N portends an enhanced activity of COF@ZIF₈₀₀ in the electrochemical reaction. The Co 2p spectra exhibited two prominent peaks of Co 2p_{1/2} and Co 2p_{3/2}, locating at ~795.6 and ~779.8 eV, respectively (Figure

7C). The deconvoluted peaks at 778.7 and 780.5 eV were assigned to Co (0) and Co-N, respectively, in which the Co-N content in COF@ZIF₈₀₀ significantly increased from 50.5% of ZIF₈₀₀ to 55.2%. The COF-shell binding with Co²⁺ promoted forming Co-N in pyrolysis process. It confirms that Co element provides more interactions with N in COF@ZIF₈₀₀, in line with the observations from N 1s spectra.

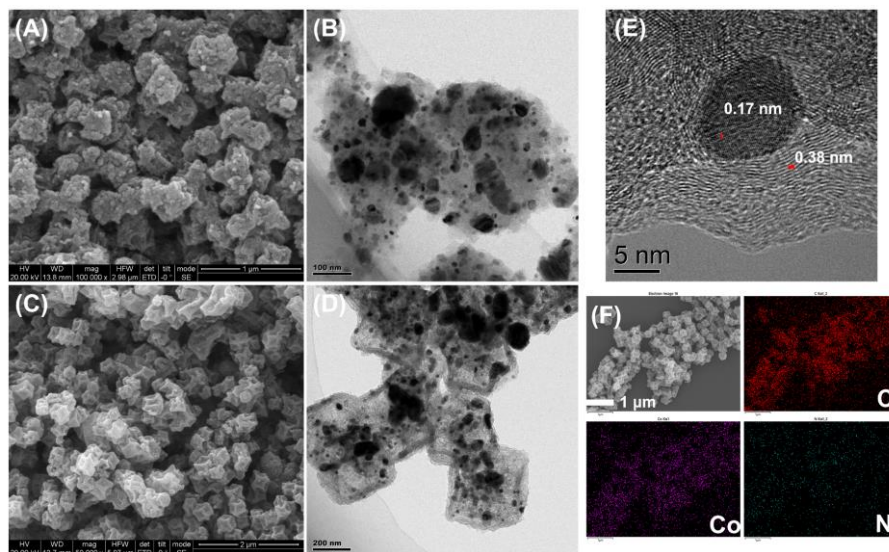


Figure 8. (A) The SEM and (B) TEM images of ZIF₈₀₀. (C) The SEM and (D) TEM images of COF@ZIF₈₀₀. (E) The HR-TEM image and (F) EDX-mapping images of COF@ZIF₈₀₀.

The morphology and structure of ZIF₈₀₀ and COF@ZIF₈₀₀ were further investigated by SEM and TEM. The SEM images showed that the ZIF₈₀₀ samples had lost the regular crystal structure of ZIF-67, resulting in obvious collapse and aggregation (Figure 8A). This was further proved by the TEM observations, which displayed the unregular broken fragments with scattering 15–50 nm particles (Figure 8B). In contrast, both SEM and TEM views presented that COF@ZIF₈₀₀ particles have dodecahedral morphology similar to that of COF@ZIF, without collapse and aggregation (Figures 8C and 8D). Moreover, the TEM image of single COF@ZIF₈₀₀ particle showed a perfect core-shell structure, being composed of ~ 40 nm thick regular shell and the

shrunk core. The Co nanoparticles with 5–10 nm size were uniformly strewed on the area of ZIF₈₀₀ core as well as the region of shell, confirming the migration of Co element from ZIF-67 core to TP-BPY-COF shell during the pyrolysis. It indicates that the pyrolysis product of TP-BPY-COF takes stronger skeleton than that of ionic bonded ZIF-67, which not only suppresses the collapse of COF@ZIF structure but also avoids the agglomeration and growth of Co particles. The high- resolution TEM image of COF@ZIF₈₀₀ showed that the ordered microstructure had interplanar spacings of 0.17 and 0.38 nm, assigned to Co (200) and nitrogen-doped graphite (002), respectively, which was well consistent with the XRD results (Figure 8E). As reported, the ordered graphitic carbon encapsulated metallic nanoparticles would enhance not only the anchoring force but also the stability in reactions.^[111] In addition, graphite-confined metal particles (e.g., Pt) have exhibited superior activities for the electrocatalysis of water oxidation because the electrons of metal atoms can penetrate through the graphene shell to promote the catalytic reaction.^[112] The EDX mapping images confirmed that all the elements of C, N and Co were uniformly distributed in the carbon matrix (Figure 8F).

The electrochemical catalytic performance of catalysts was initially evaluated by CV measurement in O₂-saturated or N₂-saturated 0.1 M KOH aqueous solution at a scan rate of 50 mV s⁻¹ (Figure 9A and 9B). The CV curves post obvious peaks for both ZIF₈₀₀ and COF@ZIF₈₀₀ only under O₂ atmosphere rather than N₂, suggesting their catalytic activity for oxygen conversion. In addition, the peak positions for ZIF₈₀₀ and COF@ZIF₈₀₀ were 0.71 and 0.75 V, respectively, indicating that COF@ZIF₈₀₀ possessed higher activity than that of ZIF₈₀₀.

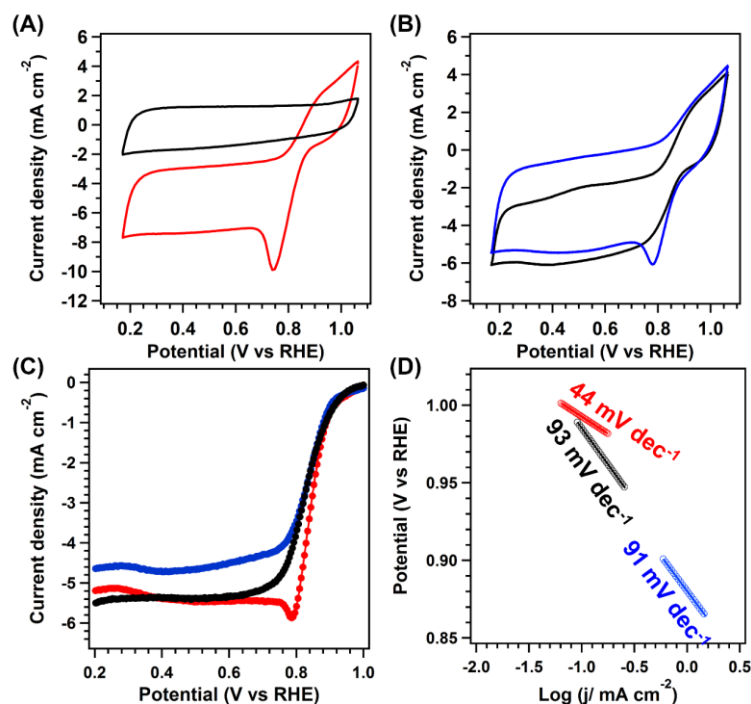


Figure 9. The CV curves of (A) COF@ZIF₈₀₀ and (B) ZIF₈₀₀ under N₂ (black) or O₂ (red and blue) atmosphere. (C) LSV curves and (D) Tafel slopes of ZIF₈₀₀ (blue), Pt/C (black) and COF@ZIF₈₀₀ (red).

The LSV curves were obtained by the RDE measurement at 1600 rpm in O₂-saturated KOH solution (Figure 9C). For comparison, the commercial Pt/C catalyst was employed as a control. The E_0 and $E_{1/2}$ for Pt/C were 0.92 and 0.81 V, respectively. The E_0 and $E_{1/2}$ for ZIF₈₀₀ were 0.96 and 0.81 V, which were close to those of Pt/C. However, the limited current density was 4.6 mA cm⁻², lower than that of Pt/C (5.5 mA cm⁻²). Notably, the COF@ZIF₈₀₀ displayed higher activity than that of Pt/C. And the E_0 and $E_{1/2}$ for COF@ZIF₈₀₀ were 0.99 and 0.85 V, which were 70 and 40 mV more positive than those of Pt/C, respectively. The corresponding Tafel slope for COF@ZIF₈₀₀ was 44 mV dec⁻¹, remarkably lower than that of Pt/C (93 mV dec⁻¹) and ZIF₈₀₀ (91 mV dec⁻¹), indicating the favourable kinetic behavior (Figure 9D). The E_0 , $E_{1/2}$ and Tafel slope for COF@ZIF₈₀₀ exceeded most reported Co-based catalysts (Table 1).

Table 1. Summary of electrocatalysts for ORR in 0.1 M KOH.

Catalysts	E_0 (V vs. RHE)	$E_{1/2}$ (V vs. RHE)	Tafel slope (mV dec ⁻¹)	Reference
COF@ZIF ₈₀₀	0.99	0.85	44	This work
Co-NC@600	0.94	0.83	67	[113]
Co ₂ P/CoN-NCNTs	0.96	0.85	49	[114]
CoTBrPP@bio-C	0.93	0.85	55	[115]
Co-NC@CC	0.94	0.81	76	[116]
FeP/Fe ₂ O ₃ @NPCA	0.95	0.84	88	[117]
Co/N-C(PA)	0.95	0.85	63	[118]
Co-SAs@NC	0.96	0.82	-	[119]
CAN-Pc(Fe/Co)	0.95	0.84	54	[120]
L-CCNTs-Co-800	0.90	0.84	54	[121]
CoNi@NCNT/NF	0.97	0.87	-	[122]
CoO _x NPs/BNG	0.95	0.81	57	[123]

With different scan rates in RDE measurements, moreover, the kinetic current densities for COF@ZIF₈₀₀ at 0.30 V was 6.28 mA cm⁻², respectively, which are much higher than those of Pt/C (5.24 mA cm⁻²) (Figures 10A-10C). The selectivity for the catalysts was then explored by the rotating ring-disk electrode (RRDE) measurements. Both of catalysts catalyzed ORR in 4e⁻ pathway.

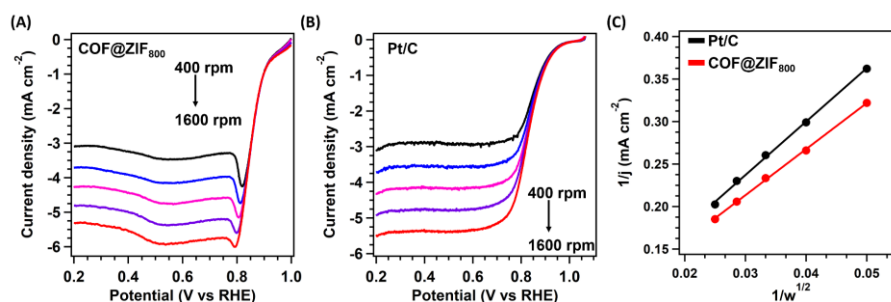


Figure 10. The LSV curves with different scan rates of (A) COF@ZIF₈₀₀ and (B) Pt/C. (C) The kinetic current densities of COF@ZIF₈₀₀ and Pt/C.

The electron transfer number for COF@ZIF₈₀₀ fluctuated from 3.79 to 3.94 in the potential range of 0.2 to 0.8 V, suggesting their 4e⁻ pathway towards ORR (Figure 11A). Correspondingly, the H₂O₂ yields were calculated in the range of

2.4% to 10.0%, which suggests the high selectivity for O₂ to H₂O. Similarly, ZIF₈₀₀ also shows 4e⁻ pathway in ORR with high selectivity. In addition, COF@ZIF₈₀₀ also displayed excellent long-term stability and chemical stability because the i-t measurement revealed current density was 100% of initial value after 20 hours (Figure 11B).

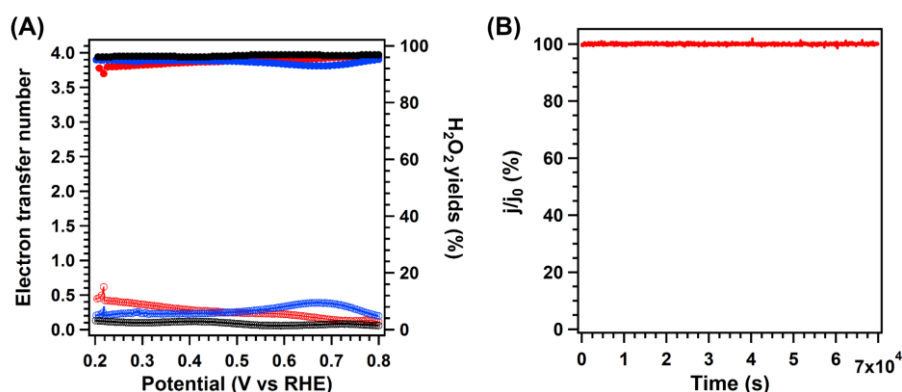


Figure 11. (A) The electron transfer number and H₂O₂ yield plots calculated from the RRDE measurements for ORR over ZIF₈₀₀ (blue), COF@ZIF₈₀₀ (red) and Pt/C (black) in oxygen-saturated KOH (0.1 M) aqueous solution. (B) Long-term stability test of COF@ZIF₈₀₀ at 0.6 V vs RHE for 20 h.

The HER performance of catalysts was tested by LSV in 1 M KOH electrolyte. As shown in Figure 12A, the overpotential for COF@ZIF₈₀₀ at a current density of 10 mA cm⁻² was 159 mV, which was positive than that of ZIF₈₀₀ (388 mV). Although the Tafel slope for COF@ZIF₈₀₀ (92 mV dec⁻¹) was higher than that of Pt/C (24 mV dec⁻¹), it displayed better kinetic activity than that of ZIF₈₀₀ (112 mV dec⁻¹, Figure 12B). The over potential and Tafel slope for COF@ZIF₈₀₀ exceeded most reported Co-based catalysts (Table 2). In addition, the V-t measurement for COF@ZIF₈₀₀ at a constant current density of 10 mA cm⁻² illustrated that such electrocatalyst maintains its potential for 20 h, confirming the harsh stability (Figure 12C).

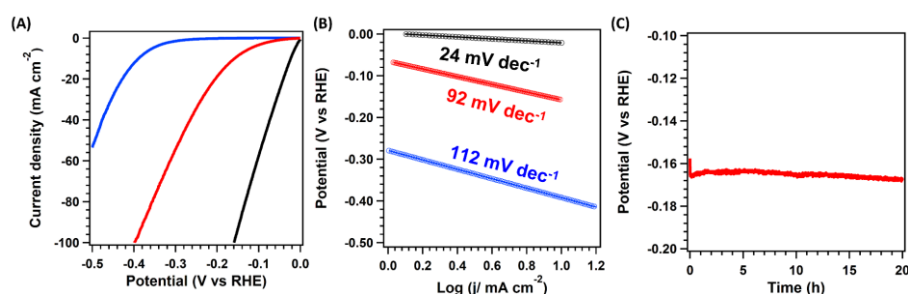


Figure 12. (A) LSV curves and (B) Tafel slopes for HER over ZIF₈₀₀ (blue), COF@ZIF₈₀₀ (red) and Pt/C (black) in oxygen-saturated KOH (1.0 M) aqueous solution. (C) Long-term stability of COF@ZIF₈₀₀ for 20 hours at a current density of 10 mA cm⁻².

Table 2. Summary of electrocatalysts for HER in 1 M KOH.

Catalysts	Overpotential @ j_{10} / mV	Tafel slope (mV dec ⁻¹)	Reference
COF@ZIF ₈₀₀	159	92	This work
CoTBrPP@bio-C	220	80	[115]
C-CoP	173	71	[123]
Co- Fe-B-P	173	96	[124]
Cu _{0.3} Co _{2.7} P/NC	220	122	[125]
FeP NPs@NPC	214	82	[126]
NiCoP/rGO	209	124	[127]
Co/CoP	253	79	[128]
Co-Ni ₃ N	194	150	[129]
Hollow Co ₃ O ₄ Microtube Arrays	190	90	[130]
Cu _{0.3} Co _{2.7} /NC-ZIFs	220	122	[131]
Co ₉ S ₈ @NOSC	320	105	[132]
Co _{0.85} Se/NiFe-LDH	320	160	[133]
NiCo ₂ S ₄ NW/NF	210	51	[134]

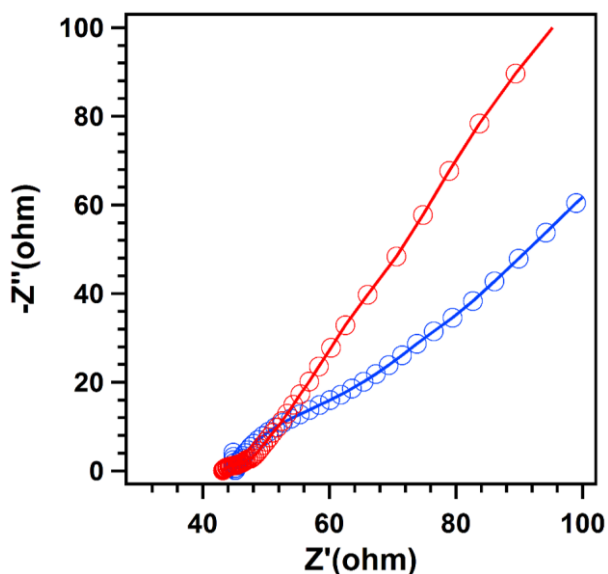


Figure 13. The EIS diagram of COF@ZIF₈₀₀ (red) and ZIF₈₀₀ (blue).

To investigate the different conductive behaviours of ZIF₈₀₀ and COF@ZIF₈₀₀, the alternating-current impedance spectroscopy was used to study the mass and electron transport for the catalysts. As shown in Figure 13, the Nyquist plots consisting of a high-to-medium-frequency depressed semicircle linked with a low-frequency sloping line in 0.1 M KOH solution. The semicircle in the high frequency region is associated with the internal resistance, while the medium-frequency semicircle is related to the R_{ct} . The R_{ct} of COF@ZIF₈₀₀ was 42.2 Ω , which was lower than that of ZIF₈₀₀ (83.2 Ω), suggesting a higher conductivity. Moreover, the COF@ZIF₈₀₀ had a higher slope than that of ZIF₈₀₀, which suggests the fast ionic diffusion. The fast mass and electron transport for COF@ZIF₈₀₀ are attributed its unique porosity and high graphitization degree.

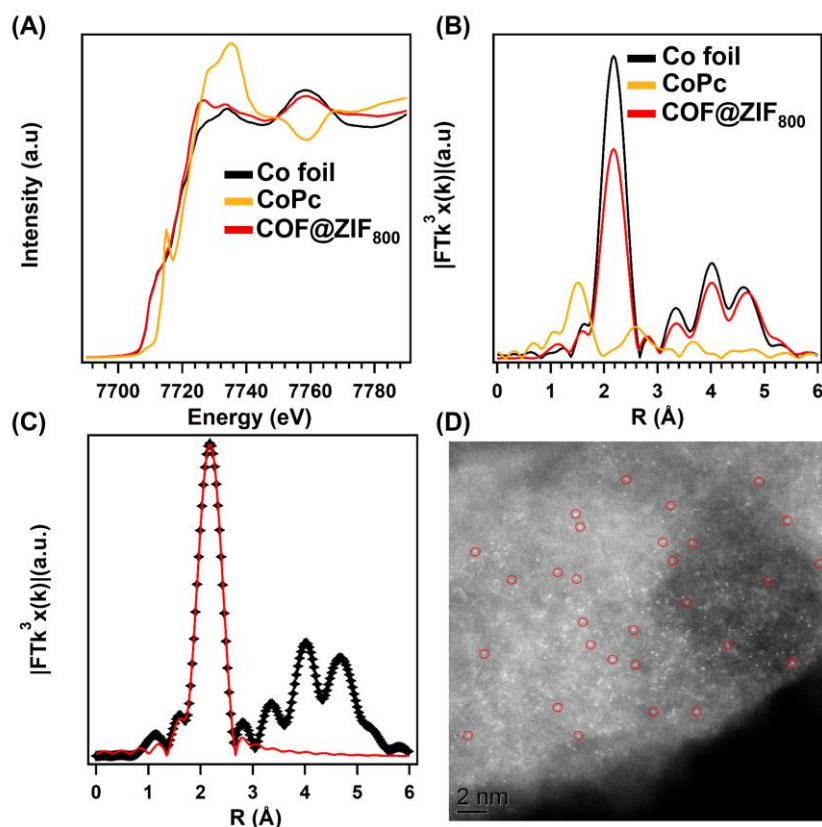


Figure 14. (A) XANES spectra, (B) Fourier transformed k^3 -weighted $\chi(k)$ -function and (C) EXAFS fitting curve for Co of the EXAFS spectra for Co foil (black), CoPc (yellow) and COF@ZIF₈₀₀ (red) K-edge. (D) The HAADF-STEM images of COF@ZIF₈₀₀.

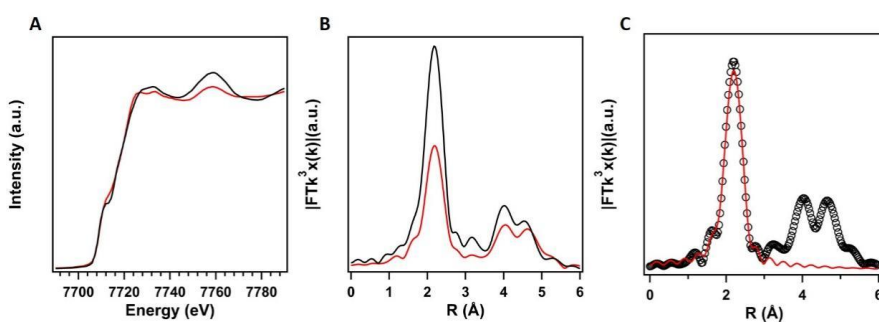


Figure 15. (A) XANES spectra and (B) Fourier transformed k^3 -weighted $\chi(k)$ -function of the EXAFS spectra for ZIF₈₀₀ (red) and Co foil (black) K-edge. (C) EXAFS fitting curve for Co in ZIF₈₀₀.

To further clarify the active sites for COF@ZIF₈₀₀ in electrochemical process, the XAFS measurement was carried out. The Co of COF@ZIF₈₀₀ displayed different near-edge structures to the corresponding oxidation states (CoPc) and

simple substances (Co foil) (Figure 14A). The peak position of Co in R-space was 2.17 Å, which was same as that of Co-Co coordination (Figure 14B). And the fitting of the obtained EXAFS data revealed that Co–N₄ and Co-Co were the dominant coordination mode of Co atoms (Figure 14C). The atomic state of Co was further verified by HAADF-STEM images. The bright dots were clearly identified, which was from the Co atoms (Figure 14D). Differently, the EXAFS data showed there was no Co-N bonds in the ZIF₈₀₀ (Figure 15). Thus, COF@ZIF₈₀₀ contains both atomic Co-N₄ and Co nanoparticles.

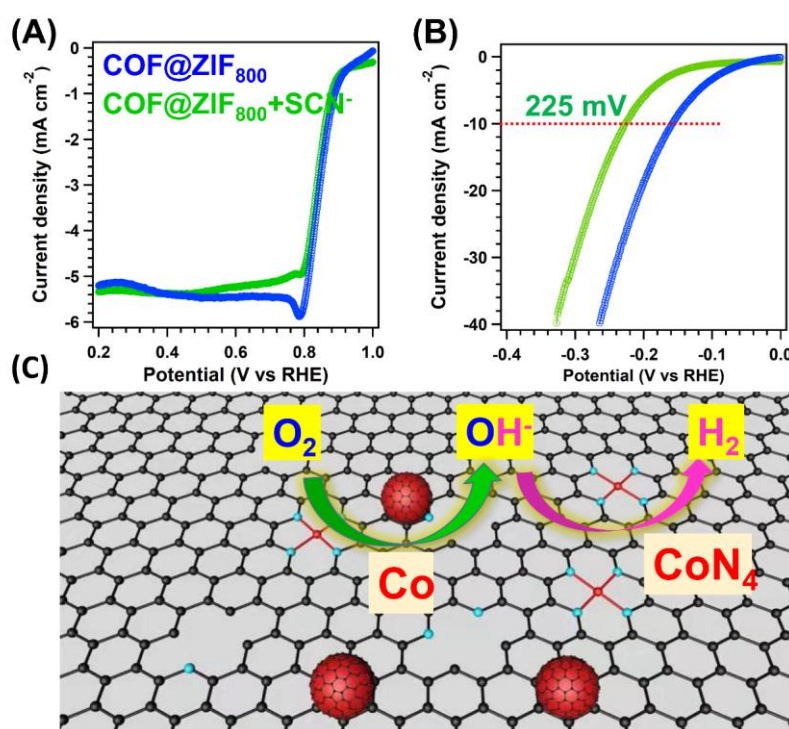


Figure 16. The LSV curves for COF@ZIF₈₀₀ (blue) and addition of KSCN (green) to the electrolytes in (C) 0.1 M KOH for ORR and (D) 1.0 M KOH for HER. (E) The catalytic mechanism for COF@ZIF₈₀₀ towards ORR and HER.

The active sites in the catalysts were explicated by the SCN⁻ deactivated experiments. With addition of SCN⁻, the COF@ZIF₈₀₀ towards ORR displayed the strong tolerance to the SCN⁻. E_{1/2} displayed slight changes to 0.84 V, while the corresponding j_{lim} was well retained (Figure 16A). Thus, N-doped carbons and Co nanoparticles embedded in the carbon contributed to the major roles in ORR. However, the over-potential for COF@ZIF₈₀₀ towards HER exhibited

negative shift to 225 mV (Figure 16B). The lower activity for HER contributed to the Co-N₄ sites blocked with SCN⁻, suggesting the Co-N₄ plays vital role in HER. Therefore, the Atomic Co-N₄ sites and Co nanoparticles sites confined in COF@ZIF-67 derived core-shell carbon frameworks play different roles in catalyzing ORR and HER (Figure 16C). The ORR and HER performance were depended on the Co nanoparticles and the Co-N₄ sites, respectively.

3.3 Conclusion

In summary, a core-shell bifunctional catalyst for ORR and HER have been demonstrated. The COF-shell prevent the collapse of the MOF-core in pyrolysis process. In addition, the core-shell morphology benefit mass transport, and the COF-derived shell facilities electron conductivity. The catalyst had Co-N₄ atoms together with Co nanoparticles embedded in the carbon, which enable to catalyze ORR and HER with high activity and excellent stability. This work provides a new platform to design multifunctional catalysts from COFs.

Chapter 4. Dual atomic catalysts from COF-derived carbon for CO₂RR by

Suppressing HER through Synergistic Effects

4.1 Introduction

Electrocatalytic CO₂RR for high-value chemicals is a promising method to curb CO₂ emissions and alleviate the energy crisis.^[135-137] Developing catalysts with high activity, selectivity and stability is a significant and challenge due to the competing reaction (HER) in the catalytic process.^[138-140] In the Chapter 3, we combined the Co-N₄ atoms together with Co nanoparticles, which belong to SACs, for constructing bifunctional electrocatalysts from a core-shell hybrid of COF and ZIF-67. However, SACs usually cannot meet requirements of electrocatalytic reactions with high activity and selectivity. Introducing a new kind of metal atoms into SACs to form the bimetallic catalytic sites is an effective method to improve the catalytic performance. It is still challenging to construct synergetic roles for the different metal atoms in the same supports because of the long distance between isolated active sites.^[141-143] To overcome the weak interaction between isolated atoms, the heteroatom modulator approach (HMA), ball milling method, atomic layer deposition (ALD), and temple-pyrolysis strategies have been used to construct dual sites.^[144-146] Developing carbon supports with high contents metal atoms is another available approach to building dual sites, since the higher loading atoms enhance the possible access to each metal atoms.^[147-148]

In this chapter, we constructed bimetal catalysts for CO₂RR with dual sites (ZnN₄ and CoN₄O) from a core-shell hybrid of COF and a MOF. The unique core-shell framework works as an ideal template for constructing high-density active sites. The outer COF-shell prevents the aggregation of the MOF-core and decreases the losses of Zn ions, N and O atoms in pyrolysis, which facilities the

formation of high Zn active sites together with heteroatoms; and the MOF-core prevents the collapse of the COF-shell under thermal treatment. The resulting hollow carbon has a hollow structure with abundant N and O atoms (10.73% for N and 8.31% for O) on the carbon walls, which immobilizes cobalt phthalocyanine (CoPc) molecules through coordination effects. The catalysts had Co and Zn contents of 2.47 and 11.05 wt.%, respectively. The as-prepared catalyst enabled to catalyse the CO₂RR with a high activity and selectivity, with a maximum FE_{CO} value of 92.6% at -0.8 V.

4.2 Results and discussions

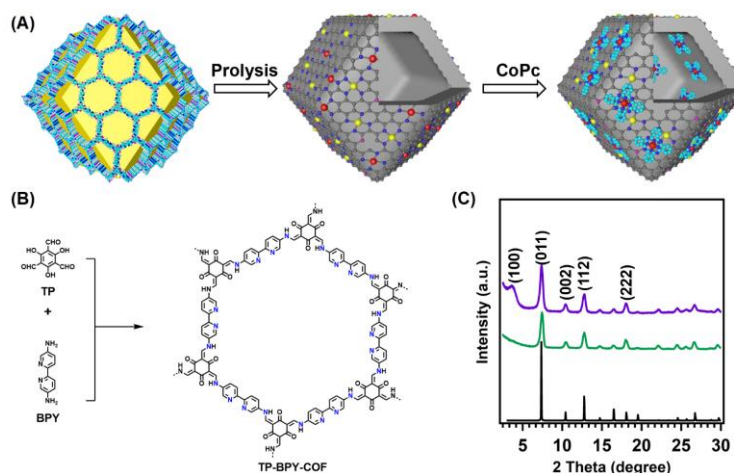


Figure 1. (A) The synthesis of COF@MOF₈₀₀-Co from COF@MOF. (B) The synthesis and structure of TP-BPY-COF. (C) The PXRD patterns of COF@MOF (purple curve), ZIF-8 (green curve) and the simulation of ZIF-8 (black curve).

The crystalline structure of prepared ZIF-8 and COF@MOF were investigated by the PXRD measurement. The PXRD patterns for ZIF-8 showed the peaks at 7.42°, 10.57°, 12.93° and 18.12°, which were from (011), (002), (112) and (222) facets (Figure 1C, blue curve), respectively, and these peaks were also identified for COF@MOF. In addition, a new peak at 3.6° was clearly identified, which was from (100) facet of the TP-BPY-COF (Figure 1C, red curve).

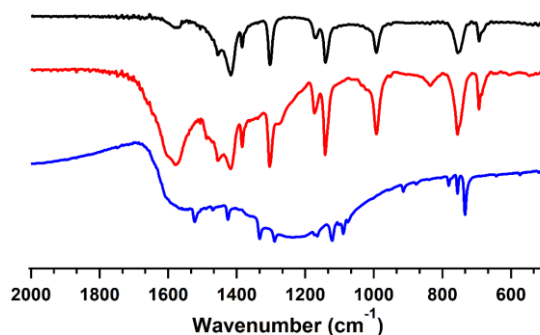


Figure 2. The FT-IR spectra for ZIF-8 (black), COF@MOF (red) and COF@MOF₈₀₀-Co (blue).

The FT-IR for the ZIF-8 showed that the peaks at 430 cm^{-1} was from Zn-N bonds. And all the peaks from the ZIF-8 were well maintained with coating TP-BPY-COF on the surface of ZIF-8 (Figure 2). And a new bond at 1624 cm^{-1} was from the imine bond of TP-BPY-COF (Figure 2, red curve), suggesting the COF was successfully synthesized.

The core-shell morphologies were revealed by the SEM and TEM images. The SEM images showed that the COF@MOF and ZIF-8 have the same dodecahedron shape and uniform particle size of 320 nm (Figures 3A-3B). Meanwhile, the TEM images illustrated that the outer surface of ZIF-8 become rough, and no aggregated bulks or particles were observed for COF@MOF, indicating that the COF was uniformly grown on ZIF-8 (Figures 3C-3D). After thermal treatment at $800\text{ }^{\circ}\text{C}$, the prepared COF@MOF₈₀₀ was in dodecahedron morphology as revealed by SEM images and TEM images, and the cavity size was about 60 nm (Figures 3E-3F).

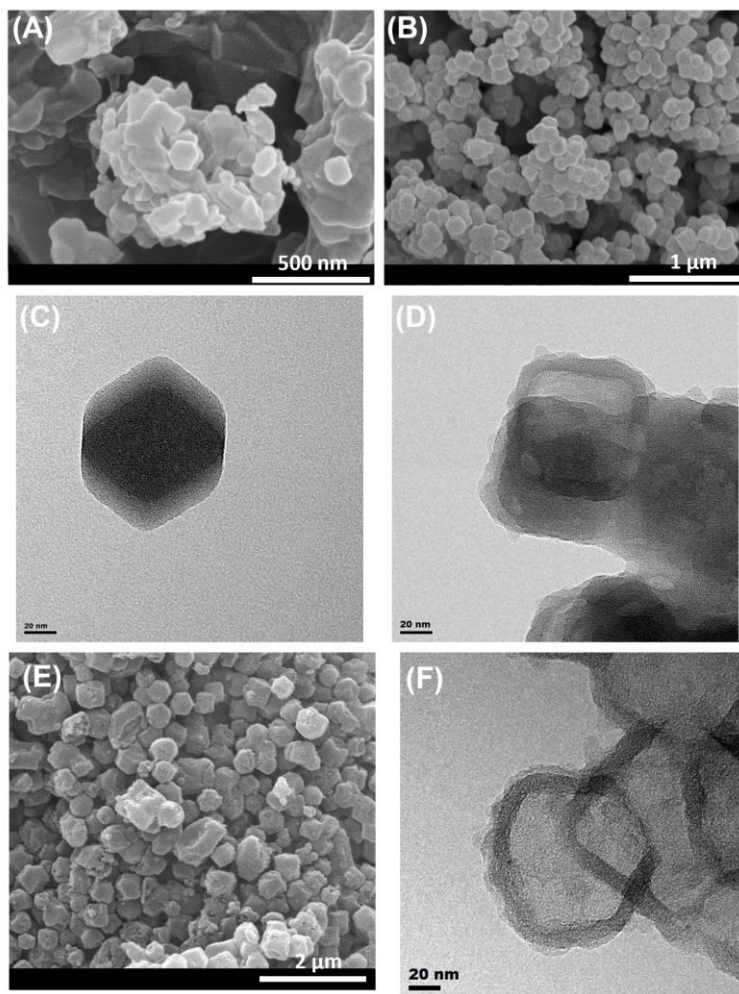


Figure 3. The SEM images of (A) ZIF-8 and (B) COF@MOF. The TEM images of (A) ZIF-8 and (B) COF@MOF. (E) The SEM and (F) TEM images of COF@MOF₈₀₀.

With absorbing CoPc in the COF@MOF₈₀₀, the SEM images showed that the COF@MOF₈₀₀-Co crystals present a dodecahedron morphology (Figure 4A), similar to that of COF@MOF₈₀₀. And the TEM images showed that the average size of COF@MOF₈₀₀-Co was ~110 nm, while the average size of COF@MOF₈₀₀ was ~80 nm (Figure 4B). Additionally, the TEM images illustrated that COF@MOF₈₀₀-Co and COF@MOF₈₀₀ displayed well-separated nanocrystals, indicating that they were composed of amorphous carbon without metal nanoparticles and clusters. High resolution TEM images showed that there were many vertical carbons in different directions with an inner layer distance

of 0.34 nm, which was from the carbonization of TP-BPY-COF, indicating that COF@MOF₈₀₀-Co and COF@MOF₈₀₀ were composed by standing carbon sheets. The HAADF-STEM images for COF@MOF₈₀₀ showed the bright dots from the atomic dispersion of Zn were in atomic states rather than nanoparticles dispersed on the carbon. With loading CoPc, the atomic state of Zn was well retained. The HAADF-STEM images for COF@MOF₈₀₀-Co showed many bright dots on the surface, which were from the atomic Zn and Co distribution on the carbon (Figure 4C). Additionally, the EDX mapping images of COF@MOF₈₀₀-Co (Figure 4D) confirmed all the elements (C, N, O Co and Zn) were well-dispersed in the skeletons of the carbon.

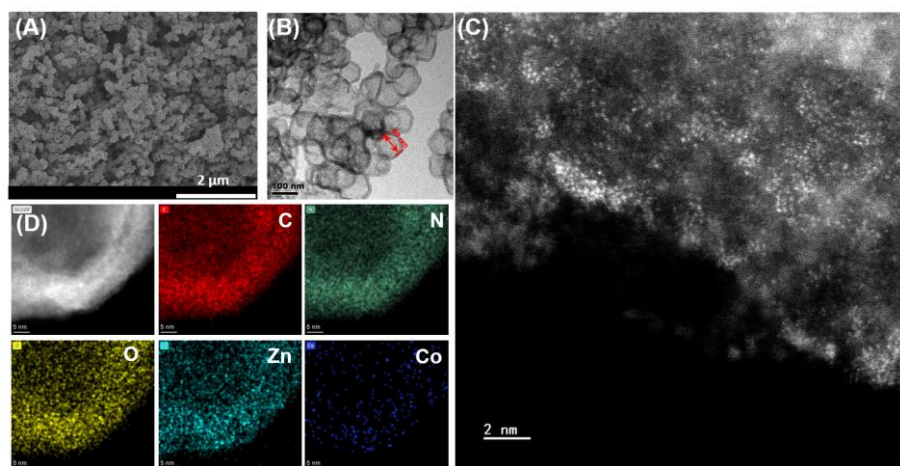


Figure 4. (A) The SEM image, (B) TEM image, (C) HAADF-STEM image and (D) EDX-mapping images of COF@MOF₈₀₀-Co.

The PXRD patterns of COF@MOF₈₀₀ demonstrated that the peak at 24.8° and 42.2° were from (002) and (101) facets of carbon (Figure 5A, blue curve). And many peaks were observed in COF@MOF₈₀₀-Co (Figure 5A, red curve), which were from CoPc. And the peaks from (002) and (101) of carbon were also observed (Figure 5A, red curve). Notably, there were no characteristic peaks for metal nanoparticles or oxides, indicating that there were no large particles or clusters, which was consistent with the results revealed by SEM and TEM images as mentioned above.

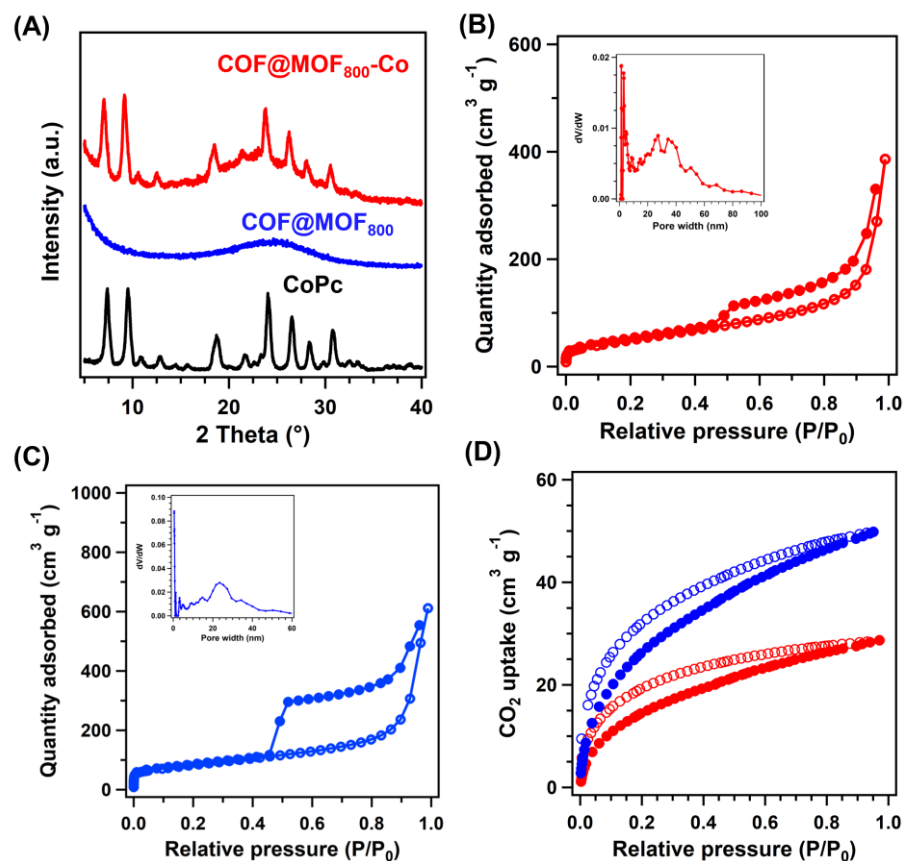


Figure 5. (A) The PXRD patterns of CoPc units (black curve), COF@MOF₈₀₀ (blue curve) and COF@MOF₈₀₀-Co (red curve). The N₂ sorption isotherm profiles at 77 K (insert: pore size distribution curve) of (B) COF@MOF₈₀₀-Co and (C) COF@MOF₈₀₀. (D) The CO₂ sorption curves of COF@MOF₈₀₀-Co (red curve) and COF@MOF₈₀₀ (blue curve) at 273 K.

The N₂ sorption curves of COF@MOF₈₀₀-Co and COF@MOF₈₀₀ exhibited the type-IV isotherms, indicating that the N₂ sorption was mainly contributed by the mesopores and macropores structures (Figures 5B-5C). The S_{BET} for COF@MOF₈₀₀ was 292.06 m² g⁻¹, with a pore volume of 0.95 cm³ g⁻¹, while the COF@MOF₈₀₀-Co had a decline S_{BET} of 182.46 m² g⁻¹ and a pore volume 0.60 cm³ g⁻¹. The pore size distribution curves showed the pores were distributed from 20 to 60 nm, while the pore sizes of COF@MOF₈₀₀-Co were distributed over a wide range from 0.5 to 60 nm, demonstrating that there were micro-/meso-/macro-porous hierarchical channels in the COF@MOF₈₀₀-Co. We have then investigated the CO₂ sorption behavior at 273 K. The CO₂ sorption curves

revealed that COF@MOF₈₀₀ has a higher CO₂ capacity of 49.85 cm³ g⁻¹ (Figure 5D, blue curve) than that of COF@MOF₈₀₀-Co (28.69 cm³ g⁻¹) (Figure 5D, red curve). The high CO₂ uptakes for COF@MOF₈₀₀ contributed to abundant O and N sites on the surface of the carbon. With binding CoPc, these binding sites were occupied with CoPc, which resulted in lower S_{BET} and a lower CO₂ uptake.

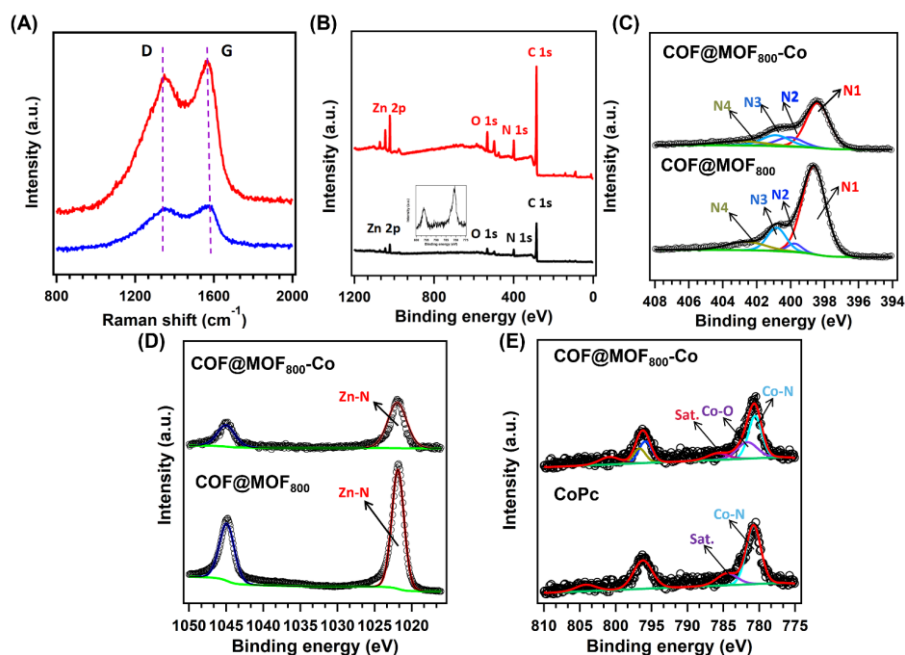


Figure 6. (A) The Raman spectra of COF@MOF₈₀₀ (blue curve) and COF@MOF₈₀₀-Co (red curve). The XPS spectra of COF@MOF₈₀₀-Co (red) and COF@MOF₈₀₀ (black). (D) High-resolution XPS spectra of Zn 2p for COF@MOF₈₀₀ and COF@MOF₈₀₀-Co. (E) High-resolution XPS spectra of Co 2p for COF@MOF₈₀₀-Co and CoPc.

The Raman spectra of COF@MOF₈₀₀-Co and COF@MOF₈₀₀ showed two peaks at 1350 cm⁻¹ and 1587 cm⁻¹, corresponding to the D and G band of sp² carbon. The intensity ratios of the D and G bands (I_D/I_G) indicated the disorders and defects in the carbon. The I_D/I_G for COF@MOF₈₀₀-Co and COF@MOF₈₀₀ were about 0.94 (Figure 6A, red curve) and 0.92 (Figure 6A, blue curve), suggesting their graphitization degrees were well retained after binding CoPc. To investigate the chemical states of COF@MOF₈₀₀-Co and COF@MOF₈₀₀, XPS was performed. The XPS spectra for COF@MOF₈₀₀-Co and COF@MOF₈₀₀

showed that peaks from C 1s, N 1s, O 1s, and Zn 2p were identified (Figure 6B). The contents for Zn, N and O in COF@MOF₈₀₀ were 10.54, 9.19, and 7.87 wt.%, respectively. We have prepared the ZIF₈₀₀ under the same condition, to prove the shell-effects of the COF. Specifically, the XPS spectra of ZIF₈₀₀ exhibited the weight of Zn, N, O and Zn were 8.31 7.56, and 6.33 wt.%, respectively, which were smaller than those in COF@MOF₈₀₀, which confirmed the COF shell prevent the losses of Zn ions, N and O atoms. With absorbing CoPc, the related contents for Zn, N, O and Co were 12.05, 15.73, 8.31 and 2.53 wt.%, respectively. The high-resolution N 1s spectrum of COF@MOF₈₀₀ can be deconvoluted into four distinct peaks of pyridinic N (N1), pyrrolic N (N2), graphite N (N3), and quaternary N (N4) at 398.48, 399.86, 400.82, and 402.92 eV, with corresponding relative contents of 68.69, 6.58, 18.18, and 6.54%, respectively. The corresponding N1, N2, N3 and N4 for COF@MOF₈₀₀-Co were 64.89, 13.27, 15.63 and 6.21%, respectively (Figure 6C). The high-resolution Zn 2p spectra of COF@MOF₈₀₀-Co and COF@MOF₈₀₀ exhibited two distinct peaks at 1021.85 eV (2p_{3/2}) and 1044.89 eV (2p_{1/2}), attributing to the Zn-N bonds (Figure 6D). Additionally, the Co 2p spectra of COF@MOF₈₀₀-Co can be deconvoluted into the peaks of Co 2p_{1/2} and Co 2p_{3/2}, with the corresponding satellite peaks at around 800.84 eV and 785.78 eV, respectively. The peak at 780.58 eV was attributed to the Co-N, and another new peak at 781.66 eV was attributed to the Co-O, in which the contents are 46.71 wt.% and 12.73 wt.%, respectively. In addition, there was no Co-O peak at the Co 2p spectra of CoPc (Figure 6E). It indicated that the O atom dominated that the ZnN₄ absorbed the CoPc, suggesting that there might be chelation between ZnN₄ atoms and CoN₄O atoms after COF@MOF₈₀₀ absorbed the CoPc.

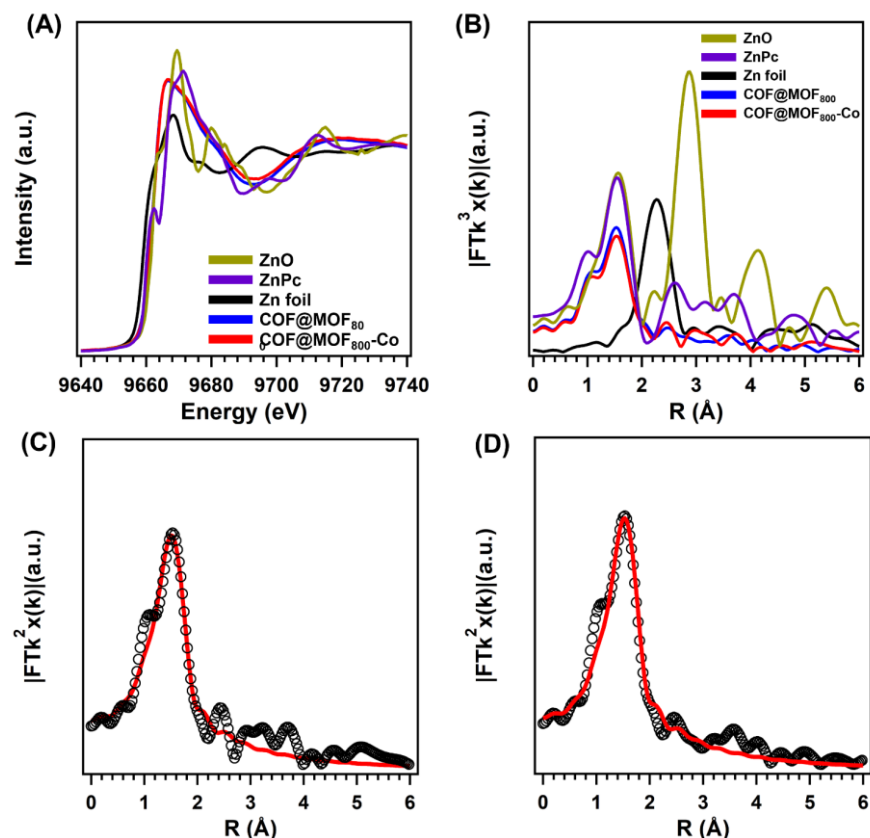


Figure 7. (A) XANES spectra and (B) the K-edge k^3 -weighted Fourier transform spectra from EXAFS for Zn of Zn foil (black curve) ZnO (yellow curve), ZnPc (purple curve), COF@MOF₈₀₀ (blue curve) and COF@MOF₈₀₀-Co (red curve). EXAFS fitting curves for Zn in (C) COF@MOF₈₀₀ and (D) COF@MOF₈₀₀-Co.

To further confirm the electronic and atomic states of Co and Zn in COF@MOF₈₀₀ and COF@MOF₈₀₀-Co, XAFS was adopted. The location of Zn absorption near-edge of COF@MOF₈₀₀ (Figure 7A, blue curve) and COF@MOF₈₀₀-Co (Figure 7A, red curve) exhibited different structures from Zn foil (Figure 7A, black curve), ZnO (Figure 7A, yellow curve), but they approached simple substances (ZnPc) (Figure 4A, black curve). Furthermore, the peak position of Zn in R-space about COF@MOF₈₀₀ and COF@MOF₈₀₀-Co was 1.98 Å, which was close to that of ZnPc coordination (Figure 7B). In addition, the EXAFS fitting results verified that Zn atoms in COF@MOF₈₀₀ and COF@MOF₈₀₀-Co were coordinated by Zn-N₄ (Figure 7C).

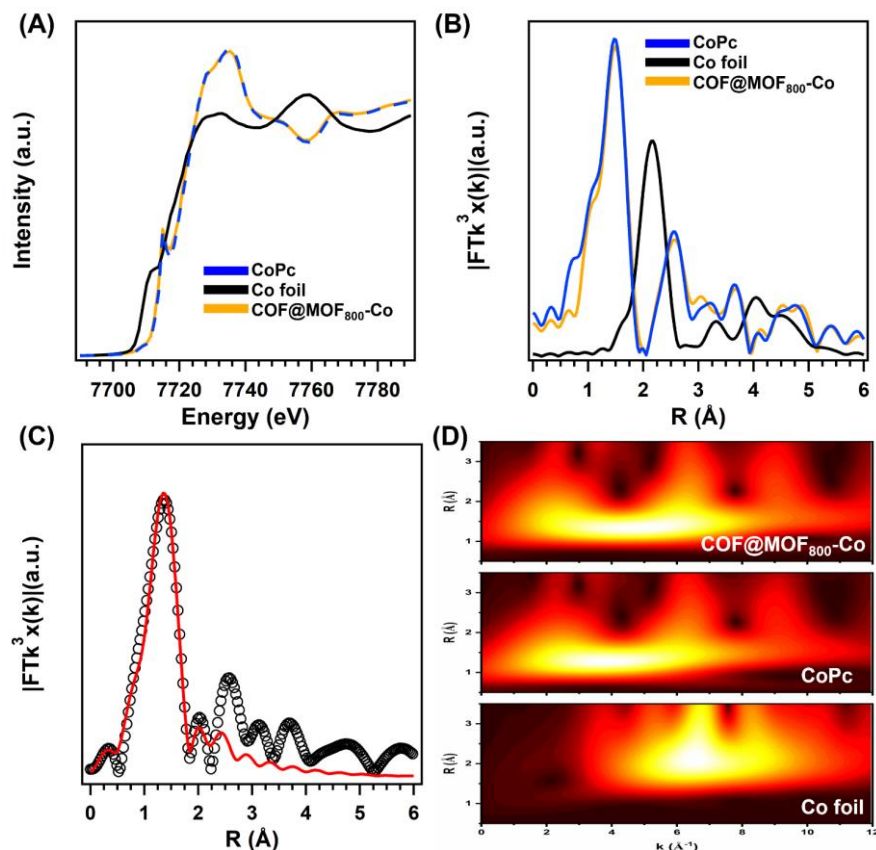


Figure 8. (A) XANES spectra and (B) the K-edge k^3 -weighted Fourier transform spectra from EXAFS for Co of Co foil (black curve) CoO (yellow curve), CoPc (purple curve), COF@MOF₈₀₀ (blue curve) and COF@MOF₈₀₀-Co (red curve). (C) EXAFS fitting curves for Co in COF@MOF₈₀₀-Co. (D) The WT-EXAFS of the Co foil, CoPc and COF@MOF₈₀₀-Co.

Table 1. Co k-edge fitting parameters.

Sample	shell	N	R (Å)	ΔE_0 (eV)	σ^2 (10^{-3}Å^2)	R-factor
Sample	Co-N	4.6±4.9	1.90±0.08	-7.7±6.7	11.0	0.002
	Co-O	1.9±1.8	2.07±0.30	-7.7±6.7	16.7	0.002

N, coordination numbers; R, the internal atomic distance; σ^2 , Debye-Waller factor; ΔE_0 , the edge-energy shift.

Correspondingly, the Co K-edge XANES spectra of COF@MOF₈₀₀-Co (Figure 8A, yellow curve) illustrated that the position of the absorption near-edge was different to that of CoPc (Figure 8A, blue curve) and Co foil (Figure 8A, black curve). Moreover, the position of Co about COF@MOF₈₀₀-Co in R-space exhibited that it has similar Co–N and Co–O coordination with peaks about at

1.90 Å and 2.07 Å, respectively (Figure 8B). Furthermore, the EXAFS fitting results of COF@MOF₈₀₀-Co revealed that the Co was in the CoN₄O coordinated model (Figure 8C and Table 1). Thus, Co and Zn existed as CoN₄O and ZnN₄ in COF@MOF₈₀₀-Co, respectively. Additionally, to further confirm the combination of Co, the WT of the Co L3-edge EXAFS oscillations was conducted (Figure 8D). COF@MOF₈₀₀-Co and CoPc exhibited an intensity maximum at 2.2 Å⁻¹ (Co-N). In contrast, for Co foil, only a predominate intensity maximum at higher k-space (6.5 Å⁻¹) was detected, suggesting the absence of the Co-Co metallic coordination. It further certified that no metal nanoparticles are present in the COF@MOF₈₀₀-Co.

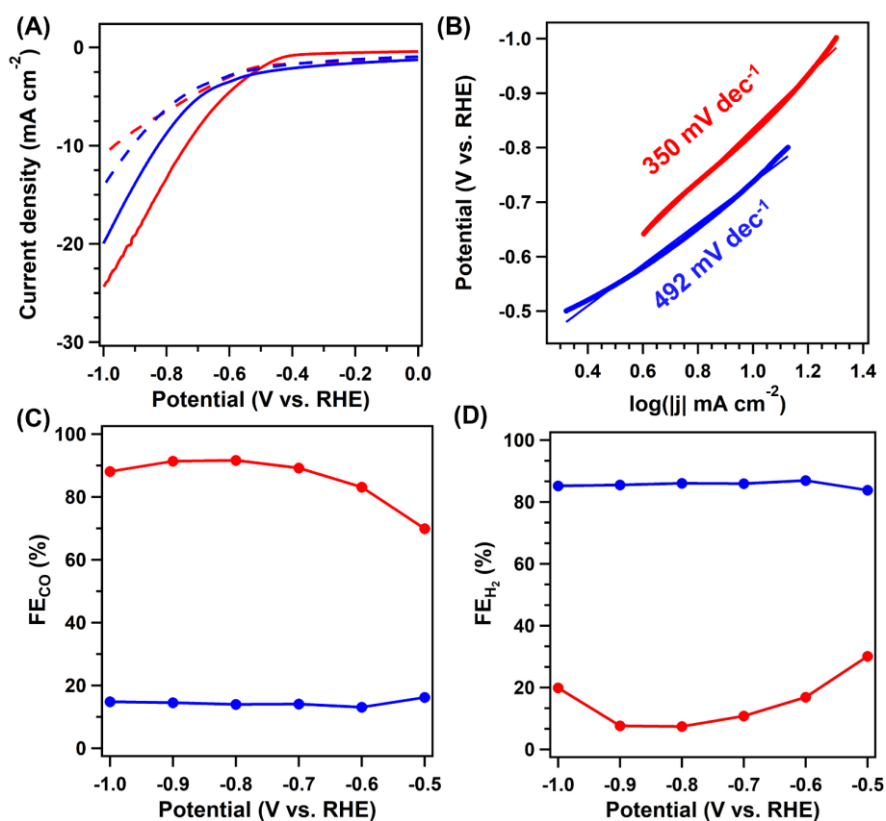


Figure 9. (A) The LSV curve in CO₂ (solid line) and Ar atmosphere (dotted line) at scan rate of 10 mV s⁻¹. (B) The corresponding Tafel slope for COF@MOF₈₀₀-Co (red curve) and COF@MOF₈₀₀ (blue curve). (C) The faradic efficiency of CO and (D) H₂ for COF@MOF₈₀₀-Co (red) and COF@MOF₈₀₀ (blue).

Given the high densities of CoN₄O and ZnN₄ in COF@MOF₈₀₀-Co, we have investigated the catalytic performance of CO₂RR for COF@MOF₈₀₀-Co in 0.5 M KHCO₃ by the H-type cell, which is separated by a proton exchange membrane. As a control, the electrocatalytic performance of COF@MOF₈₀₀ was also investigated. The LSV for COF@MOF₈₀₀-Co and COF@MOF₈₀₀ was conducted from 0 to -1.0 V (vs. RHE) at a scan rate of 10 mV s⁻¹ under the CO₂ or Ar atmosphere, respectively. The LSV curves for COF@MOF₈₀₀-Co (red curve) and COF@MOF₈₀₀ (blue curve) showed the current densities under CO₂ atmosphere (solid curve) were much higher than those under the Ar atmosphere (dotted line) at the same potentials, indicating that their activities are originated from the CO₂RR (Figure 9A). The E₀ determined at a current density of 1 mA cm⁻² for COF@MOF₈₀₀-Co was 0.38 V, which was more positive than that of COF@MOF₈₀₀ (0.53 V) in CO₂, suggesting that COF@MOF₈₀₀-Co were more favourable to CO₂RR. The Tafel slope is a significant parameter to elucidate the rate-determining step of CO₂RR. The corresponding Tafel slope of COF@MOF₈₀₀-Co (Figure 9B, red curve) was 350 mV dec⁻¹, smaller than that of COF@MOF₈₀₀ (492 mV dec⁻¹) (Figure 5B, blue curve), indicating its higher kinetic behavior.^[29] The gas and liquid chromatography measurement illustrated that the production was only CO and H₂ without any other products during the process of CO₂RR. The FE_{CO} were obtained for the catalysts at different potentials. The COF@MOF₈₀₀-Co had FE_{CO} of 69.9%, 83.1%, 89.2%, 92.6%, 92.4% and 89.1% at -0.5, -0.6 V, -0.7, -0.8, -0.9 and -1.0 V (Figure 9C, red curve), respectively. And the maximum FE_{CO} reached 92.6% at -0.8 V, which was higher than many other single and dual atomic electrocatalysts (Table 2). On the contrary, the COF@MOF₈₀₀ exhibited low activity and selectivity towards CO₂RR, with the FE_{CO} of 16.19%, 13.06%, 14.07%, 13.95%, 14.51% and 14.82% at the same potential ranges (Figure 9C, blue curve). To confirm the suppressed effects on HER, we have calculated the FE for H₂ over COF@MOF₈₀₀ and COF@MOF₈₀₀-Co. Accordingly, without the CoN₄O site in the catalysts, COF@MOF₈₀₀ had a much higher activity for HER, with FE_{H₂}

values of 83.81%, 86.94%, 85.93%, 86.05%, 85.49% and 85.18% at -0.5 , -0.6 V, -0.7 , -0.8 , -0.9 and -1.0 V (Figure 9D, blue curve). And the corresponding FE_{H_2} for COF@MOF₈₀₀-Co were 30.1%, 16.9%, 10.8%, 7.4%, 7.6% and 19.9% at -0.5 , -0.6 V, -0.7 , -0.8 , -0.9 and -1.0 V (Figure 9D, red curve). Thus, the HER was successfully suppressed.

Table 2. Comparison of CO₂ uptake and FE_{CO} of various catalysts for CO₂ electroreduction.

Catalyst	E (V vs. RHE)	FE_{CO} (%)	TOF (h ⁻¹)	Reference
COF@MOF ₈₀₀ -Co	-0.8	93	1370.24	This work
CoPc-CN/CNT	-0.5	88	5040	[149]
Ni SAs/N-C	-0.9	72	3868	[150]
Nanoporous Ag	-0.5	90	51	[151]
COF-367-Co	-0.7	91	165	[75]
COF-366-F-Co	-0.7	87	-	[76]
COF-300-AR on Ag film	-0.9	80	-	[77]
Ni SAs/N-C	-1.0	72	5273	[152]
SE-Ni SAs@PNC	-1.1	88	47805	[153]
Sn-Ti-O	-	94	-	[154]
In-doped Cu@Cu ₂ O	-0.8	88	-	[154]
CoSA/HCNFs	-0.9	91	-	[155]

We have prepared COF@MOF₉₅₀-Co containing CoN₄O sites without ZnN₄ sites, and investigated the CO₂RR activity. COF@MOF₉₅₀-Co had E_0 value of 0.46 V, which was more negative than that of COF@MOF₈₀₀-Co. And the corresponding values of FE_{CO} for the COF@MOF₉₅₀-Co were 45.5%, 62.4%, 74.2%, 76.7%, 67.5% and 44.8% at -0.5 , -0.6 V, -0.7 , -0.8 , -0.9 and -1.0 V, respectively (Figures 10A and 10B). It suggested that the synergistic effects of CoN₄O and ZnN₄ in COF@MOF₈₀₀-Co had higher CO₂RR performance than that of solely CoN₄O site in COF@MOF₉₅₀-Co or ZnN₄ site in COF@MOF₈₀₀.

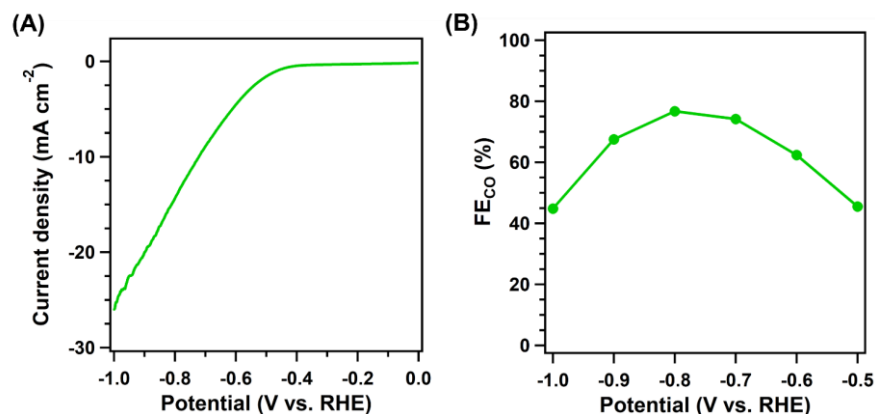


Figure 10. (A) The LSV curve and (B) the FE_{CO} calculated from -0.5 to -1.0 V of COF@MOF₉₅₀-Co.

The j_{CO} of COF@MOF₈₀₀-Co (Figure 11A, red curve) increased with the increasing the potentials, delivering 15.57 mA cm^{-2} at -1.0 V, which is significantly higher than that of COF@MOF₈₀₀ (1.05 mA cm^{-2}) (Figure 11A, blue curve). Furthermore, the TOF of COF@MOF₈₀₀-Co (Figure 11B, red curve) and COF@MOF₈₀₀ (Figure 11B, blue curve) were calculated from -0.5 V to -1.0 V. The TOF value of COF@MOF₈₀₀-Co reached the highest value of 1370.24 h^{-1} at -1.0 V, while the highest TOF value for COF@MOF₈₀₀ was 23.34 h^{-1} at -1.0 V. Thus, the COF@MOF₈₀₀-Co displayed much higher activity and selectivity than that of COF@MOF₈₀₀.

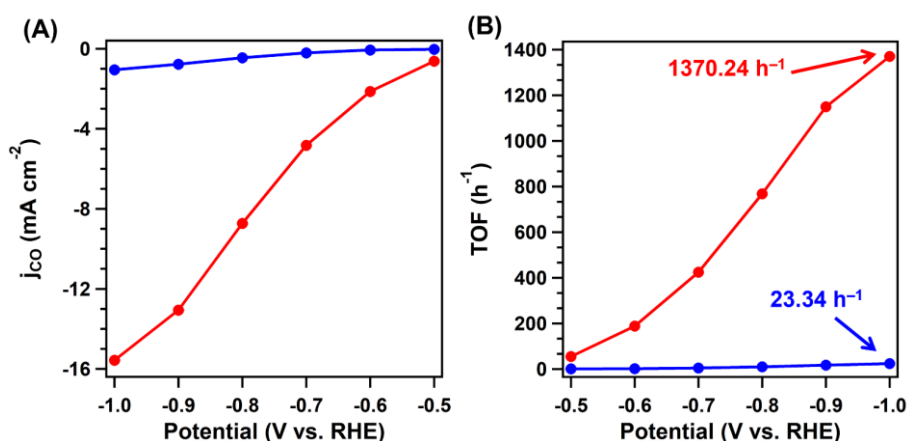


Figure 11. (A) The partial CO current density and (B) the corresponding TOF values at different applied potential for COF@MOF₈₀₀-Co (red curve) and COF@MOF₈₀₀ (blue curve).

The EIS was conducted to investigate the different ionic and electronic transport behavior of COF@MOF₈₀₀-Co and COF@MOF₈₀₀. According to the Nyquist plots, COF@MOF₈₀₀-Co has lower R_{ct} of 95.1 Ω (Figure 12A, red curve) than that of COF@MOF₈₀₀ (99.3 Ω) (Figure 12A, blue curve), revealing that there was a fast electron transfer process of CO₂RR on the surface of COF@MOF₈₀₀-Co. It suggested that the synergy of CoN₄O and ZnN₄ can facilitate the electron transport. The ECSA can provide the capacitance to evaluate the performance of electrocatalysts. Accordingly, the COF@MOF₈₀₀-Co (red curve) had a smaller ECSA of 9.1 mF cm^{-2} than that of COF@MOF₈₀₀ (29.7 mF cm^{-2} , blue curve). The low ECSA was due to the inner and outer surface of the carbon shell of COF@MOF₈₀₀ being covered by CoPc (Figure 12B).

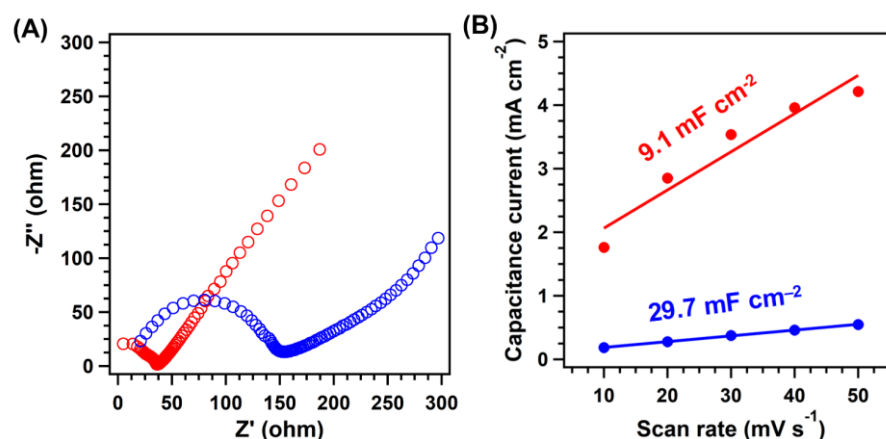


Figure 12. (A) The EIS spectra and (B) ECSA slopes of the COF@MOF₈₀₀-Co (red curve) and COF@MOF₈₀₀ (blue curve).

The long-term stability is a serious issue for SACs towards CO₂RR. The durable stability for COF@MOF₈₀₀-Co was investigated at -0.8 V for 30 h. The current density was 10 mA cm^{-2} after 30 h (Figure 13, red curve), about 94.5% of the initial value, and FE_{CO} was well retained (92.6%) (Figure 13, blue curve).

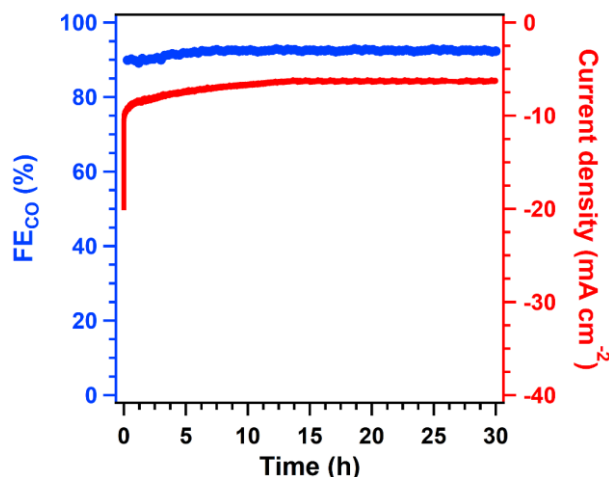


Figure 13. The current density (red curve) and FE_{CO} (blue curve) for COF@MOF₈₀₀-Co measured at 0.85 V vs. RHE for 30 h.

To investigate the catalytic performance of COF@MOF₈₀₀-Co for CO₂RR, we adopted the DFT calculation to determine the Gibbs lowest free-energy pathway about the CO₂RR on Co sites (Figure 14A) and Zn sites (Figure 14B) in COF@MOF₈₀₀-Co and Zn sites (Figure 14C) in COF@MOF₈₀₀. The CO₂RR mainly involves three steps: CO₂ was absorbed and protonated to form *COOH, which was then converted to *CO; finally, *CO dissociated from the metal sites to form CO molecular and desorbed. Accordingly, the RDS for the three models are the generation of COOH*. The ΔG for Co sites in COF@MOF₈₀₀-Co was 0.25 eV, much lower than Zn sites of COF@MOF₈₀₀-Co (0.58 eV), and COF@MOF₈₀₀ (1.32 eV) (Figure 14D). Considering that HER is the competing reaction for CO₂RR, the corresponding ΔG for HER on three different sites was calculated. The RDS for Co sites was from H* to H₂ with a ΔG , while the RDS for the Zn sites in COF@MOF₈₀₀-Co (0.58 eV) and COF@MOF₈₀₀ were forming the H* on the catalytic sites, with ΔG of 0.36 eV, and ΔG of 0.70 eV for ZnN₄-O, respectively (Figure 14E), suggesting the Co sites had higher activity for HER than those of Zn sites. To clearly identify the catalytic process, the limiting potential differences between CO₂RR and HER ($UL(CO_2) - UL(H_2)$) were also calculated. $UL(CO_2) - UL(H_2)$ for Co sites was -0.11 eV, indicating the HER was successfully suppressed by CO₂RR. Different from Co sites, the

main reactions for Zn sites were HER, and the $UL(CO_2)-UL(H_2)$ for Zn sites in $COF@MOF_{800}-Co$ and $COF@MOF_{800}$ were 0.21 eV and 0.62 eV, respectively. The smaller value of $UL(CO_2)-UL(H_2)$ indicates the synergistic effects of Co and Zn in $COF@MOF_{800}-Co$ enabled to suppress the competing reaction (Figure 14F).

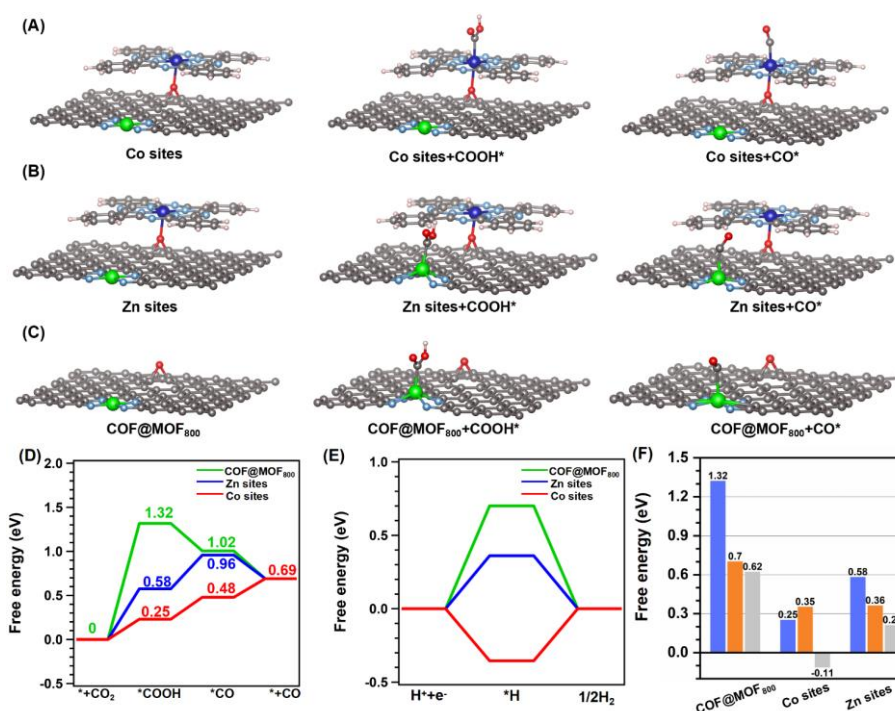


Figure 14. The schematic mechanism for CO₂RR on (A) Co sites and (B) Zn sites in $COF@MOF_{800}-Co$ and (C) Zn sites in $COF@MOF_{800}$, respectively. The balls in green, blue, grey, cyan, red and pink represent Zn, Co, C, N, O and H atoms. (D) The relative energy diagram of CO₂RR, and (E) HER for Co sites (red curve) and Zn sites (green curve) in $COF@MOF_{800}-Co$ and (C) Zn sites (blue curve) in $COF@MOF_{800}$ (blue curve). (F) The overpotentials for the RDS of the catalytic sites in CO₂RR (blue: CO₂RR; orange: HER; gray: the values of $UL(CO_2)-UL(H_2)$).

4.3 Conclusion

In summary, we have developed a new synergetic dual atomic catalyst for CO₂RR. The synergistic CoN₄O and ZnN₄ sites significantly improve the

electron transport rate and the generation of COOH* intermediate, which is beneficial for the process of CO₂RR. The catalyst showed superior activity selectivity and long-term stability over many other electrocatalysts. Its maximum FE_{CO} and TOF values reached 92.6% at -0.8 V and 1370.24 h⁻¹ at -1.0 V, respectively. This work not only provided new insights for the preparation of carbon-supported bimetallic SACs but also offered a new method to develop catalytic carbons from COFs.

Chapter 5. Dimensionally Controlled Interlayer Spaces of Covalent Organic Frameworks for the Oxygen Evolution Reaction

5.1 Introduction

The COF-derivatives cannot realize the precise control for the topology and dimensions; thus, further hindered us to explore the influence of COFs' topologies, building blocks and frameworks for the electrocatalysis performance. For the topologies of COFs, the networks of most COFs can be extended into 1D, 2D and 3D directions, using different topological building blocks.^[156-160] The topology of COFs has a significant impact on their properties and functions.^[161-163] For instance, 2D COFs have one dimensional porous channels that facilitate ionic conduction, whereas 3D COFs have high surface areas, which is beneficial for gas uptakes.^[164-168] However, owing to weaker pi-pi stacking of 1D chains compared with 2D layer stacking, 1D COFs have been rarely reported, making crystal processing challenging. The unique properties of 1D COFs make them a promising material for various applications; their synthesis and applications are still being explored. Thus, we studied the influence of topologies for the electrocatalytic performance in this chapter.

In Chapter 5, we have demonstrated dimensional-controlled interlayer space of COFs for OER. The 1D catalytic COF had weaker stacking interaction between the 1D chains than that from two-dimensional COFs, which allowed for easier expansion of the interlayer distance in catalytic process, leading to enhanced catalytic activity. Moreover, the electronic states were well modulated with extending the length of conjugating units by integrating the alkynyl units. The optimized catalyst achieved an overpotential of 225 mV and Tafel slope of 76 mV dec⁻¹ in 1.0 M KOH, outperforming other 2D or 3D COFs. Theoretical calculations demonstrated that the alkynyl units facilitated the OOH* desorption

on the Fe sites, which further improved the activity.

Herein, we synthesized the 1D catalytic COF using four-connected pyrene-based units and the non-linear phenanthroline building blocks to immobilize Fe ions, which showed much higher activity than that from the controlled 2D COF. The space between the chains were easily expanded easily owing to weaker interactions, resulting in more exposed catalytic sites (Figure 1A). These findings highlight the advantages of 1D COFs as promising candidates for highly efficient OER catalysis and pave the way for future research in this field.

5.2 Results and discussion

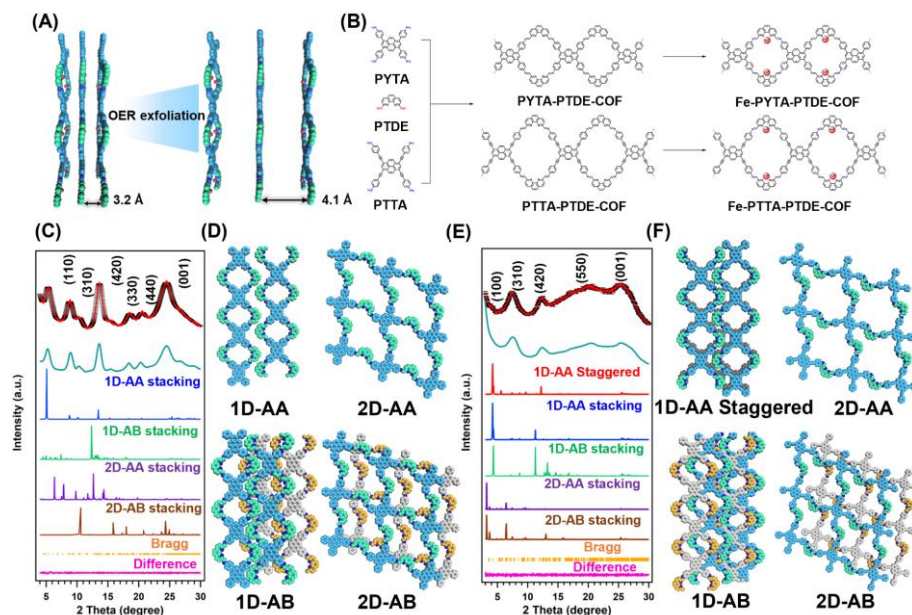


Figure 1. (A) The scheme of OER exfoliation for COFs. (B) Chemical structures and synthesis of PYTA-PTDE-COF, PTTA-PTDE-COF, Fe-PYTA-PTDE-COF and Fe-PTTA-PTDE-COF from PTDE, PTTA, PYTA units. (C) The PXRD profiles for PYTA-PTDE-COF of the experimentally observed (black), Pawley refined (red), simulated using the 1D AA (blue), 1D AB (green), 2D AA (brown), 2D AB (purple) stacking modes, Bragg positions (orange), their difference (pink), and Fe-PYTA-PTDE-COF (cyan). (D) The theoretically modelled 1D-AA, 1D-AB, 2D-AA and 2D-AB stacking models for PYTA-PTDE-COF. (E) The PXRD profiles for PTTA-PTDE-COF of the experimentally observed (black), Pawley refined (red), simulated using the 1D AA staggered (red), 1D AA (blue), 1D AB (green), 2D AA (brown), 2D AB (purple) stacking modes, Bragg positions (orange), their difference (pink) and Fe-PTTA-PTDE-COF (cyan). (F) The theoretically modelled 1D AA staggered, 1D-AB, 2D-AA and 2D-AB stacking models for PTTA-PTDE-COF.

The new COF (PYTA-PTDE-COF) was synthesized from and 1,10-phenanthroline-2,9-dicarbaldehyde (PTDE) in a mixed solvent of mesitylene / dioxane (0.5/0.5 mL) and 6M acetic acid at 120 °C for 7 days, with 85% yield.

The PTTA-PTDE-COF was synthesized by using 4,4',4'',4'''-(pyrene-1,3,6,8-tetrayltetrakis(ethyne-2,1-diyl))tetraaniline (PTTA) as a knot under the same condition, with a yield of 82% (Figure 1B). The as-prepared PYTA-PTDE-COF and PTTA-PTDE-COF were then used to anchor the Fe (II) via the coordination effects between phenanthroline and metal sites to yield Fe-PYTA-PTDE-COF and Fe-PTTA-PTDE-COF, respectively (Figure 1B). The as-prepared PYTA-PTDE-COF and PTTA-PTDE-COF were then used to anchor the Fe (II) via the coordination effects between phenanthroline and metal sites to yield Fe-PYTA-PTDE-COF and Fe-PTTA-PTDE-COF, respectively (Figure 1B).

PXRD are adopted to investigate crystal structures of as-synthesized COFs and Fe-COFs. The PXRD patterns for PYTA-PTDE-COF showed the peaks from (100), (210), (110), (311), (130) and (001) facets were at 5.31° , 8.87° , 13.59° , 18.53° , 20.53° and 24.52° , respectively (Figure 1C). The stimulated parameters reveal that the stimulation models are identical with the experiments (R_{wp} and R_p of 2.12% and 1.66%, respectively). In addition, we stimulated 1D and 2D topologies with AA and AB stacking models of PYTA-PTDE-COF. (Figure 1D). Importantly, the PXRD patterns of these stacking modes are different from the experiments, suggesting that PYTA-PTDE-COF adopted the 1D topology with AA stacking model. Furthermore, the chains of PYTA-PTDE-COF are stacked through pi-pi interactions with the interlayer space of 3.5 Å. With introducing the C≡C units in the COF, the PTTA-PTDE-COF showed a crystal structure with peaks at 4.13° , 6.48° , 11.26° , 24.43° and 26.03° due to the (100), (310), (420), (550) and (001) facets (Figure 1E). Furthermore, the stimulated parameters agreed with the experiments (R_{wp} and R_p were 2.48% and 2.24%, respectively). Correspondingly, the 1D and 2D with different stacking models of PTTA-PTDE-COF were simulated (Figure 1F). Notably, the PXRD profiles are in accordance with 1D AA staggered stacking model rather than other models, further confirming its 1D topology. And the corresponding interlayer distance was of 3.2 Å, which is shorter than that of the PYTA-PTDE-COF. With binding Fe ions by phenanthroline units, PXRD profiles revealed that all the

peaks from COFs are clearly identified, indicating their ordered structures were well retained (Figure 1C and 1E, cyan curve).

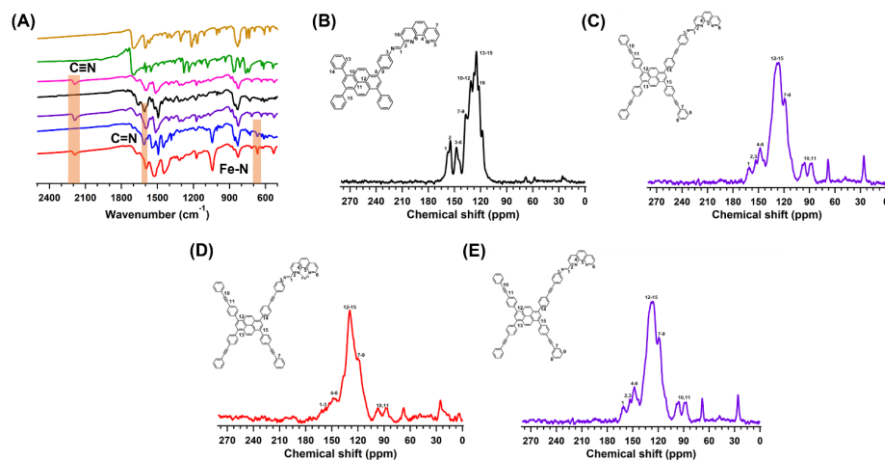


Figure 2. (A) The FT-IR spectra of PTDE (green), PYTA (brown), PTEA (pink), PYTA-PTDE-COF (black), PTTA-PTDE-COF (purple), Fe-PYTA-PTDE-COF (blue) and Fe-PTTA-PTDE-COF (red). The ^{13}C NMR spectra of (B) PYTA-PTDE-COF, (B) PTTA-PTDE-COF, (C) Fe-PYTA-PTDE-COF and (D) Fe-PTTA-PTDE-COF.

The FT-IR spectrum for the PYTA-PTDE-COF showed the strong vibration bond from C=N linkages was at 1618 cm^{-1} , indicating successful synthesis of the COF (Figure 2A).^[169] And the peaks from C=N linkage was also identified at 1598 cm^{-1} for PTTA-PTDE-COF, with a new bond at 2180 cm^{-1} from the C≡C vibration.^[170] After immobilizing Fe sites in the COFs, the bonds positions of C=N bonds in Fe-PYTA-PTDE-COF and Fe-PTTA-PTDE-COF showed slight changes, indicating that the skeletons of COFs were well retained. Meanwhile, the Fe-N bonds at 690 cm^{-1} were also identified over the Fe-PYTA-PTDE-COF and Fe-PTTA-PTDE-COF. The solid-state ^{13}C NMR spectrum confirmed the structures of these four COFs. The characteristic signals at 157 and 161 ppm attributed to $-\text{C}=\text{N}$ of PYTA-PTDE-COF and PTTA-PTDE-COF, respectively, suggesting the successful synthesis (Figures 2B and 2C). Additionally, a peak at 147 ppm corresponded to the carbon atoms of pyridine N for PYTA-PTDE-COF and PTTA-PTDE-COF. Furthermore, peaks in the

range from 117 to 140 ppm originated from the benzene units for PYTA-PTDE-COF and PTTA-PTDE-COF, while the peak at ~ 90 ppm is ascribed to the carbon atoms of the acetylene group for PTTA-PTDE-COF.^[171] After coordinating Fe^{2+} , the ^{13}C NMR spectra of Fe-PYTA-PTDE-COF and Fe-PTTA-PTDE-COF are almost identical to that of PYTA-PTDE-COF and PTTA-PTDE-COF, indicating the structural preservation after the post-treatment, while the slight positive shift ~ 2 and 3 ppm are assigned to the carbon atom of pyridine N because of the coordination with Fe^{2+} for Fe-PYTA-PTDE-COF and Fe-PTTA-PTDE-COF (Figures 2D-2E).

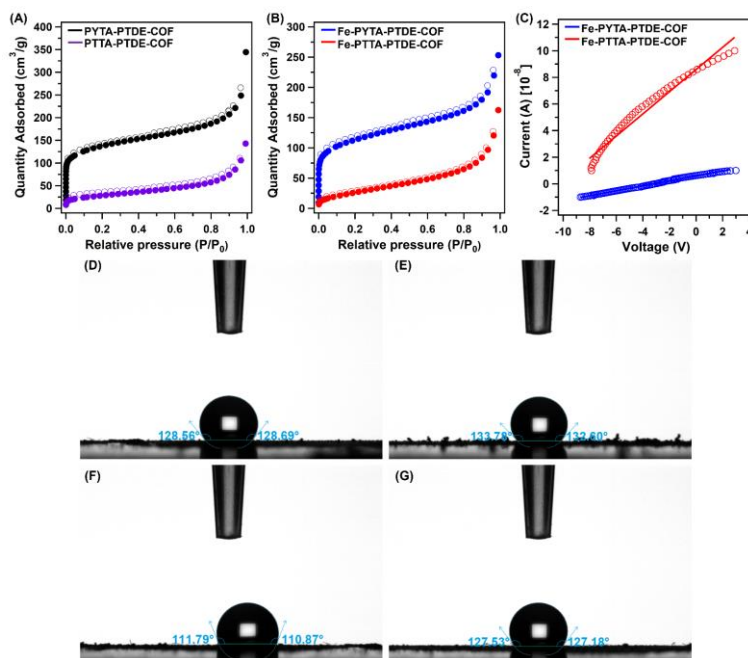


Figure 3. (A-B) The nitrogen sorption isotherms of PYTA-PTDE-COF (black), PTTA-PTDE-COF (purple), Fe-PYTA-PTDE-COF (blue) and Fe-PTTA-PTDE-COF (red) at 77 K, respectively. (C) The I-V curves of Fe-PYTA-PTDE-COF (blue) and Fe-PTTA-PTDE-COF (red) at 298 K. The WCA of (D) PYTA-PTDE-COF, (E) PTTA-PTDE-COF, (F) Fe-PYTA-PTDE-COF and (G) Fe-PTTA-PTDE-COF.

The porous structures are beneficial for the mass transport in the process of catalysis. The nitrogen sorption curves at 77 K were conducted to investigate the attribute of porous structures for COFs. The PYTA-PTDE-COF and PTTA-

PTDE-COF exhibited microporous sorption behaviour, and the S_{BET} of 462 and $108 \text{ m}^2 \text{ g}^{-1}$, following pore volumes of 0.53 and $0.22 \text{ cm}^3 \text{ g}^{-1}$, respectively (Figure 3A). In addition, the main pore sizes of PYTA-PTDE-COF and PTTA-PTDE-COF are 0.81 and 1.3 nm , respectively. With the addition of Fe^{2+} , the Fe-PYTA-PTDE-COF and Fe-PTTA-PTDE-COF exhibit the smaller S_{BET} of 384 and $99 \text{ m}^2 \text{ g}^{-1}$ compared to the original COFs, owing to the introduction of Fe atoms in pores (Figure 3B). The electronic conductivity was important for the COFs in OER. Thus, we tested the conductivity of Fe-PYTA-PTDE-COF and Fe-PTTA-PTDE-COF. The electrical conductivity for Fe-PTTA-PTDE-COF was determined to be $2.45 \times 10^{-8} \text{ S cm}^{-1}$, which was 24 times of that Fe-PYTA-PTDE-COF ($1.02 \times 10^{-9} \text{ S cm}^{-1}$) (Figure 3C). These results suggested that the acetylene bond promote the electron transfer and enhance the conductivity. In addition, we tested the contact angles of water on the four synthesized 1D COFs.

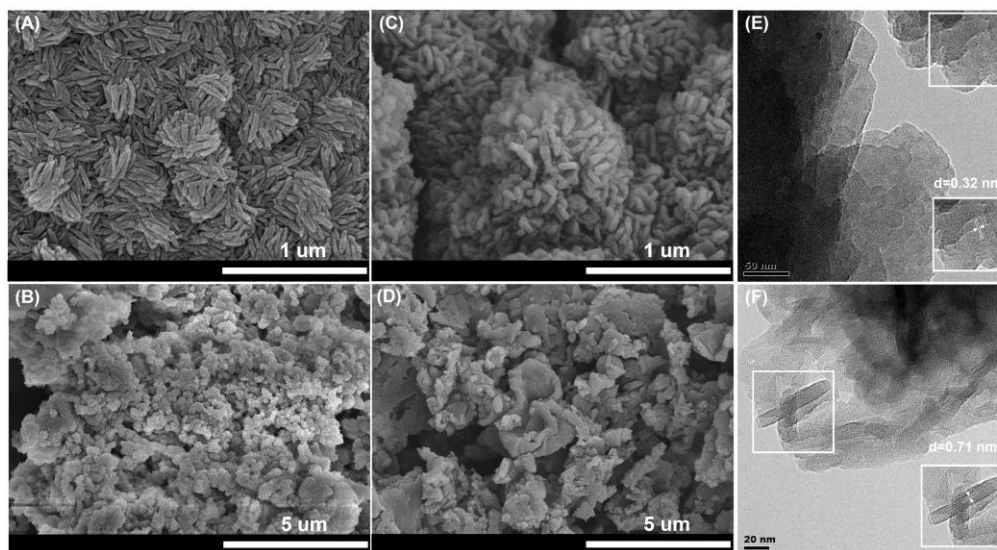


Figure 4. The SEM images of (A) PYTA-PTDE-COF, (B) PTTA-PTDE-COF, (C) Fe-PYTA-PTDE-COF and (D) Fe-PTTA-PTDE-COF. The TEM images of (E) PYTA-PTDE-COF and (F) PTTA-PTDE-COF.

Specifically, the WCAs of the PYTA-PTDE-COF and PTTA-PTDE-COF were 128.56° and 133.78° , respectively, indicating that the effects of alkynyl groups on the surface hydrophobicity are important. In addition, introducing of iron ions

can result in a slight increase of the surface hydrophilicity (Fe-PYTA-PTDE-COF with 111.79° and Fe-PTTA-PTDE-COF with 127.53°) (Figures 3D-3G). The SEM images show that PYTA-PTDE-COF had a nanofiber-shape morphology and PTTA-PTDE-COF exhibited a flower shape (Figures 4A and 4B). In addition, the Fe-PYTA-PTDE-COF and Fe-PTTA-PTDE-COF still kept the same morphologies as original COFs, indicating the stable property (Figures 4C and 4D). The TEM and HR-TEM images showed the obvious lattice images, suggesting the high crystallinity for the PYTA-PTDE-COF and PTTA-PTDE-COF (Figures 4E and 4F).

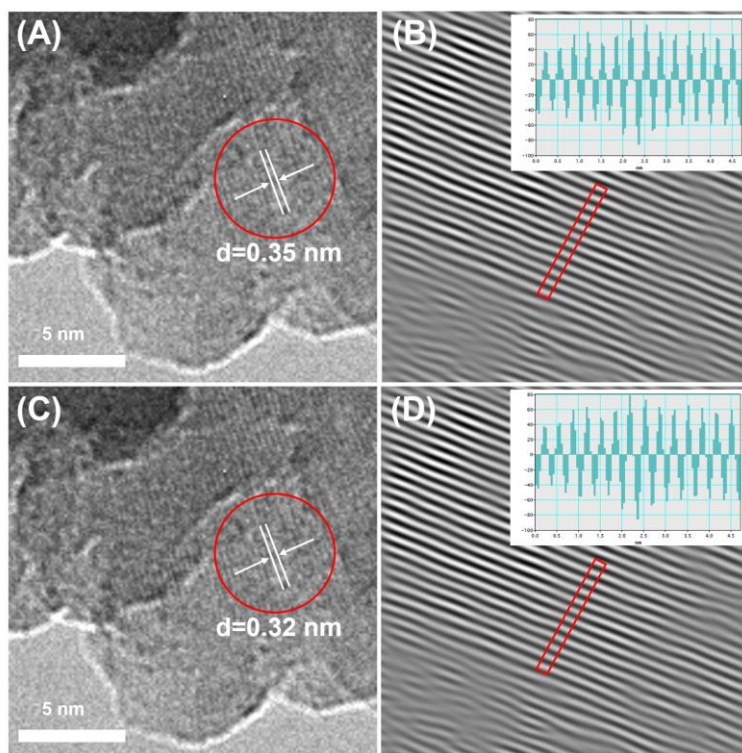


Figure 5. The HR-TEM images and FFT translation of (A-B) Fe-PYTA-PTDE-COF and (C-D) Fe-PTTA-PTDE-COF.

Furthermore, the absence of clusters in the TEM images of Fe-PYTA-PTDE-COF and Fe-PTTA-PTDE-COF indicated the homogeneous distribution (Figure S14-S15). The HR-TEM images and inverse FFT transformation illustrated that a crystal lattice corresponding to the (001) and (020) facets of Fe-PYTA-PTDE-COF and Fe-PTTA-PTDE-COF, respectively (Figures 5A-5D).

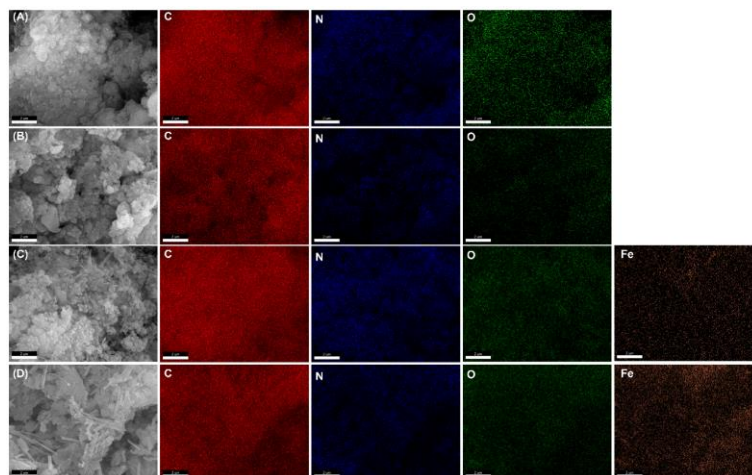


Figure 6. The EDX mapping images of (A) PYTA-PTDE-COF, (B) PTTA-PTDE-COF, (C) Fe-PYTA-PTDE-COF and (D) Fe-PTTA-PTDE-COF.

EDX mapping images revealed all elements were even distributed in the skeletons of COFs (Figures 6A-6D).

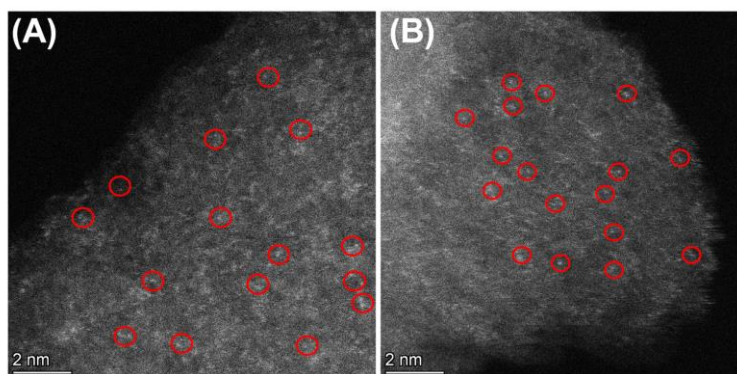


Figure 7. The HAADF-STEM images of (A) Fe-PYTA-PTDE-COF and (B) Fe-PTTA-PTDE-COF.

In addition, The HAADF-STEM images for Fe-PYTA-PTDE-COF and Fe-PTTA-PTDE-COF showed the bright dots from the atomic dispersion of Fe were in atomic states rather than nanoparticles dispersed on the skeletons (Figures 7A and 7B).

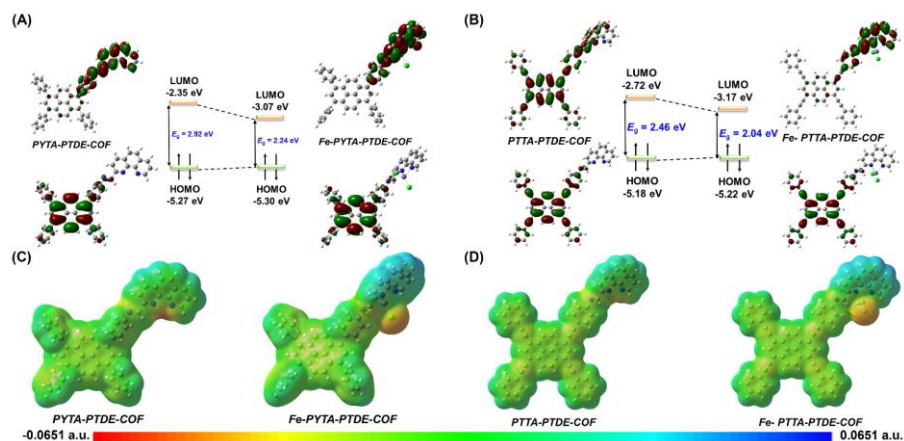


Figure 8. DFT calculated molecular orbitals and energy diagrams of (A) PYTA-PTDE-COF and Fe-PYTA-PTDE-COF, as well as (B) PTTA-PTDE-COF and Fe-PTTA-PTDE-COF at the B3LYP/6-31G(d) level. The ESP surface maps for optimized structures of (C) PYTA-PTDE-COF and Fe-PYTA-PTDE-COF, (D) PTTA-PTDE-COF and Fe-PTTA-PTDE-COF.

The LUMO and HOMO of these COFs were calculated to investigate the effects of Fe and alkyne on the electronic distribution and charge transfer. After introducing the alkyne, the LUMO of PTTA-PTDE-COF are fully delocalized over the entire molecule, indicating the extended π -conjugated structures, which can further provide better electrical conductivity and develop the catalytic activity (Figure 8A).^[172-174] Moreover, the HOMO-LUMO energy gap of PTTA-PTDE-COF are lower than that of PYTA-PTDE-COF, indicating the higher conductivity and chemical reactivity for potential reaction. Normally, a small HOMO-LUMO energy gap indicates high activity which can activate complex of any potential reaction.^[175-177] In addition, after Fe coordination, the LUMO-HOMO bandgap of Fe-PYTA-PTDE-COF (2.24 eV) and Fe-PTTA-PTDE-COF (2.04 eV) are lower than that of PYTA-PTDE-COF (2.92 eV) and PTTA-PTDE-COF (2.46 eV) (Figure 8B). These distinctive donor-acceptor properties and the LUMO-HOMO distribution of Fe-PTTA-PTDE-COF originate from the easier charge transfer between the Fe coordination and alkyne units. Furthermore, ESP of these COF model compounds revealed that the Fe^{2+} can regulate the charge

distribution. As shown in Figures 8C and 8D, the electron-rich region (negative potential) of PYTA-PTDE-COF and PTTA-PTDE-COF are mainly distributed around the pyridine N, while after coupling with Fe^{2+} the pyrene backbone became more electron rich (negative potential) and the N-phenanthroline linker became more electron-deficient (positive potential), indicating the formation of an internal electric field thus promoting the OER.^[178-179]

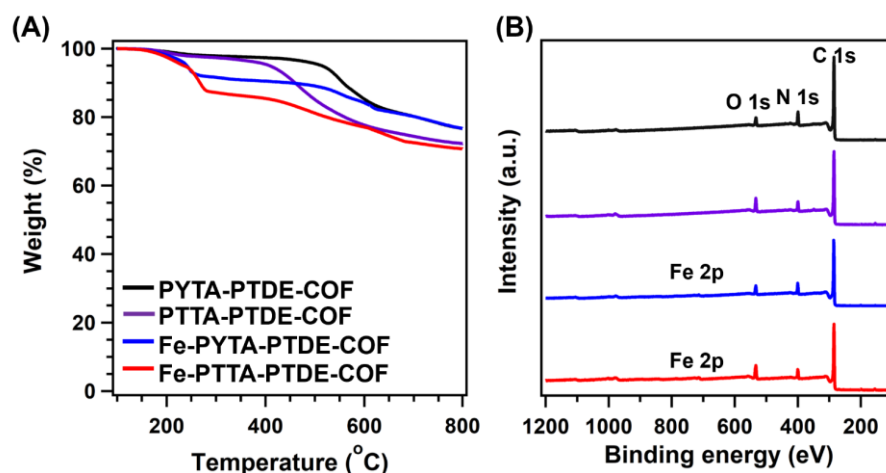


Figure 9. (A) The TGA curves and (B) XPS spectra of PYTA-PTDE-COF (black), PTTA-PTDE-COF (purple), Fe-PYTA-PTDE-COF (blue) and Fe-PTTA-PTDE-COF (red).

The TGA under nitrogen atmosphere suggested that PYTA-PTDE-COF and PTTA-PTDE-COF were stable up to 500 and 350 °C, respectively, while the Fe-PYTA-PTDE-COF and Fe-PTTA-PTDE-COF showed decomposition after 200 °C under N_2 atmosphere (Figure 9A), indicating their good thermal stability. Additionally, the XPS was adopted to study the electron states. Specifically, the peaks attributed to C, N, O, and Fe were observed (Figure 9B).

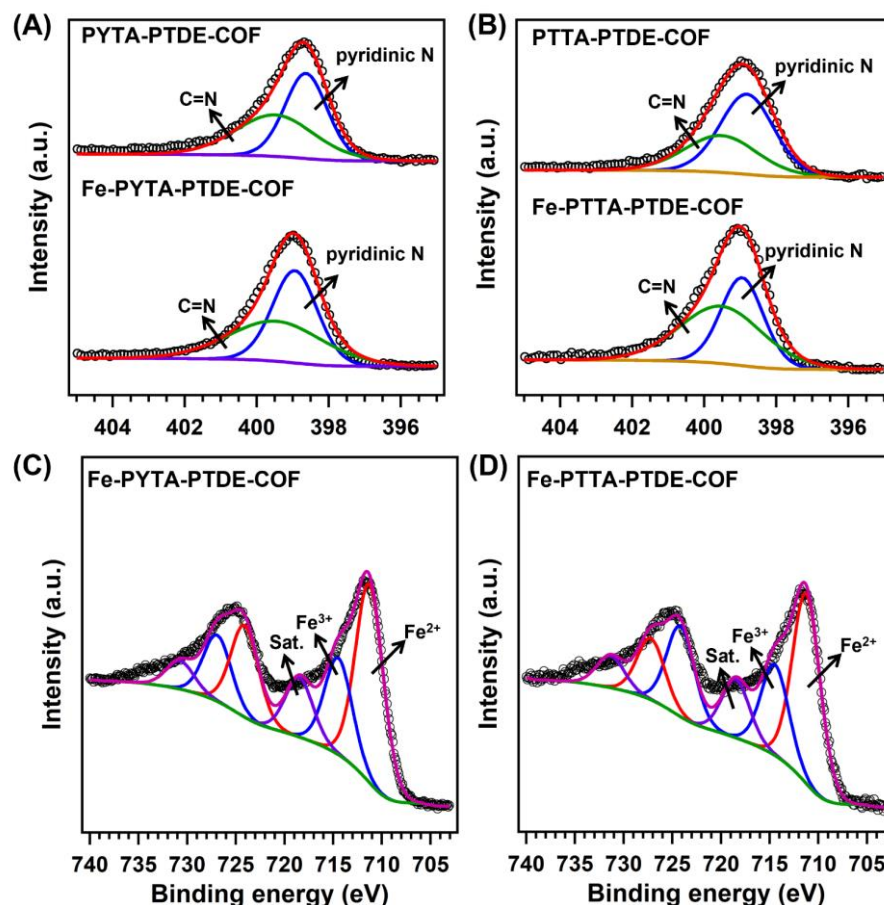


Figure 10. The high-resolution N 1s spectra of (A) PYTA-PTDE-COF and Fe-PYTA-PTDE-COF, (B) PTTA-PTDE-COF and Fe-PTTA-PTDE-COF. The high-resolution Fe 2p spectra of (C) Fe-PYTA-PTDE-COF and (D) Fe-PTTA-PTDE-COF.

The high-resolution N 1s spectra of the PYTA-PTDE-COF and PTTA-PTDE-COF showed peaks from C=N of imine bonds and pyridine N of PTDE units, respectively (Figures 10A and 10B). After adding the iron salts, the pyridine N of these two COFs showed the positive shifts of ~ 0.3 and ~ 0.18 eV, respectively, suggesting the interaction between Fe and pyridine nitrogen. In addition, the high-resolution of Fe 2p demonstrated the Fe ions were in +2 and +3 valence states of Fe-PYTA-PTDE-COF and Fe-PTTA-PTDE-COF (Figures 10C and 10D). The weight contents of Fe in Fe-PYTA-PTDE-COF and Fe-PTTA-PTDE-COF were 2.96% and 3.12%, as obtained by the ICP-OES measurement.

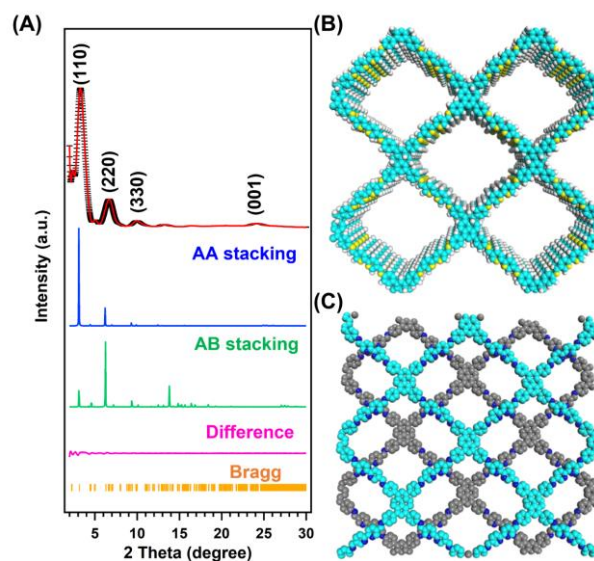


Figure 11. (A) The PXRD profiles for 2D-COF of the experimentally observed (black), Pawley refined (red), simulated using the 2D AA (blue), 2D AB (green) stacking modes, Bragg positions (orange) and their difference (pink). The theoretically modelled (B) 2D-AA and (B) 2D-AB stacking models for 2D-COF.

Then, we investigated the catalytic OER performance. Considering the OER performance could be influenced by different topologies, we have synthesized a 2D COF and Fe-2D-COF as a control. Specifically, the PXRD was adopted to investigate crystal structures of the 2D-COF and Fe-2D-COF. The PXRD patterns for 2D-COF showed the peaks from 3.11° , 6.20° , 9.31° and 24.98° due to the (110), (220), (330) and (001) facets, respectively (Figure 11A). The stimulated parameters reveal that the stimulation models are identical with the experiments (R_{wp} and R_p of 2.76% and 2.38%, respectively). In addition, we also stimulated AB stacking models of 2D-COF (Figure 11B). Notably, the PXRD patterns of the stacking model is different from the experiments, suggesting that 2D-COF adopted the AA stacking model. Furthermore, Fe-2D-COF also adopted AA stacking models in 2D AA topology (Figure 11C).

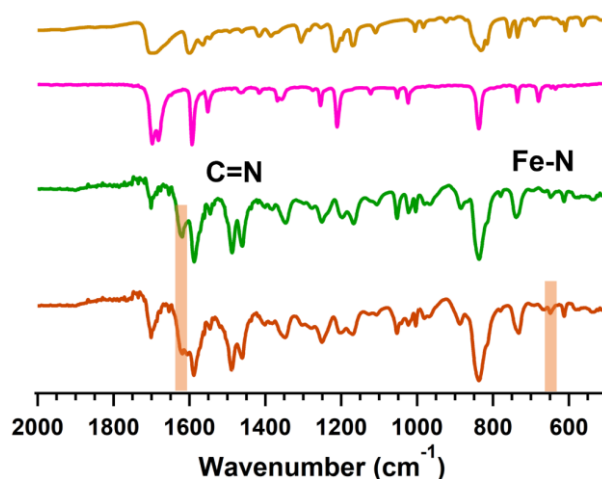


Figure 12. FT-IR spectra of PYTA (yellow), BPY (pink), 2D-COF (green) and Fe-2D-COF (brown).

The FT-IR spectrum of 2D-COF showed the strong vibration bond from C=N linkages was at 1624 cm^{-1} , indicating successful synthesis of the COF (Figure 12). And the peaks from C-N linkage was also identified at 1193 cm^{-1} for dipyriddy units of the 2D-COF. With immobilizing Fe sites in the 2D-COF, the bonds positions of C=N bonds in Fe-2D-COF showed slight changes, indicating that the skeletons of COFs were well retained. Meanwhile, the new peaks at 690 cm^{-1} were from Fe-N bonds in Fe-2D-COF.

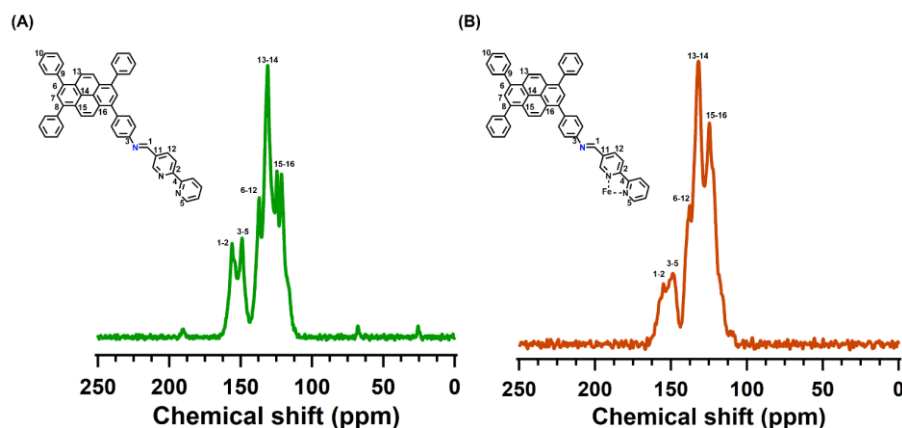


Figure 13. The solid-state ^{13}C NMR spectra of (A) 2D-COF and (B) Fe-2D-COF.

The solid-state ^{13}C NMR spectrum was further conducted to confirm the chemical structures of the 2D-COF and Fe-2D-COF. The characteristic signal at 156 ppm can be assigned to $-\text{C}=\text{N}$ of 2D-COF, respectively, which confirms the success of the condensation reaction (Figure 13A). Additionally, the peaks at 149 ppm corresponded to the carbon atoms of pyridine N for 2D-COF. The peaks from 117 to 140 ppm were assigned to the carbon atoms of the benzene units for 2D-COF. After coordinating Fe^{2+} , the ^{13}C NMR spectra of Fe-2D-COF are almost identical to that of 2D-COF, indicating the structural preservation after the post-treatment, while the slight positive shift ~ 2 and 3 ppm are assigned to the carbon atom of pyridine N because of the coordination with Fe^{2+} for Fe-2D-COF (Figure 13B).

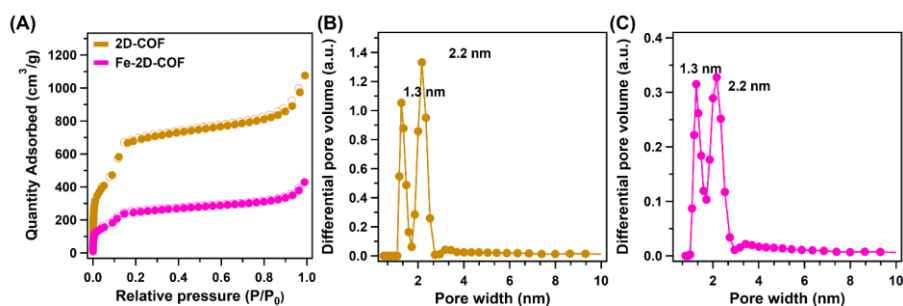


Figure 14. (A) The nitrogen sorption isotherms of 2D-COF (brown) and Fe-2D-COF (pink) at 77 K, respectively. The pore distribution curves of (B) 2D-COF and (C) Fe-2D-COF.

We investigated the porosity of the 2D-COF and Fe-2D-COF through nitrogen sorption isotherm measurements at 77 K. They exhibited microporous sorption behavior, with S_{BET} of 2200 and 950 $\text{m}^2 \text{g}^{-1}$, with pore volumes of 1.67 and 0.66 $\text{cm}^3 \text{g}^{-1}$, respectively (Figure 14A). The pore size distribution curves showed that the main pore sizes of 2D-COF and Fe-2D-COF were 1.3 and 2.2 nm, respectively (Figure 14B).

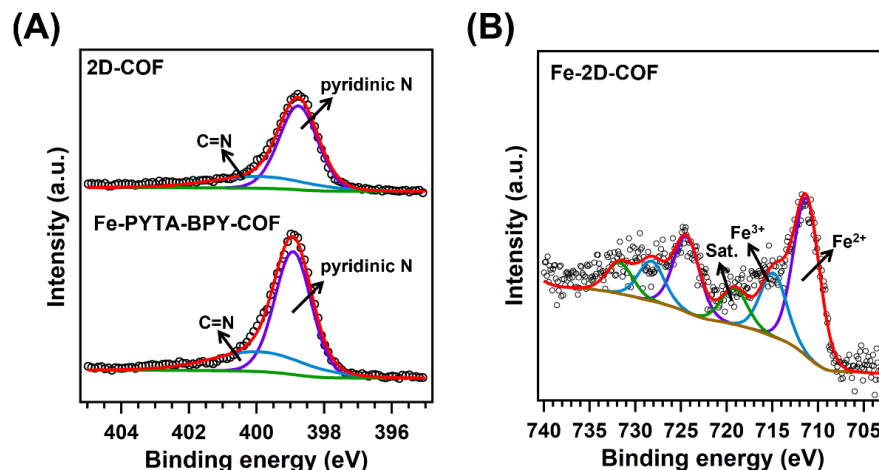


Figure 15. The high-resolution XPS spectra of (A) N 1s and (B) Fe 2p for 2D-COF and Fe-2D-COF.

The XPS spectra showed peaks corresponding to C, N, O, and Fe in the prepared COFs. The high-resolution N 1s spectra of the 2D-COF showed peaks from C=N of imine bonds and pyridine N of BPY units. After adding the iron salts, the pyridine N of Fe-2D-COF showed the positive shifts of ~ 0.2 eV, indicating the coordination between Fe and pyridine N (Figure 15A). In addition, the Fe 2p spectra showed the Fe elements were in +2 and +3 valence states of Fe-2D-COF (Figure 15B). The weight content of Fe in Fe-2D-COF was 3.12%, as obtained by ICP-OES measurement.

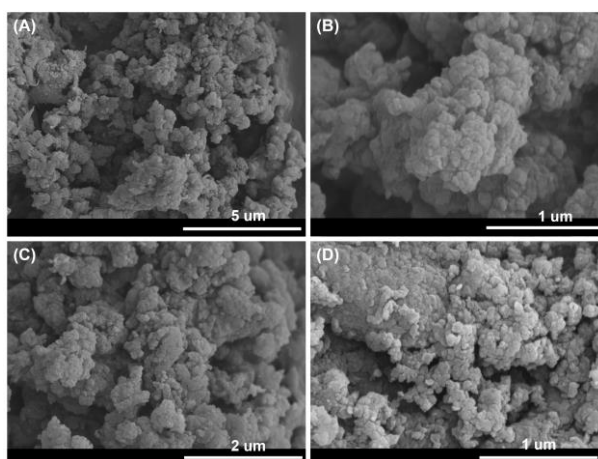


Figure 16. SEM images of (A-B) 2D-COF and (C-D) Fe-2D-COF.

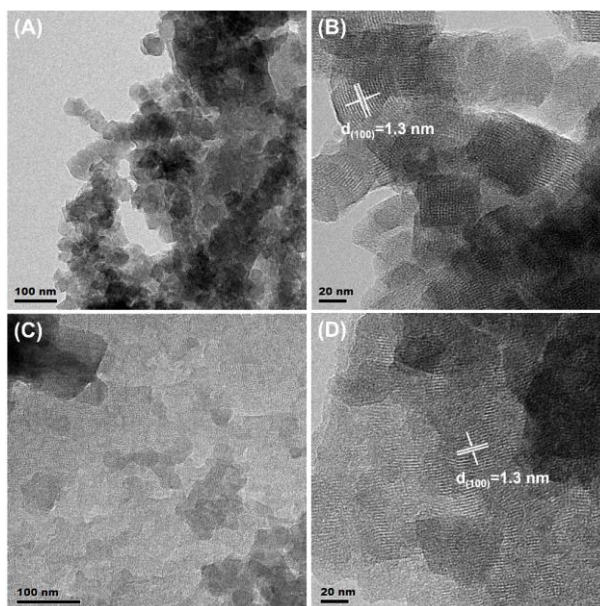


Figure 17. TEM and HR-TEM images of (A-B) 2D-COF and (C-D) Fe-2D-COF.

The SEM images show that 2D-COF and Fe-2D-COF were composed of microcrystalline particles (Figure 16). The TEM and HR-TEM images showed the obvious lattice images show the obvious lattices, suggesting the high crystallinity for the 2D-COF and Fe-2D-COF (Figure 17). No clusters or nanoparticles are exhibited in the TEM images of Fe-2D-COF, indicating the homogeneous distribution. The HR-TEM images illustrated that a crystal lattice corresponding to the (100) facets of 2D-COF and Fe-2D-COF, respectively.

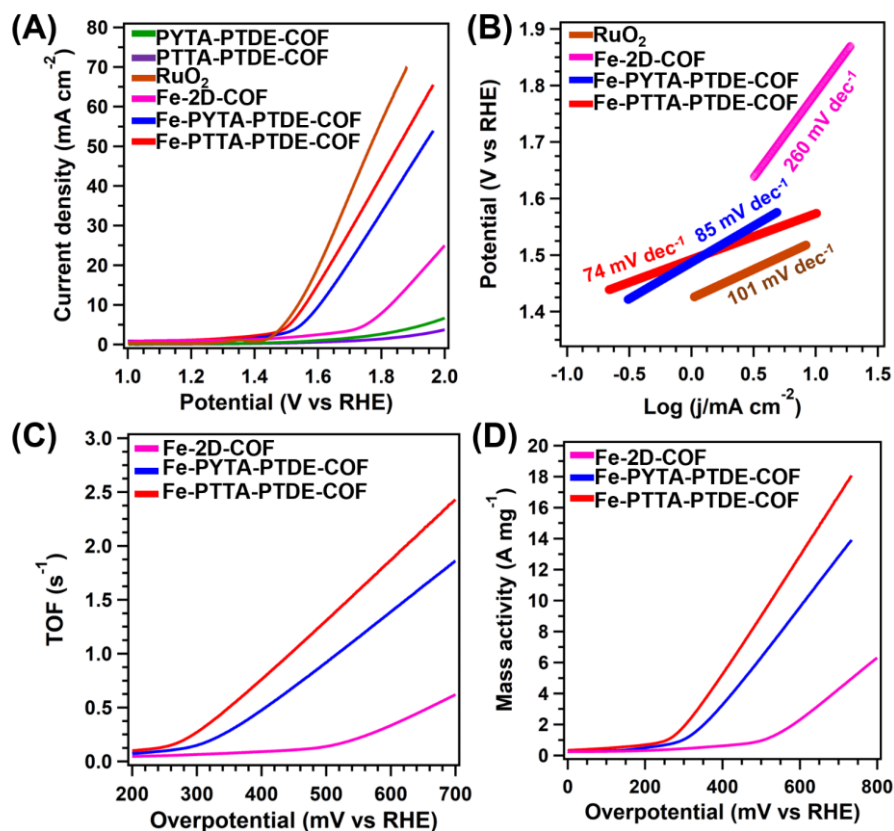


Figure 18. (A) The LSV curves, (B) the corresponding Tafel slopes, (C) the corresponding TOF values and (D) the mass activity over PYTA-PTDE-COF (green), PTTA-PTDE-COF (purple), RuO₂ (brown), Fe-PYTA-PTDE-COF (blue), Fe-2D-COF (pink) and Fe-PTTA-PTDE-COF (red) in oxygen-saturated KOH (0.1 M) aqueous solution.

We investigated the OER performance of these COFs in 0.1 M alkaline solutions under O₂ atmosphere. LSV curves demonstrated the overpotential (η_{10}) for Fe-PTTA-PTDE-COF was 328 mV at 10 mA cm⁻², with the corresponding Tafel slope of 78 mV dec⁻¹ (Figures 18A and 18B). In addition, the Fe-PYTA-PTDE-COF demonstrated the η_{10} of 374 mV and a corresponding Tafel slope of 87 mV dec⁻¹. Furthermore, these two COFs showed higher activity and kinetics than that of Fe-2D-COF (η_{10} of 590 and Tafel slope of 260 mV dec⁻¹) and close to that of the commercial RuO₂ (η_{10} of 335 mV and Tafel slope of 101 mV dec⁻¹). Correspondingly, the TOF were calculated of these COFs in 0.1 M KOH (Figure 18C). The TOF values for Fe-PYTA-PTDE-COF and Fe-PTTA-PTDE-COF

were 0.47 and 0.76 s^{-1} at an overpotential of 400 mV, which are superior to 2D controlled COF (0.09 s^{-1}), suggesting the superior kinetic performance. Meanwhile, the mass activity of Fe-PTTA-PTDE-COF is 5.23 A mg^{-1} at 400 mV, which is higher than Fe-PYTA-PTDE-COF (3.26 A mg^{-1}) and Fe-2D-COF (0.62 A mg^{-1}) in 0.1 M KOH, respectively, further implying the high intrinsic catalytic activity (Figure 18D).

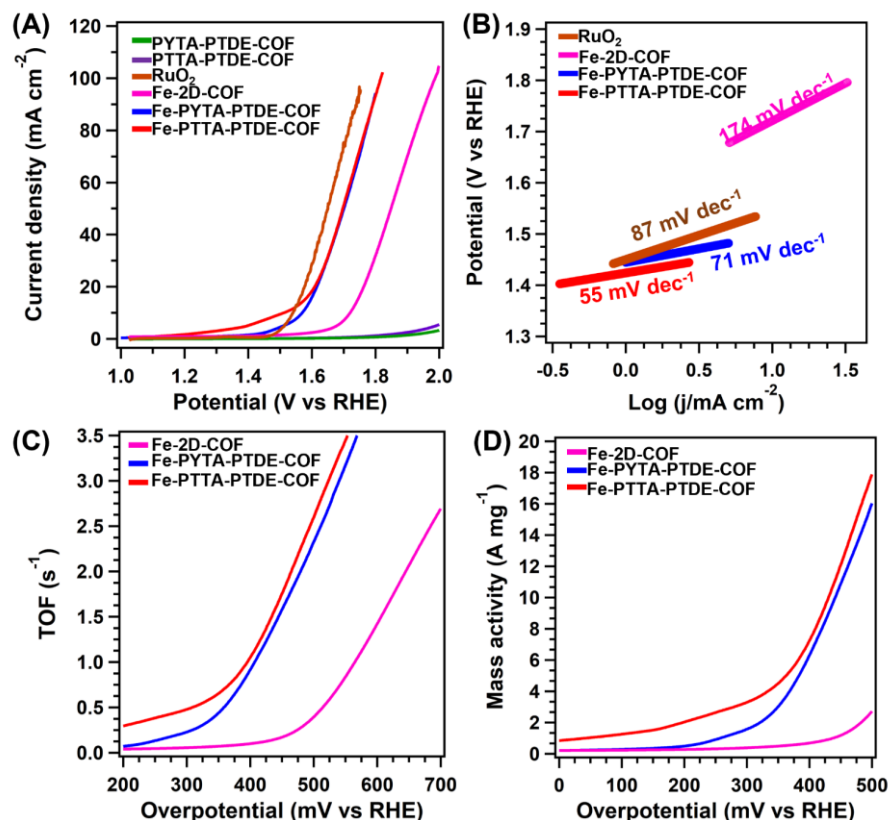


Figure 19. (A) The LSV curves, (B) the corresponding Tafel slopes, (C) the corresponding TOF values and (D) the mass activity over PYTA-PTDE-COF (green), PTTA-PTDE-COF (purple), RuO_2 (brown), Fe-PYTA-PTDE-COF (blue), Fe-2D-COF (pink) and Fe-PTTA-PTDE-COF (red) in oxygen-saturated KOH (1.0 M) aqueous solution.

We also tested the OER performance in 1.0 M KOH aqueous solution. Exactly, the values of η_{10} are 350 and 280 mV for Fe-PYTA-PTDE-COF and Fe-PTTA-PTDE-COF, with relative Tafel slopes of 79 and 71 mV dec^{-1} , respectively, which outperform Fe-2D-COF electrodes (490 mV and 180 mV dec^{-1}) and close

to the pristine RuO₂ (290 mV and 87 mV dec⁻¹), indicating favourable reaction kinetics in the OER process (Figures 19A and 19B). Correspondingly, the TOF values for Fe-PYTA-PTDE-COF and Fe-PTTA-PTDE-COF were 0.97 and 2.01 s⁻¹ at an overpotential of 400 mV, which are superior to Fe-2D-COF (0.11 s⁻¹) in 1.0 M KOH (Figure 19C). The mass activity of Fe-PTTA-PTDE-COF is 13.86 A mg⁻¹ at 400 mV, which is higher than that of Fe-PYTA-PTDE-COF (6.66 A mg⁻¹) and Fe-2D-COF (0.71 A mg⁻¹), respectively (Figure 19D). Importantly, the OER overpotentials and Tafel slopes of Fe-PTTA-PTDE-COF exceeded most reported Fe-based OER electrocatalysts (Table 1).

Table 1. Summary of recently reported OER performances of other reported COF derived electrocatalysts under alkaline conditions.

Electrocatalyst	Electrolyte	Overpotential (at 10 mA cm ⁻²) (mV)	Tafel slope (mV dec ⁻¹)	Reference
Fe-PTTA-PTDE-COF	0.1 M KOH	328	57	This work
	1.0 M KOH	225	67	
Fe-PYTA-PTDE-COF	0.1 M KOH	374	92	
	1.0 M KOH	340	71	
macro-TpBpy-Co	0.1 M KOH	380	54	[70]
TpBpy-Co	0.1 M KOH	430	58	[70]
Co-TEP-COF/CNTs	1.0 M KOH	410	61	[180]
TEPP-COF/CF	1.0 M KOH	381	113	[181]
Co-TAPP-COF	1.0 M KOH	473	89	[182]
Co-TABPP-COF	1.0 M KOH	487	95	[182]
Co-TAPP-COF-Fe	1.0 M KOH	416	68	[183]
3D-Co	0.1 M KOH	429	94	[120]
Co _{0.2} V _{0.8} @COF-SO ₃	1.0 M KOH	345	65	[184]
Co _{0.8} V _{0.2} @COF-SO ₃	1.0 M KOH	336	70	[184]
Co@COF-SO ₃	1.0 M KOH	363	85	[184]
V@COF-SO ₃	1.0 M KOH	480	157	[184]
Co _{0.5} V _{0.5} @COF-SO ₃	1.0 M KOH	318	62	[184]
Ni-SAC@COF	1.0 M KOH	337	45	[185]
Fe-SAC@COF	1.0 M KOH	290	51	[185]
Ni-COF	1.0 M KOH	335	55	[46]
Co-COF	1.0 M KOH	347	69	[46]
Cu-COF	1.0 M KOH	384	72	[46]

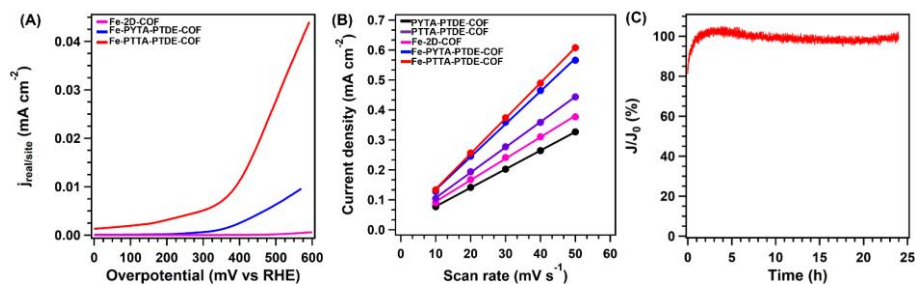


Figure 20. The $j_{\text{real/site}}$ values for Fe-PYTA-PTDE-COF (blue), Fe-2D-COF (pink) and Fe-PTTA-PTDE-COF (red) versus applied potential. (B) The C_{dl} values for PYTA-PTDE-COF (black), PTTA-PYTA-COF (purple), Fe-PYTA-PTDE-COF (blue), Fe-PTTA-PTDE-COF and (C) Fe-2D-COF (pink). Chronoamperometry test for OER of Fe-PTTA-PTDE-COF on the carbon paper at a potential of 1.6 V in 1.0 M KOH under O_2 atmosphere.

In addition, the superior OER performance of Fe-PYTA-PTDE-COF and Fe-PTTA-PTDE-COF with respect to Fe-2D-COF can be attributed to the much more actives, further identifying by the normalization process from current density to the activity per active sites ($j_{\text{real/site}}$).^[13] Specifically, the much higher $j_{\text{real/site}}$ for Fe-PTTA-PTDE-COF indicates abundant exposed active sites compared to Fe-2D-COF (Figure 20A). The ECSAs were confirmed using the electrochemical C_{dl} . The C_{dl} for Fe-PYTA-PTDE-COF and Fe-PTTA-PTDE-COF were 10.95 and 11.21 mF cm^{-2} , respectively, which were higher than that of Fe-2D-COF (8.43 mF cm^{-2}), confirming that the 1D topology provides a higher active surface in the catalytic process (Figure 20B). The long-term stability for Fe-PTTA-PTDE-COF on the Ni foam towards OER showed that the activity can be well retained after 25 hours (Figure 20C). However, the obvious improvement of current density within 5 hours was observed. Thus, it is reasonable to assume that the stripping of COF causes the exposure of more active sites.

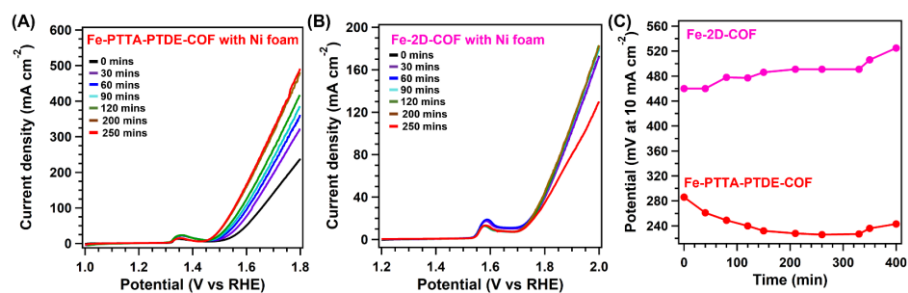


Figure 21. The LSV curves of (A) Fe-PTTA-PTDE-COF and (B) Fe-2D-COF at different time (from 0 to 250 mins) after the chronoamperometry test. (C) The plot of potential (at 10 mA cm⁻²) versus time (min) for Fe-PTTA-PTDE-COF (red) and Fe-2D-COF (pink).

To reveal the advantages of 1D structure, the OER performance of Fe-PTTA-PTDE-COF and Fe-2D-COF are conducted at intervals with the chronoamperometry method progresses (Figures 21A and 21B). Specifically, we tested a LSV curve every 30 mins with the continue of the chronoamperometry test of the Fe-PTTA-PTDE-COF on the Ni foam (from 0 to 250 minutes). For example, we conducted chronoamperometry test within 0 to 250 mins, then tested the LSV curves every 30 mins to verify the change of the OER performance which are influenced by the distance between layers. The LSV curves showed the η_{10} for Fe-PTTA-PTDE-COF remarkably decreases from 293 mV to 225 mV, while the η_{10} of Fe-2D-COF kept 480 mV (Figure 21C).

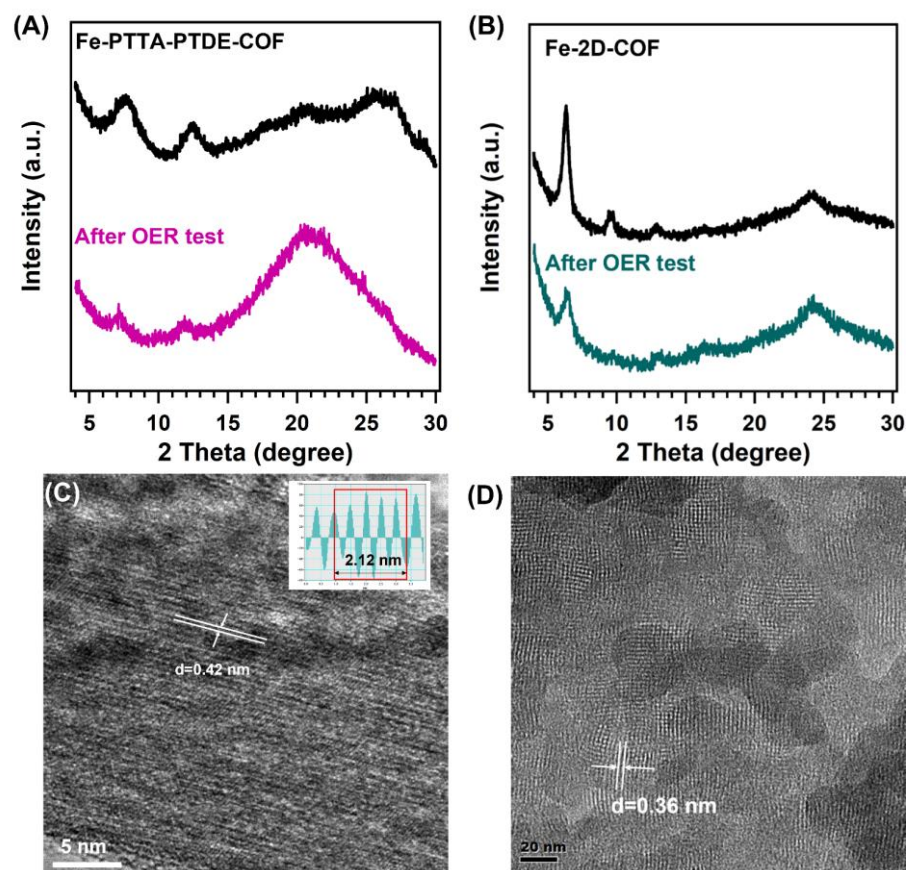


Figure 22. The PXR patterns of (A) Fe-PTTA-PTDE-COF and (B) Fe-2D-COF before and after the long-term test. The TEM images and inverse FFT transformation of (C) Fe-PTTA-PTDE-COF and (D) Fe-2D-COF after the chronoamperometry test.

The PXR patterns of Fe-PTTA-PTDE-COF demonstrated the absence of new peaks after long-term stability test, while the (001) facet exhibited a negative shift from 26.03° to 21.51° , suggesting the increasement of distance between layers (Figure 22A). However, the PXR patterns of Fe-2D-COF showed no change of the position for peaks after long-term stability test (Figure 22B). Then, the HR-TEM images of Fe-PTTA-PTDE-COF after the chronoamperometry method showed that the distance of layers was expanded to 0.42 nm from 0.32 nm (Figure 22C). However, the HR-TEM images of Fe-2D-COF illustrated that the interlayer distance did not change after the chronoamperometry method (Figure 22D).

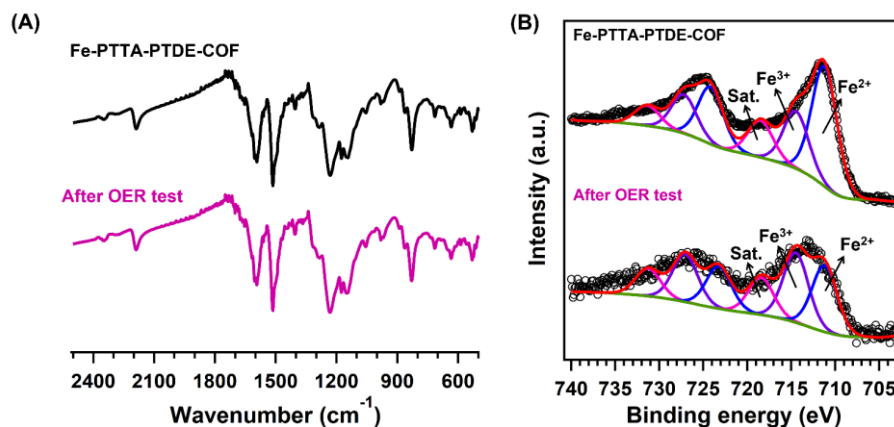


Figure 23. (A) The FT-IR spectra and (B) the XPS spectra of Fe 2p for Fe-PTTA-PTDE-COF before and after the OER test.

The FT-IR spectra showed all the peaks from the catalysts were well retained, indicating the absence of decomposition of linkages (Figure 23A). Meanwhile, the XPS spectra for Fe 2p of Fe-PTTA-PTDE-COF further revealed that Fe elements also kept the same states before and after the long-term stability measurement (Figure 23B). These results revealed the easier expansion of the interlayer distance due to the weaker stacking interaction between the 1D chains during the catalytic process, which hardly achieved in 2D COFs.

To investigate the catalytic mechanism, the reaction energetics of OER on Fe-PYTA-PTDE-COF and Fe-PTTA-PTDE-COF were simulated by using DFT calculations. (Figures 24A and 24B). Specifically, the DFT calculation illustrated the RDS for Fe-PYTA-PTDE-COF and Fe-PTTA-PTDE-COF in OER were the desorption of OOH* to O₂ (Figure 24C). And the ΔG for Fe-PTTA-PTDE-COF was 3.654 eV, smaller than that of Fe-PYTA-PTDE-COF (4.091 eV), indicating the catalytic activity showed obvious improved with enhancing the electron donor via introducing alkynyl units in PYTA units.

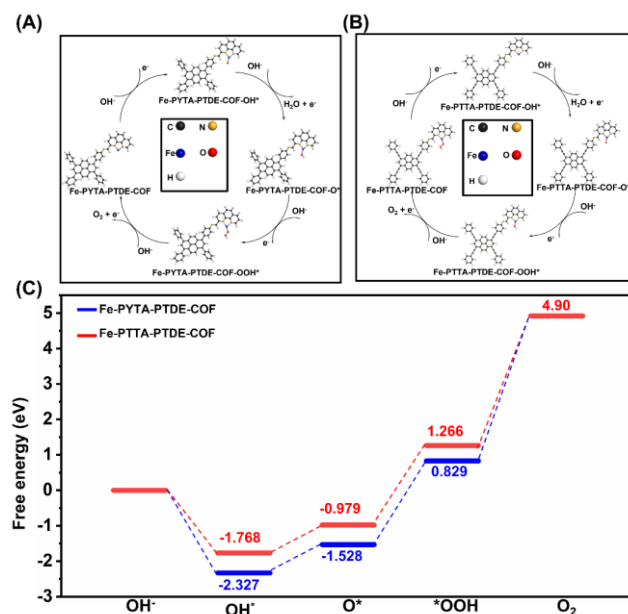


Figure 24. The catalytic OER mechanism cycles of the (A) Fe-PYTA-PTDE-COF and (B) Fe-PTTA-PTDE-COF model (C-black, N-yellow, H-white, O-red, Fe-blue). (C) The free energy profiles for the catalytic COFs in OER process.

5.3 Conclusion

In this chapter, we have demonstrated 1D COFs with enlarged interlayer space by self-expanding process for catalysing OER. The weaker stacking interaction between the 1D chains made the interlayer distance easily expanded in catalytic process, which resulted in more exposed catalytic sites, and thus further improved the catalytic activity. In addition, we modulated the electronic conductivity and charge transfer ability by introducing conjugated alkynyl units in the frameworks. The optimized catalyst achieved the high activity than other 2D or 3D COFs. The theoretical calculation showed the alkynyl facilitates the OOH^* desorption on the Fe sites, and thus improved the activity. This work gives us a new insight for design high-efficiency catalytic COFs for OER.

Chapter 6. Ladder Type Covalent Organic Frameworks Constructed with Natural Units for the Oxygen and Carbon Dioxide Reduction Reactions

6.1 Introduction

In the chapter 5, we discussed the influence of electrocatalytic performance using topologies of COFs. Considering the synthesis strategy is important for COFs except the dimensions and topologies, we adopted different building blocks to construct COFs for exploring the potential development of structures over COFs arrangement. To achieve a high activity in electrocatalysis, various metal centers in knots (e.g., porphyrin, phthalocyanine and the derivatives), along with diverse linkers characterized by distinct topologies, lengths and electronic states are orchestrated within these frameworks.^[166,186] However, it is noteworthy that these catalytic COFs have predominantly centered around the utilization of pre-defined building blocks, while the incorporation of natural units in COF synthesis remains an unexplored avenue. In chapter 6, we employed the natural units to construct COFs for both ORR and CO₂RR. The incorporation of EA units introduced ladder-like conjugation within the frameworks, resulting in enhanced electronic conductivity. This EA-based COF exhibited remarkable catalytic activity, selectivity and stability in both ORR and CO₂RR. Theoretical calculations revealed that the EA linker facilitated the formation of intermediates in the catalytic process, enhancing the overall efficiency. Consequently, this study not only expands the repertoire of COFs but also provides a promising avenue for developing highly efficient energy storage and conversion systems.

In this chapter, we constructed a catalytic COF utilizing the natural phenolic compound (EA) as the linker, dedicated to catalysing the ORR and CO₂RR. Through a base-catalysed substitution, the hydroxyl groups within the EA units

reacted with electron-deficient perfluorinated phthalocyanines, resulting in the formation of the catalytic COFs.^[187] Notably, the ladder-type configuration of the EA blocks confers an extended effective π -conjugation length to the COF, thereby enhancing the electron transfer capabilities. Furthermore, the presence of carbonyl and alkoxy groups within the EA sites enhances electronic conductivity, thereby substantiating higher levels of activity and selectivity in both ORR and CO₂RR. This study offers novel insights into the synthesis and catalytic chemistry of COFs.

6.2 Results and discussion

The CoPc-EA-COF was synthesized by using CoPc and EA monomers as building blocks through the nucleophilic aromatic substitution reaction, in a mixed solvent of mesitylene / DMF (0.5/0.5 mL) and Et₃N (0.1 mL) at 100 °C for 7 days with a yield of 85%. The controlled COF, CoPc-BP-COF, was constructed employing BP as a linker under the same conditions, with a yield of 82% (Figure 1A). The ladder-type conjugated building blocks (with independent but tied strands of bonds) enable to promote the charge conduction.^[39] In addition, the weight contents of Co determined by the ICP-OES were 3.78% and 3.85% for CoPc-EA-COF and CoPc-BP-COF, respectively.

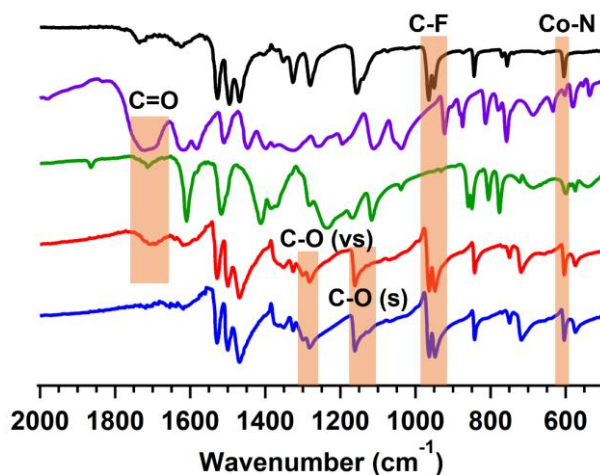


Figure 1. FT-IR spectra of CoPc-EA-COF (red), CoPc-BP-COF (blue), monomer of CoPc (black), EA (purple) and BP (green).

For the characterization of the structures and compositions of CoPc-EA-COF and CoPc-BP-COF, FT-IR spectroscopy was employed (Figure 1A). The FT-IR spectra for the CoPc-EA-COF exhibited distinctive vibration bands at 1280 and 1152 cm^{-1} , corresponding to the symmetric and asymmetric stretching vibrations of the C–O bonds. Additionally, announced peaks were observed at 1550 and 1450 cm^{-1} , attributed to the vibration bands of the benzene rings present in the phthalocyanine compound (Figure 1). Furthermore, predominant signals at 950 cm^{-1} were attributed to the C–F bonds within the phthalocyanine structure. Additionally, the evident peak at 1710 cm^{-1} , originating from the EA monomers, indicated the presence of C=O bonds within EA units. The appearance of C–O bonds confirmed the formation of dioxin-linked COFs, thus providing robust evidence for the successful synthesis of both CoPc-EA-COF and CoPc-BP-COF.

The crystal structures of the synthesized COFs were investigated by using PXRD measurements. The PXRD pattern of CoPc-EA-COF distinctly presented peaks corresponding to the (100) and (001) facets at 5.46° and 28.72°, respectively (Figures 2A and 2B). Through Pawley refinements, it was ascertained that the theoretical structures agreed well with the experimental results, yielding R_{wp} and R_p values of 3.72 and 4.08%, respectively. The stacking state of CoPc-EA-COF interlayer was simulated by considering different models of AA, AA', and AB stacking (Figures 2C-2E). Accordingly, the simulated diffraction pattern of AA' stacking matched well with the experimental values (Figures 2B & 2E).^[34] Peak indexing indicated that CoPc-EA-COF adopted the AA' stacking configuration in a $P2/M$ space group, with $a = b = 26 \text{ \AA}$, $c = 5 \text{ \AA}$, and $\alpha = \beta = \gamma = 90^\circ$. Additionally, CoPc-BP-COF demonstrated good crystallinity with prominent peaks observed 5.37° and 28.26° corresponding to the (100) and (001) facets (Figure 2F). The structure simulations in conjunction with Pawley refinements, it was deduced that CoPc-BP-COF shared the same stacking model as CoPc-EA-COF, with lattice parameters of $a = b = 26 \text{ \AA}$, $c = 5 \text{ \AA}$, and $\alpha = \beta = \gamma = 90^\circ$ (Figures 2F-2I).

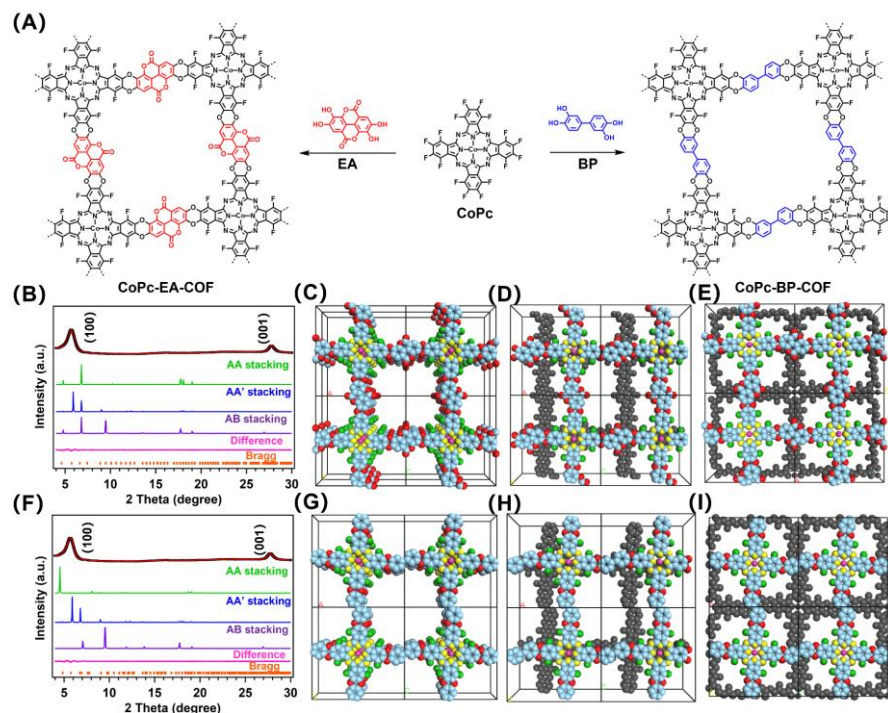


Figure 2. (A) Schematic synthesis procedure of CoPc-EA-COF and CoPc-BP-COF. (B) PXRD patterns CoPc-EA-COF. Line colour follows experimentally observed (black), Pawley refined (red), Bragg positions (orange) and their difference (pink), simulated using the AA' (blue) and AB (purple) stacking modes. Simulated packing structures of CoPc-EA-COF for (C) AA, (D) AA' and (E) AB stacking modes (C: cyan; N: pink; F: yellow; Co: blue and O: green). (F) PXRD patterns CoPc-BP-COF. Simulated packing structures of CoPc-EA-COF for (G) AA, (H) AA' and (I) AB stacking modes.

The porosities both of CoPc-EA-COF and CoPc-BP-COF were evaluated through nitrogen sorption measurement conducted at 77 K. Both COFs exhibited type I isotherms, indicative of microporous characteristics. CoPc-BP-COF manifested a S_{BET} of $150.2 \text{ m}^2 \text{ g}^{-1}$, a pore volume of $0.21 \text{ cm}^3 \text{ g}^{-1}$ and pore size of 1.49 nm (Figures 3A and 3B). By contrast, CoPc-EA-COF showed a slightly lower S_{BET} of $150.17 \text{ m}^2 \text{ g}^{-1}$, accompanied by a corresponding pore size of 1.49 nm and pore volume of $0.21 \text{ cm}^3 \text{ g}^{-1}$ (Figures 3A and 3C). Furthermore, the CoPc-EA-COF and CoPc-BP-COF exhibited CO_2 uptakes of 33.1 and $27.8 \text{ cm}^3 \text{ g}^{-1}$ at 273 K under 1 bar, respectively (Figure 3B).

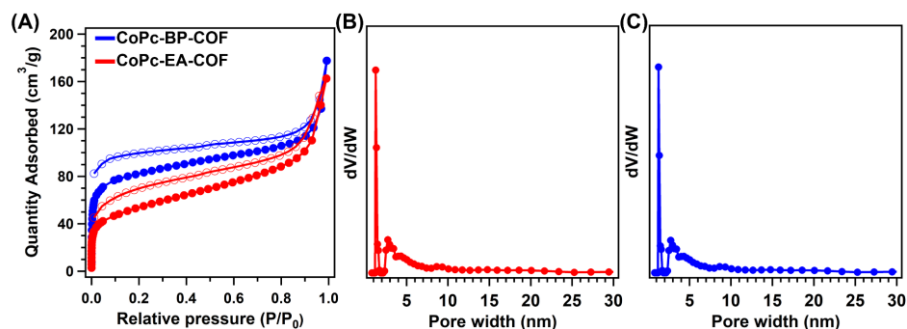


Figure 3. (A) The nitrogen-sorption isotherms at 77 K, the pore distribution curves of (B) CoPc-BP-COF (blue) and (C) CoPc-EA-COF (red).

The higher CO₂ uptake for CoPc-EA-COF could be attributed not only to a Lewis acid-base interaction between the coordinated metal ions and absorbed CO₂ molecules but also to the synergy between its microporous nature and the presence of heteroatom-rich channels within the CoPc-EA-COF structure.^[188]

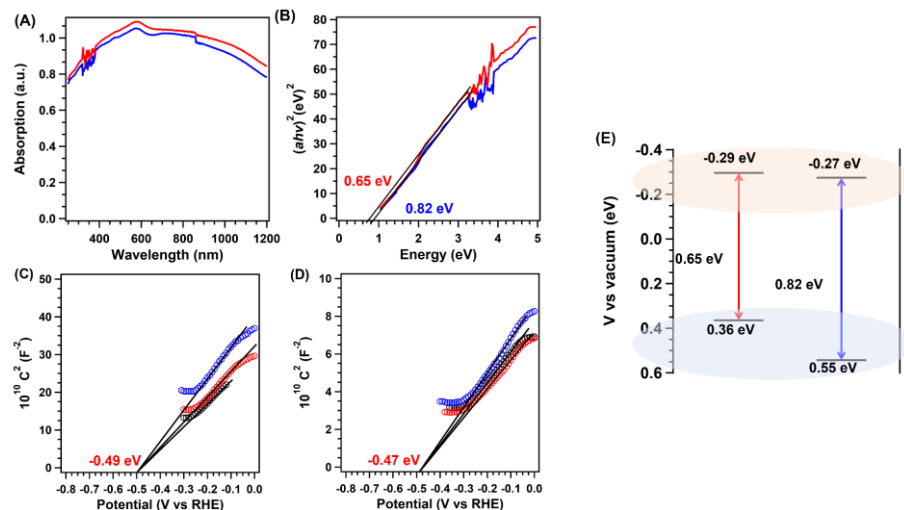


Figure 4. (A) The UV-Vis spectra and (B) Tauc plots for CoPc-EA-COF (red) and CoPc-BP-COF (blue). Mott-Schottky plots of (C) CoPc-EA-COF and (D) CoPc-BP-COF from 500 Hz to 1500 Hz. (E) Energy gaps (HOMO and LUMO) of CoPc-EA-COF (red) and CoPc-BP-COF (blue).

The band gaps of COFs were calculated by the UV-Vis spectra (Figures 4A and 4B), and the corresponding Tauc plots indicated that both ladder-type COFs possessed narrow band gaps, measuring of 0.65 and 0.82 eV, respectively. The presence of EA blocks within the COFs contributed to the reduction of these

bandgaps, thereby enhancing electronic conductivity.^[189] Mott–Schottky measurements were carried out for evaluating the reductive capability of the COFs. The obtained flat band potential values for CoPc-EA-COF and CoPc-BP-COF were -0.29 and -0.27 eV, respectively (Figures 4C and 4D). Additionally, the valence band positions for both COFs were 0.36 and 0.55 eV, respectively, indicating the superior reductive capacity of CoPc-EA-COF (Figure 4E).^[66]

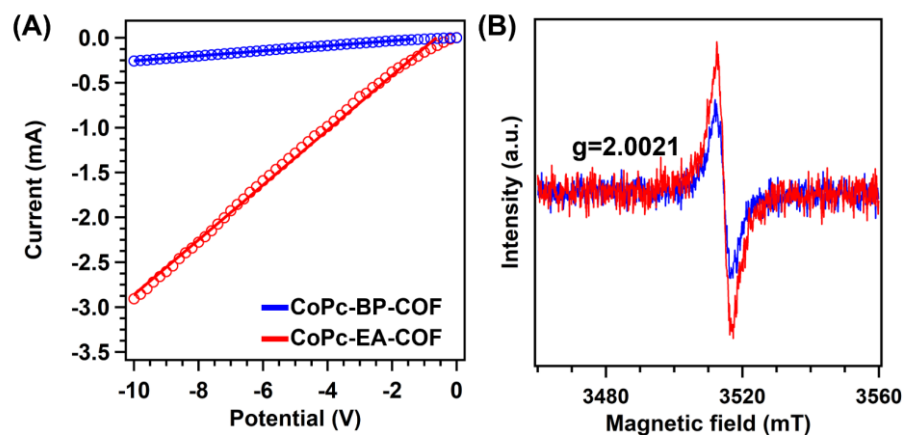


Figure 5. (A) I-V curves at 298 K and (B) EPR spectra of CoPc-EA-COF (red) and CoPc-BP-COF (blue).

Furthermore, the electronic conductivities were quantified using four-probe measurements at 298 K. The determined electrical conductivities were 0.67 and 0.46 mS cm^{-1} , respectively (Figure 5A). Moreover, EPR was employed revealing a common g value of 2.0033 for both COFs, attributed to radicals within the frameworks (Figure 5B). Notably, CoPc-EA-COF exhibited a more pronounced radical signal compared to CoPc-BP-COF, signifying a higher concentration of radicals, which in turn amplified the electrocatalysis reaction.

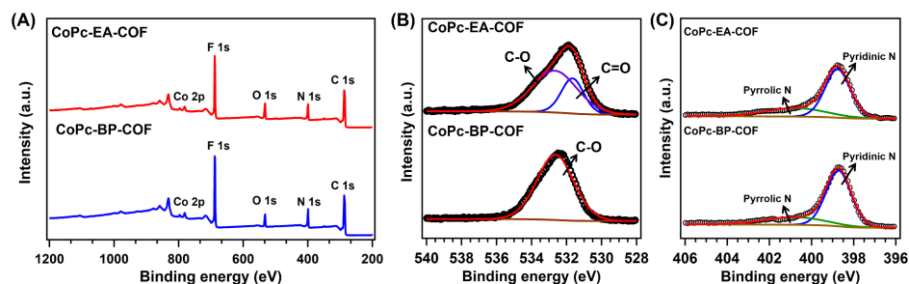


Figure 6. (A) The XPS spectra, (B) The high-resolution O 1s spectra and (C) the high-resolution N 1s spectra of the CoPc-EA-COF and CoPc-BP-COF.

XPS was subsequently employed to explore the valence states of heteroatoms in CoPc-EA-COF and CoPc-BP-COF. In the comprehensive spectra, distinct peaks corresponding to elements such as C, N, O, F, and Co were prominently discernible (Figure 6A). Upon closer examination, high-resolution O 1s spectra from CoPc-EA-COF and CoPc-BP-COF exhibited peaks originating from C-O bonds positioned at 532.67 and 532.65 eV, respectively, thus corroborating the successful formation of dioxin bonds (Figure 6B).^[62] Additionally, the characteristic C=O bond peak from EA units at 531.66 eV was distinctly observable in CoPc-EA-COF.^[190] Moreover, the high-resolution N 1s spectra of both CoPc-EA-COF and CoPc-BP-COF showed peaks emanating from pyridinic N at 398.96 eV and pyrrolic N at 400.75 eV, inherent to CoPc units, respectively (Figure 6C).^[191]

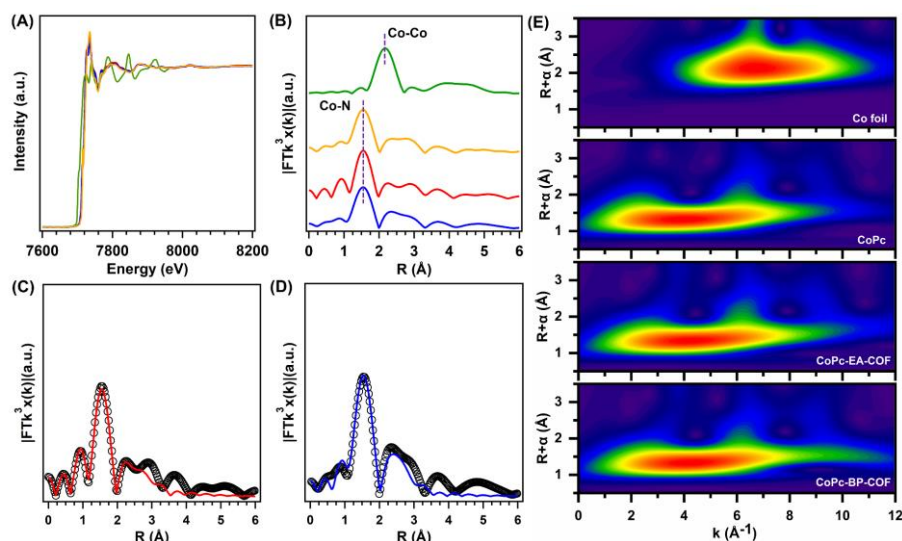


Figure 7. (A) XANES spectra of the Co K-edge and (B) the corresponding Co K-edge k^3 -weighted Fourier transform spectra of the standard Co foil (green), CoPc (yellow), CoPc-EA-COF (red) and CoPc-BP-COF (blue). EXAFS fitting curves for Co in (C) CoPc-EA-COF and (D) CoPc-BP-COF. (E) The WT-EXAFS of the Co foil, CoPc, CoPc-EA-COF and CoPc-BP-COF.

XAFS analysis was carried out to provide a more comprehensive understanding of the electronic and atomic states of Co within CoPc-EA-COF and CoPc-BP-COF. As shown in Figure 7A, the Co absorption near-edge profiles of CoPc-

EA-COF (red) and CoPc-BP-COF (blue) exhibited distinct features compared to Co foil (green) yet approached the profiles of simple CoPc compounds (yellow). Moreover, the Co peak positions in the R-space for these two COFs were approximately $1.91 \pm 0.01 \text{ \AA}$, closely resembling that of CoPc coordination (Figure 7B). In addition, the EXAFS fitting results demonstrated the presence of Co-N₄ coordination for Co atoms within both CoPc-EA-COF and CoPc-BP-COF (Figures 7C and 7D). Further bolstering this, a WT analysis was conducted on the Co L³-edge EXAFS oscillations (Figure 7E). The intensity maximum at 4.2 \AA^{-1} (Co-N) was consistent for CoPc-EA-COF, CoPc-BP-COF, and CoPc. Conversely, Co foil predominantly displayed a higher k-space intensity maximum (6.5 \AA^{-1}), indicative of the absence of Co-Co metallic coordination. This finding offers additional evidence that no metal nanoparticles were present within either of the COFs.

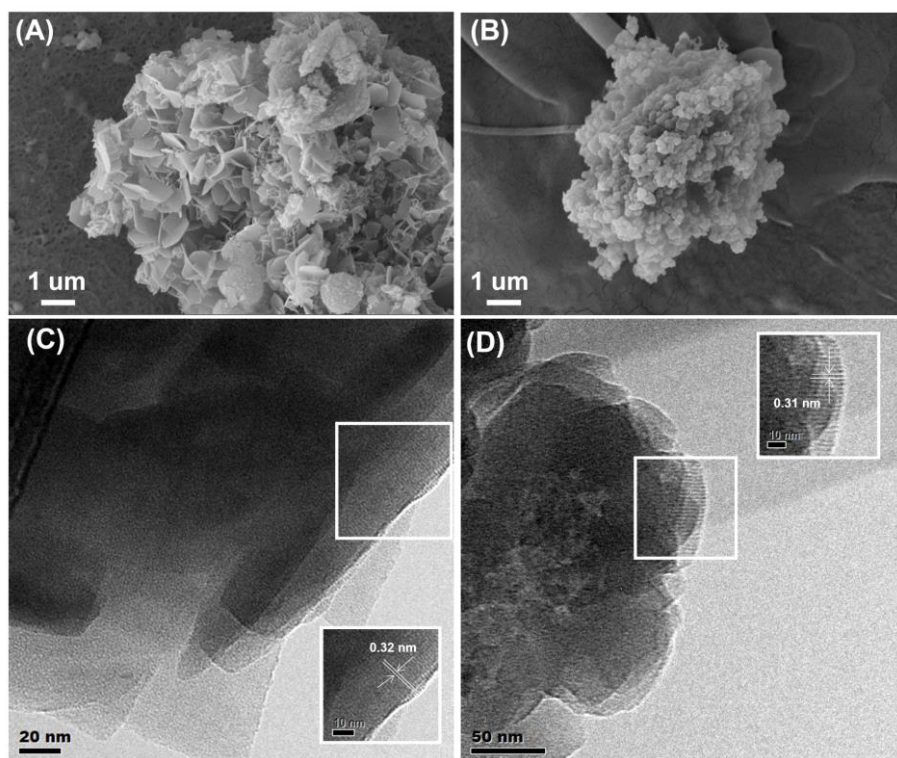


Figure 8. The SEM images of (A) CoPc-EA-COF and (B) CoPc-BP-COF. The TEM images of (C) CoPc-EA-COF and (D) CoPc-BP-COF.

SEM and TEM were performed to study the morphologies of CoPc-EA-COF and CoPc-BP-COF. SEM images showed that CoPc-BP-COF was composed of microcrystalline particles, ranging from 50–100 nm in diameter (Figure 8A). Moreover, the SEM images of CoPc-EA-COF revealed the presence of flower-shaped flakes measuring 200–300 nm in diameter (Figure 8B). Furthermore, TEM images illustrated the layered structure of both CoPc-EA-COF and CoPc-BP-COF. The HR-TEM images further demonstrated the well-aligned lattice fringes, confirming their robust crystalline nature. The spacing observed in these images corresponded to the (001) facets, measuring 0.32 and 0.31 nm for CoPc-EA-COF and CoPc-EA-COF, respectively (Figures 8C and 8D).

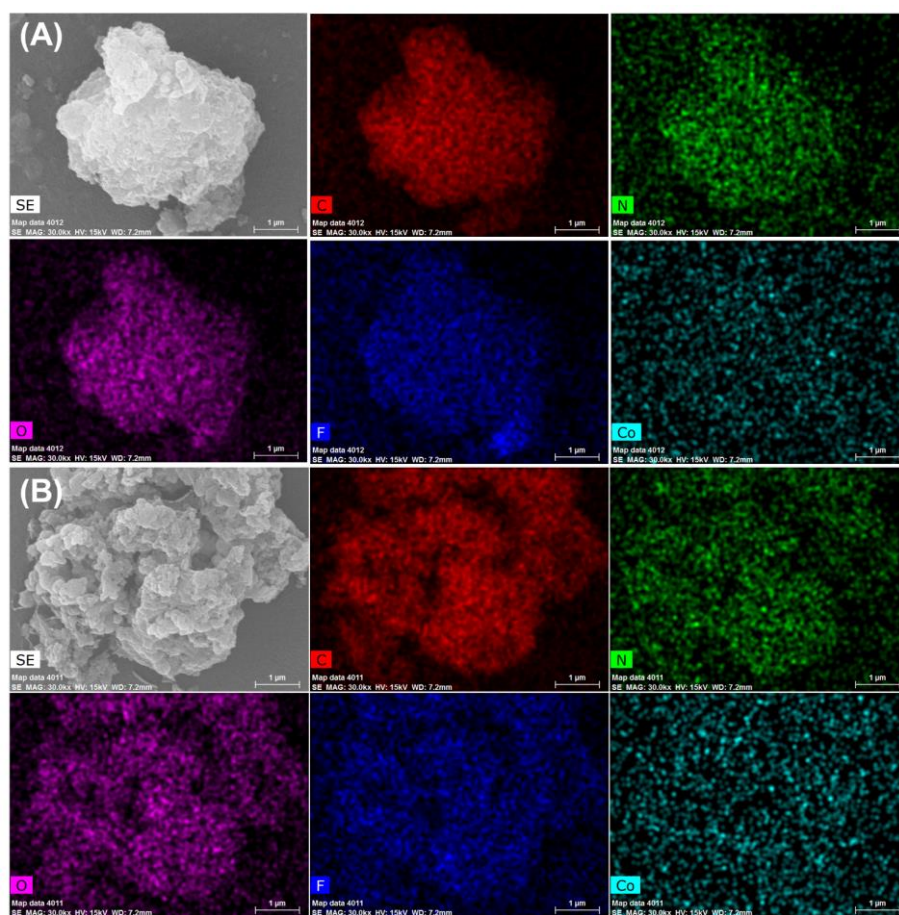


Figure 9. The EDX mapping images of (A) CoPc-EA-COF and (B) CoPc-BP-COF.

Additionally, EDX mapping images demonstrated the uniform dispersion of all constituent elements (C, N, O, F, and Co) throughout the structure (Figure 9).

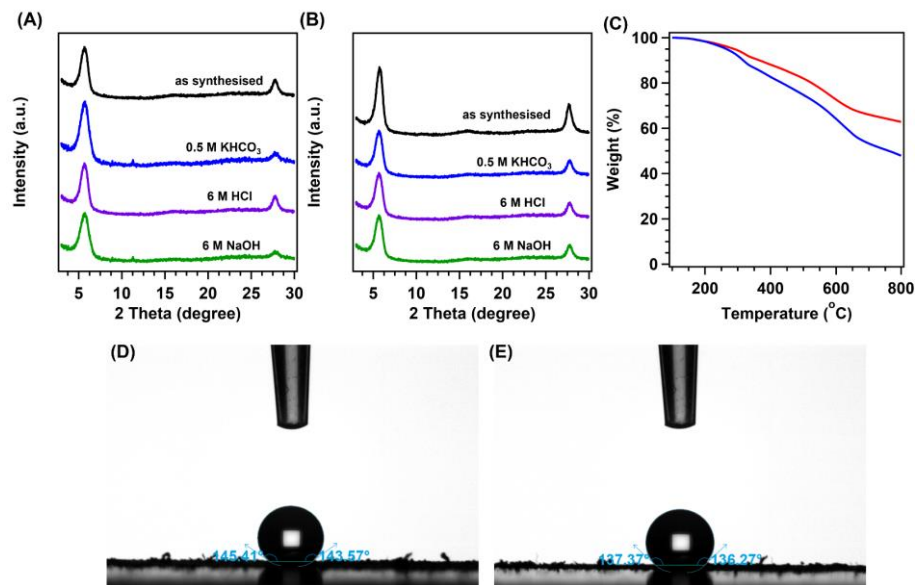


Figure 10. The PXR D patterns of (A) CoPc-EA-COF and (B) CoPc-BP-COF after the treatment in different conditions. (C) The TGA curves of CoPc-EA-COF (red) and CoPc-BP-COF (blue). The WCAs of (D) CoPc-EA-COF and (E) CoPc-BP-COF.

The chemical stability of both CoPc-EA-COF and CoPc-BP-COF was investigated through exposure to harsh conditions, involving KHCO_3 (0.5 M), aqueous HCl (6 M), and NaOH (6 M) solutions for one week. Notably, the PXR D patterns of CoPc-EA-COF and CoPc-BP-COF retained their peak positions and intensities without noteworthy alterations, suggesting the preservation of crystallinity even under such harsh conditions, primarily attributable to presence of dioxin linkages (Figures 10A and 10B). Furthermore, TGA curves indicated that the decompositions of CoPc-EA-COF and CoPc-BP-COF reached 9.7 and 18.3%, respectively, at 300 °C under an N_2 atmosphere (Figure 10C). Moreover, the hydrophobic nature of CoPc-EA-COF and CoPc-BP-COF was evaluated through WCA measurements (Figures 10D and 10E). The measured WCAs for CoPc-EA-COF and CoPc-BP-COF were determined to be $145.41 \pm 3.2^\circ$ and $137.37 \pm 2.7^\circ$, respectively. In the context of electro-catalyzing ORR and CO_2RR , the hydrophobic properties of the catalyst are crucial to protect the active sites by mitigating competitive water adsorption.

This, in turn, contributes to improved selectivity and energy efficiency within the electrocatalytic processes.^[192]

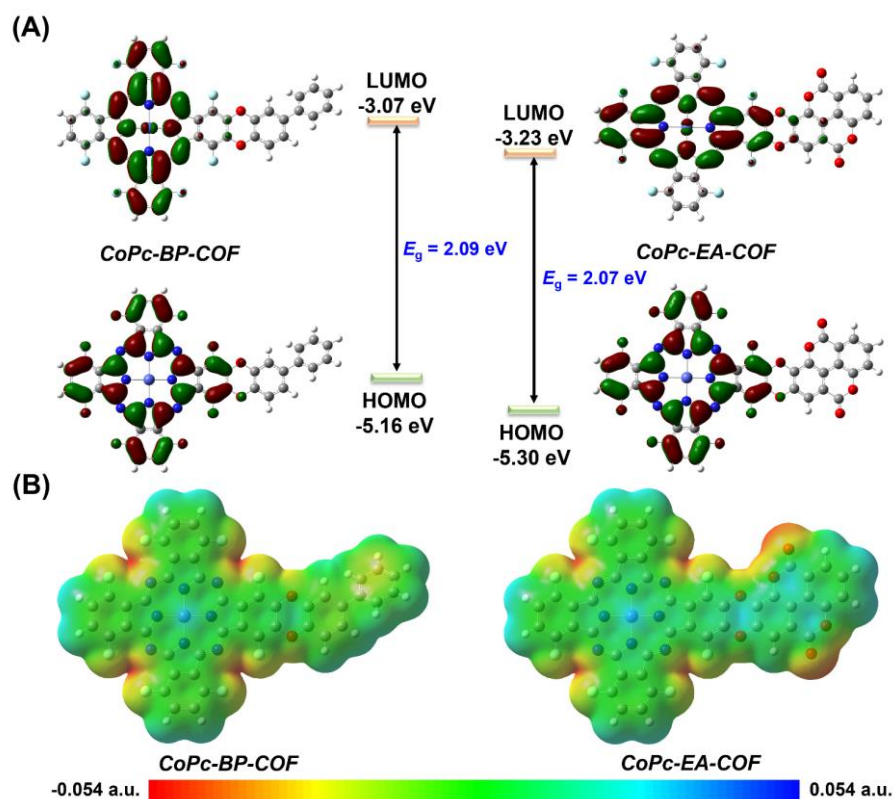


Figure 11. (A) DFT calculated molecular orbitals and energy diagrams of CoPc-BP-COF and CoPc-EA-COF at the B3LYP/6-31G(d) level. All calculations were corrected for dispersion (D3BJ). (B) The ESP surface maps for optimized structures of CoPc-BP-COF and CoPc-EA-COF.

To investigate the impact of ladder π -conjugation and heteroatoms on electronic distribution and charge transfer, the LUMO and HOMO of CoPc-BP-COF and CoPc-EA-COF were computed. Following the introduction of abundant heteroatoms, the LUMO of CoPc-EA-COF became fully delocalized across the entire molecule, indicating extended π -conjugated structures that can enhance electrical conductivity and catalytic activity (Figure 11A).^[172-174] Furthermore, the HOMO-LUMO energy gaps of CoPc-EA-COF and CoPc-BP-COF were small relative to other COFs due to the potential narrowing of energy gaps through ladder π -conjugation. Additionally, the ESP analysis of CoPc-EA-COF

and CoPc-BP-COF model compounds revealed that heteroatoms can regulate charge distribution. As shown in Figure 11B, the electron-rich region (negative potential) of CoPc-BP-COF was primarily localized around the CoPc units. Conversely, the backbone of CoPc-EA-COF exhibited increased electron-richness (negative potential), while the CoPc units became more electron-deficient (positive potential) following the incorporation of heteroatom. This pattern indicated the formation of an internal electric field, further promoting the electrocatalysis reaction.^[178-179]

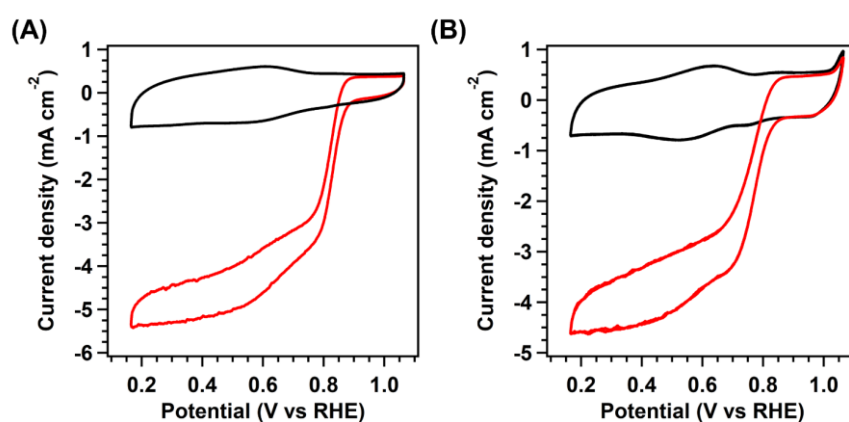


Figure 12. CV curves of (A) CoPc-EA-COF and (B) CoPc-BP-COF (black curve: nitrogen atmosphere; red curve: oxygen atmosphere).

Given the high electronic conductivity, reductive ability, and presence of atomic Co sites in the COFs, their catalytic performance towards ORR and CO₂RR was investigated. The ORR behavior was tested in a 0.1 M KOH aqueous solution. We adopted the CV measurements in O₂ or N₂-saturated solutions. An evident peak at 0.58 V versus RHE was observed for CoPc-EA-COF under the O₂ atmosphere, while no peaks were observed under N₂-saturated conditions, confirming its reactivity for ORR (Figure 12A). CoPc-BP-COF offered a more negative reduction peak at 0.52 V, indicating the lower activity for ORR in compared to CoPc-EA-COF (Figure 12B).

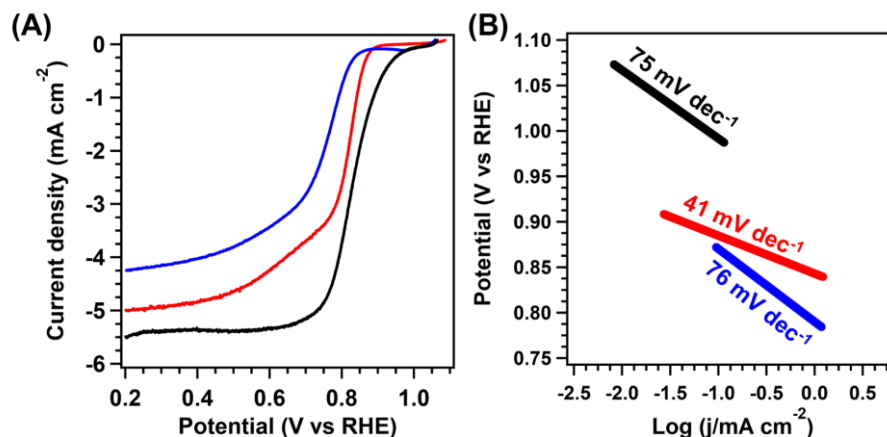
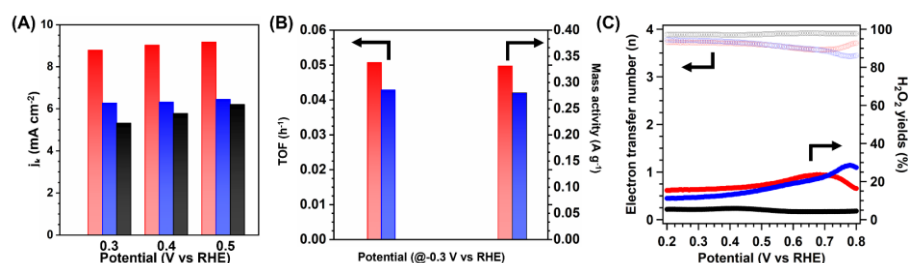


Figure 13. (A) LSV curves and (B) the corresponding Tafel slopes over CoPc-EA-COF (red), CoPc-BP-COF (blue) and commercial Pt/C (black) in O_2 -saturated KOH (0.1 M) aqueous solution.

Subsequently, RDE measurements were conducted at the scan rate of 1600 rpm to explore ORR activity. As a control, the catalytic performance of commercial Pt/C was also investigated. LSV curves revealed that the Pt/C exhibited E_o and $E_{1/2}$ of 0.953 and 0.839 V, respectively, with a j_{lim} of 5.52 mA cm^{-2} (Figure 13A, black curve). Additionally, CoPc-BP-COF exhibited the E_o , $E_{1/2}$, and j_{lim} values of 0.856, 0.753 V, and 4.23 mA cm^{-2} , respectively (Figure 13A, blue curve). Using the EA linker, CoPc-EA-COF demonstrated ORR activity closely resembling that of Pt/C, with E_o and $E_{1/2}$ values of 0.901 and 0.803 V, respectively (Figure 13A, red curve). Furthermore, CoPc-EA-COF displayed a j_{lim} of 5.03 mA cm^{-2} , surpassing that of CoPc-BP-COF. The kinetic behaviour of COFs towards ORR was further probed through Tafel slopes. The Tafel slope for CoPc-EA-COF was 41 mV dec^{-1} (Figure 13B), considerably lower than that of CoPc-BP-COF (76 mV dec^{-1}), indicating faster kinetic behaviour for the former. Importantly, the $E_{1/2}$ values of CoPc-EA-COF exceeded those of other reported COF electrocatalysts (Table 1).

Table 1. Summary of recently reported ORR performances of other reported COF/MOF derived electrocatalysts under alkaline conditions.

Catalysts	E_o (V vs RHE)	$E_{1/2}$ (V vs RHE)	Tafel slope (mV dec ⁻¹)	Reference
CoPc-EA-COF	0.90	0.80	41	This work
CoPc-BP-COF	0.86	0.74	76	This work
COF-366-Co	0.77	0.70	111	[70]
Co TPFP/CNT	0.86	0.81	60	[193]
Co TPP/CNT	0.86	0.81	72	[193]
Co-TAPP-COF-Fe	0.95	0.84	110	[183]
PCN-221-Co/C	0.80	0.70	78	[194]
PCN-222-Co/C	0.80	0.69	72	[194]
PCN-226-Co/C	0.83	0.75	59	[194]
Co-PCOF/graphene	0.90	0.81	53	[195]
Fe-PCOF/graphene	0.90	0.74	86	[195]
Mn-PCOF/graphene	0.90	0.76	81	[195]
JUC-527	-	0.63	72	[63]
JUC-528	-	0.70	73	[63]

**Figure 14.** (A) The kinetic current density, (B) the corresponding values of TOF and mass activity and (C) The electron transfer number and H₂O₂ yield plots calculated from the RRDE measurements over CoPc-EA-COF (red), CoPc-BP-COF (blue) and commercial Pt/C (black) in O₂-saturated KOH (0.1 M) aqueous solution.

For deeper insight into kinetic performance, the LSV curves at different scan rates were obtained. The corresponding kinetic current densities for CoPc-EA-COF, CoPc-BP-COF, and commercial Pt/C were 9.13, 6.48, and 6.32 mA cm⁻²

at a potential of 0.5 V, respectively (Figures 14A). The TOF value and mass activity were determined for the COFs in a 0.1 M KOH solution. At a potential of -0.3 V versus RHE, CoPc-EA-COF exhibited a TOF value of 0.51 s $^{-1}$ and a mass activity of 0.35 A g $^{-1}$ both of which surpassed those of CoPc-BP-COF (0.42 s $^{-1}$ for TOF and 0.26 A g $^{-1}$ for mass activity), underscoring its high intrinsic catalytic activity (Figure 14B). Furthermore, RRDE experiments were conducted to evaluate the selectivity of electron pathways. Specifically, the electron transfer numbers (n) values for both COFs exceeded 3.5, with corresponding H $_2$ O $_2$ yields below 20% across the range of 0.2 to 0.8 V. This observation further supports the notion of $4e^-$ pathway towards ORR for both COFs (Figure 14C).

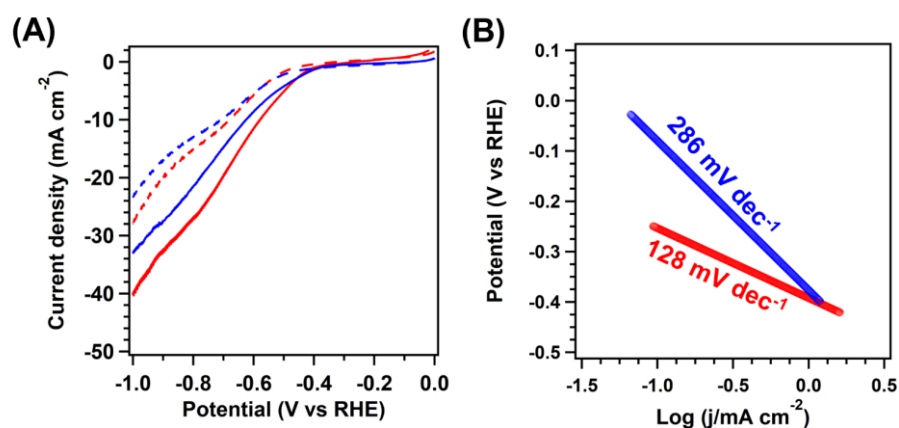


Figure 15. (A) LSV curves in CO $_2$ (solid line) and Ar atmosphere (dotted line), (B) Tafel slopes of CoPc-EA-COF (red) and CoPc-BP-COF (blue).

The CO $_2$ RR performance of these two COFs was evaluated in a 0.5 M KHCO $_3$ aqueous solution under a CO $_2$ atmosphere using a standard H-cell. Initially, LSV curves demonstrated higher current densities under the CO $_2$ atmosphere relative to the Ar atmosphere, indicative of the superior CO $_2$ reductive activity of both COFs (Figure 15A). Furthermore, CoPc-EA-COF displayed higher current densities than CoPc-BP-COF at the same potentials, suggesting its greater activity (Figure 15A). Additionally, CoPc-EA-COF exhibited a Tafel slope of

128 mV dec^{-1} , notably smaller than that of CoPc-BP-COF (286 mV dec^{-1}) (Figure 15B).

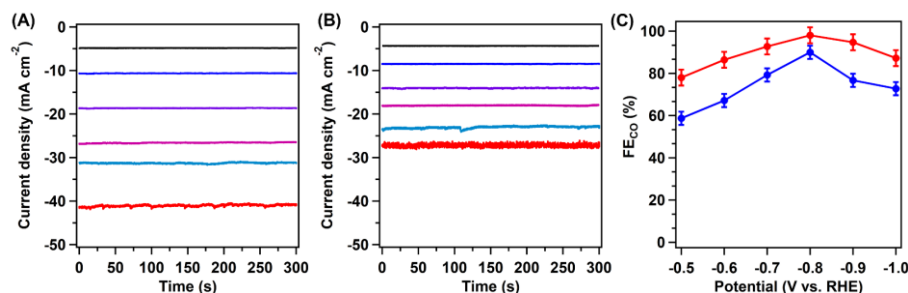


Figure 16. Chronoamperometric responses of (A) CoPc-EA-COF and (B) CoPc-BP-COF at -0.5 (black), -0.6 (blue), -0.7 (purple), -0.8 (pink), -0.9 (cyan), and -1.0 V (red) (vs. RHE). (C) The faradic efficiency of CO for CoPc-EA-COF and CoPc-BP-COF.

The reduction products of CO_2RR were assessed using gas and liquid chromatography, revealing the presence of only CO and H_2 . The time-dependent total-geometric-current densities of CoPc-EA-COF and CoPc-BP-COF were measured over each potential between -0.5 and -1.0 V for 300 s (Figures 16A and 16B). The FE_{CO} over the CoPc-BP-COF were 58.7, 67.2, 79.2, 89.9, 76.6, and 72.7% at -0.5 , -0.6 , -0.7 , -0.8 , -0.9 , and -1.0 V, respectively (Figure 16C). Notably, the CoPc-EA-COF displayed considerably higher selectivity than that of base COF at same potential, yielding FE_{CO} values of 78.2, 86.4, 92.7, 98.2, 94.7, and 87.2% (Figure 16C, red curve).

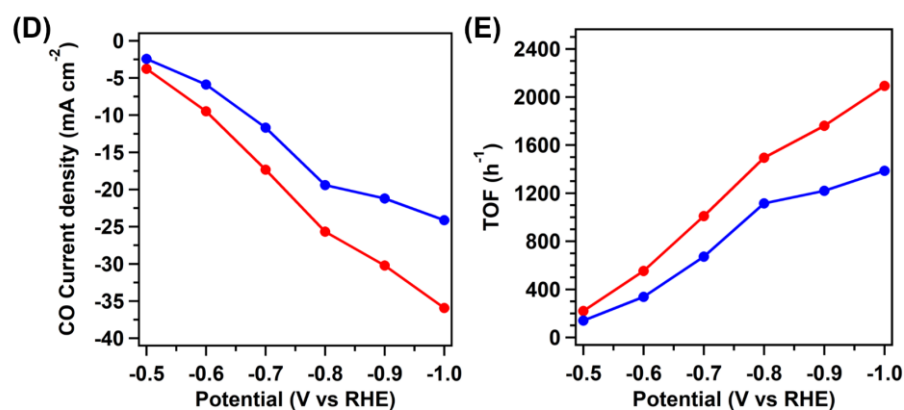


Figure 17. (A) The partial CO current density and (B) the corresponding TOF values of CoPc-EA-COF and CoPc-BP-COF.

Furthermore, the absolute values of the j_{CO} were calculated to assess the CO_2RR activity of the COFs. Specifically, at a potential of -1.0 V, the CoPc-EA-COF exhibited the highest j_{CO} of 35.94 mA cm^{-2} , while CoPc-BP-COF reached a maximum j_{CO} on was 24.12 mA cm^{-2} at the same potential (Figure 17A). Additionally, the TOFs of the COFs were calculated by considering the cobalt atoms as active sites. At -1.0 V, the highest TOF values achieved were 2092 h^{-1} for CoPc-EA-COF and 1386 h^{-1} for CoPc-BP-COF (Figure 17B). Importantly, the FE_{CO} and j_{CO} values of CoPc-EA-COF surpassed those reported COF electrocatalysts (Table 2).

Table 2. Summary of recently reported CO_2RR performances of other reported COF derived electrocatalysts under alkaline conditions (Electrolyte 0.5 M KHCO_3).

Electrocatalyst	FE_{CO} (%) at -0.8 V	FE_{CO} (%) at -1.0 V	j_{CO} (mA cm^{-2}) at -1.0 V	Reference
CoPc-EA-COF	98.2	87.23	35.16	This work
COF-367-Co	91	~85	33.0	[75]
CoPc-PI-COF-1	95	-	21.2	[83]
CoP-BDT _{HexO} -COF	98	~90	10.8	[196]
TAPP(Co)-B18C6-COF	93	71	9.5	[197]
COF@CoPor	88.5	73.8	12.5	[198]
Co-TTCOF	~88	-	~2.5	[199]

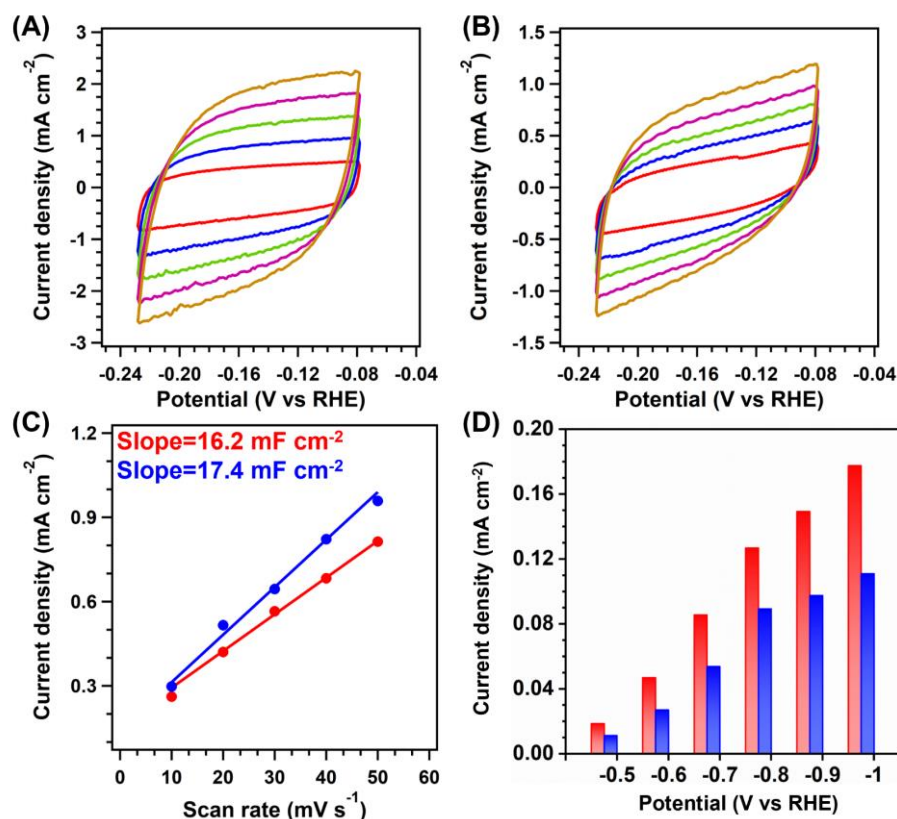


Figure 18. The CV curves from 10 mV s^{-1} to 50 mV s^{-1} for (A) CoPc-EA-COF and (B) CoPc-BP-COF. (C) The ECSA slopes and (D) the CO current density by the normalized ECSA for CoPc-EA-COF (red) and CoPc-BP-COF (blue).

The C_{dl} values were determined using CV measurements. The resulting C_{dl} values for CoPc-EA-COF and CoPc-BP-COF were 16.2 and 17.4 mF cm^{-2} , respectively (Figures 18A-18C).^[200] The exposed active sites on the catalysts were characterized using the electrochemically ECSA of the COFs, where the formula $\text{ECSA} = C_{dl}/C_s$, and $C_s = 0.04 \text{ mF cm}^{-2}$. CoPc-BP-COF had a larger ECSA (435) compared to CoPc-EA-COF (405), aligning with its CO_2RR performance. Moreover, the normalized current densities on the COFs (j_{CO} per ECSA) were analysed (Figure 18D). Within the potential range of -0.5 to -1.0 V, CoPc-EA-COF consistently displayed higher normalized current density than CoPc-BP-COF, confirming that the combination of ladder linkages and heteroatoms could amplify COF activity towards CO_2RR .

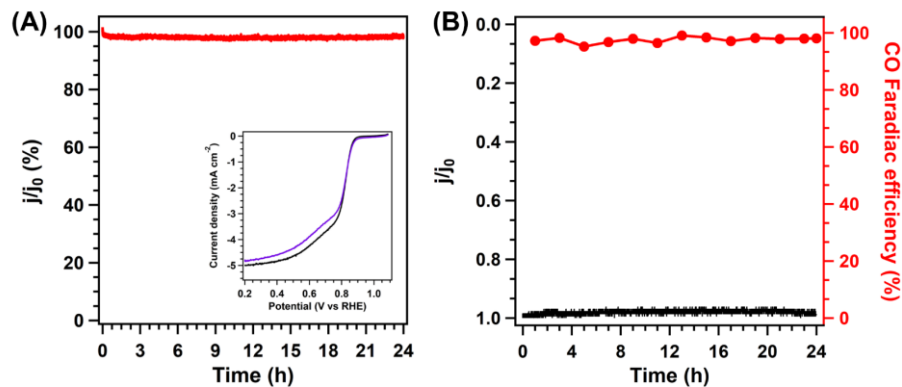


Figure 19. (A) Chronoamperometry tests for ORR of CoPc-EA-COF at a potential of -0.8 V in 0.1 M KOH (insert: LSV curves before and after the stability test). (B) Chronoamperometry test for CO_2RR of CoPc-EA-COF at a potential of -0.8 V in 0.5 M KHCO_3 under CO_2 atmosphere.

CoPc-EA-COF kept stable in the long-term stability test of ORR, in which the degradation of current density was less than 2.5% after 24 h (Figure 19A). Similarly, the activity for CO_2RR was well preserved at -0.8 V in CO_2 -saturated KHCO_3 for 24 h (Figure 19B). The FE_{CO} maintained around 98% and the ratio of immediate current density to initial j_0 was $> 97.8\%$ during the test, confirming the reliable stability of CoPc-EA-COF.

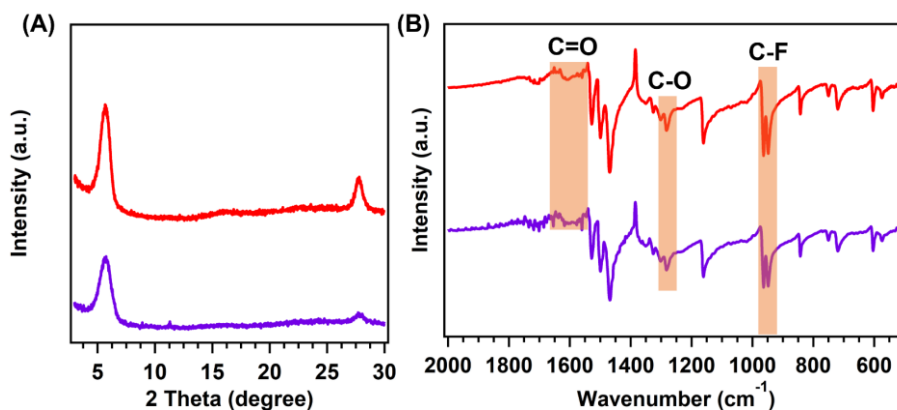


Figure 20. (A) The PXRD patterns and (B) FT-IR spectra of CoPc-EA-COF before (red) or after (purple) the chronoamperometry tests.

In addition, the PXRD and FT-IR measurements further proved that no visible changes were observed after the long-term stability tests, demonstrating that the

intrinsic composition and structure of CoPc-EA-COF were maintained (Figures 20A and 20B).

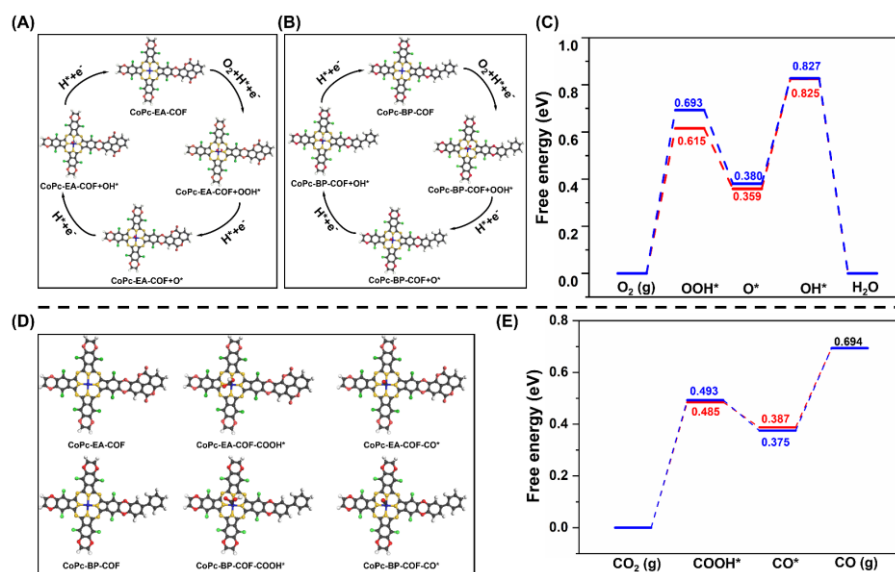


Figure 21. The catalytic ORR mechanism cycles of the (A) CoPc-EA-COF and (B) CoPc-BP-COF model (C-black, N-yellow, H-white, O-red, F-green, Co-blue). (C) The free energy profiles for the CoPc-EA-COF (red) and CoPc-BP-COF (blue) in ORR process. (D) Reaction mechanism for CO₂RR catalyzed by CoPc-EA-COF and CoPc-BP-COF, respectively. (E) Calculated free energy diagram of CO₂RR on the catalytic COFs in CO₂RR process.

The potential reaction mechanism of electrocatalytic oxygen and CO₂ reduction on CoPc-EA-COF and CoPc-BP-COF was further evaluated by the DFT. DFT calculations revealed that the RDS for COFs in ORR were associated with the formation of O* from OOH* (Figures 21A and 21B). As shown in the free energy profiles, the formation of OOH* is the rate-determining step (Figure 21C). Correspondingly, the ΔG for OOH* formation on CoPc-EA-COF (0.615 eV) was much lower than that of CoPc-BP-COF (0.693 eV), indicating its high catalytic activity towards ORR due to the abundant embedding heteroatoms. Conversely, CO₂RR involves three steps: CO₂ absorption, COOH* formation, and CO* formation, involving a proton-coupled single electron transfer, as well as CO desorption. The ΔG values for the step of CO₂ to COOH* were 0.485

and 0.493 eV for CoPc-EA-COF and CoPc-BP-COF, respectively, aligning with the notable electroreduction activity and selectivity of CoPc-EA-COF (Figures 21D and 21E). These findings signify not only the favourable active site of the Co-N₄ within the frameworks but also the efficient synergistic electron modulation from heteroatoms and ladder conjugation.

6.3 Conclusion

In this chapter, we employed the natural building blocks to construct catalytic COFs for both ORR and CO₂RR. The incorporation of EA units introduced ladder-like conjugation within the frameworks, resulting in enhanced electronic conductivity. This EA-based COF exhibited remarkable catalytic activity, selectivity and stability in both ORR and CO₂RR. Theoretical calculations revealed that the EA linker facilitated the formation of intermediates in the catalytic process, enhancing the overall efficiency. Consequently, this study not only expands the repertoire of COFs but also provides a promising avenue for developing highly efficient energy storage and conversion systems.

Chapter 7. Modulating Density of Catalytic Sites in Multiple-Component Covalent Organic Frameworks for Electrocatalytic Carbon Dioxide Reduction

7.1 Introduction

Except space dimensions and building blocks, the density of catalytic sites in COFs to tune the catalytic behavior for CO₂RR is ignored, because it is generally assumed that the more metals results in better catalytic activity. Thus, the correlation between the density of metal atoms and catalytic performances have not been explored. The electrocatalytic CO₂RR into value-added fuels and chemical feedstock is a prospective technology to achieve carbon neutralization.^[201-202] However, there are still several problems in the electrocatalysis process for CO₂RR, including the large energy which activated the inert CO₂, the multielectron transfer processes and the low availability of catalytic sites led the poor product selectivity and the competitive HER.^[203] The catalytic properties not only depend on the kinds of metal centres and their coordination environments, but also rely on the density of the metal atoms.^[204-206] However, how to precisely control the contents of metal sites is hardly achieved in the carbon-based catalysts. In chapter 7, a skeleton engineering strategy based on the multiple-component synthesis to construct the controllable metal density in the skeletons was first reported, which build the quantitative correlation between the metal density and catalytic performance.

In this chapter, we demonstrated for the first time the multiple-component synthesis strategy to construct the controllable metal density in the skeletons of COFs. This strategy enables a quantitative correlation between the metal density and catalytic performance and shows us how to optimize the activity and selectivity. To exclude the effects of linkers and linkages in the COFs for CO₂RR,

all the H₂Pc and NiPc are confused with benzene units directly, without any other building units. The alternate H₂Pc in the skeletons enables to promote the electron transfer to the NiPc units. The optimized COF showed high activity and selectivity, with TOFs of 4909.87 h⁻¹ at -1.0 V and FE_{CO} of 95.37% at -0.8 V, respectively. This opens a way to guide the predesign electrocatalysts with higher atomic utilization efficiency.

7.2 Results and discussion

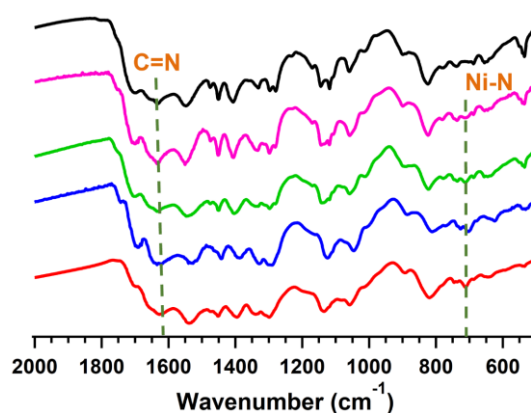


Figure 1. FT-IR spectra of H₂Pc-COF (black), 0.25NiPc-COF (pink), 0.5NiPc-COF (red), 0.75NiPc-COF (blue) and NiPc-COF (green).

The structures of as-synthesized COFs were investigated using FT-IR spectroscopy. It demonstrated that the obvious peak at about 1625 cm⁻¹ was assigned to C=N bonds for H₂Pc-COF.^[207] And the peaks at nearly 750 cm⁻¹ originated from the Ni-N bonds of XNiPc-COFs. These results suggested that the COFs have been successfully synthesized (Figure 1).

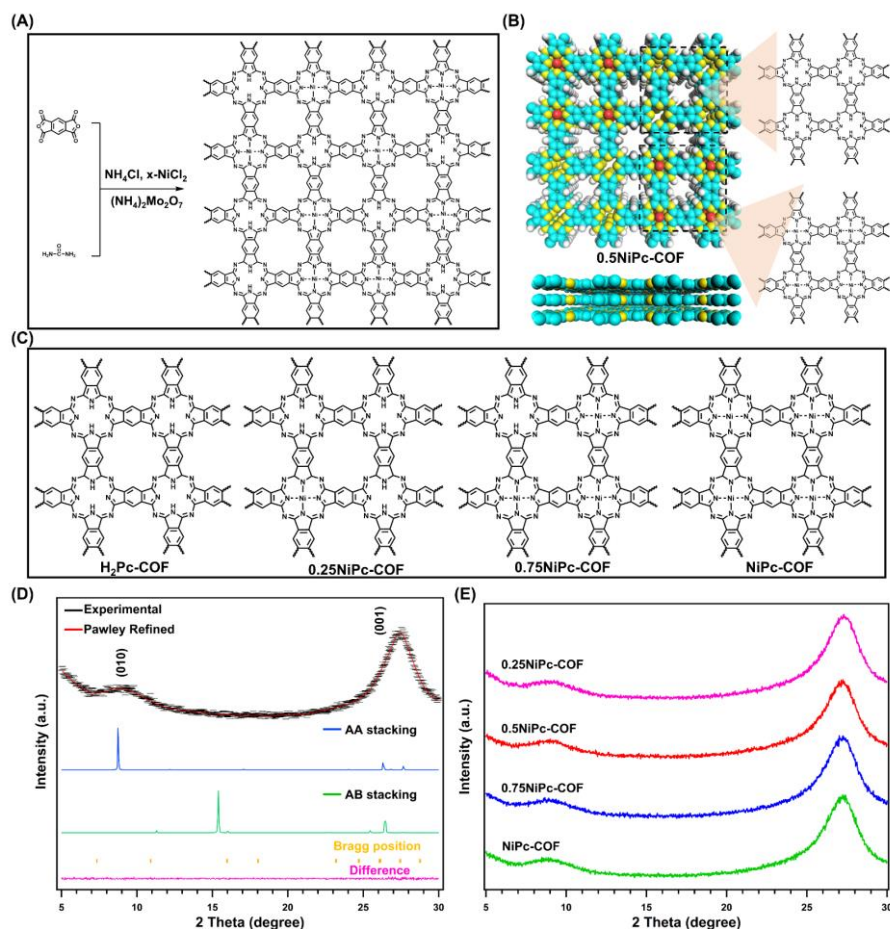


Figure 2. (A) Synthesis of XNiPc-COFs ($\text{H}_2\text{Pc-COF}$, 0.25NiPc-COF , 0.5NiPc-COF , 0.75NiPc-COF and NiPc-COF) from PADA, urea, NH_4Cl , NiCl_3 and $(\text{NH}_4)_2\text{Mo}_2\text{O}_7$, respectively, with (B) top view and side view of the slipped AA stacking structure (C-cyan, N-yellow, Ni-red) for 0.75NiPc-COF s. (C) The structures of $\text{H}_2\text{Pc-COF}$, 0.25NiPc-COF , 0.75NiPc-COF and NiPc-COF . (D) PXRD profiles of $\text{H}_2\text{Pc-COF}$ of the experimentally observed (black), Pawley refined (red) and their difference (pink), simulated using the AA (blue) and staggered AB (green) stacking modes. (E) PXRD profiles of 0.25NiPc-COF (pink), 0.5NiPc-COF (red), 0.75NiPc-COF (blue) and NiPc-COF (green).

We constructed and simulated the theoretical structure of these COFs as shown in Figures 2A-2C. PXRD measurement was conducted to confirm the crystallinities of these COFs. Exactly, the peaks at 8.4° and 27.5° were clearly observed, which were from (010) and (001) facets of $\text{H}_2\text{Pc-COF}$ (Figure 2D).

Additionally, the theoretical structure was simulated by the Materials Studio package. The simulated PXRD patterns are in good agreement with experimental results (R_{wp} of 3.23% and R_p of 2.96%, respectively). Furthermore, the AA stacking models of H₂Pc-COF matched well with the experimental results and adopted the $P4M$ space group, following the cell parameters of $a = 10.70 \text{ \AA}$, $b = 10.70 \text{ \AA}$, $c = 3.45 \text{ \AA}$, $\alpha = \beta = \gamma = 90^\circ$. With immobilizing Ni atoms in the COFs (0.25NiPc-COF, 0.5NiPc-COF, 0.75NiPc-COF and NiPc-COF), the obvious peaks from (010) and (001) were confirmed without position shift, confirming the crystal structures were as same as that of metal-free COFs (Figure 2E).

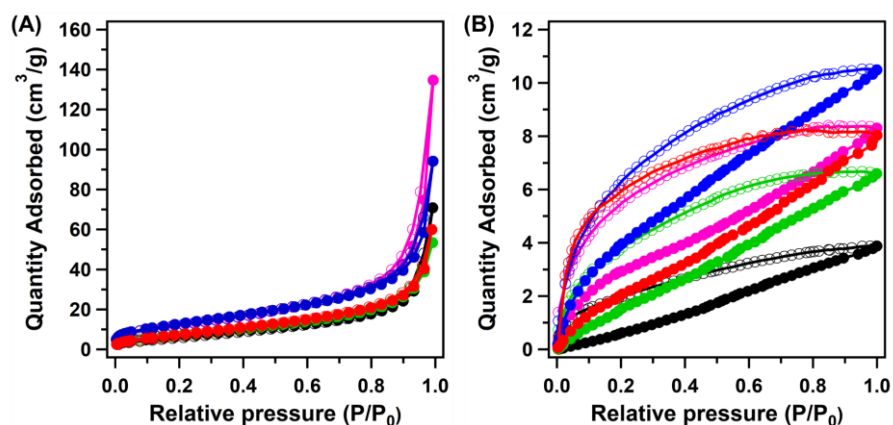


Figure 3. (A) The N₂ adsorption curves at 77 K and (B) the CO₂ adsorption curves at 298 K of H₂Pc-COF (black), 0.25NiPc-COF (pink), 0.5NiPc-COF (red), 0.75NiPc-COF (blue) and NiPc-COF (green).

The porous structures of five as-synthesized COFs were confirmed using nitrogen adsorption isotherm at 77 K. These H₂Pc-COF and XNiPc-COF demonstrated the curves with IV-types (Figure 3). Correspondingly, the S_{BET} for H₂Pc-COF, 0.25NiPc-COF, 0.5NiPc-COF, 0.75NiPc-COF and NiPc-COF were 24.32, 28.98, 28.11, 46.76 and 88.66 m² g⁻¹, with pore volumes of 0.11, 0.09, 0.08, 0.15 and 0.21 cm³ g⁻¹, respectively. The low permanent porosity could be attributed to the random displacement of the 2D layers to some extent.⁴⁹ Considering the important role of CO₂ absorption ability for CO₂RR, the CO₂

sorption behaviour at 298 K was investigated. The CO₂ physical-sorption capacity depends on the surface areas and the chemical-sorption rely on the numbers of binding sites. With increasing the contents of Ni, the larger sorption loops suggested the higher binding ability of CO₂. The H₂Pc-COF, 0.25NiPc-COF, 0.5NiPc-COF, 0.75NiPc-COF and NiPc-COF had moderate CO₂ uptake capacities of 3.88, 6.60, 10.51, 8.31 and 8.04 cm³ g⁻¹ at 1.0 bar, respectively (Figures 3B). With introducing the Ni sites in the COFs, the CO₂ uptake capacity was obviously improved, which is benefit for improving catalytic activity of CO₂RR.

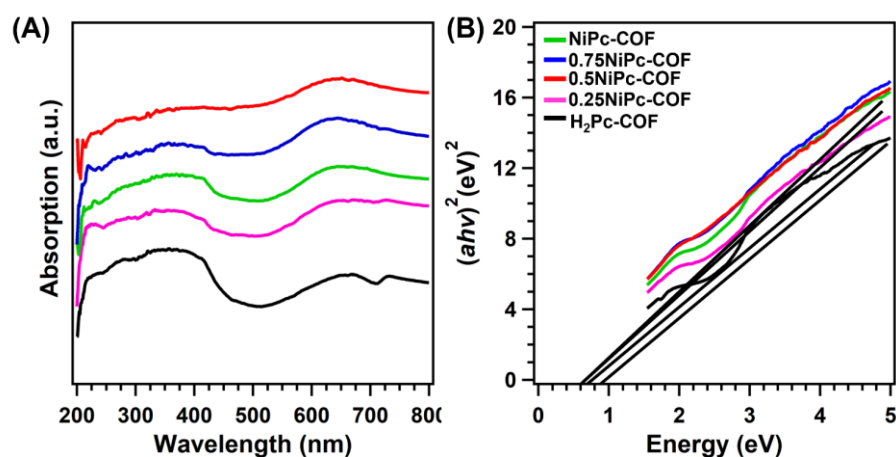


Figure 4. (A) The UV-Vis spectra and (B) Tauc plots of H₂Pc-COF (black), 0.25NiPc-COF (pink), 0.5NiPc-COF (red), 0.75NiPc-COF (blue) and NiPc-COF (green).

To explore the properties of prepared XNiPc-COFs, the UV-Vis spectroscopy was adopted (Figure 4A). Specifically, the Tauc plots demonstrated that the H₂Pc-COF, 0.25NiPc-COF, 0.5NiPc-COF, 0.75NiPc-COF and NiPc-COF had band gaps of 0.39, 0.32, 0.18, 0.28 and 0.27 eV, respectively, indicating that 0.75NiPc-COF favoured the electron transfer in the process of electrocatalysis CO₂RR (Figure 4B).^[208]

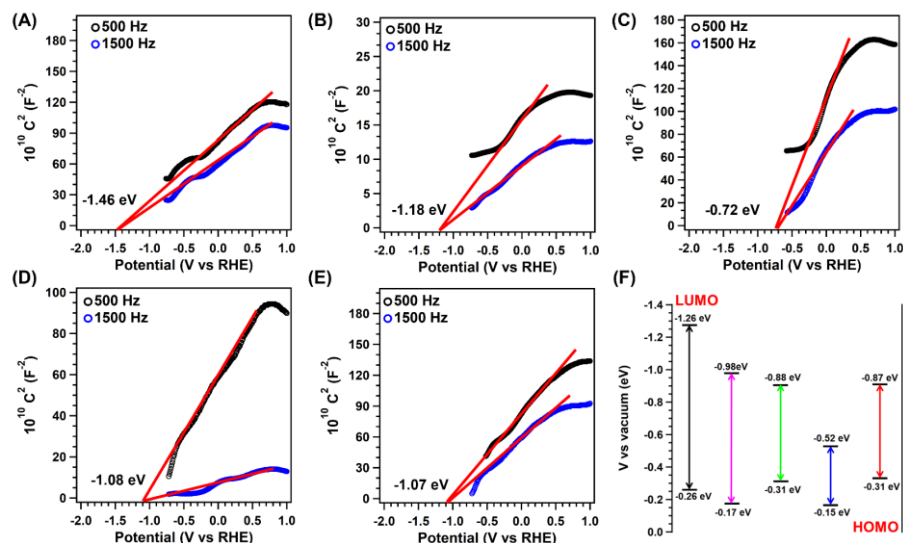


Figure 5. The Mott-Schottky curves of (A) H_2Pc -COF, (B) $0.25NiPc$ -COF, (C) $0.5NiPc$ -COF, (D) $0.75NiPc$ -COF and (E) $NiPc$ -COF from 500 to 1500 Hz. (F) The energy gap (HOMO and LUMO) of H_2Pc -COF (black), $0.25NiPc$ -COF (pink), $0.5NiPc$ -COF (red), $0.75NiPc$ -COF (blue) and $NiPc$ -COF (green).

Then, the HOMO and LUMO were identified using the Mott-Schottky method. The HOMO positions for H_2Pc -COF, $0.25NiPc$ -COF, $0.5NiPc$ -COF, $0.75NiPc$ -COF and $NiPc$ -COF were -0.26, -0.17, -0.15, -0.31 and -0.31 eV, respectively, indicating that $0.75NiPc$ possessed better reduction performance than that of other COFs (Figures 5A-5F).

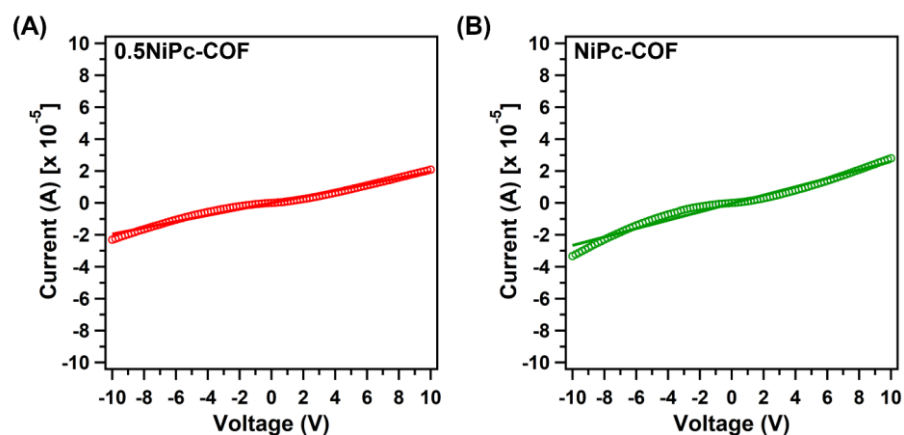


Figure 6. The I-V curves of (A) $0.5NiPc$ -COF and (B) $NiPc$ -COF by the four-probe measurement at 298 K.

We also tested the conductivity of NiPc-COF and 0.5NiPc-COF by the four-probe method at 298 K. The electrical conductivity for NiPc-COF was determined to be $2.8 \times 10^{-5} \text{ S cm}^{-1}$, which is closed to the 0.5NiPc-COF ($2.5 \times 10^{-5} \text{ S cm}^{-1}$) (Figure 6).

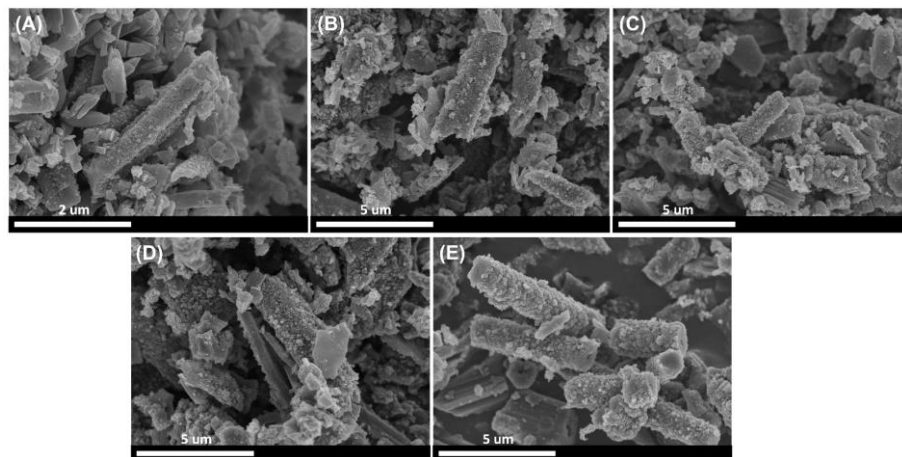


Figure 7. The SEM images of (A) H₂Pc-COF, (B) 0.25NiPc-COF, (C) 0.5NiPc-COF, (D) 0.75NiPc-COF and (E) NiPc-COF.

The SEM demonstrated that H₂Pc-COF was in rodlike shape as the same the other four synthesized XNiPc-COFs (Figure 7).

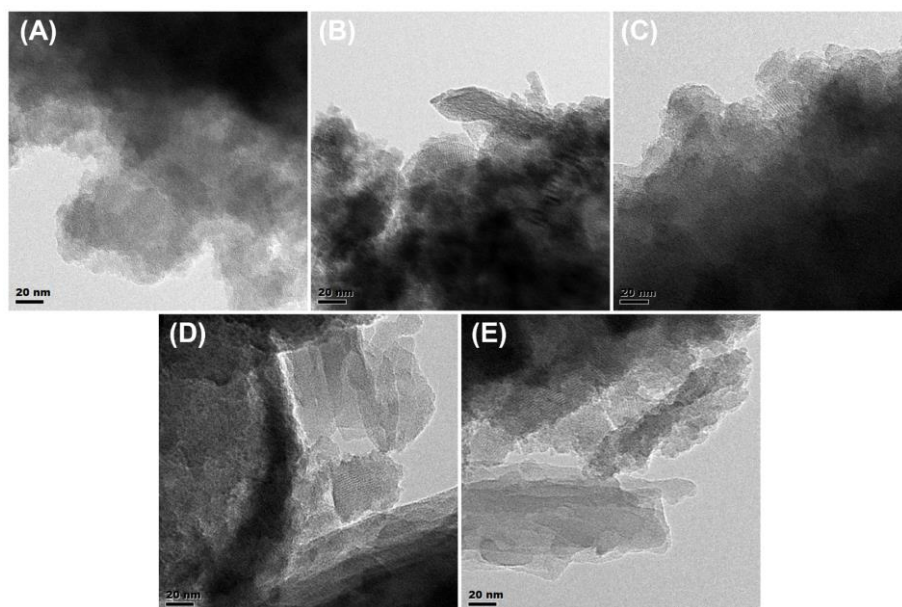


Figure 8. The TEM images of (A) H₂Pc-COF, (B) 0.25NiPc-COF, (C) 0.5NiPc-COF, (D) 0.75NiPc-COF and (E) NiPc-COF.

In addition, the TEM and HR-TEM characterization of H₂Pc-COF exhibited the interlayer distance of 1.6 nm, confirming the crystal structure (Figure 8). With the addition of nickel, NiPc-COF also exhibited a good crystallinity with the similar morphologies. These results suggested that there is no significant morphological difference with the introduction of nickel, further indicating that the structure is well preserved.

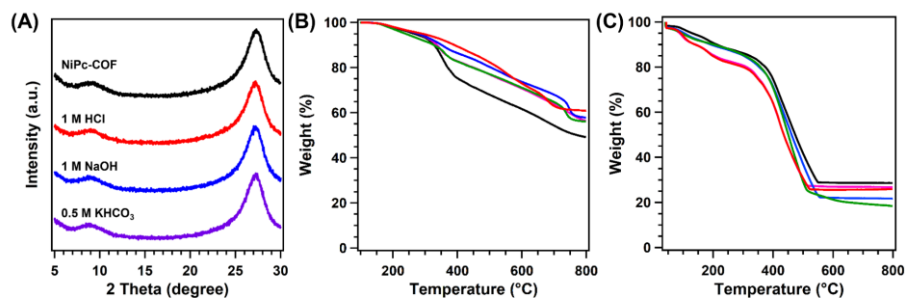


Figure 9. (A) The PXRD patterns of NiPc-COF in the harsh conditions. Thermogravimetric curves under (B) the nitrogen and (C) the air atmosphere of H₂Pc-COF (black), 0.25NiPc-COF (pink), 0.5NiPc-COF (red), 0.75NiPc-COF (blue) and NiPc-COF (green).

Then, the chemical and thermal stability of XNiPc-COFs were studied. The XNiPc-COFs were immersed into harsh conditions, including HCl (1.0 M), NaOH (1.0 M) and KHCO₃ (0.5 M) for one week. The mass and crystallinity showed no obvious change from PXRD patterns, suggesting the well retained crystal structure (Figure 9A). We have also used the TGA measurement to investigate the thermal stability, confirming that no obvious change up to 300 °C under N₂ of these XNiPc-COFs (Figure 9B). Then, we also tested the thermal stability of these COFs under air atmosphere by the TGA measurement. The TGA curves demonstrated that the H₂Pc-COF, 0.25NiPc-COF, 0.5NiPc-COF, 0.75NiPc-COF and NiPc-COF left 29%, 27%, 25%, 22% and 20% after 550 °C under air (Figure 9C).

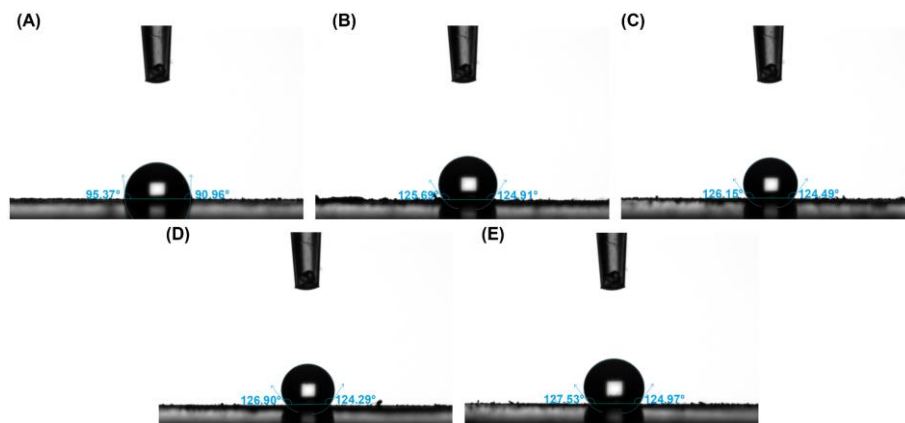


Figure 10. The WCAs of (A) H₂Pc-COF, (B) 0.25NiPc-COF, (C) 0.5NiPc-COF, (D) 0.75NiPc-COF and (E) NiPc-COF.

Moreover, the hydrophobic characteristics of these COFs were conducted by the contact angle measurements with water (Figure 10). The WCA of the H₂Pc-COF was $95.37 \pm 4.3^\circ$, while the 0.25NiPc-COF, 0.5NiPc-COF, 0.75NiPc-COF and NiPc-COF were $125.69 \pm 5.8^\circ$, $126.15 \pm 3.1^\circ$, $126.9 \pm 4.6^\circ$ and $127.53 \pm 3.4^\circ$, respectively. The H₂Pc-COF demonstrated a lower WCA compared with that of NiPc-contained COFs, suggesting that water could be accessible to the surface, further facilitating proton transfer and hindering CO₂RR.^[192]

XPS was performed to explore the chemical structures and electron states of these COFs. Correspondingly, the high-resolution N 1s spectra of these H₂Pc-COF demonstrated peaks at 398.02 and 399.37 eV for pyrrole N and pyridine N, respectively. After the introduction of nickel, the N 1s spectra of 0.25NiPc-COF, 0.5NiPc-COF, 0.75NiPc-COF showed a positive shift compared with that of the H₂Pc-COF. Specifically, the pyridine N had a positive shift of about 0.3 eV, while the pyrrole N had no change, suggesting the successful coordination between pyridine N and nickel (Figure 11A). Additionally, the high-resolution Ni 2p spectra of 0.25NiPc-COF, 0.5NiPc-COF, 0.75NiPc-COF and NiPc-COF exhibited two distinct peaks at about 855.12 eV (2p_{3/2}) and 872.43 eV (2p_{1/2}), attributing to the Ni-N coordination (Figure 11B). Furthermore, the binding energy of Ni-N was slightly negative shift with 0.13 eV for 0.25NiPc-COF,

0.5NiPc-COF and 0.75NiPc-COF compared with that of NiPc-COF due to the H₂Pc units adjusted the local electron density of the active Ni-N sites, which benefits the adsorption of reactant molecules and transfers more electrons to the reaction.

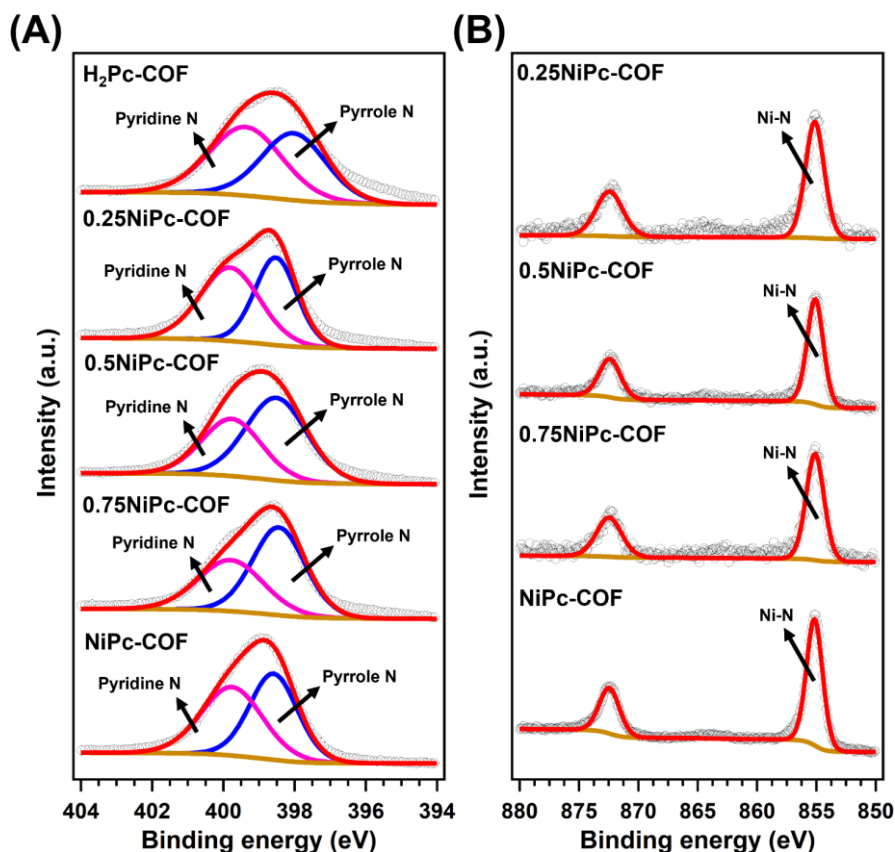


Figure 11. (A) The XPS spectra of N 1s and (B) Ni 2p for H₂Pc-COF, 0.25NiPc-COF, 0.5NiPc-COF, 0.75NiPc-COF and NiPc-COF.

To further study the CO₂ adsorption sites in these COFs, the in-situ XPS was measured under the ambient pressure with 0.1 mbar CO₂ atmosphere. Specifically, the high-resolution N 1s spectra of H₂Pc-COF demonstrated that the absence of shift for pyridine N, while the pyrrole N showed a positive shift with the value of 0.3 eV (Figure 12A). With immobilizing Ni atoms, the high-resolution N 1s spectra of NiPc-COF also exhibited the same trends with that of the H₂Pc-COF. In addition, the high-resolution N 1s spectra of other XNiPc-COFs also exhibited a positive shift of the pyridine N (Figures 12B-12E). These results suggested that the pyrrole N as ‘CO₂ traps’ in the vacancies of the

structure can adsorb CO₂ which can accelerate the electron supply and transport, further boosting the CO₂RR.^[209]

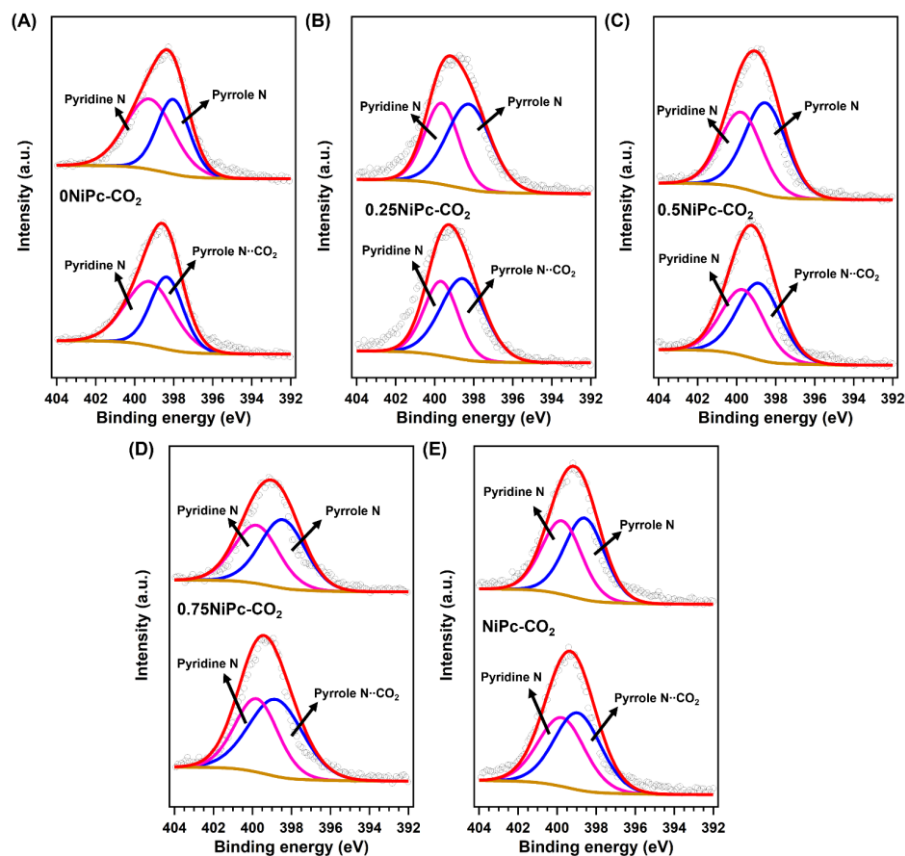


Figure 12. The XPS spectra of N 1s of (A) H₂Pc-COF, (B) 0.25NiPc-COF, (C) 0.5NiPc-COF, (D) 0.75NiPc-COF and (E) NiPc-COF in-situ the CO₂ adsorption under the moderate pressure.

The XAFS measurements were adopted to further confirm the electronic and atomic states of Ni in 0.25NiPc-COF, 0.5NiPc-COF, 0.75NiPc-COF and NiPc-COF. As shown in Figure 13A, the location of Ni absorption near-edge of 0.25NiPc-COF (pink curve), 0.5NiPc-COF (green curve), 0.75NiPc-COF (blue curve) and NiPc-COF (red curve) exhibited different structures from Ni foil and NiO, but they approached simple substances (NiPc) (purple curve). Furthermore, the peak positions of Ni in R-space about 0.25NiPc-COF, 0.5NiPc-COF, 0.75NiPc-COF and NiPc-COF were 4.9 ± 0.7 , 4.6 ± 1.2 , 4.8 ± 1.5 and 4.7 ± 1.4 Å, which was close to that of NiPc coordination (Figure 13B). In addition, the EXAFS fitting results demonstrated the existence of Ni-N₄ coordination for Ni

atom in 0.25NiPc-COF, 0.5NiPc-COF, 0.75NiPc-COF and NiPc-COF. Additionally, to further confirm the combination of Ni, the WT of the Ni L³-edge EXAFS oscillations was conducted (Figure 13C). 0.5NiPc-COF and NiPc exhibited an intensity maximum at 2.3 Å⁻¹ (Ni-N), while only a predominate intensity maximum at higher k-space (6.2 Å⁻¹) for Ni foil and 6.5 Å⁻¹ for NiO, suggesting the absence of the Ni-Ni or Ni-O metallic coordination, further proving that no metal nanoparticles are present in four COFs.

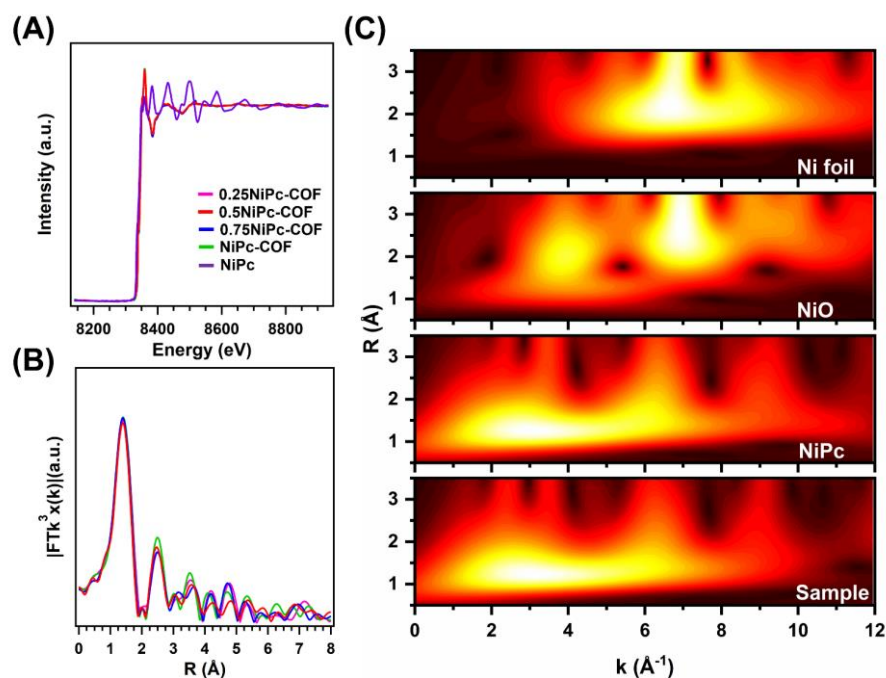


Figure 13. (A) The XANES spectra and (BB) the K-edge k³-weighted Fourier transform spectra from EXAFS for Ni of NiPc (purple curve), 0.25NiPc-COF (pink curve), 0.5NiPc-COF (red curve), 0.75NiPc-COF (blue curve) and NiPc-COF (green curve). (C) The WT-EXAFS of the Ni foil, NiPc and 0.5NiPc-COF.

To further investigate the CO₂RR performance of the XNiPc-COFs, using a H-cell separated by a Nafion-117 membrane in the 0.5 M KHCO₃ solution with a three-electrode configuration under the saturated CO₂. The LSV demonstrated that these XNiPc-COFs had a small onset potential (Figure 14A).

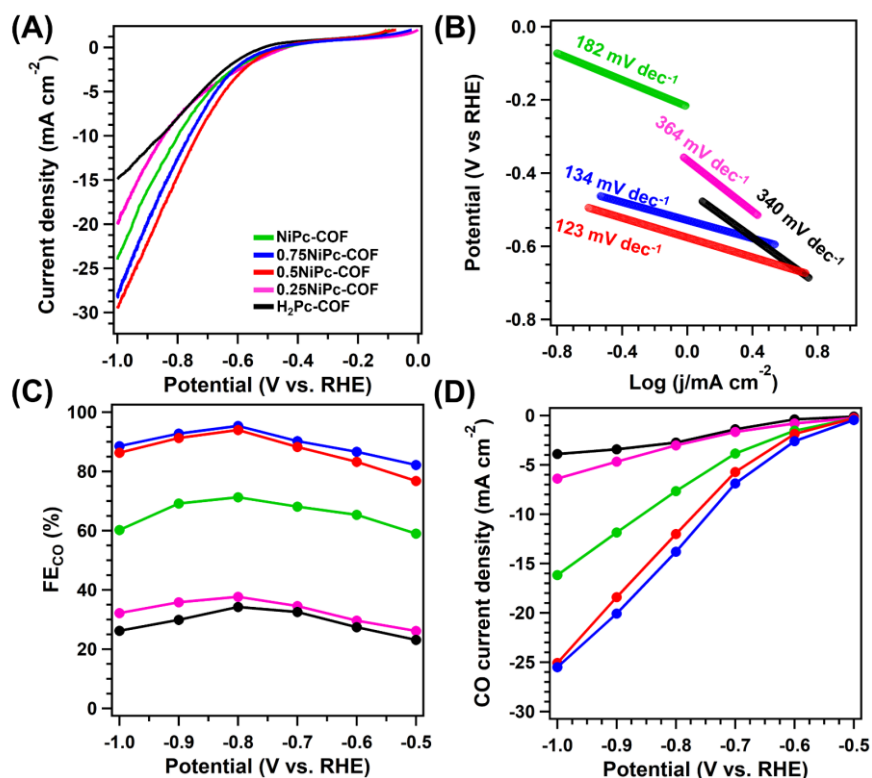


Figure 14. (A) LSV curves, (B) Tafel slopes, (C) CO faradaic efficiency and (D) the partial CO current density for H₂Pc-COF (black curve), 0.25NiPc-COF (pink curve), 0.5NiPc-COF (red curve), 0.75NiPc-COF (blue curve), NiPc-COF (green curve) from -0.5 to -1.0 V in 0.5 M KHCO₃ under CO₂ atmosphere.

The kinetic behaviours for synthesized COFs were revealed by Tafel slopes (Figure 14B). And the Tafel slope of the 0.5NiPc-COF, 0.75NiPc-COF were 134 and 123 mV dec⁻¹, which much lower than that of H₂Pc-COF, 0.25NiPc-COF and NiPc-COF with values of 340, 364 and 182 mV dec⁻¹, respectively, indicating that the formation of *COOH from the adsorbed CO₂ via a proton-coupled electron transfer process is the RDS for the 0.5NiPc-COF and 0.75NiPc-COF.^[136] However, the much higher Tafel slopes of H₂Pc-COF, 0.25NiPc-COF and NiPc-COF suggested the slow kinetic process.

To explore the selectivity of COFs for CO₂RR, the gas products at different applied potentials from -0.5 to -1.0 V for 300 s were analysed. It showed CO and H₂ were observed, and no liquid product was produced in the CO₂RR process. The FE_{CO} for the H₂Pc-COF were 23.12%, 27.41%, 32.56%, 34.21%,

29.88% and 26.18% from -0.5 to -1.0 V, respectively (Figure 14C, black curve). In addition, we calculated the j_{CO} to evaluate the activity. The $\text{H}_2\text{Pc-COF}$ demonstrated the maximum j_{CO} of 3.91 mA cm^{-2} at -1.0 V. The selectivity was highly improved with the increasement of Ni-N sites of the structure, suggesting that H_2Pc units were not the active origin for CO_2RR (Table 1).

Table 1. Summary of recently reported CO_2RR performances of other reported COF derived electrocatalysts under alkaline conditions.

Electrocatalyst	FE_{CO} (%)	TOF (s^{-1})	j_{CO} (mA cm^{-2})	Reference
NiPc-COF	76	1.1	16	This work
0.75NiPc-COF	95	1.	26	
0.5NiPc-COF	93	1.3	25	
0.25NiPc-COF	49	0.8	6	
0NiPc-COF	34	0.4	4	
CoPc-PI-COF-1	95	4.9	21	[83]
COF-300-AR	80	-	-	[77]
NiPc-COF	93	1.1	35	[81]
COF-367-Co	91	0.5	33	[75]
NiPor-CTF	91	0.5	53	[210]
CoPc-2 H_2Por COF	95	-	-	[211]
Co-TTCOF	91	1.3	3	[199]

Although 0.25NiPc-COF has delivered more positive E_0 , the selectivity and activity for CO products are still limited. And the maximum FE_{CO} was 37.66% at -0.8 V with a highest j_{CO} of 6.34 mA cm^{-2} at -1.0 V, suggesting the more H_2Pc units in the frameworks caused H_2 as the major products. When the ratio between the H_2Pc and NiPc were 1/1 in 0.5NiPc-COF, the activity and selectivity for producing CO showed obvious enhanced (the maximum FE_{CO} was 92.52% at -0.8 V with a highest j_{CO} of 25.08 mA cm^{-2} at -1.0 V) (Figure 14D, red curve). The 0.75NiPc-COF had higher selectivity than that of other XNiPc-COF in the same potential range, with FE_{CO} of 82.19%, 86.62%, 90.22%, 95.37%, 92.77%, and 88.54%, respectively (Figure 14C, blue curve). The highest j_{CO} was 25.50 mA cm^{-2} at -1.0 V, which was close to that of the 0.5NiPc-

COFs, (Figure 14D, blue curve). The FE_{CO} for the NiPc-COF were 65.97%, 69.32%, 73.12%, 75.68%, 73.17%, and 67.21% at the same potentials (Figure 14C, red curve), and the highest j_{CO} was 16.17 mA cm^{-2} at a potential of -1.0 V , which was much lower than that of 0.5NiPc-COF and 0.75NiPc-COF (Figure 14D, green curve). These results further indicated that the alternate structure of H_2Pc and NiPc can improve the CO selectivity due to the H_2Pc units adjusted the local electron density of the active Ni-N sites, further improving the CO_2RR .

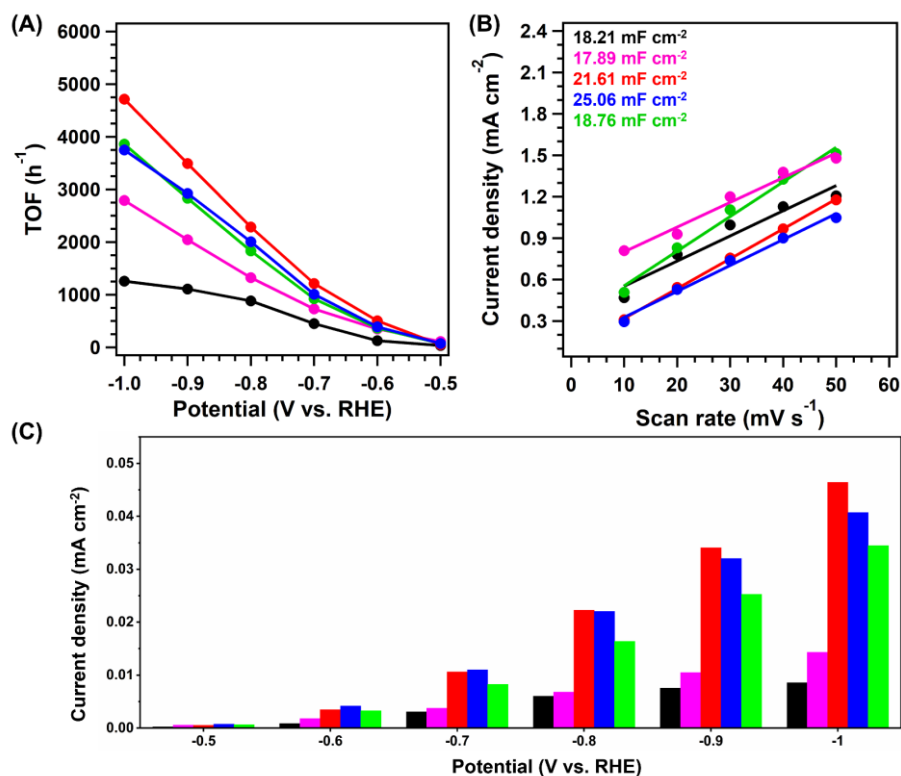


Figure 15. (A) The corresponding TOF values, (B) the ECSA slopes and (C) the current density normalized by ECSA for H_2Pc -COF (black curve), 0.25NiPc-COF (pink curve), 0.5NiPc-COF (red curve), 0.75NiPc-COF (blue curve), NiPc-COF (green curve) from -0.5 to -1.0 V in 0.5 M KHCO_3 under CO_2 atmosphere.

The TOFs of these XNiPc-COFs were calculated in the potential range of -0.5 to -1.0 V based on the loading of Ni-N sites in the XNiPc-COFs and N sites in the H_2Pc -COF as the catalytic origin. The calculated TOF values for the H_2Pc -COF, 0.25NiPc-COF, 0.5NiPc-COF, 0.75NiPc-COF and NiPc-COF were 1258.64, 2790.41, 4713.53, 3749.88 and 3860.12 h^{-1} at -1.0 V , respectively

(Figure 15A). Thus, the alternate structure of H₂Pc and NiPc with the ratio of 1/1 for the 0.5NiPc-COF, which possessed high utilization efficiency of Ni-N sites, facilitated both its activity and selectivity. Giving that the different catalytic behaviours of the XNiPc-COFs, the electrochemical ECSAs were measured. Specifically, the electrochemical C_{dl} were obtained using CV plots. The C_{dl} values for the H₂Pc-COF, 0.25NiPc-COF, 0.5NiPc-COF, 0.75NiPc-COF and NiPc-COF were 18.21, 17.89, 21.61, 25.06, and 18.76 mF cm⁻², respectively (Figure 15B). And the ECSA were then calculated by ECSA = C_{dl}/C_s, in which the C_s is 0.04 mF cm⁻².^[212-214] Therefore, the evaluated ECSA for H₂Pc-COF, 0.25NiPc-COF, 0.5NiPc-COF, 0.75NiPc-COF and NiPc-COF were 455.25, 447.25, 540.25, 626.50 and 469. To investigate the different surface catalytic activity, we have normalized the j_{CO} by ECSA, and the corresponding current density for the catalytic COFs at different potentials were in the order of 0.5NiPc-COF > 0.75NiPc-COF > NiPc-COF > 0.25NiPc-COF > H₂Pc-COF at different potentials, which further confirming the highest activity for 0.5NiPc-COF (Figure 15C).

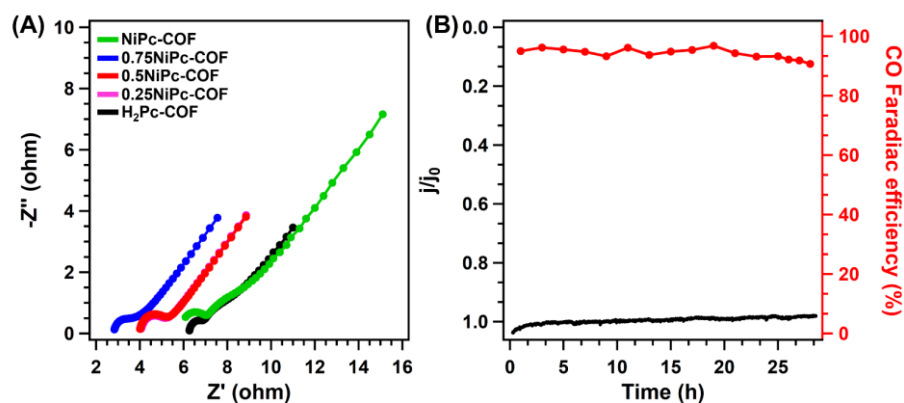


Figure 16. (A) The EIS spectra of H₂Pc-COF (black curve), 0.25NiPc-COF (pink curve), 0.5NiPc-COF (red curve), 0.75NiPc-COF (blue curve), NiPc-COF (green curve). (B) The long-term test of current density (black) and FE_{CO} (red) for the 0.25NiPc-COF.

Furthermore, EIS was investigated. Nyquist plots and corresponding parameters showed that with the increasement of Ni-N sites, the 0.25NiPc-COF (61.18 Ω),

0.5NiPc-COF (33.27 Ω), 0.75NiPc-COF (59.71 Ω) and NiPc-COF (58.31 Ω). Specifically, they exhibited lower R_{ct} than that of the H₂Pc-COF (101.33 Ω), indicating that they were capable of faster electron transfer (Figure 16A). In addition, the H₂Pc-COF showed the lowest diffusive resistance (3.32 Ω) compared with 0.25NiPc-COF (3.82 Ω), 0.5NiPc-COF (6.27 Ω), 0.75NiPc-COF (6.12 Ω) and NiPc-COF (7.02 Ω), revealing that the H₂Pc could ensure faster electron transfer from the electrodes to CO₂. The long-term stability of the 0.5NiPc-COF was investigated at -0.8 V in CO₂-saturated KHCO₃ for 24 h (Figure 16B). Specifically, a slight attenuation of FE_{CO} from 95.37% to 90.68% with a steady current density of 13.6 mA cm⁻², indicating the excellent long-term stability.

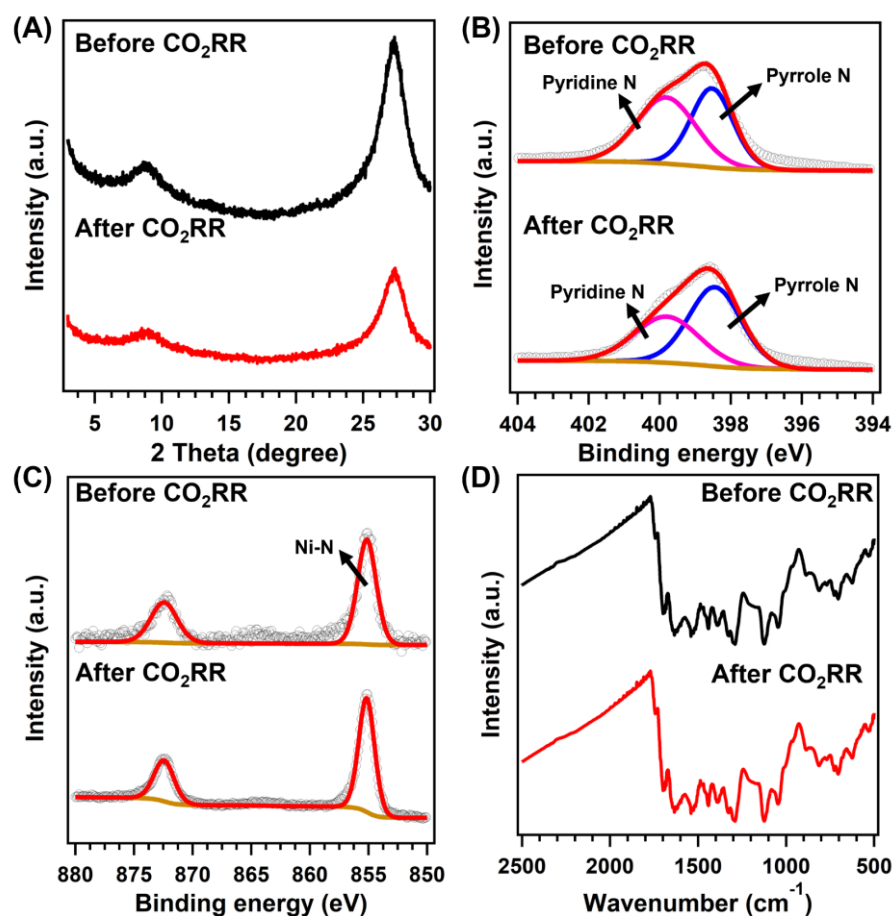


Figure 17. (A) The PXRD patterns, (B) the XPS spectra of N 1s, (C) Ni 2p and (D) the FT-IR spectra for 0.25NiPc-COF before and after the long-term test.

After the long-term stability measurement, the PXRD patterns and FT-IR and XPS spectra were obtained to confirm the structure. Specifically, the PXRD patterns revealed no obvious change of these peaks, indicating the maintenance of the structure. (Figure 17A). Meanwhile, after the durability test, the Ni 2p and N 1s peaks observed, corresponding to are in good agreement with those found for fresh 0.5NiPc-COF (Figures 17B and 17C). Furthermore, the FT-IR spectra disclose the lack of any significant band change between fresh 0.5NiPc-COF and used catalyst (Figure 17D). These results demonstrated their remarkable durability of these XNiPc-COFs in electrocatalysis CO₂RR process.

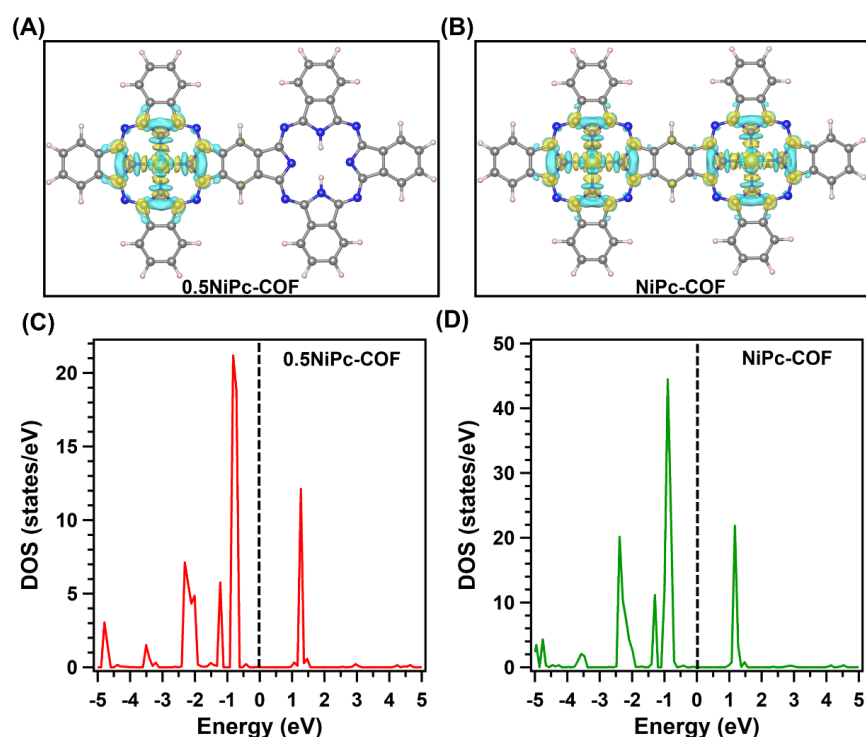


Figure 18. The electron density difference of (A) 0.5NiPc-COF and (B) NiPc-COF (The yellow and blue areas represent a gain and loss of electrons, respectively.). The pDOS plots of (C) 0.5NiPc-COF and (D) NiPc-COF.

DFT calculations were adopted to further explain why 0.5NiPc-COF provides a better CO₂RR performance than NiPc-COF. Based on the experimental results, Ni-N was considered to be the active site for the CO₂RR, and 0.5NiPc-COF with a ratio of H₂Pc and NiPc of 1:1 and NiPc-COF structure models were constructed. the charge density difference of 0.5NiPc-COF clearly revealed that

the Ni-N sites lost electrons ($0.949 e^-$) when the intermediates adsorption, while the NiPc-COF lost $1.062 e^-$ in this process, indicating the alternate structure of H₂Pc and NiPc could weaken the CO₂RR energy barrier (Figures 18A and 18B). The H₂Pc units donated their electrons to NiPc units in the frameworks, and enhance the electron density of Ni sites with greater nucleophilicity and a stronger bond with Lewis acidic CO₂ molecules. In addition, the pDOS plots were obtained for 0.5NiPc-COF and NiPc-COF (Figures 18C and 18D). The d band of the Ni-N site of 0.5NiPc-COF accommodates more electrons than that of NiPc-COF, further confirming that the electrons from H₂Pc are successfully transferred to NiPc.

7.3 Conclusion

In this study, a skeleton engineering strategy based on the multiple-component synthesis to construct the controllable metal density in the skeletons was first reported, which build the quantitative correlation between the metal density and catalytic performance. By establishing COFs with of vacancies and Ni-N sites, the 0.5NiPc-COF catalyzed CO₂RR with high selectivity and activity (FE_{CO} of 95.37% at -0.8 V and TOF of $4713.53 h^{-1}$ at -1.0 V). The design and modulation density of catalytic sites in COFs proposed not only new insights into electrocatalysis or energy conversion, but also guidance of constructing COFs with alternate structures of vacancies and metal sites for achieving high catalytic performance.

Chapter 8. Multilevel Post-synthetic Modification of Covalent Organic

Frameworks for Electrocatalytic CO₂ Reduction

8.1 Introduction

In the chapters 5-7, we studied how to construct new COFs with different topologies, building blocks and catalytic sites. However, how to improve the electrocatalytic performance of temple COFs remained unexplored. The skeleton of COFs is also significant element for the chemical properties and electrocatalysis CO₂RR performance. Specifically, the amine-linkages enhance the binding ability of CO₂ molecules, and the ionic frameworks enable to improve the electronic conductivity and the charge transfer along the frameworks. However, directly synthesis of covalent organic frameworks with amine-linkages and ionic frameworks is hardly achieved due to the electrostatic repulsion and predicament for the strength of the linkage. From the perspective of structure, the types of catalytic centers, electronic states of the linker molecules, and linkage diversities have been adopted to assemble different catalytic COFs.^[204-206] By changing the building units or linkages, the corresponding properties of COFs, such as the binding ability of CO₂ and the electron conductivity, can be adjusted.^[196,214] Thus, a COF structure containing both amine bonds, which possess superior binding ability of CO₂ molecules, and ionization skeletons, which have a high conductivity, is desirable for highly efficient CO₂RR.

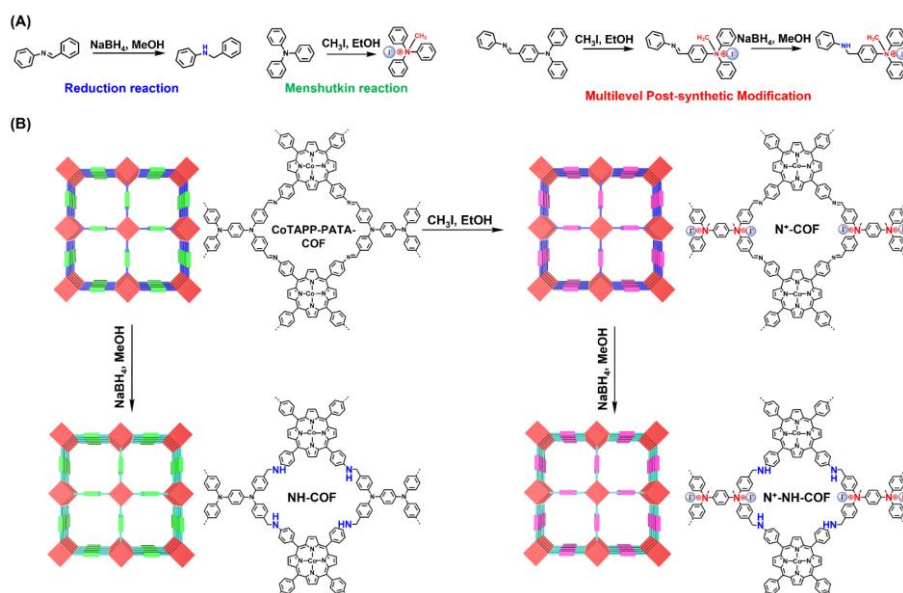
The bottom-up synthetic approach is the most common method to directly construct functional COFs.^[82,210] Challenged by the steric hindrance effect, the solubility difference and the microscopic reversibility, however, some functionalities cannot be introduced directly into COFs *via* the bottom-up syntheses.^[151,163,215] For the pre-designed COF that contains amine bonds and

ionization skeletons, the existing covalent connection methods (*e.g.*, boroxine rings, imine bonds and β -ketoenamine linkage) do not support to obtain C-N linkage through the bottom-up synthesis directly, and the electrostatic repulsion effects of ionic building units impede the direct formation of ionization skeletons.^[35,216-217] Alternatively, the post-synthetic modification strategy provide a promising chance to construct new functional skeletons, pores, and linkages at the molecular level with controllable catalytic properties.^[218-220] Several single-step post-modifications were proposed to endow the base COFs with special properties. Deng *et al.* constructed imine-COFs by a post-reduction method to improve gas diffusion on electrode.^[77] Guo *et al.* used Viologens $(C_5H_4NR)_2^{n+}$ to construct a cationic radical framework from the 2,2'-bipyridine-based COF, which showed high photothermal conversion efficiencies.^[221] Thus, it is expectable to obtain the COF with reduced imine linkage and ionic skeleton if the single-step post-modification of reduction and ionization can be well integrated. However, the integrated multilevel post-modification is rarely reported, because that not only a robust base COF is required but also the interference of multistep should be well avoided. In the view of COF design, 4,4',4'',4'''-(1,4-phenylenebis(azanetriyl))tetrabenzaldehyde (PATA) unit contains ammonium groups which are potential to transfer to ionic skeleton, and 5,10,15,20-tetrakis(4-aminophenyl)porphinato]-cobalt (TAPP(Co)) unit can achieve efficient charge transfer due to their conjugated macrocyclic structures. In addition, we previously proved that CoTAPP-PATA-COF, composed by PATA and TAPP(Co), possesses good crystallinity, high surface areas, and excellent chemical stability. Thus, CoTAPP-PATA-COF is expected as a template for constructing multilevel post-synthetic modification COFs for CO₂RR.

In chapter 8, we demonstrate a multilevel post-synthetic modification strategy to construct catalytic COFs for CO₂RR. The N⁺-NH-COF (N⁺: ionic modification; NH: reduction modification), which was constructed from CoTAPP-PATA-COF by the multilevel post-synthetic modification, showed a

maximum FE_{CO} of 97.32% at -0.8 V with a CO current density of -28.01 mA cm^{-2} and the TOF value of 9922.68 h^{-1} at -1.0 V vs. RHE. The excellent electrocatalytic properties can be attributed to the superior binding ability of CO_2 molecules from C-N bonds and high conductivity from ionization skeletons in these COFs. The results showed that reduction of C=N linkages into the C-N bond and ionization of the linkers significantly improve the selectivity and activity.

8.2 Results and discussion



Scheme 1. Schematic illustration of multilevel post-synthetic modification. (A) Effects of reduction reaction, Menshutkin reaction and multilevel post-synthetic modification on the bond change and charge state. (B) The synthesis of N^+ -COF, NH-COF and N^+ -NH-COF from the base COF (CoTAPP-PATA-COF).

The base COF (CoTAPP-PATA-COF) was synthesized from CoTAPP and PATA using the solvothermal method described in our previous study. The C=N linkages of the COF were reduced by adding $NaBH_4$ in dimethylacetamide to yield NH-COF, and the PATA units were ionized through *in situ* ammonium groups *via* Menshutkin reactions to obtain the N^+ -COF (Scheme 1A).^[222] The

base COF was modified through sequential double post-functionalization (reduction and ionization) to obtain the N^+ -NH-COF (Scheme 1B).

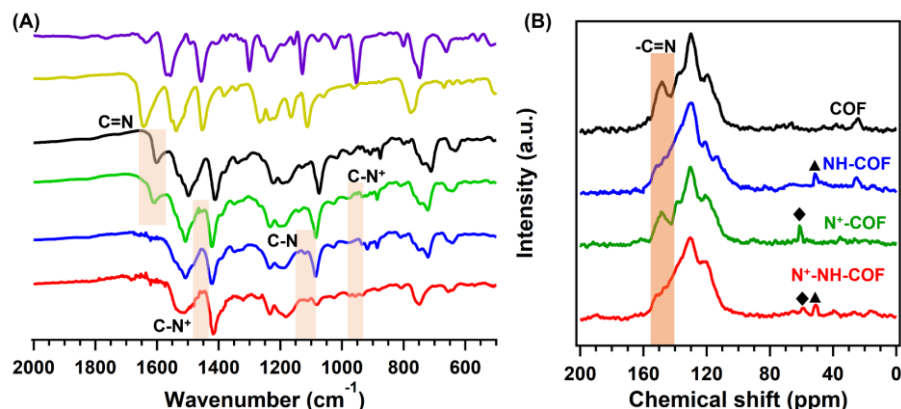


Figure 1. (A) FT-IR spectra and (B) ^{13}C NMR spectra of CoTAPP-PATA-COF (black), N^+ -COF (green), NH-COF (blue), N^+ -NH-COF (red), PATA (yellow) and CoTAPP (purple).

The successful functionalization on the linkage reduction and the skeleton ionization were first elucidated by the FT-IR. Compared with the base COF, the C=N linkage at 1622 cm^{-1} was retained, while a new peak raised at 1470 cm^{-1} , being ascribed to $-N^+-(CH_3)_2^-$ in the FT-IR spectrum of ionized N^+ -COF (Figure 1A). This reveals that the skeleton ionization was solely realized by the Menshutkin reaction. After the reduction modification, in contrast, the FT-IR spectra of NH-COF and the N^+ -NH-COF revealed that the C=N vibration at 1622 cm^{-1} was totally replaced by the new signals of C-N at 1157 cm^{-1} (Figure 1A). This indicates that the C=N linkages were fully converted into C-N bonds. Apart from C-N vibrations, furthermore, the ionic $-N^+-(CH_3)_2^-$ was also detected for the FT-IR spectrum of N^+ -NH-COF. Moreover, the Co-N bond at 660 cm^{-1} was observed in all four COFs, indicating that the post-modifications were harmless to the Co-N coordination. The functionalization of COFs was further confirmed by using the solid ^{13}C NMR (Figure 1B). The C=N signals (148 ppm) in CoTAPP-PATA-COF and N^+ -COF were completely replaced by the new C-N signals at 51 ppm for the NH-COF and N^+ -NH-COF. In addition, N^+ -COF and N^+ -NH-COF exhibited a new peak belonging to methyl groups at 60 ppm. These

results indicate that the successful reduction of $-\text{C}=\text{N}$ and the methylation with charge state changes. On the other hand, the FT-IR and ^{13}C NMR results also reveal that the Menshutkin reaction is selective for the methylation of C-N bonds rather than the co-existed C=N bonds.

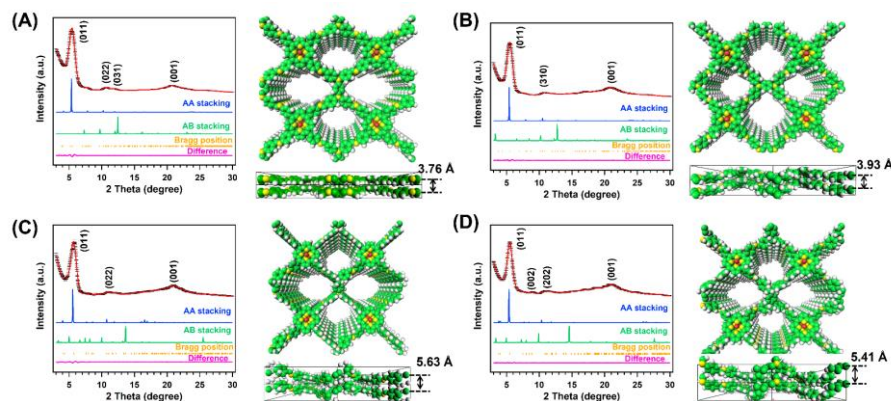


Figure 2. The PXRD profiles and simulated structures of (A) CoTAPP-PATA-COF, (B) NH-COF, (C) N^+ -COF and (D) N^+ -NH-COF. Line colour follows: experimentally observed (black), Pawley refined (red), Bragg positions (orange) and their difference (pink), simulated using the AA (blue) and staggered AB (green) stacking modes. Atom colour in the theoretically modelled eclipsed-AA stacking models: C-green, N-yellow, H-white, Co-red.

The crystalline structures of CoTAPP-PATA-COF, N^+ -COF, NH-COF and N^+ -NH-COF were investigated by the PXRD measurements. The PXRD pattern of CoTAPP-PATA-COF showed the peaks of (011), (022), (031) and (001) facets at 5.15° , 11.02° , 12.23° and 21.84° , respectively (Figure 2A). The Pawley refinements revealed that the theoretical structures were in accordance with the experimental results with R_{wp} and R_p of 3.04% and 2.98%, respectively. According to the DFTB method, the base COF adopted AA stacking model, which enable to provide the open channels for mass transport (Figure 2A). For the NH-COF, the peaks from (011), (310) and (001) were also identified (Figure 2B). The Pawley refinements revealed that the simulated results were in accordance with the experimental results. And NH-COF adopts an eclipsed stacking in a PM space group with refined cell parameters of $a = 22.51 \text{ \AA}$, $b =$

23.45 Å, $c = 5.41$ Å, $\alpha = \beta = \gamma = 90^\circ$, with the corresponding R_{wp} of 2.64% and R_p of 2.06%. The N^+ -COF also displayed a good crystallinity with intense peaks at 5.15° (011), 11.12° (022), and 21.97° (001) (Figure 2C). Both of the ionized COFs adopted AA stacking models. Notably, the crystallinity of the N^+ -NH-COF was well maintained after the double post-modification, offering the peaks from (011), (002), (202) and (001) at 5.15° , 11.12° , 12.32° and 22.17° , respectively (Figure 2D). The highly crystalline structures were further confirmed by the Pawley refinements, with the corresponding R_{wp} of 2.67% and 3.78%, R_p of 2.26% and 3.03% for N^+ -COF and N^+ -NH-COF, respectively.

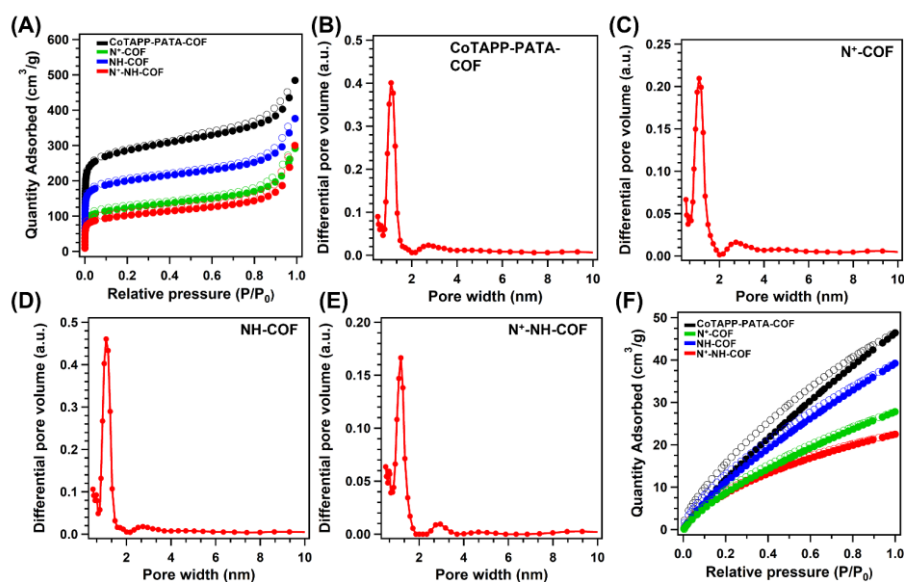


Figure 3. (A) The nitrogen-sorption isotherms at 77 K and the pore distribution curves of (B) CoTAPP-PATA-COF, (C) N^+ -COF, (D) NH-COF and (E) N^+ -NH-COF. (F) The CO_2 absorption curves at 273 K for CoTAPP-PATA-COF (black), N^+ -COF (green), NH-COF (blue) and N^+ -NH-COF (red).

The porous structures of COFs are crucial for the mass transport and the accessibility of active sites during electrocatalysis. The porosity of these COFs was investigated through nitrogen sorption isotherm measurements at 77 K. The CoTAPP-PATA-COF exhibited a microporous sorption behavior with a S_{BET} of $943.72 \text{ m}^2 \text{ g}^{-1}$ (Figure 3A, black curve), delivering a pore volume of $0.75 \text{ cm}^3 \text{ g}^{-1}$ and a pore size of 1.1 nm (Figure 3B). After the post modifications, the S_{BET}

changed to 410.69, 659.05, and 340.19 $\text{m}^2 \text{g}^{-1}$ for N^+ -COF, NH-COF, and N^+ -NH-COF, respectively. Additionally, the corresponding pore volumes declined to 0.45, 0.58, and 0.46 $\text{cm}^3 \text{g}^{-1}$, while the pore sizes kept no change for N^+ -COF, NH-COF, and N^+ -NH-COF, respectively (Figures 3C-3E). Considering the critical roles of CO_2 absorption on CO_2RR , we investigated the CO_2 sorption behaviors at 273 K. The CO_2 uptakes of the CoTAPP-PATA-COF, N^+ -COF, NH-COF, and N^+ -NH-COF were 46.43, 27.80, 39.23, and 22.50 $\text{cm}^3 \text{g}^{-1}$ at 1 bar, respectively (Figure 3F). Benefiting from the abundant C-N bonds, the NH-COF showed a high CO_2 adsorption capacity although the surface area and pore volume were relatively decreased.

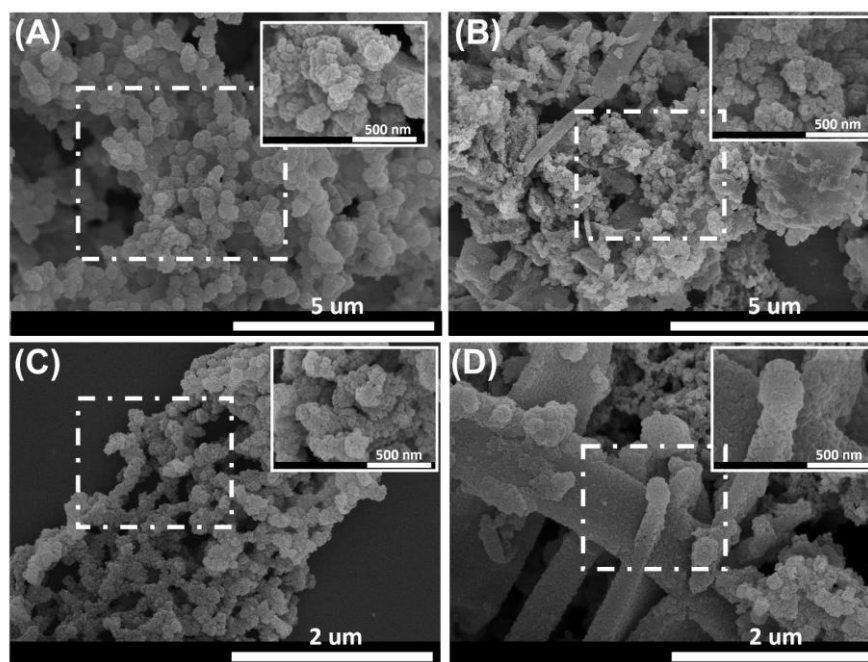


Figure 4. FE-SEM images of (A) CoTAPP-PATA-COF, (B) N^+ -COF, (C) NH-COF and (D) N^+ -NH-COF.

The morphologies of the COFs were studied *via* the SEM and TEM. These post-modified COFs exhibited similar morphologies to that of base COF without significant morphological changes, suggesting that the structure is well preserved (Figures 4A-4D).

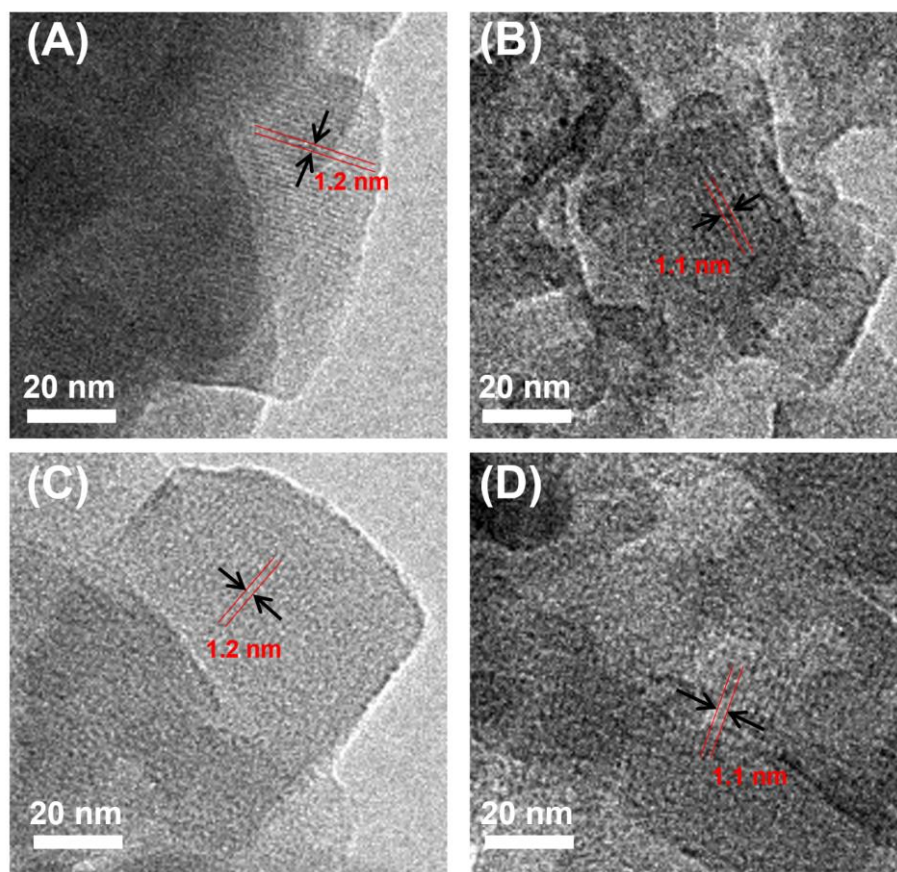


Figure 5. HR-TEM images of (A) CoTAPP-PATA-COF, (B) N⁺-COF, (C) NH-COF and (D) N⁺-NH-COF.

This was further confirmed by the TEM observations. The HR-TEM images showed the ordered straight channels with diameters of ~ 1.1 nm in the COFs, in accordance with the pore sizes determined by the N₂ absorptions, indicating that the mass transfer paths and the crystallinity of post-modified COFs were well protected (Figures 5A-5D).

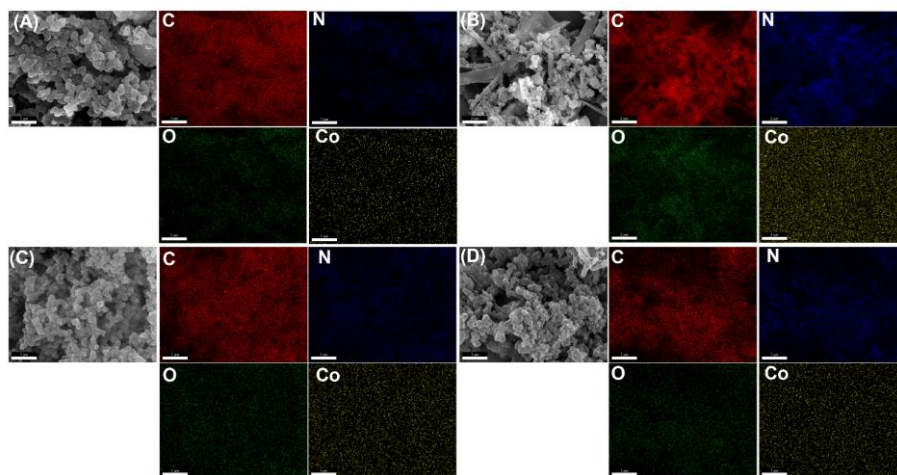


Figure 6. EDX-mapping images of (A) CoTAPP-PATA-COF, (B) N^+ -COF, (C) NH-COF and (D) N^+ -NH-COF.

EDX mapping images revealed that all elements were uniformly distributed in the COFs (Figures 6A-6D).

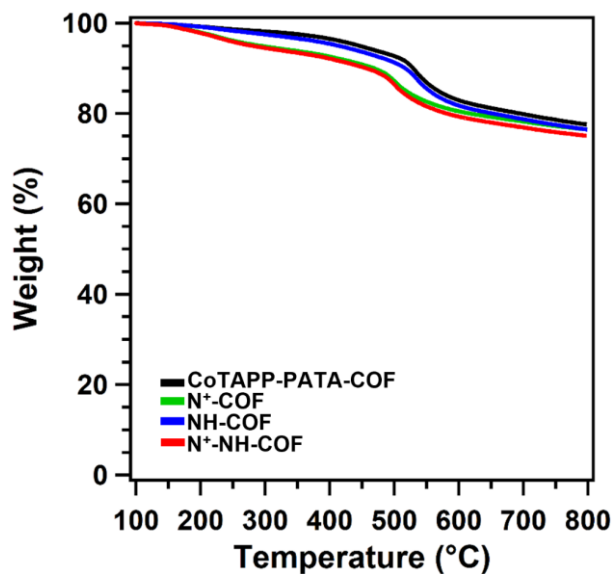


Figure 7. TGA curves of CoTAPP-PATA-COF (black), N^+ -COF (green), NH-COF (blue) and N^+ -NH-COF (red).

Furthermore, the TGA measurements showed that the post-modified COFs kept the similar thermal stability to that of base COF, and no significant mass loss was observed at the temperature < 480 °C in N_2 (Figure 7).

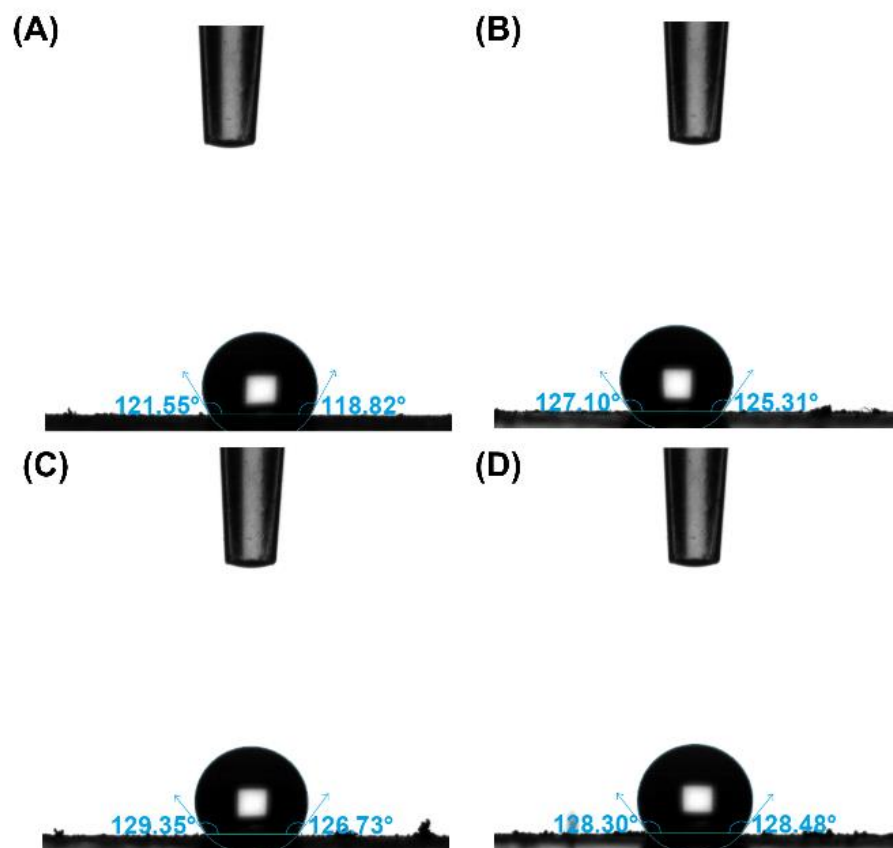


Figure 8. The contact angles of water for (A) CoTAPP-PATA-COF, (B) N⁺-COF, (C) NH-COF and (D) N⁺-NH-COF.

In addition, the hydrophobicity of these COFs was evaluated by the WCA measurements (Figures 8A-8D). The measured WCAs of the CoTAPP-PATA-COF, N⁺-COF, NH-COF, and N⁺-NH-COF were $121.6 \pm 3.2^\circ$, $127.1 \pm 2.6^\circ$, $129.4 \pm 3.1^\circ$, and $128.3 \pm 2.7^\circ$, respectively, indicating that the effects of post modifications on the surface hydrophilicity are negligible. For the electrocatalysis of CO₂RR, the hydrophobic nature of catalyst is crucial to protect the active sites through suppressing the competitive adsorption of water, leading to the improvements of selectivity and energy efficiency.^[192]

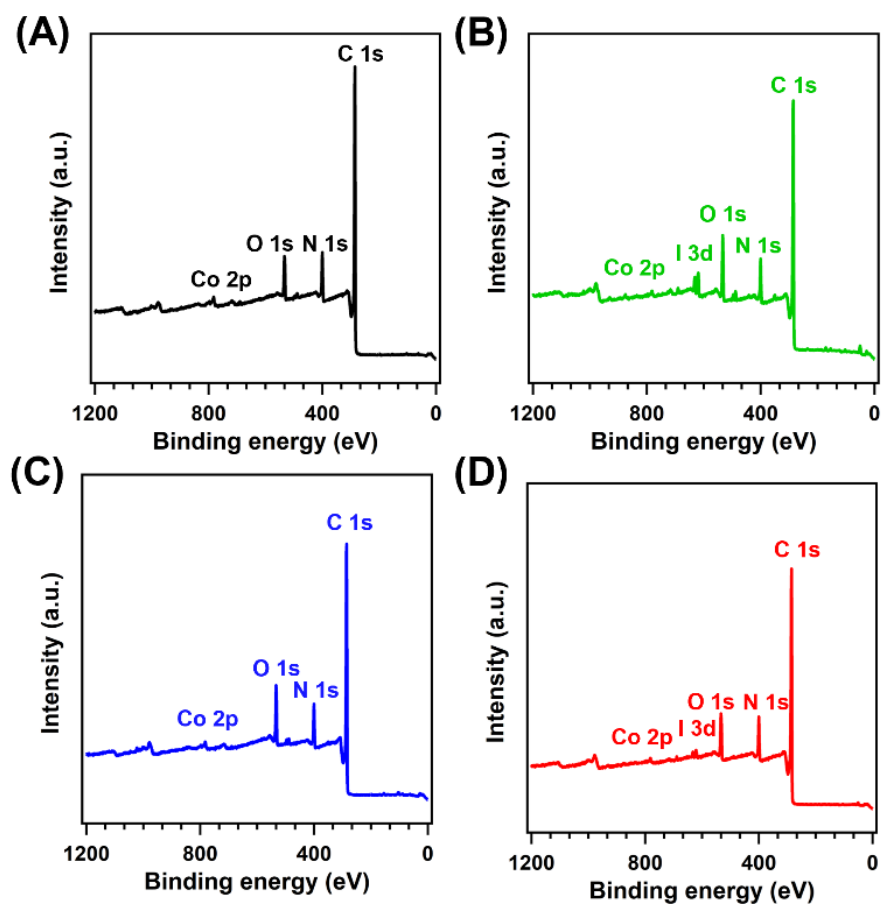


Figure 9. The XPS spectra of (A) CoTAPP-PATA-COF, (B) N^+ -COF, (C) NH-COF and (D) N^+ -NH-COF.

The chemical structures and electron states of the COFs were investigated *via* XPS. The XPS spectra showed peaks corresponding to C, N, O, and Co in the prepared COFs (Figures 9A-9D). The Co content was 4.0, 4.0, 3.7, and 3.7 wt.% in the CoTAPP-PATA-COF, N^+ -COF, NH-COF, and N^+ -NH-COF, respectively, which are close to the values obtained from the ICP-OES measurements (*i.e.*, 3.6, 3.5, 3.3, and 3.1 wt.%, respectively).

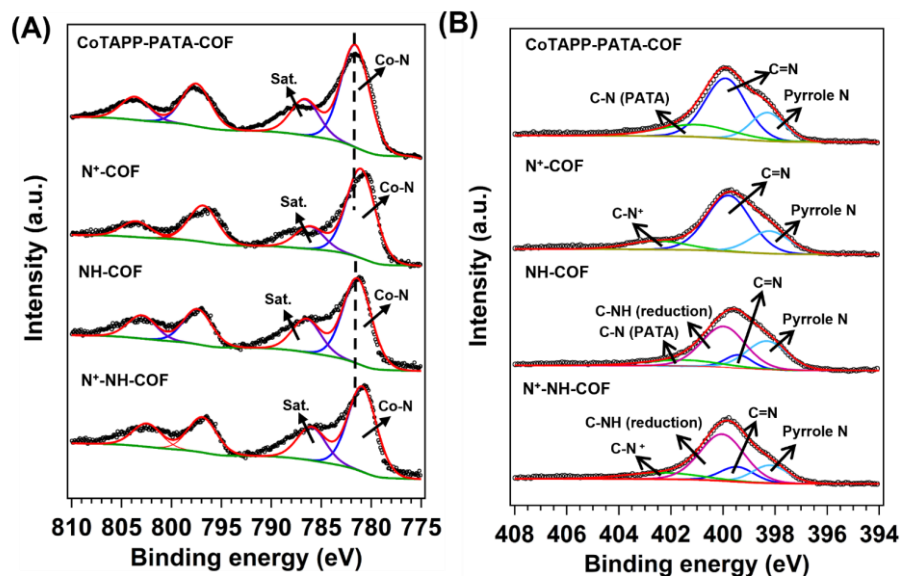


Figure 10. The XPS spectra of (A) Co 2p and (B) N 1s for CoTAPP-PATA-COF, N⁺-COF, NH-COF and N⁺-NH-COF.

Furthermore, the high-resolution Co 2p spectra of the four COFs exhibited Co-N coordination, which confirmed that the Co-N sites were well retained after the multilevel post-modifications (Figure 10A). In detail, compared with CoTAPP-PATA-COF (781.38 eV) and NH-COF (781.36 eV), the Co 2p_{3/2} spectra of N⁺-COF (780.92 eV) and N⁺-NH-COF (780.90 eV) showed a negative shift of ~0.45 eV, which is ascribed to the electron-withdrawing effect of methyl groups.^[223] This proves that the skeletons in N⁺-COF and N⁺-NH-COF have been ionized by the CH₃I modification. The high-resolution N 1s spectrum of the CoTAPP-PATA-COF was deconvoluted into three peaks of pyrrole N (398.29 eV), C=N (399.62 eV) and C-N (401.03 eV) with relative contents of 28.14, 55.88 and 15.97 at.%, respectively (Figure 10B). In comparison, the N 1s spectrum of the NH-COF showed that the content of C=N was decreased to 14.74% while a new C-NH peak appeared at 400.23 eV with a content of 46.09%. Moreover, the N⁺-COF displayed a new peak at 402.34 eV, which was attributed to N⁺-CH₃ bonds. Due to the reduced linkages and the ionic linkers, the peaks of C-NH and N⁺-CH₃ were identified at 400.03 and 402.34 eV, respectively, in the N 1s spectrum of the N⁺-NH-COF (Figure 10B). Therefore, the linkages and skeletons were

fully modulated, as expected.

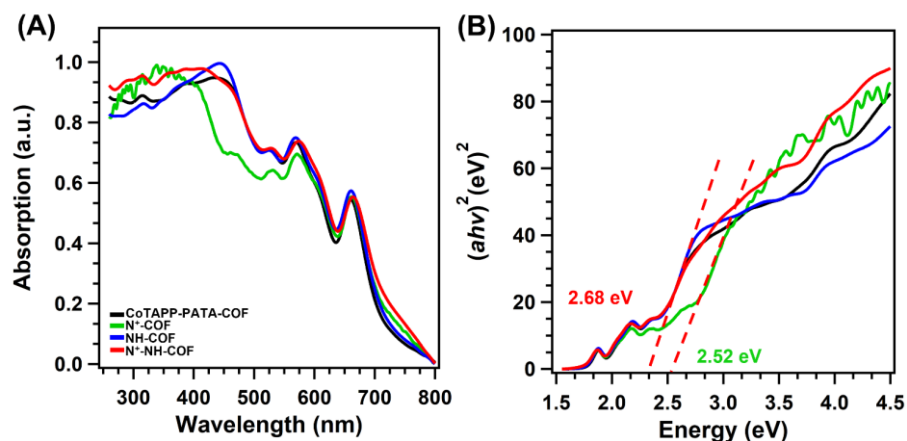


Figure 11. (A) The UV-vis absorption and (B) Tauc plots for CoTAPP-PATA-COF (black), N⁺-COF (green), NH-COF (blue) and N⁺-NH-COF (red).

To investigate the different properties of the base and functionalized COFs, the UV-Vis spectroscopy was adopted to determine their band gaps (Figure 11A). Accordingly, the band gaps of the CoTAPP-PATA-COF, N⁺-COF, NH-COF, and N⁺-NH-COF were determined as 2.68, 2.52, 2.66, and 2.67 eV, respectively (Figure 3C inset). As the conductivity increased with the decrease of gap value, the N⁺-COF has the highest conductivity compared with that of other COFs, indicating that the ionization units could improve the conductivity.

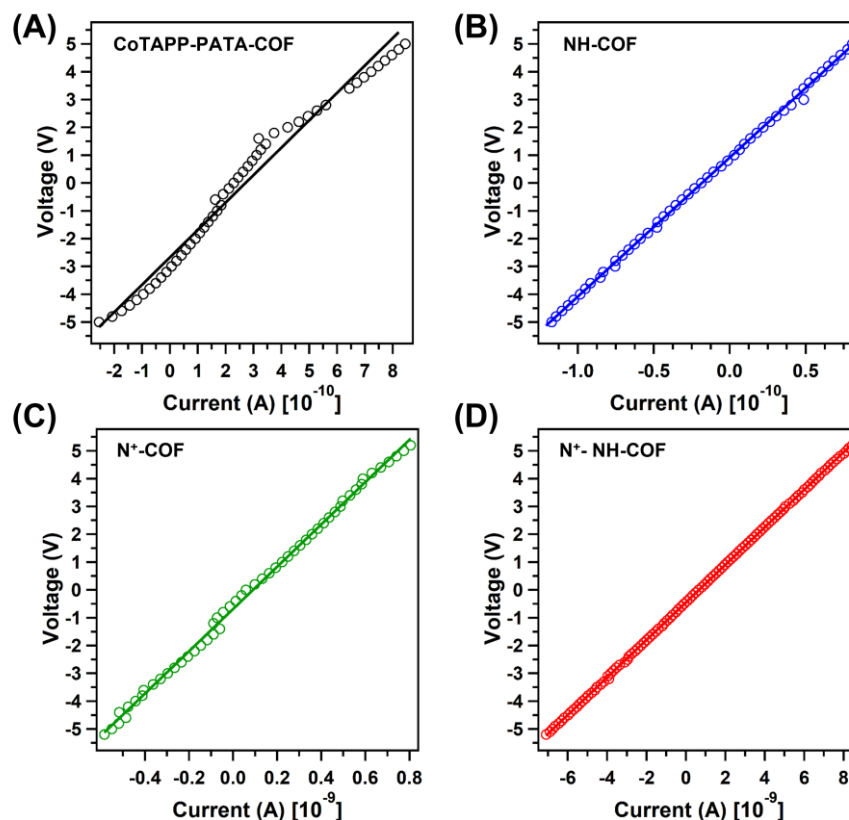


Figure 12. The I-V curves of (A) CoTAPP-PATA-COF, (B) NH-COF, (C) N⁺-COF and (D) N⁺-NH-COF by the four-probe measurement at 298 K.

To confirm the electronic conductivity change, the CoTAPP-PATA-COF, N⁺-COF, NH-COF and N⁺-NH-COF were measured by the four-probe method at 298 K (Figures 12A-12D). N⁺-NH-COF and N⁺-COF have the similar electronic conductivity of $6.7 \times 10^{-9} \text{ S m}^{-1}$ and $8.1 \times 10^{-9} \text{ S m}^{-1}$, respectively, which are one order of magnitude larger than those of CoTAPP-PATA-COF ($8.5 \times 10^{-10} \text{ S m}^{-1}$) and NH-COF ($3.0 \times 10^{-10} \text{ S m}^{-1}$). It suggests that the ionized skeletons can promote the electron transfer along the frameworks, and thus improving the activity.

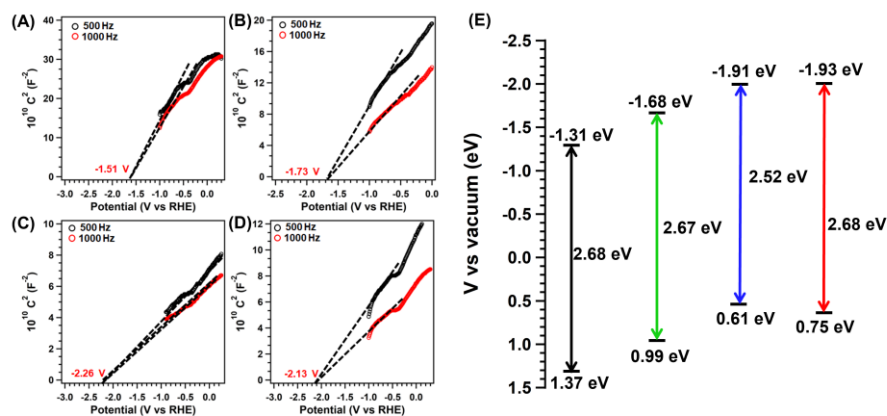


Figure 13. Mott–Schottky plots of (A) CoTAPP-PATA-COF, (B) N^+ -COF, (C) NH-COF and (D) N^+ -NH-COF from 500 Hz and 1000 Hz. (E) The energy gap (HOMO and LUMO) for CoTAPP-PATA-COF (black), N^+ -COF (green), NH-COF (blue) and N^+ -NH-COF (red).

The HOMO and LUMO were calculated to investigate the electron conduction properties using the Mott–Schottky method (Figures 13A-13D). The HOMO positions of the CoTAPP-PATA-COF, N^+ -COF, NH-COF, and N^+ -NH-COF were 1.37, 0.99, 0.61, and 0.75 eV, respectively, suggesting that the multilevel post-synthetic modification effectively improved the reduction capacity of COFs (Figure 13E).

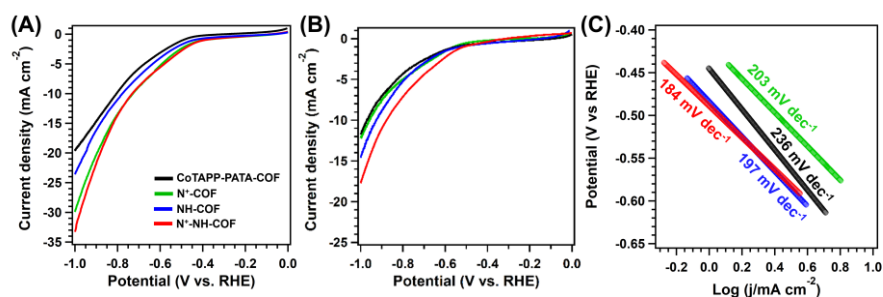


Figure 14. The LSV curves of (A) under CO_2 atmosphere, (B) under Ar atmosphere and (C) Tafel slopes for CoTAPP-PATA-COF (black), N^+ -COF (green), NH-COF (blue) and N^+ -NH-COF (red) from -0.5 to -1.0 V in 0.5 M $KHCO_3$.

The CO_2 RR performance of the catalytic COFs was investigated in a $KHCO_3$ aqueous solution (0.5 M, pH 7.2) saturated with CO_2 using a standard two-

compartment electrochemical cell. The COFs were mixed with carbon black at a weight ratio of 5/8. Firstly, the LSV measurements were conducted at a scan rate of 10 mV s^{-1} from 0 to -1.0 V vs. RHE (Figure 14A). Compared with N_2 saturated solution, a significantly higher current density was observed in the CO_2 saturated solution, indicating the superior CO_2 reduction activity of COFs (Figure 14B). The LSV curves showed that the current densities of the CoTAPP-PATA-COF and NH-COF were close in the same potential range. In comparison, the current densities of N^+ -COF and N^+ -NH-COF were increased, suggesting that the ionized skeletons promoted electron transfer and enhanced the current density (Figure 14A). The corresponding Tafel slope of the CoTAPP-PATA-COF was 236 mV dec^{-1} , which declined to 203, 197, and 184 mV dec^{-1} for N^+ -COF, NH-COF, and N^+ -NH-COF, respectively (Figure 14C). It suggests that the post modifications significantly improve the electrocatalytic CO_2RR kinetics.

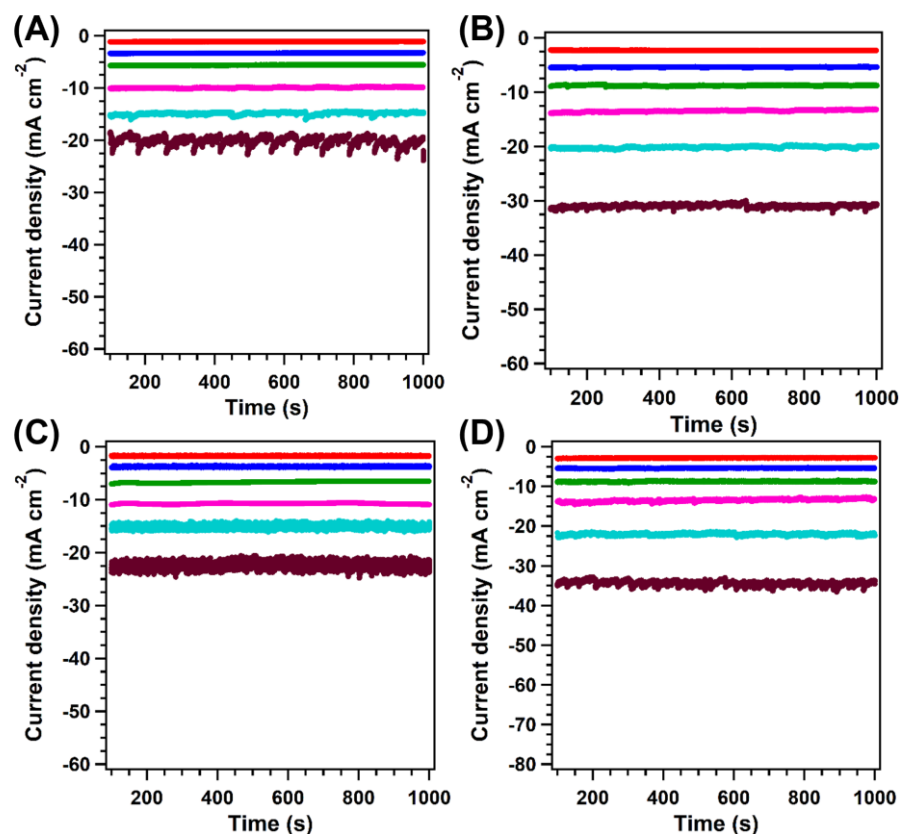


Figure 15. Chronoamperometric responses of (A) CoTAPP-PATA-COF, (B) N⁺-COF, (C) NH-COF and (D) N⁺-NH-COF at -0.5 (red), -0.6 (blue), -0.7 (green), -0.8 (pink), -0.9 (cyan), and -1.0 V (brown) (vs. RHE).

The reduction products of CO₂RR were analysed *via* the gas and liquid chromatography, and only CO and H₂ were detected. The constant time-dependent total geometric current densities of the CoTAPP-PATA-COF, N⁺-COF, NH-COF, and N⁺-NH-COF were determined for each potential between -0.5 and -1.0 V for 1000 s, indicating that the COF catalysts had good stability (Figures 15A-15D).

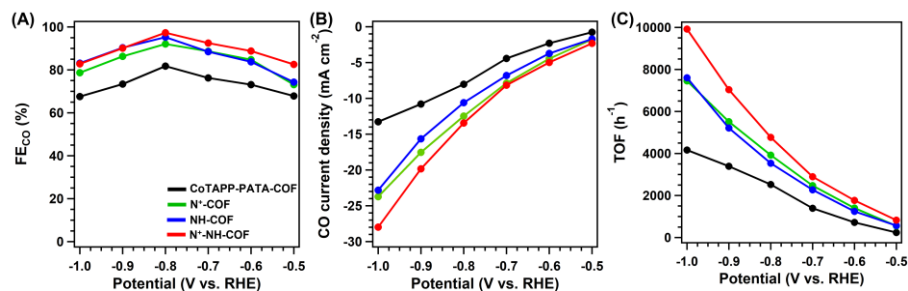


Figure 16. (A) CO faradaic efficiency, (B) the partial CO current density and (C) the corresponding TOF value for CoTAPP-PATA-COF (black), N⁺-COF (green), NH-COF (blue) and N⁺-NH-COF (red) from -0.5 to -1.0 V in 0.5 M KHCO₃ under CO₂ atmosphere.

The FE_{CO} of the CoTAPP-PATA-COF were 67.84%, 73.11%, 76.26%, 81.75%, 73.42%, and 67.54% at -0.5 , -0.6 , -0.7 , -0.8 , -0.9 , and -1.0 V, respectively (Figure 16A, black curve). In addition to the selectivity, the activity was revealed by the j_{CO} of the catalyst. The CoTAPP-PATA-COF exhibited the highest j_{CO} of 13.26 mA cm⁻² at a potential of -1.0 V (Figure 16B, black curve). The CO selectivity was remarkably improved on the COFs that contain C-N linkages and/or skeleton ionization. The N⁺-COF had considerably higher selectivity than the base COF at the same potential, delivering FE_{CO} of 73.12%, 84.75%, 88.71%, 92.07%, 86.31%, and 78.66% at -0.5 , -0.6 , -0.7 , -0.8 , -0.9 , and -1.0 V, respectively (Figure 16A, green curve). The highest j_{CO} on N⁺-COF was 23.73 mA cm⁻² at -1.0 V, which was higher than that of the base COF (Figure 16B, green curve). The FE_{CO} for the NH-COF were 74.26%, 83.75%, 88.49%, 95.26%, 90.31%, and 83.12%, which are higher than that of CoTAPP-PATA-COF and N⁺-COF at the same potentials (Figure 16A, blue curve). The highest j_{CO} on NH-COF was 22.83 mA cm⁻² at -1.0 V, being also higher than that of base COF (Figure 16B, blue curve). In comparison, the N⁺-NH-COF achieved FE_{CO} of 82.56%, 88.76%, 92.51%, 97.32%, 90.12%, and 82.78% from -0.5 to -1.0 V (Figure 16A, red curve) and the highest j_{CO} of 28.01 mA cm⁻² at -1.0 V (Figure 16B, red curve), which are higher than those of other COFs. Therefore, the C-N linkages improved the catalytic selectivity, and the ionic skeleton

contributed to higher activity. The TOFs of the prepared COFs were obtained at different potentials by accounting the amount of CoTAPP units as electrocatalytically active sites. The highest TOF values obtained for the CoTAPP-PATA-COF, N⁺-COF, NH-COF, and N⁺-NH-COF were 4166.19, 7453.19, 7604.63, and 9922.68 h⁻¹ at -1.0 V, respectively (Figure 16C). As the N⁺-NH-COF yielded the highest TOF in compared to other COFs, it demonstrated that the multilevel post modification boosted both CO₂RR activity and CO selectivity of the base COF.

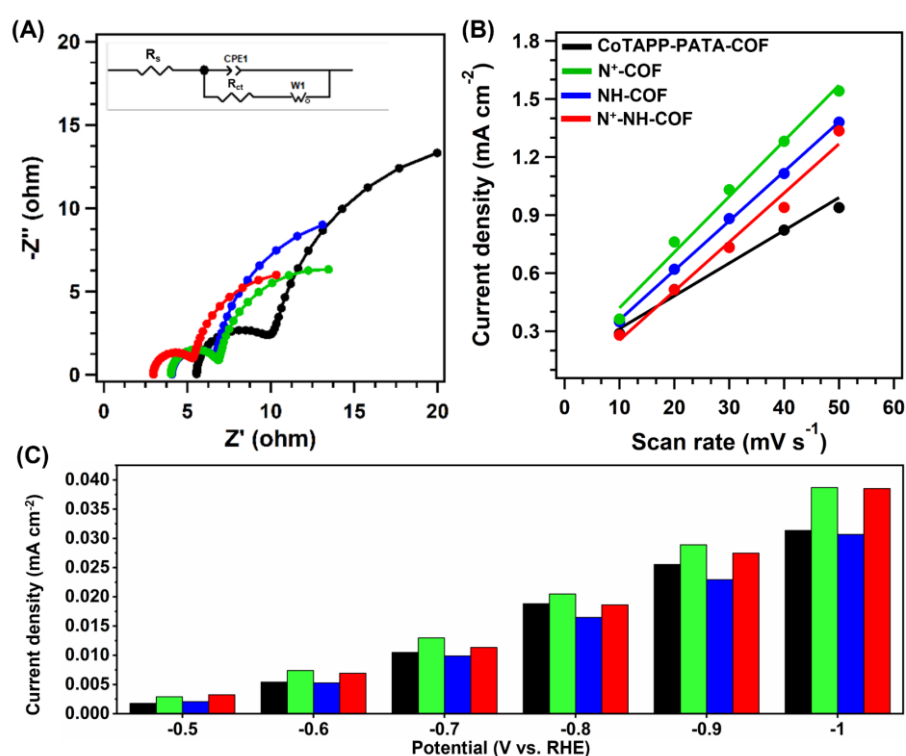


Figure 17. (A) The EIS spectra, (B) the ECSA slopes and (C) the CO current density by the normalized ECSA for CoTAPP-PATA-COF (black), N⁺-COF (green), NH-COF (blue) and N⁺-NH-COF (red) from -0.5 to -1.0 V in 0.5 M KHCO₃ under CO₂ atmosphere.

Furthermore, the Nyquist plots showed that the R_{ct} over N⁺-COF and N⁺-NH-COF were 36 and 24 Ω , respectively, being smaller than that of CoTAPP-PATA-COF (52 Ω) and NH-COF (42 Ω). This suggested that the ionization of skeletons enhanced the charge transfer capacity of COFs (Figure 17A). The

electrochemical C_{dl} were calculated using the CV plots in a potential range of -0.16 to -0.36 V at the scan rates of 10 - 50 mV s^{-1} . Correspondingly, the C_{dl} values for the CoTAPP-PATA-COF, N^+ -COF, NH-COF, and N^+ -NH-COF were 16.92 , 26.34 , 24.37 , and 28.76 mF cm^{-2} , respectively (Figure 17B). To investigate the exposed active sites, the ECSAs of the COFs were then calculated by $\text{ECSA} = C_{dl}/C_s$, where the C_s is 0.04 mF cm^{-2} . N^+ -NH-COF offered the highest ECSA (719) relative to CoTAPP-PATA-COF (423), N^+ -COF (659), and NH-COF (609), which is in line with its CO_2RR performance. Moreover, the ECSA of N^+ -COF was higher than the base COF and NH-COF, suggesting that the ionic frameworks provided more active sites.^[200] The normalized current densities on the COFs, *i.e.*, j_{CO} per ECSA, were further evaluated (Figure 17C). Within the potential range of -0.5 to -1.0 V, the ionized COFs of N^+ -COF and N^+ -NH-COF always exhibited the higher normalized current density than that of un-ionized COFs of CoTAPP-PATA-COF and NH-COF, confirming that the ionization helps to improve the COF activity towards CO_2RR .

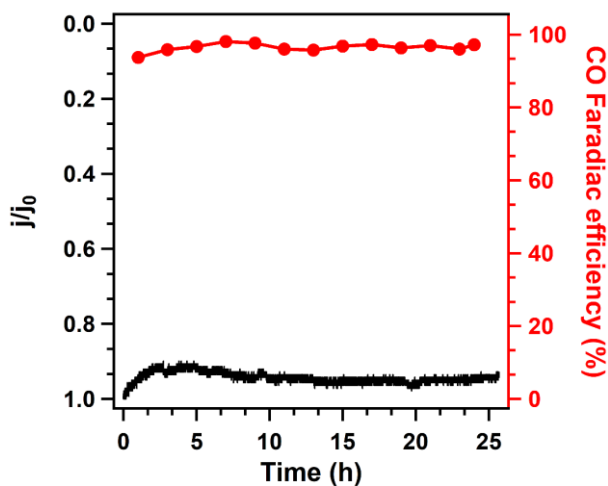


Figure 18. Chronoamperometry test for CO_2RR of N^+ -NH-COF at a potential of -0.8 V in 0.5 M KHCO_3 under CO_2 atmosphere.

Moreover, the long-term stability of the N^+ -NH-COF was evaluated at -0.8 V in CO_2 -saturated KHCO_3 for 25 h (Figure 18). The FE_{CO} kept stable around 97% and the relative current density (j/j_0) was $> 94.5\%$ within 25 h, indicating the excellent long-term stability of N^+ -NH-COF for CO_2RR .

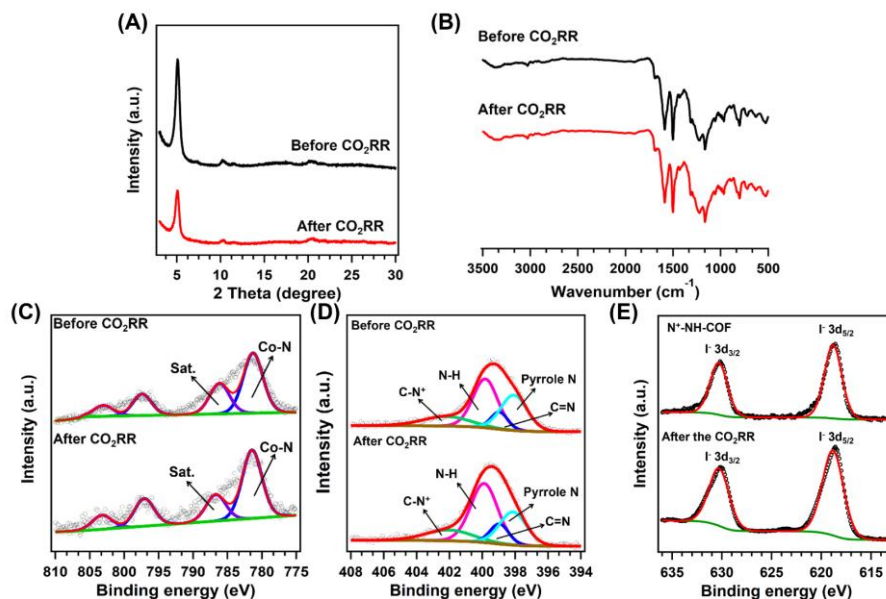


Figure 19. (A) The PXRD patterns, (B) FTIR spectra, the XPS spectra of (C) Co 2p, (D) N 1s and (E) I 3d for N^+ -NH-COF before and after the long-term test.

To confirm the stability, the used N^+ -NH-COF was checked by the PXRD, FT-IR and XPS measurements after the long-term stability test. The PXRD patterns showed that all peaks were fully retained, and no new peaks were observed after the long-term stability test (Figure 19A). The FT-IR spectra showed that all the peaks of the N^+ -NH-COF were well maintained (Figure 19B). Additionally, the Co 2p, I 3d and N 1s spectra showed the same states to that of fresh sample (Figures 19C-19E). Thus, the structure of the N^+ -NH-COF was retained.

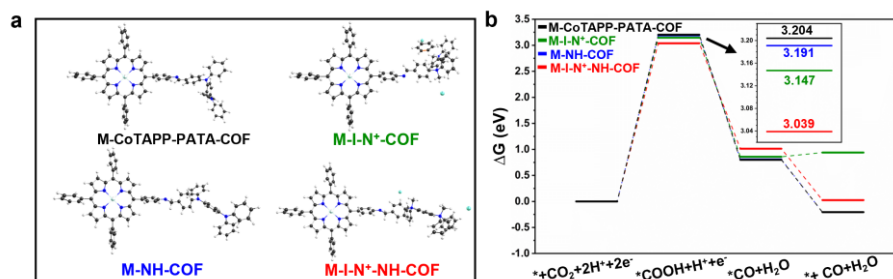


Figure 20. (a) The optimized geometrical structures and (b) Calculated ΔG diagram of M-CoTAPP-PATA-COF, M-I- N^+ -COF, M-NH-COF and M-I- N^+ -NH-COF catalysing CO_2RR (M-Model).

To further understand the different performance of CoTAPP-PATA-COF, N⁺-COF, NH-COF and N⁺-NH-COF for CO₂RR, the DFT calculations were carried out at the theoretical level of CAM-B3LYP/6-311G(d) (SDD for Co) for the cluster models of these four COFs. Reasonable geometrical, electronical and thermodynamic information could be obtained with cluster models for COFs and similar systems. All structures along the potential energy surfaces were optimized without any restrictions. Frequencies were further performed to confirm that all optimized geometries are local minima and to obtain the Gibbs free energies. In the calculation, the four model molecules were labelled as M-CoTAPP-PATA-COF, M-I-N⁺-COF, M-NH-COF and M-I-N⁺-NH-COF, respectively, where the counter ion I⁻ was considered for the N⁺-COF and N⁺-NH-COF (Figure 20a). As shown in Figure 20b, CO₂RR includes four steps: the absorption of CO₂, formation of *COOH and *CO where a proton coupled a single electron transfer take place for each step, and CO desorption from the active metal centre. From CO₂ to the product CO, the CO₂RR catalysed by M-I-N⁺-COF and M-I-N⁺-NH-COF are slightly endergonic, while those catalysed by M-CoTAPP-PATA-COF and M-NH-COF are exergonic. This is in accordance with the excellent catalytic ability of the four COFs. The relative free energies of *COOH formation are higher than the initial state of CO₂ (*i.e.*, the relative zero point of free energies), while the process from *COOH to the final product CO are largely exergonic. This indicates that the formation of *COOH is the rate control step. The lowest free energy changes of *COOH state for M-I-N⁺-NH-COF is in line with its best performance from a thermodynamic viewpoint. In addition, both M-I-N⁺-COF and M-I-N⁺-NH-COF have the lower ΔG of *COOH than those of M-CoTAPP-PATA-COF and M-NH-COF, which indicates a stronger promotion effect of ionization than the neutral ones.

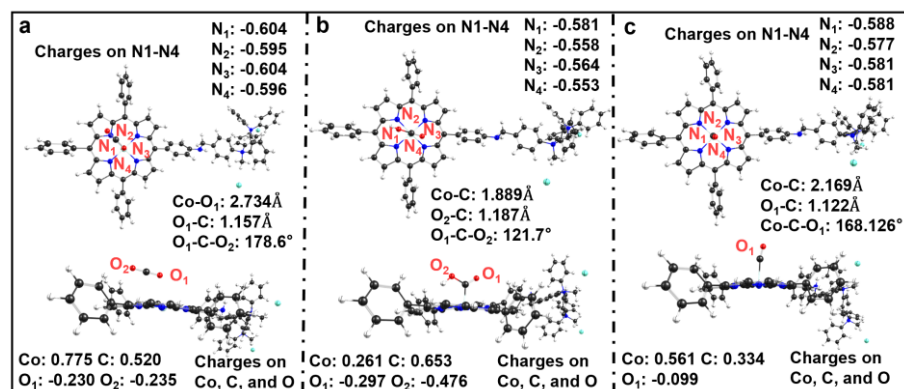


Figure 21. The optimized geometrical structures of stationary points along the reaction pathway of M-I-N⁺-NH-COF catalyzing CO₂RR reaction, (a) CO₂^{*}, (b) COOH^{*}, (c) CO^{*}, along with the main geometrical parameters and the Mulliken charges on main atoms. The black, red, white, blue, light cyan and dark cyan balls represent carbon, oxygen, hydrogen, nitrogen, cobalt and iodine atoms, respectively.

As shown in Figures 21a-21c, we provided the main geometrical parameters and the Mulliken charges on main atoms for stationary points along the reaction pathway of M-I-N⁺-NH-COF catalysing CO₂RR. The oxygen O₁ atom in CO₂ coordinates with Co atom in M-I-N⁺-NH-COF. The Co-O₁ bond is 2.734 Å and the charge transfer from M-I-N⁺-NH-COF to CO₂ is negligible because the total charge on CO₂ is nearly zero (Figure 21a). The formation of *COOH by the proton transfer makes the distortion of CO₂ portion with the angle of O₁-C-O₂ decreases from 178.6° to 121.7°, along with the elongation of C-O₂ bond to from 1.154 Å to 1.343 Å (Figure 21b). The shortened Co-C bond results a stronger charge transfer between M-I-N⁺-NH-COF and CO₂. The departure of *OH leads to the formation of *CO, where Co is of a vertical orientation with a Co-C-O bond angle of 168.1° (Figure 21c). As the same as M-I-N⁺-NH-COF, CO₂ was adsorbed with the coordination between Co and oxygen, while the intermediates of *COOH and *CO were coordinated with Co with the C atoms in the case of CoTAPP-PATA-COF calculations.

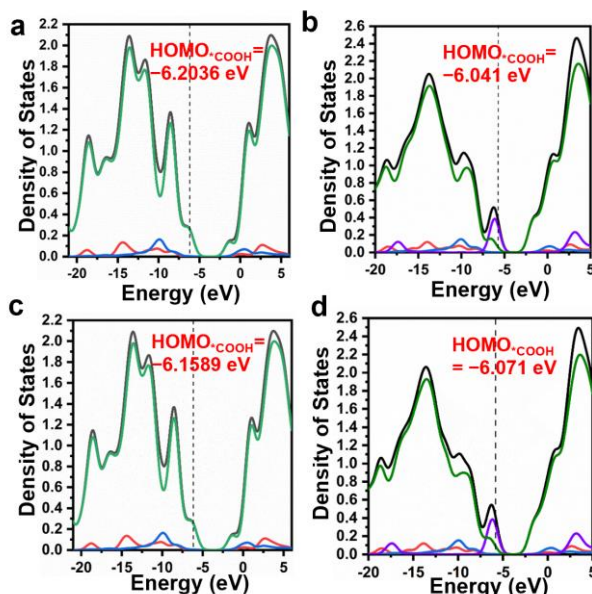


Figure 22. The TDOSs (black lines), PDOSs of Co (blue lines), COOH (red lines), remainder of COOH* (green lines) and counter ion I- (purple line) for (a) M-CoTAPP-PATA-COF, (b) M-I-N⁺-COF, (c) M-NH-COF and (d) M-I-N⁺-NH-COF catalysing CO₂RR.

Furthermore, in Figures 22a-22d, we listed the PDOSs of Co (blue lines), COOH (red lines) and remainder of *COOH (green lines) for adsorption state of COOH on M-CoTAPP-PATA-COF, M-I-N⁺-COF, M-NH-COF and M-I-N⁺-NH-COF. It could be found that the contribution of Co is larger in M-I-N⁺-COF and M-I-N⁺-NH-COF than in M-CoTAPP-PATA-COF and M-NH-COF, indicating that the introducing of methyl groups strengthens the electronic density on Co atom. This may promote the interaction between the Co and COOH portion during the reaction. All above calculated results are in consistent with the experimental observations.

8.3 Conclusion

In this chapter, a multilevel post-function strategy was first demonstrated to modulate the properties of COFs (porosity, crystallinity, and electron states), which can contribute to their tuneable catalytic performance for CO₂RR. By

constructing catalytic COFs with ionic and NH linkers, the catalytic COFs allow catalysing CO₂RR with high activity and a maximum TOF value of 9922.68 h⁻¹ at -1.0 V, and high selectivity with the highest FE_{CO} of 97.32% at -0.8 V. This work provides us a more in-depth understanding of COFs and their applications in electrochemical energy storage and conversion systems. Meanwhile, it also guides us to construct multilevel post-synthetic modification COFs for achieving both tailored activity and high stability.

Chapter 9. Conclusion and Perspectives

9.1 Summary of the thesis

This thesis focused on the design of novel functional COFs. Regulating skeleton activity, catalytic site density, building units, and dimensional topology witnessed these functional COFs being applied in the efficient electrocatalytic CO₂ and O₂ reduction reactions. In terms of structure characterization, we analysed the crystal structure of the synthesized COFs using PXRD patterns combined with the theoretical structure (*Materials Studio*). Then, we clarified the chemical and physical properties by N₂ adsorption, FT-IR, ¹³C NMR, and other characterization methods. We discussed the relationship between the structure and functional COFs based on the crystal structure and corresponding features and the electrocatalysis behaviours of these COF-based catalysts. These results and studies paved the way for the new design and synthesis of COF-based catalysts with high activity and selectivity and provided new insight into the energy conversion. The conclusions of this thesis include the following aspects: (1) In chapter 3, a core-shell bifunctional catalyst using COF derivatives for oxygen reduction and hydrogen evolution reactions have been demonstrated. The COF-shell prevent the collapse of the MOF-core in pyrolysis process. In addition, the core-shell morphology benefit mass transport, and the COF-derived shell facilitates electron conductivity. The catalyst had Co-N₄ atoms together with Co nanoparticles embedded in the carbon, which enable to catalyse ORR and HER with high activity and excellent stability. This work provides a new platform to design multifunctional catalysts from COFs.

(2) Owing to the Co-N₄ atoms together with Co nanoparticles belong to single metal catalyst, we consider constructing dual atomic catalyst to further improve the electrocatalysis performance. In chapter 4, we further developed a new synergetic dual atomic catalyst for CO₂RR using COF-derivatives. The

synergistic CoN₄O and ZnN₄ sites significantly improve the electron transport rate and the generation of COOH* intermediate, which is beneficial for the process of CO₂RR. The catalyst showed superior activity selectivity and long-term stability over many other electrocatalysts. Its maximum FE_{CO} and TOF values reached 92.6% at -0.8 V and 1370.24 h⁻¹ at -1.0 V, respectively. This work not only provided new insights for the preparation of carbon-supported bimetallic SACs but also offered a new method to develop catalytic carbons from COFs.

(3) The COF-derivatives cannot realize the precise control for the topology dimensions further promote us to explore the influence of COFs' topologies for the electrocatalysis performance. In chapter 5, we synthesized the 1D catalytic COF using four-connected pyrene based units and the non-linear phenanthroline building blocks to immobilize Fe ions, which showed much higher activity than that from the controlled 2D COF. The space between the chains were easily expanded easily owing to weaker interactions, resulting in more exposed catalytic sites. These findings highlight the advantages of 1D COFs as promising candidates for highly efficient OER catalysis and pave the way for future research in this field.

(4) Considering the synthesis strategy is important for COFs, we adopted natural units to construct COFs for exploring the potential development of structures. In chapter 6, we employed the natural building blocks to construct catalytic COFs for both ORR and CO₂RR. The incorporation of EA units introduced ladder-like conjugation within the frameworks, resulting in enhanced electronic conductivity. This EA-based COF exhibited remarkable catalytic activity, selectivity and stability in both ORR and CO₂RR. Theoretical calculations revealed that the EA linker facilitated the formation of intermediates in the catalytic process, enhancing the overall efficiency. Consequently, this study not only expands the repertoire of COFs but also provides a promising avenue for developing highly efficient energy storage and conversion systems.

(5) Except space dimensions and building blocks, the density of catalytic sites

in COFs to tune the catalytic behaviour for CO₂RR is ignored, because it is generally assumed that the more metals results in better catalytic activity. Thus, the correlation between the density of metal atoms and catalytic performances have not been explored. In chapter 7, a skeleton engineering strategy based on the multiple-component synthesis to construct the controllable metal density in the skeletons was first reported, which build the quantitative correlation between the metal density and catalytic performance. By establishing COFs with of vacancies and Ni-N sites, the 0.5NiPc-COF catalysed CO₂RR with high selectivity and activity (FE_{CO} of 95.37% at -0.8 V and TOF of 4713.53 h⁻¹ at -1.0 V). The design and modulation density of catalytic sites in COFs proposed not only new insights into electrocatalysis or energy conversion, but also guidance of constructing COFs with alternate structures of vacancies and metal sites for achieving high catalytic performance.

(6) The skeleton of COFs is also significant element for the chemical properties and electrocatalysis CO₂RR performance. Specifically, the amine-linkages enhance the binding ability of CO₂ molecules, and the ionic frameworks enable to improve the electronic conductivity and the charge transfer along the frameworks. However, directly synthesis of covalent organic frameworks with amine-linkages and ionic frameworks is hardly achieved due to the electrostatic repulsion and predicament for the strength of the linkage. In chapter 8, a multilevel post-function strategy was demonstrated to modulate the properties of COFs (porosity, crystallinity, and electron states), which can contribute to their tuneable catalytic performance for CO₂RR. By constructing catalytic COFs with ionic and NH linkers, the catalytic COFs allow catalysing CO₂RR with high activity and a maximum TOF value of 9922.68 h⁻¹ at -1.0 V, and high selectivity with the highest FE_{CO} of 97.32% at -0.8 V. This work guides us to construct multilevel post-synthetic modification COFs for achieving both tailored activity and high stability.

9.2 Outlook and Feature work

COFs, as a new kind of crystalline organic porous material, have highly ordered organic structural units and multilevel pores in the structures, which could be assembled into a variety of structures by designing and synthesizing different building blocks to achieve applications in various fields, including gas / molecular adsorption, sensor, energy conversion, and storage. Thus, these features provide a new chance for COFs to play an essential role in electrocatalytic reactions and energy conversions:

(1) Its ordered porous structures make COFs have a large theoretical specific surface area, resulting in a higher volume density of active sites and the accessibility of substrates, further having a unique advantage in electrocatalysis reactions.

(2) The well-designed functional COFs can be applied in various electrocatalytic reactions.

(3) Compared with the structure of other frameworks (i.e., MOFs and zeolites), COFs are connected through stable covalent bonds; thus, the application has higher environmental tolerance under harsh electrocatalytic conditions.

(4) COF is highly modifiable. Given the high stability and crystallinity, COFs can be modified or loaded with other functional groups and materials, such as inorganic semiconductors and co-catalysts (i.e., carbon black and MoS₂), through strong covalent bonds. While ensuring the stability of this heterogeneous composite material, it can also combine the advantages of these materials to achieve synergistic effects, such as electron transfer, substrate adsorption, and activation in electrocatalysis. However, although COFs have been found to have these advantages as mentioned above, there are still many problems in practical application, and the problems in the field of catalytic reduction are mainly reflected in the following aspects:

(1) Porous materials' order degree (crystallinity) is closely related to their catalytic performance. Owing to the crystallinity of COF is challenging to

improve by current conventional synthesis methods, the purity of its crystal phase is low, and the specific surface area of most COF is lower than theoretical values, thus failing to realize its potential in small molecule catalysis. However, an effective strategy is needed to improve the crystallinity of COFs. In addition, how to obtain two-dimensional and three-dimensional COF with large single crystals is still the direction of future efforts.

(2) The organic building blocks with high performance need to be developed; meanwhile, assembling these units into the framework is expected to play an essential role in the electrocatalysis reactions. It has been reported that many homogeneous molecular catalysts have been successfully used in high-efficiency catalytic reactions, and the assembly of COFs based on these molecular catalysts will be an effective method to solve the above problems.

(3) The utilization of active sites should be improved. Many studies confirmed that metal atoms are significant for catalytic performance. Therefore, improving the catalytic density of sites and combining frameworks with active metal sites are essential for enhancing catalytic activity. Thus, controlling active sites should be a direction of future development.

(4) In the catalytic CO₂ reduction reaction field, it has yet to be reported that COF-based catalysts successfully translate CO₂ to multi-carbon products (C₂⁺, such as methanol). Therefore, exploring the electron transfer behaviours in the functional COFs is an important direction.

(5) At present, the preparation of COFs is mainly based on powder and lab-grade membranes, while the large-scale production and device processing of COF are rarely reported. Hence, controlling the form of COF in other ways, such as cross-linked polymerization or base load, is also a problem that needs attention in this field.

In summary, the chemical and physics features of COFs, such as crystallinity, structural stability, large specific surface area, porosity, and structural designability, make COFs essential in small molecule catalysis, such as oxygen and carbon dioxide.

Reference

1. Stock, N.; Biswas, S., Synthesis of Metal-Organic Frameworks (MOFs): Routes to Various MOF Topologies, Morphologies, and Composites. *Chem. Rev.* **2012**, *112*, 933-969.
2. Wu, D.; Xu, F.; Sun, B.; Fu, R.; He, H.; Matyjaszewski, K., Design and Preparation of Porous Polymers. *Chem. Rev.* **2012**, *112*, 3959-4015.
3. Das, S.; Heasman, P.; Ben, T.; Qiu, S., Porous Organic Materials: Strategic Design and Structure–Function Correlation. *Chem. Rev.* **2017**, *117*, 1515-1563.
4. Slater, A. G.; Cooper, A. I., Function-led design of new porous materials. *Science* **2015**, *348*, aaa8075.
5. Waller, P. J.; Gándara, F.; Yaghi, O. M., Chemistry of Covalent Organic Frameworks. *Acc. Chem. Res.* **2015**, *48*, 3053-3063.
6. Diercks, C. S.; Yaghi, O. M., The atom, the molecule, and the covalent organic framework. *Science* **2017**, *355*, eaal1585.
7. Furukawa, H.; Yaghi, O. M., Storage of Hydrogen, Methane, and Carbon Dioxide in Highly Porous Covalent Organic Frameworks for Clean Energy Applications. *J. Am. Chem. Soc.* **2009**, *131*, 8875-8883.
8. Xu, Y.; Jin, S.; Xu, H.; Nagai, A.; Jiang, D., Conjugated microporous polymers: design, synthesis and application. *Chem. Soc. Rev.* **2013**, *42*, 8012-8031.
9. Jin, Y.; Wang, Q.; Taynton, P.; Zhang, W., Dynamic Covalent Chemistry Approaches Toward Macrocycles, Molecular Cages, and Polymers. *Acc. Chem. Res.* **2014**, *47*, 1575-1586.
10. Côté, A. P.; El-Kaderi, H. M.; Furukawa, H.; Hunt, J. R.; Yaghi, O. M., Reticular Synthesis of Microporous and Mesoporous 2D Covalent Organic Frameworks. *J. Am. Chem. Soc.* **2007**, *129*, 12914-12915.
11. Côté, A. P.; Benin, A. I.; Ockwig, N. W.; O'Keeffe, M.; Matzger, A. J.; Yaghi, O. M., Porous, Crystalline, Covalent Organic Frameworks. *Science* **2005**, *310*,

1166-1170.

12. Du, Y.; Yang, H.; Whiteley, J. M.; Wan, S.; Jin, Y.; Lee, S.-H.; Zhang, W., Ionic Covalent Organic Frameworks with Spiroborate Linkage. *Angew. Chem. Int. Ed.* **2016**, *55*, 1737-1741.

13. Chen, X.; Addicoat, M.; Irle, S.; Nagai, A.; Jiang, D., Control of Crystallinity and Porosity of Covalent Organic Frameworks by Managing Interlayer Interactions Based on Self-Complementary π -Electronic Force. *J. Am. Chem. Soc.* **2013**, *135*, 546-549.

14. Uribe-Romo, F. J.; Doonan, C. J.; Furukawa, H.; Oisaki, K.; Yaghi, O. M., Crystalline Covalent Organic Frameworks with Hydrazone Linkages. *J. Am. Chem. Soc.* **2011**, *133*, 11478-11481.

15. Dalapati, S.; Jin, S.; Gao, J.; Xu, Y.; Nagai, A.; Jiang, D., An Azine-Linked Covalent Organic Framework. *J. Am. Chem. Soc.* **2013**, *135*, 17310-17313.

16. Guo, J.; Xu, Y.; Jin, S.; Chen, L.; Kaji, T.; Honsho, Y.; Addicoat, M. A.; Kim, J.; Saeki, A.; Ihee, H.; Seki, S.; Irle, S.; Hiramoto, M.; Gao, J.; Jiang, D., Conjugated organic framework with three-dimensionally ordered stable structure and delocalized π clouds. *Nat. Commun.* **2013**, *4*, 2736.

17. Zhao, W.; Yu, C.; Zhao, J.; Chen, F.; Guan, X.; Li, H.; Tang, B.; Yu, G.; Valtchev, V.; Yan, Y.; Qiu, S.; Fang, Q., 3D Hydrazone-Functionalized Covalent Organic Frameworks as pH-Triggered Rotary Switches. *Small* **2021**, *17*, 2102630.

18. Fang, Q.; Zhuang, Z.; Gu, S.; Kaspar, R. B.; Zheng, J.; Wang, J.; Qiu, S.; Yan, Y., Designed synthesis of large-pore crystalline polyimide covalent organic frameworks. *Nat. Commun.* **2014**, *5*, 4503.

19. Kuhn, P.; Antonietti, M.; Thomas, A., Porous, Covalent Triazine-Based Frameworks Prepared by Ionothermal Synthesis. *Angew. Chem. Int. Ed.* **2008**, *47*, 3450-3453.

20. Jackson, K. T.; Reich, T. E.; El-Kaderi, H. M., Targeted synthesis of a porous borazine-linked covalent organic framework. *Chem. Commun.* **2012**, *48*, 8823-8825.

Reference

21. Chen, X.; Addicoat, M.; Jin, E.; Xu, H.; Hayashi, T.; Xu, F.; Huang, N.; Irle, S.; Jiang, D., Designed synthesis of double-stage two-dimensional covalent organic frameworks. *Sci. Rep.* **2015**, *5*, 14650.
22. Spitler, E. L.; Giovino, M. R.; White, S. L.; Dichtel, W. R., A mechanistic study of Lewis acid-catalyzed covalent organic framework formation. *Chem. Sci.* **2011**, *2*, 1588-1593.
23. Lanni, L. M.; Tilford, R. W.; Bharathy, M.; Lavigne, J. J., Enhanced Hydrolytic Stability of Self-Assembling Alkylated Two-Dimensional Covalent Organic Frameworks. *J. Am. Chem. Soc.* **2011**, *133*, 13975-13983.
24. Xu, H.; Gao, J.; Jiang, D., Stable, crystalline, porous, covalent organic frameworks as a platform for chiral organocatalysts. *Nat. Chem.* **2015**, *7*, 905-912.
25. Jin, E.; Asada, M.; Xu, Q.; Dalapati, S.; Addicoat, M. A.; Brady, M. A.; Xu, H.; Nakamura, T.; Heine, T.; Chen, Q.; Jiang, D., Two-dimensional sp² carbon-conjugated covalent organic frameworks. *Science* **2017**, *357*, 673-676.
26. Zhang, B.; Wei, M.; Mao, H.; Pei, X.; Alshmiri, S. A.; Reimer, J. A.; Yaghi, O. M., Crystalline Dioxin-Linked Covalent Organic Frameworks from Irreversible Reactions. *J. Am. Chem. Soc.* **2018**, *140*, 12715-12719.
27. Yue, Y.; Cai, P.; Xu, K.; Li, H.; Chen, H.; Zhou, H.-C.; Huang, N., Stable Bimetallic Polyphthalocyanine Covalent Organic Frameworks as Superior Electrocatalysts. *J. Am. Chem. Soc.* **2021**, *143*, 18052-18060.
28. Xu, H.-S.; Luo, Y.; Li, X.; See, P. Z.; Chen, Z.; Ma, T.; Liang, L.; Leng, K.; Abdelwahab, I.; Wang, L.; Li, R.; Shi, X.; Zhou, Y.; Lu, X. F.; Zhao, X.; Liu, C.; Sun, J.; Loh, K. P., Single crystal of a one-dimensional metallo-covalent organic framework. *Nat. Commun.* **2020**, *11*, 1434.
29. Nguyen, H. L.; Gropp, C.; Yaghi, O. M., Reticulating 1D Ribbons into 2D Covalent Organic Frameworks by Imine and Imide Linkages. *J. Am. Chem. Soc.* **2020**, *142*, 2771-2776.
30. An, S.; Li, X.; Shang, S.; Xu, T.; Yang, S.; Cui, C.-X.; Peng, C.; Liu, H.; Xu, Q.; Jiang, Z.; Hu, J., One-Dimensional Covalent Organic Frameworks for the

Reference

- 2e⁻ Oxygen Reduction Reaction. *Angew. Chem. Int. Ed.* **2023**, *62*, e202218742.
31. Zhao, Y.; Feng, K.; Yu, Y., A Review on Covalent Organic Frameworks as Artificial Interface Layers for Li and Zn Metal Anodes in Rechargeable Batteries. *Adv. Sci.* **2023**, 2308087. DOI: 10.1002/advs.202308087.
32. Ding, X.; Guo, J.; Feng, X.; Honsho, Y.; Guo, J.; Seki, S.; Maitrad, P.; Saeki, A.; Nagase, S.; Jiang, D., Synthesis of Metallophthalocyanine Covalent Organic Frameworks That Exhibit High Carrier Mobility and Photoconductivity. *Angew. Chem. Int. Ed.* **2011**, *50*, 1289-1293.
33. Xie, Y.; Li, J.; Lin, C.; Gui, B.; Ji, C.; Yuan, D.; Sun, J.; Wang, C., Tuning the Topology of Three-Dimensional Covalent Organic Frameworks via Steric Control: From pts to Unprecedented ljh. *J. Am. Chem. Soc.* **2021**, *143*, 7279-7284.
34. Wang, S.; Li, X.-X.; Da, L.; Wang, Y.; Xiang, Z.; Wang, W.; Zhang, Y.-B.; Cao, D., A Three-Dimensional sp² Carbon-Conjugated Covalent Organic Framework. *J. Am. Chem. Soc.* **2021**, *143*, 15562-15566.
35. Uribe-Romo, F. J.; Hunt, J. R.; Furukawa, H.; Klöck, C.; O'Keeffe, M.; Yaghi, O. M., A Crystalline Imine-Linked 3D Porous Covalent Organic Framework. *J. Am. Chem. Soc.* **2009**, *131*, 4570-4571.
36. Ma, T.; Kapustin, E. A.; Yin, S. X.; Liang, L.; Zhou, Z.; Niu, J.; Li, L.-H.; Wang, Y.; Su, J.; Li, J.; Wang, X.; Wang, W. D.; Wang, W.; Sun, J.; Yaghi, O. M., Single-crystal x-ray diffraction structures of covalent organic frameworks. *Science* **2018**, *361*, 48-52.
37. Xu, L.; Ding, S.-Y.; Liu, J.; Sun, J.; Wang, W.; Zheng, Q.-Y., Highly crystalline covalent organic frameworks from flexible building blocks. *Chem. Commun.* **2016**, *52*, 4706-4709.
38. Campbell, N. L.; Clowes, R.; Ritchie, L. K.; Cooper, A. I., Rapid Microwave Synthesis and Purification of Porous Covalent Organic Frameworks. *Chem. Mater.* **2009**, *21*, 204-206.
39. Ritchie, L. K.; Trewin, A.; Reguera-Galan, A.; Hasell, T.; Cooper, A. I., Synthesis of COF-5 using microwave irradiation and conventional solvothermal

Reference

- routes. *Microporous Mesoporous Mater.* **2010**, *132*, 132-136.
40. Wei, H.; Chai, S.; Hu, N.; Yang, Z.; Wei, L.; Wang, L., The microwave-assisted solvothermal synthesis of a crystalline two-dimensional covalent organic framework with high CO₂ capacity. *Chem. Commun.* **2015**, *51*, 12178-12181.
41. Ren, S.; Bojdys, M. J.; Dawson, R.; Laybourn, A.; Khimyak, Y. Z.; Adams, D. J.; Cooper, A. I., Porous, Fluorescent, Covalent Triazine-Based Frameworks Via Room-Temperature and Microwave-Assisted Synthesis. *Adv. Mater.* **2012**, *24*, 2357-2361.
42. Bojdys, M. J.; Jeromenok, J.; Thomas, A.; Antonietti, M., Rational Extension of the Family of Layered, Covalent, Triazine-Based Frameworks with Regular Porosity. *Adv. Mater.* **2010**, *22*, 2202-2205.
43. Ding, X.; Chen, L.; Honsho, Y.; Feng, X.; Saengsawang, O.; Guo, J.; Saeki, A.; Seki, S.; Irle, S.; Nagase, S.; Parasuk, V.; Jiang, D., An n-Channel Two-Dimensional Covalent Organic Framework. *J. Am. Chem. Soc.* **2011**, *133*, 14510-14513.
44. Huang, N.; Zhai, L.; Xu, H.; Jiang, D., Stable Covalent Organic Frameworks for Exceptional Mercury Removal from Aqueous Solutions. *J. Am. Chem. Soc.* **2017**, *139*, 2428-2434.
45. Sun, Q.; Aguila, B.; Perman, J.; Earl, L. D.; Abney, C. W.; Cheng, Y.; Wei, H.; Nguyen, N.; Wojtas, L.; Ma, S., Postsynthetically Modified Covalent Organic Frameworks for Efficient and Effective Mercury Removal. *J. Am. Chem. Soc.* **2017**, *139*, 2786-2793.
46. Zhou, W.; Yang, L.; Wang, X.; Zhao, W.; Yang, J.; Zhai, D.; Sun, L.; Deng, W., In Silico Design of Covalent Organic Framework-Based Electrocatalysts. *JACS Au* **2021**, *1*, 1497-1505.
47. Li, X.; Yang, S.; Liu, M.; Yang, X.; Xu, Q.; Zeng, G.; Jiang, Z., Catalytic Linkage Engineering of Covalent Organic Frameworks for the Oxygen Reduction Reaction. *Angew. Chem. Int. Ed.* **2023**, *62*, e202304356.
48. Zhang, H.; Zhu, M.; Schmidt, O. G.; Chen, S.; Zhang, K., Covalent Organic

Reference

- Frameworks for Efficient Energy Electrocatalysis: Rational Design and Progress. *Adv. Energy Sustainability Res.* **2021**, *2*, 2000090.
49. Wang, Y.-R.; Ding, H.-M.; Ma, X.-Y.; Liu, M.; Yang, Y.-L.; Chen, Y.; Li, S.-L.; Lan, Y.-Q., Imparting CO₂ Electroreduction Auxiliary for Integrated Morphology Tuning and Performance Boosting in a Porphyrin-based Covalent Organic Framework. *Angew. Chem. Int. Ed.* **2022**, *61*, e202114648.
50. Wang, J.; Zhao, C.-X.; Liu, J.-N.; Song, Y.-W.; Huang, J.-Q.; Li, B.-Q., Dual-atom catalysts for oxygen electrocatalysis. *Nano Energy* **2022**, *104*, 107927.
51. Zhao, Y.; Adiyeri Saseendran, D. P.; Huang, C.; Triana, C. A.; Marks, W. R.; Chen, H.; Zhao, H.; Patzke, G. R., Oxygen Evolution/Reduction Reaction Catalysts: From In Situ Monitoring and Reaction Mechanisms to Rational Design. *Chem. Rev.* **2023**, *123*, 6257-6358.
52. Ge, X.; Sumboja, A.; Wu, D.; An, T.; Li, B.; Goh, F. W. T.; Hor, T. S. A.; Zong, Y.; Liu, Z., Oxygen Reduction in Alkaline Media: From Mechanisms to Recent Advances of Catalysts. *ACS Catal.* **2015**, *5*, 4643-4667.
53. Dai, L.; Xue, Y.; Qu, L.; Choi, H.-J.; Baek, J.-B., Metal-Free Catalysts for Oxygen Reduction Reaction. *Chem. Rev.* **2015**, *115*, 4823-4892.
54. Chandra, S.; Kundu, T.; Kandambeth, S.; BabaRao, R.; Marathe, Y.; Kunjir, S. M.; Banerjee, R., Phosphoric Acid Loaded Azo (-N=N-) Based Covalent Organic Framework for Proton Conduction. *J. Am. Chem. Soc.* **2014**, *136*, 6570-6573.
55. Liu, M.; Xiao, X.; Li, Q.; Luo, L.; Ding, M.; Zhang, B.; Li, Y.; Zou, J.; Jiang, B., Recent progress of electrocatalysts for oxygen reduction in fuel cells. *J. Colloid Interface Sci.* **2022**, *607*, 791-815.
56. Ding, Y.; Zhou, W.; Gao, J.; Sun, F.; Zhao, G., H₂O₂ Electrogenation from O₂ Electroreduction by N-Doped Carbon Materials: A Mini-Review on Preparation Methods, Selectivity of N Sites, and Prospects. *Adv. Mater. Interfaces* **2021**, *8*, 2002091.
57. He, H.; Liu, S.; Liu, Y.; Zhou, L.; Wen, H.; Shen, R.; Zhang, H.; Guo, X.; Jiang, J.; Li, B., Review and perspectives on carbon-based electrocatalysts for

Reference

the production of H₂O₂ via two-electron oxygen reduction. *Green Chem.* **2023**, *25*, 9501-9542.

58. Li, X.; Yang, S.; Xu, Q., Metal-Free Covalent Organic Frameworks for the Oxygen Reduction Reaction. *Chem. -Eur. J.* **2023**, e202302997, DOI: 10.1002/chem.202302997.

59. Zuo, Q.; Cheng, G.; Luo, W., A reduced graphene oxide/covalent cobalt porphyrin framework for efficient oxygen reduction reaction. *Dalton Trans.* **2017**, *46*, 9344-9348.

60. Yue, J.-Y.; Wang, Y.-T.; Wu, X.; Yang, P.; Ma, Y.; Liu, X.-H.; Tang, B., Two-dimensional porphyrin covalent organic frameworks with tunable catalytic active sites for the oxygen reduction reaction. *Chem. Commun.* **2021**, *57*, 12619-12622.

61. Liu, M.; Liu, S.; Cui, C.-X.; Miao, Q.; He, Y.; Li, X.; Xu, Q.; Zeng, G., Construction of Catalytic Covalent Organic Frameworks with Redox-Active Sites for the Oxygen Reduction and the Oxygen Evolution Reaction. *Angew. Chem. Int. Ed.* **2022**, *61*, e202213522.

62. Liu, M.; Yang, S.; Liu, S.; Miao, Q.; Yang, X.; Li, X.; Xu, Q.; Zeng, G., Construction of Atomic Metal-N₂ Sites by Interlayers of Covalent Organic Frameworks for Electrochemical H₂O₂ Synthesis. *Small* **2022**, *18*, 2204757.

63. Li, D.; Li, C.; Zhang, L.; Li, H.; Zhu, L.; Yang, D.; Fang, Q.; Qiu, S.; Yao, X., Metal-Free Thiophene-Sulfur Covalent Organic Frameworks: Precise and Controllable Synthesis of Catalytic Active Sites for Oxygen Reduction. *J. Am. Chem. Soc.* **2020**, *142*, 8104-8108.

64. Bao, R.; Xiang, Z.; Qiao, Z.; Yang, Y.; Zhang, Y.; Cao, D.; Wang, S., Designing Thiophene-Enriched Fully Conjugated 3D Covalent Organic Framework as Metal-Free Oxygen Reduction Catalyst for Hydrogen Fuel Cells. *Angew. Chem. Int. Ed.* **2023**, *62*, e202216751.

65. Yan, X.; Wang, B.; Ren, J.; Long, X.; Yang, D., An Unsaturated Bond Strategy to Regulate Active Centers of Metal-Free Covalent Organic Frameworks for Efficient Oxygen Reduction. *Angew. Chem. Int. Ed.* **2022**, *61*,

e202209583.

66. You, Z.; Wang, B.; Zhao, Z.; Zhang, Q.; Song, W.; Zhang, C.; Long, X.; Xia, Y., Metal-Free Carbon-Based Covalent Organic Frameworks with Heteroatom-Free Units Boost Efficient Oxygen Reduction. *Adv. Mater.* **2023**, *35*, 2209129.
67. Hao, S.; Sheng, H.; Liu, M.; Huang, J.; Zheng, G.; Zhang, F.; Liu, X.; Su, Z.; Hu, J.; Qian, Y.; Zhou, L.; He, Y.; Song, B.; Lei, L.; Zhang, X.; Jin, S., Torsion strained iridium oxide for efficient acidic water oxidation in proton exchange membrane electrolyzers. *Nat. Nanotechnol.* **2021**, *16*, 1371-1377.
68. Song, J.; Wei, C.; Huang, Z.-F.; Liu, C.; Zeng, L.; Wang, X.; Xu, Z. J., A review on fundamentals for designing oxygen evolution electrocatalysts. *Chem. Soc. Rev.* **2020**, *49*, 2196-2214.
69. Aiyappa, H. B.; Thote, J.; Shinde, D. B.; Banerjee, R.; Kurungot, S., Cobalt-Modified Covalent Organic Framework as a Robust Water Oxidation Electrocatalyst. *Chem. Mater.* **2016**, *28*, 4375-4379.
70. Zhao, X.; Pachfule, P.; Li, S.; Langenhahn, T.; Ye, M.; Schlesiger, C.; Praetz, S.; Schmidt, J.; Thomas, A., Macro/Microporous Covalent Organic Frameworks for Efficient Electrocatalysis. *J. Am. Chem. Soc.* **2019**, *141*, 6623-6630.
71. Lai, W.; Qiao, Y.; Zhang, J.; Lin, Z.; Huang, H., Design strategies for markedly enhancing energy efficiency in the electrocatalytic CO₂ reduction reaction. *Energy Environ. Sci.* **2022**, *15*, 3603-3629.
72. Chen, C.; Li, Y.; Yang, P., Address the “alkalinity problem” in CO₂ electrolysis with catalyst design and translation. *Joule* **2021**, *5*, 737-742.
73. Kibria, M. G.; Edwards, J. P.; Gabardo, C. M.; Dinh, C.-T.; Seifitokaldani, A.; Sinton, D.; Sargent, E. H., Electrochemical CO₂ Reduction into Chemical Feedstocks: From Mechanistic Electrocatalysis Models to System Design. *Adv. Mater.* **2019**, *31*, 1807166.
74. Huang, X.; Zhang, Y.-B., Reticular materials for electrochemical reduction of CO₂. *Coord. Chem. Rev.* **2021**, *427*, 213564.
75. Lin, S.; Diercks, C. S.; Zhang, Y.-B.; Kornienko, N.; Nichols, E. M.; Zhao, Y.; Paris, A. R.; Kim, D.; Yang, P.; Yaghi, O. M.; Chang, C. J., Covalent organic

Reference

- frameworks comprising cobalt porphyrins for catalytic CO₂ reduction in water. *Science* **2015**, *349*, 1208-1213.
76. Diercks, C. S.; Lin, S.; Kornienko, N.; Kapustin, E. A.; Nichols, E. M.; Zhu, C.; Zhao, Y.; Chang, C. J.; Yaghi, O. M., Reticular Electronic Tuning of Porphyrin Active Sites in Covalent Organic Frameworks for Electrocatalytic Carbon Dioxide Reduction. *J. Am. Chem. Soc.* **2018**, *140*, 1116-1122.
77. Liu, H.; Chu, J.; Yin, Z.; Cai, X.; Zhuang, L.; Deng, H., Covalent Organic Frameworks Linked by Amine Bonding for Concerted Electrochemical Reduction of CO₂. *Chem* **2018**, *4*, 1696-1709.
78. Cheung, P. L.; Lee, S. K.; Kubiak, C. P., Facile Solvent-Free Synthesis of Thin Iron Porphyrin COFs on Carbon Cloth Electrodes for CO₂ Reduction. *Chem. Mater.* **2019**, *31*, 1908-1919.
79. Lu, Y.; Zhang, J.; Wei, W.; Ma, D.-D.; Wu, X.-T.; Zhu, Q.-L., Efficient Carbon Dioxide Electroreduction over Ultrathin Covalent Organic Framework Nanolayers with Isolated Cobalt Porphyrin Units. *ACS Appl. Mater. Interfaces* **2020**, *12*, 37986-37992.
80. Wu, Q.; Mao, M.-J.; Wu, Q.-J.; Liang, J.; Huang, Y.-B.; Cao, R., Construction of Donor–Acceptor Heterojunctions in Covalent Organic Framework for Enhanced CO₂ Electroreduction. *Small* **2021**, *17*, 2004933.
81. Zhang, M.-D.; Si, D.-H.; Yi, J.-D.; Zhao, S.-S.; Huang, Y.-B.; Cao, R., Conductive Phthalocyanine-Based Covalent Organic Framework for Highly Efficient Electroreduction of Carbon Dioxide. *Small* **2020**, *16*, 2005254.
82. Huang, N.; Lee, K. H.; Yue, Y.; Xu, X.; Irlle, S.; Jiang, Q.; Jiang, D., A Stable and Conductive Metallophthalocyanine Framework for Electrocatalytic Carbon Dioxide Reduction in Water. *Angew. Chem. Int. Ed.* **2020**, *59*, 16587-16593.
83. Han, B.; Jin, Y.; Chen, B.; Zhou, W.; Yu, B.; Wei, C.; Wang, H.; Wang, K.; Chen, Y.; Chen, B.; Jiang, J., Maximizing Electroactive Sites in a Three-Dimensional Covalent Organic Framework for Significantly Improved Carbon Dioxide Reduction Electrocatalysis. *Angew. Chem. Int. Ed.* **2022**, *61*, e202114244.

Reference

84. Ma, W.; Yu, P.; Ohsaka, T.; Mao, L., An efficient electrocatalyst for oxygen reduction reaction derived from a Co-porphyrin-based covalent organic framework. *Electrochem. Commun.* **2015**, *52*, 53-57.
85. Zhuang, X.; Zhao, W.; Zhang, F.; Cao, Y.; Liu, F.; Bi, S.; Feng, X., A two-dimensional conjugated polymer framework with fully sp²-bonded carbon skeleton. *Polym. Chem.* **2016**, *7*, 4176-4181.
86. Xu, Q.; Zhang, H.; Guo, Y.; Qian, J.; Yang, S.; Luo, D.; Gao, P.; Wu, D.; Li, X.; Jiang, Z.; Sun, Y., Standing Carbon-Supported Trace Levels of Metal Derived from Covalent Organic Framework for Electrocatalysis. *Small* **2019**, *15*, 1905363.
87. Yang, S.; Li, X.; Tan, T.; Mao, J.; Xu, Q.; Liu, M.; Miao, Q.; Mei, B.; Qiao, P.; Gu, S.; Sun, F.; Ma, J.; Zeng, G.; Jiang, Z., A fully-conjugated covalent organic framework-derived carbon supporting ultra-close single atom sites for ORR. *Appl. Catal., B* **2022**, *307*, 121147.
88. Li, X.; Yang, S.; Liu, M.; Liu, S.; Miao, Q.; Duan, Z.; Qiao, P.; Lin, J.; Sun, F.; Xu, Q.; Jiang, Z., Immobilization of Platinum Nanoparticles on Covalent Organic Framework-Derived Carbon for Oxygen Reduction Catalysis. *Small Struct.* **2023**, *4*, 2200320.
89. Miao, Q.; Chen, Z.; Li, X.; Liu, M.; Liu, G.; Yang, X.; Guo, Z.; Yu, C.; Xu, Q.; Zeng, G., Construction of Catalytic Fe₂N₅P Sites in Covalent Organic Framework-Derived Carbon for Catalyzing the Oxygen Reduction Reaction. *ACS Catal.* **2023**, *13*, 11127-11135.
90. Gao, J.; Liu, B., Progress of Electrochemical Hydrogen Peroxide Synthesis over Single Atom Catalysts. *ACS Mater. Lett.* **2020**, *2*, 1008-1024.
91. Hannagan, R. T.; Giannakakis, G.; Flytzani-Stephanopoulos, M.; Sykes, E. C. H., Single-Atom Alloy Catalysis. *Chem. Rev.* **2020**, *120*, 12044-12088.
92. Solomon, E. I.; Stahl, S. S., Introduction: Oxygen Reduction and Activation in Catalysis. *Chem. Rev.* **2018**, *118*, 2299-2301.
93. Wang, Y.; Su, H.; He, Y.; Li, L.; Zhu, S.; Shen, H.; Xie, P.; Fu, X.; Zhou, G.; Feng, C.; Zhao, D.; Xiao, F.; Zhu, X.; Zeng, Y.; Shao, M.; Chen, S.; Wu, G.;

Reference

- Zeng, J.; Wang, C., Advanced Electrocatalysts with Single-Metal-Atom Active Sites. *Chem. Rev.* **2020**, *120*, 12217-12314.
94. Jin, Z.; Li, P.; Meng, Y.; Fang, Z.; Xiao, D.; Yu, G., Understanding the inter-site distance effect in single-atom catalysts for oxygen electroreduction. *Nat. Catal.* **2021**, *4*, 615-622.
95. Li, J.; Alsudairi, A.; Ma, Z.-F.; Mukerjee, S.; Jia, Q., Asymmetric Volcano Trend in Oxygen Reduction Activity of Pt and Non-Pt Catalysts: In Situ Identification of the Site-Blocking Effect. *J. Am. Chem. Soc.* **2017**, *139*, 1384-1387.
96. Liu, Z.; Zhao, Z.; Peng, B.; Duan, X.; Huang, Y., Beyond Extended Surfaces: Understanding the Oxygen Reduction Reaction on Nanocatalysts. *J. Am. Chem. Soc.* **2020**, *142*, 17812-17827.
97. Chia, X.; Pumera, M., Characteristics and performance of two-dimensional materials for electrocatalysis. *Nat. Catal.* **2018**, *1*, 909-921.
98. Gao, R.; Yan, D., Recent Development of Ni/Fe-Based Micro/Nanostructures toward Photo/Electrochemical Water Oxidation. *Adv. Funct. Mater.* **2020**, *10*, 1900954.
99. Li, H.; Kelly, S.; Guevarra, D.; Wang, Z.; Wang, Y.; Haber, J. A.; Anand, M.; Gunasooriya, G. T. K. K.; Abraham, C. S.; Vijay, S.; Gregoire, J. M.; Nørskov, J. K., Analysis of the limitations in the oxygen reduction activity of transition metal oxide surfaces. *Nat. Catal.* **2021**, *4*, 463-468.
100. Askins, E. J.; Zoric, M. R.; Li, M.; Luo, Z.; Amine, K.; Glusac, K. D., Toward a mechanistic understanding of electrocatalytic nanocarbon. *Nat. Commun.* **2021**, *12*, 3288.
101. Dey, S.; Mondal, B.; Chatterjee, S.; Rana, A.; Amanullah, S. K.; Dey, A., Molecular electrocatalysts for the oxygen reduction reaction. *Nat. Rev. Chem.* **2017**, *1*, 0098.
102. Douka, A. I.; Xu, Y.; Yang, H.; Zaman, S.; Yan, Y.; Liu, H.; Salam, M. A.; Xia, B. Y., A Zeolitic-Imidazole Frameworks-Derived Interconnected Macroporous Carbon Matrix for Efficient Oxygen Electrocatalysis in

Reference

- Rechargeable Zinc-Air Batteries. *Adv. Mater.* **2020**, *32*, e2002170.
103. He, T.; Geng, K.; Jiang, D., Engineering Covalent Organic Frameworks for Light-Driven Hydrogen Production from Water. *ACS Mater. Lett.* **2019**, *1*, 203-208.
104. Li, Z.; He, T.; Gong, Y.; Jiang, D., Covalent Organic Frameworks: Pore Design and Interface Engineering. *Acc. Chem. Res.* **2020**, *53*, 1672-1685.
105. Wei, S.; Zhang, F.; Zhang, W.; Qiang, P.; Yu, K.; Fu, X.; Wu, D.; Bi, S.; Zhang, F., Semiconducting 2D Triazine-Cored Covalent Organic Frameworks with Unsubstituted Olefin Linkages. *J. Am. Chem. Soc.* **2019**, *141*, 14272-14279.
106. Xu, Q.; Tang, Y.; Zhai, L.; Chen, Q.; Jiang, D., Pyrolysis of covalent organic frameworks: a general strategy for template converting conventional skeletons into conducting microporous carbons for high-performance energy storage. *Chem. Commun.* **2017**, *53*, 11690-11693.
107. Dutta, S.; Kumari, N.; Dubbu, S.; Jang, S. W.; Kumar, A.; Ohtsu, H.; Kim, J.; Cho, S. H.; Kawano, M.; Lee, I. S., Highly Mesoporous Metal-Organic Frameworks as Synergistic Multimodal Catalytic Platforms for Divergent Cascade Reactions. *Angew. Chem. Int. Ed.* **2020**, *59*, 3416-3422.
108. Biswal, B. P.; Valligatla, S.; Wang, M.; Banerjee, T.; Saad, N. A.; Mariserla, B. M. K.; Chandrasekhar, N.; Becker, D.; Addicoat, M.; Senkovska, I.; Berger, R.; Rao, D. N.; Kaskel, S.; Feng, X., Nonlinear Optical Switching in Regioregular Porphyrin Covalent Organic Frameworks. *Angew. Chem. Int. Ed.* **2019**, *58*, 6896-6900.
109. Hou, C.-C.; Wang, Y.; Zou, L.; Wang, M.; Liu, H.; Liu, Z.; Wang, H.-F.; Li, C.; Xu, Q., A Gas-Steamed MOF Route to P-Doped Open Carbon Cages with Enhanced Zn-Ion Energy Storage Capability and Ultrastability. *Adv. Mater.* **2021**, *33*, 2101698.
110. Lv, Q.; Si, W.; He, J.; Sun, L.; Zhang, C.; Wang, N.; Yang, Z.; Li, X.; Wang, X.; Deng, W.; Long, Y.; Huang, C.; Li, Y., Selectively nitrogen-doped carbon materials as superior metal-free catalysts for oxygen reduction. *Nat. Commun.* **2018**, *9*, 3376.

Reference

111. Zhu, Z.; Xu, Y.; Qi, B.; Zeng, G.; Wu, P.; Liu, G.; Wang, W.; Cui, F.; Sun, Y., Adsorption-intensified degradation of organic pollutants over bifunctional α -Fe@carbon nanofibres. *Environ. Sci.: Nano* **2017**, *4*, 302-306.
112. Zhang, Y.; Liu, G.; Shi, L.; Wu, P.; Zeng, G.; Zhang, C.; Yang, N.; Li, S.; Sun, Y., Quantitative Conversion of Methanol to Methyl Formate on Graphene-Confined Nano-Oxides. *iScience* **2020**, *23*, 101157.
113. Roy, S.; Mari, S.; Sai, M. K.; Sarma, S. C.; Sarkar, S.; Peter, S. C., Highly efficient bifunctional oxygen reduction/evolution activity of a non-precious nanocomposite derived from a tetrazine-COF. *Nanoscale* **2020**, *12*, 22718-22734.
114. Diao, J.; Qiu, Y.; Liu, S.; Wang, W.; Chen, K.; Li, H.; Yuan, W.; Qu, Y.; Guo, X., Interfacial Engineering of W_2N/WC Heterostructures Derived from Solid-State Synthesis: A Highly Efficient Trifunctional Electrocatalyst for ORR, OER, and HER. *Adv. Mater.* **2020**, *32*, e1905679.
115. Lv, X.; Chen, Y.; Wu, Y.; Wang, H.; Wang, X.; Wei, C.; Xiao, Z.; Yang, G.; Jiang, J., A Br-regulated transition metal active-site anchoring and exposure strategy in biomass-derived carbon nanosheets for obtaining robust ORR/HER electrocatalysts at all pH values. *J. Mater. Chem. A* **2019**, *7*, 27089-27098.
116. Wu, K.; Zhang, L.; Yuan, Y.; Zhong, L.; Chen, Z.; Chi, X.; Lu, H.; Chen, Z.; Zou, R.; Li, T.; Jiang, C.; Chen, Y.; Peng, X.; Lu, J., An Iron-Decorated Carbon Aerogel for Rechargeable Flow and Flexible Zn–Air Batteries. *Adv. Mater.* **2020**, *32*, 2002292.
117. Du, J.; Wu, G.; Liang, K.; Yang, J.; Zhang, Y.; Lin, Y.; Zheng, X.; Yu, Z. Q.; Wu, Y.; Hong, X., Rapid Controllable Synthesis of Atomically Dispersed Co on Carbon under High Voltage within One Minute. *Small* **2021**, *17*, e2007264.
118. Han, X.; Ling, X.; Wang, Y.; Ma, T.; Zhong, C.; Hu, W.; Deng, Y., Generation of Nanoparticle, Atomic-Cluster, and Single-Atom Cobalt Catalysts from Zeolitic Imidazole Frameworks by Spatial Isolation and Their Use in Zinc-Air Batteries. *Angew. Chem. Int. Ed.* **2019**, *58*, 5359-5364.
119. Yang, S.; Yu, Y.; Dou, M.; Zhang, Z.; Dai, L.; Wang, F., Two-Dimensional

Reference

Conjugated Aromatic Networks as High-Site-Density and Single-Atom Electrocatalysts for the Oxygen Reduction Reaction. *Angew. Chem. Int. Ed.* **2019**, *58*, 14724-14730.

120. Liang, Z.; Fan, X.; Lei, H.; Qi, J.; Li, Y.; Gao, J.; Huo, M.; Yuan, H.; Zhang, W.; Lin, H.; Zheng, H.; Cao, R., Cobalt-Nitrogen-Doped Helical Carbonaceous Nanotubes as a Class of Efficient Electrocatalysts for the Oxygen Reduction Reaction. *Angew. Chem. Int. Ed.* **2018**, *57*, 13187-13191.

121. Niu, W.; Pakhira, S.; Marcus, K.; Li, Z.; Mendoza-Cortes, J. L.; Yang, Y., Apically Dominant Mechanism for Improving Catalytic Activities of N-Doped Carbon Nanotube Arrays in Rechargeable Zinc-Air Battery. *Adv. Funct. Mater.* **2018**, *8*, 1800480.

122. Tong, Y.; Chen, P.; Zhou, T.; Xu, K.; Chu, W.; Wu, C.; Xie, Y., A Bifunctional Hybrid Electrocatalyst for Oxygen Reduction and Evolution: Cobalt Oxide Nanoparticles Strongly Coupled to B,N-Decorated Graphene. *Angew. Chem. Int. Ed.* **2017**, *56*, 7121-7125.

123. Li, W.; Cheng, G.; Sun, M.; Wu, Z.; Liu, G.; Su, D.; Lan, B.; Mai, S.; Chen, L.; Yu, L., C-CoP hollow microporous nanocages based on phosphating regulation: a high-performance bifunctional electrocatalyst for overall water splitting. *Nanoscale* **2019**, *11*, 17084-17092.

124. Wu, Z.; Nie, D.; Song, M.; Jiao, T.; Fu, G.; Liu, X., Facile synthesis of Co-Fe-B-P nanochains as an efficient bifunctional electrocatalyst for overall water-splitting. *Nanoscale* **2019**, *11*, 7506-7512.

125. Song, J.; Zhu, C.; Xu, B. Z.; Fu, S.; Engelhard, M. H.; Ye, R.; Du, D.; Beckman, S. P.; Lin, Y., Bimetallic Cobalt-Based Phosphide Zeolitic Imidazolate Framework: CoPxPhase-Dependent Electrical Conductivity and Hydrogen Atom Adsorption Energy for Efficient Overall Water Splitting. *Adv. Funct. Mater.* **2017**, *7*, 1601555.

126. Pu, Z.; Amiin, I. S.; Zhang, C.; Wang, M.; Kou, Z.; Mu, S., Phytic acid-derivative transition metal phosphides encapsulated in N,P-codoped carbon: an efficient and durable hydrogen evolution electrocatalyst in a wide pH range.

Nanoscale **2017**, *9*, 3555-3560.

127. Li, J.; Yan, M.; Zhou, X.; Huang, Z.-Q.; Xia, Z.; Chang, C.-R.; Ma, Y.; Qu, Y., Mechanistic Insights on Ternary Ni₂xCo_xP for Hydrogen Evolution and Their Hybrids with Graphene as Highly Efficient and Robust Catalysts for Overall Water Splitting. *Adv. Funct. Mater.* **2016**, *26*, 6785-6796.

128. Xue, Z.-H.; Su, H.; Yu, Q.-Y.; Zhang, B.; Wang, H.-H.; Li, X.-H.; Chen, J.-S., Janus Co/CoP Nanoparticles as Efficient Mott-Schottky Electrocatalysts for Overall Water Splitting in Wide pH Range. *Adv. Funct. Mater.* **2017**, *7*, 1602355.

129. Zhu, C.; Wang, A. L.; Xiao, W.; Chao, D.; Zhang, X.; Tiep, N. H.; Chen, S.; Kang, J.; Wang, X.; Ding, J.; Wang, J.; Zhang, H.; Fan, H. J., In Situ Grown Epitaxial Heterojunction Exhibits High-Performance Electrocatalytic Water Splitting. *Adv. Mater.* **2018**, *30*, e1705516.

130. Zhu, Y. P.; Ma, T. Y.; Jaroniec, M.; Qiao, S. Z., Self-Templating Synthesis of Hollow Co₃O₄ Microtube Arrays for Highly Efficient Water Electrolysis. *Angew. Chem. Int. Ed.* **2017**, *56*, 1324-1328.

131. Song, J.; Zhu, C.; Xu, B. Z.; Fu, S.; Engelhard, M. H.; Ye, R.; Du, D.; Beckman, S. P.; Lin, Y., Bimetallic Cobalt-Based Phosphide Zeolitic Imidazolate Framework: CoP_x Phase-Dependent Electrical Conductivity and Hydrogen Atom Adsorption Energy for Efficient Overall Water Splitting. *Adv. Funct. Mater.* **2017**, *7*, 1601555.

132. Huang, S.; Meng, Y.; He, S.; Goswami, A.; Wu, Q.; Li, J.; Tong, S.; Asefa, T.; Wu, M., N-, O-, and S-Tridoped Carbon-Encapsulated Co₉S₈ Nanomaterials: Efficient Bifunctional Electrocatalysts for Overall Water Splitting. *Adv. Funct. Mater.* **2017**, *27*, 1606585.

133. Hou, Y.; Lohe, M. R.; Zhang, J.; Liu, S.; Zhuang, X.; Feng, X., Vertically oriented cobalt selenide/NiFe layered-double-hydroxide nanosheets supported on exfoliated graphene foil: an efficient 3D electrode for overall water splitting. *Energy Environ. Sci.* **2016**, *9*, 478-483.

134. Sivanantham, A.; Ganesan, P.; Shanmugam, S., Hierarchical NiCo₂S₄ Nanowire Arrays Supported on Ni Foam: An Efficient and Durable Bifunctional

Electrocatalyst for Oxygen and Hydrogen Evolution Reactions. *Adv. Funct. Mater.* **2016**, *26*, 4661-4672.

135. Nitopi, S.; Bertheussen, E.; Scott, S. B.; Liu, X.; Engstfeld, A. K.; Horch, S.; Seger, B.; Stephens, I. E. L.; Chan, K.; Hahn, C.; Nørskov, J. K.; Jaramillo, T. F.; Chorkendorff, I., Progress and Perspectives of Electrochemical CO₂ Reduction on Copper in Aqueous Electrolyte. *Chem. Rev.* **2019**, *119*, 7610-7672.

136. Wang, L.; Chen, W.; Zhang, D.; Du, Y.; Amal, R.; Qiao, S.; Wu, J.; Yin, Z., Surface strategies for catalytic CO₂ reduction: from two-dimensional materials to nanoclusters to single atoms. *Chem. Soc. Rev.* **2019**, *48*, 5310-5349.

137. Yang, D.; Zuo, S.; Yang, H.; Zhou, Y.; Lu, Q.; Wang, X., Tailoring Layer Number of 2D Porphyrin-Based MOFs Towards Photocoupled Electroreduction of CO₂. *Adv. Mater.* **2022**, *34*, 2107293.

138. Zeng, Z.; Gan, L. Y.; Bin Yang, H.; Su, X.; Gao, J.; Liu, W.; Matsumoto, H.; Gong, J.; Zhang, J.; Cai, W.; Zhang, Z.; Yan, Y.; Liu, B.; Chen, P., Orbital coupling of hetero-diatomic nickel-iron site for bifunctional electrocatalysis of CO₂ reduction and oxygen evolution. *Nat. Commun.* **2021**, *12*, 4088.

139. Zhang, Y.; Dong, L.-Z.; Li, S.; Huang, X.; Chang, J.-N.; Wang, J.-H.; Zhou, J.; Li, S.-L.; Lan, Y.-Q., Coordination environment dependent selectivity of single-site-Cu enriched crystalline porous catalysts in CO₂ reduction to CH₄. *Nat. Commun.* **2021**, *12*, 6390.

140. Zheng, Y.; Vasileff, A.; Zhou, X.; Jiao, Y.; Jaroniec, M.; Qiao, S.-Z., Understanding the Roadmap for Electrochemical Reduction of CO₂ to Multi-Carbon Oxygenates and Hydrocarbons on Copper-Based Catalysts. *J. Am. Chem. Soc.* **2019**, *141*, 7646-7659.

141. Fu, J.; Dong, J.; Si, R.; Sun, K.; Zhang, J.; Li, M.; Yu, N.; Zhang, B.; Humphrey, M. G.; Fu, Q.; Huang, J., Synergistic Effects for Enhanced Catalysis in a Dual Single-Atom Catalyst. *ACS Catal.* **2021**, *11*, 1952-1961.

142. Zhang, L.; Si, R.; Liu, H.; Chen, N.; Wang, Q.; Adair, K.; Wang, Z.; Chen, J.; Song, Z.; Li, J.; Banis, M. N.; Li, R.; Sham, T.-K.; Gu, M.; Liu, L.-M.; Botton, G. A.; Sun, X., Atomic layer deposited Pt-Ru dual-metal dimers and identifying

Reference

- their active sites for hydrogen evolution reaction. *Nat. Commun.* **2019**, *10*, 4936.
143. Zheng, T.; Liu, C.; Guo, C.; Zhang, M.; Li, X.; Jiang, Q.; Xue, W.; Li, H.; Li, A.; Pao, C.-W.; Xiao, J.; Xia, C.; Zeng, J., Copper-catalysed exclusive CO₂ to pure formic acid conversion via single-atom alloying. *Nat. Nanotechnol.* **2021**, *16*, 1386-1393.
144. Chen, H.; Zhang, Y.; He, Q.; Zhang, H.; Xu, S.; He, X.; Ji, H., A facile route to fabricate double atom catalysts with controllable atomic spacing for the r-WGS reaction. *J. Mater. Chem. A* **2020**, *8*, 2364-2368.
145. Chen, J.; Li, H.; Fan, C.; Meng, Q.; Tang, Y.; Qiu, X.; Fu, G.; Ma, T., Dual Single-Atomic Ni-N₄ and Fe-N₄ Sites Constructing Janus Hollow Graphene for Selective Oxygen Electrocatalysis. *Adv. Mater.* **2020**, *32*, 2003134.
146. Wei, Y.-S.; Sun, L.; Wang, M.; Hong, J.; Zou, L.; Liu, H.; Wang, Y.; Zhang, M.; Liu, Z.; Li, Y.; Horike, S.; Suenaga, K.; Xu, Q., Fabricating Dual-Atom Iron Catalysts for Efficient Oxygen Evolution Reaction: A Heteroatom Modulator Approach. *Angew. Chem. Int. Ed.* **2020**, *59*, 16013-16022.
147. Xu, Q.; Li, Q.; Guo, Y.; Luo, D.; Qian, J.; Li, X.; Wang, Y., Multiscale Hierarchically Engineered Carbon Nanosheets Derived from Covalent Organic Framework for Potassium-Ion Batteries. *Small Methods* **2020**, *4*, 2000159.
148. Zhou, W.; Su, H.; Li, Y.; Liu, M.; Zhang, H.; Zhang, X.; Sun, X.; Xu, Y.; Liu, Q.; Wei, S., Identification of the Evolving Dynamics of Coordination-Unsaturated Iron Atomic Active Sites under Reaction Conditions. *ACS Energy Lett.* **2021**, *6*, 3359-3366.
149. Zhang, X.; Wu, Z.; Zhang, X.; Li, L.; Li, Y.; Xu, H.; Li, X.; Yu, X.; Zhang, Z.; Liang, Y.; Wang, H., Highly selective and active CO₂ reduction electrocatalysts based on cobalt phthalocyanine/carbon nanotube hybrid structures. *Nat. Commun.* **2017**, *8*, 14675.
150. Meng, D. L.; Zhang, M. D.; Si, D. H.; Mao, M. J.; Hou, Y.; Huang, Y. B.; Cao, R., Highly Selective Tandem Electroreduction of CO₂ to Ethylene over Atomically Isolated Nickel-Nitrogen Site/Copper Nanoparticle Catalysts. *Angew. Chem. Int. Ed.* **2021**, *60*, 25485-25492.

Reference

151. Lu, Q.; Rosen, J.; Zhou, Y.; Hutchings, G. S.; Kimmel, Y. C.; Chen, J. G.; Jiao, F., A selective and efficient electrocatalyst for carbon dioxide reduction. *Nat. Commun.* **2014**, *5*, 3242.
152. Zhao, C.; Dai, X.; Yao, T.; Chen, W.; Wang, X.; Wang, J.; Yang, J.; Wei, S.; Wu, Y.; Li, Y., Ionic Exchange of Metal–Organic Frameworks to Access Single Nickel Sites for Efficient Electroreduction of CO₂. *J. Am. Chem. Soc.* **2017**, *139*, 8078-8081.
153. Yi, J. D.; Si, D. H.; Xie, R.; Yin, Q.; Zhang, M. D.; Wu, Q.; Chai, G. L.; Huang, Y. B.; Cao, R., Conductive Two-Dimensional Phthalocyanine-based Metal-Organic Framework Nanosheets for Efficient Electroreduction of CO₂. *Angew. Chem. Int. Ed.* **2021**, *60*, 17108-17114.
154. Wang, M.; Ren, X.; Yuan, G.; Niu, X.; Xu, Q.; Gao, W.; Zhu, S.; Wang, Q., Selective electroreduction of CO₂ to CO over co-electrodeposited dendritic core-shell indium-doped Cu@Cu₂O catalyst. *J. CO₂ Util.* **2020**, *37*, 204-212.
155. Yang, H.; Lin, Q.; Wu, Y.; Li, G.; Hu, Q.; Chai, X.; Ren, X.; Zhang, Q.; Liu, J.; He, C., Highly efficient utilization of single atoms via constructing 3D and free-standing electrodes for CO₂ reduction with ultrahigh current density. *Nano Energy* **2020**, *70*, 104454.
156. Zhu, Q.; Wang, X.; Clowes, R.; Cui, P.; Chen, L.; Little, M. A.; Cooper, A. I., 3D Cage COFs: A Dynamic Three-Dimensional Covalent Organic Framework with High-Connectivity Organic Cage Nodes. *J. Am. Chem. Soc.* **2020**, *142*, 16842-16848.
157. Wang, L.; Xu, C.; Zhang, W.; Zhang, Q.; Zhao, M.; Zeng, C.; Jiang, Q.; Gu, C.; Ma, Y., Electrocleavage Synthesis of Solution-Processed, Imine-Linked, and Crystalline Covalent Organic Framework Thin Films. *J. Am. Chem. Soc.* **2022**, *144*, 8961-8968.
158. Koner, K.; Karak, S.; Kandambeth, S.; Karak, S.; Thomas, N.; Leanza, L.; Perego, C.; Pesce, L.; Capelli, R.; Moun, M.; Bhakar, M.; Ajithkumar, T. G.; Pavan, G. M.; Banerjee, R., Porous covalent organic nanotubes and their assembly in loops and toroids. *Nat. Chem.* **2022**, *14*, 507-514.

Reference

159. Zhang, Y.; Wei, C.; Wu, M.-X.; Wang, Y.; Jiang, H.; Zhou, G.; Tang, X.; Liu, X., A high-performance COF-based aqueous zinc-bromine battery. *Chem. Eng. J.* **2023**, *451*, 138915.
160. Yang, C.; Qian, C.; Yu, M.; Liao, Y., Manipulation of band gap and hydrophilicity in vinylene-linked covalent organic frameworks for improved visible-light-driven hydrogen evolution by end-capping strategy. *Chem. Eng. J.* **2023**, *454*, 140341.
161. Li, Y.; Chen, Q.; Xu, T.; Xie, Z.; Liu, J.; Yu, X.; Ma, S.; Qin, T.; Chen, L., De Novo Design and Facile Synthesis of 2D Covalent Organic Frameworks: A Two-in-One Strategy. *J. Am. Chem. Soc.* **2019**, *141*, 13822-13828.
162. Su, Y.; Li, B.; Xu, H.; Lu, C.; Wang, S.; Chen, B.; Wang, Z.; Wang, W.; Otake, K.-i.; Kitagawa, S.; Huang, L.; Gu, C., Multi-Component Synthesis of a Buta-1,3-diene-Linked Covalent Organic Framework. *J. Am. Chem. Soc.* **2022**, *144*, 18218-18222.
163. Su, Y.; Wan, Y.; Xu, H.; Otake, K.-i.; Tang, X.; Huang, L.; Kitagawa, S.; Gu, C., Crystalline and Stable Benzofuran-Linked Covalent Organic Frameworks from Irreversible Cascade Reactions. *J. Am. Chem. Soc.* **2020**, *142*, 13316-13321.
164. Shao, P.; Li, J.; Chen, F.; Ma, L.; Li, Q.; Zhang, M.; Zhou, J.; Yin, A.; Feng, X.; Wang, B., Flexible Films of Covalent Organic Frameworks with Ultralow Dielectric Constants under High Humidity. *Angew. Chem. Int. Ed.* **2018**, *57*, 16501-16505.
165. Xu, X.; Zhang, S.; Xu, K.; Chen, H.; Fan, X.; Huang, N., Janus Dione-Based Conjugated Covalent Organic Frameworks with High Conductivity as Superior Cathode Materials. *J. Am. Chem. Soc.* **2023**, *145*, 1022-1030.
166. Li, Z.; Sheng, L.; Hsueh, C.; Wang, X.; Cui, H.; Gao, H.; Wu, Y.; Wang, J.; Tang, Y.; Xu, H.; He, X., Three-Dimensional Covalent Organic Frameworks with hea Topology. *Chem. Mater.* **2021**, *33*, 9618-9623.
167. Li, Z.; Sheng, L.; Wang, H.; Wang, X.; Li, M.; Xu, Y.; Cui, H.; Zhang, H.; Liang, H.; Xu, H.; He, X., Three-Dimensional Covalent Organic Framework

Reference

- with ceq Topology. *J. Am. Chem. Soc.* **2021**, *143*, 92-96.
168. Kang, C.; Zhang, Z.; Kusaka, S.; Negita, K.; Usadi, A. K.; Calabro, D. C.; Baugh, L. S.; Wang, Y.; Zou, X.; Huang, Z.; Matsuda, R.; Zhao, D., Covalent organic framework atropisomers with multiple gas-triggered structural flexibilities. *Nat. Mater.* **2023**, *22*, 636-643.
169. Chen, W.; Wang, L.; Mo, D.; He, F.; Wen, Z.; Wu, X.; Xu, H.; Chen, L., Modulating Benzothiadiazole-Based Covalent Organic Frameworks via Halogenation for Enhanced Photocatalytic Water Splitting. *Angew. Chem. Int. Ed.* **2020**, *59*, 16902-16909.
170. Pachfule, P.; Acharjya, A.; Roeser, J.; Langenhahn, T.; Schwarze, M.; Schomäcker, R.; Thomas, A.; Schmidt, J., Diacetylene Functionalized Covalent Organic Framework (COF) for Photocatalytic Hydrogen Generation. *J. Am. Chem. Soc.* **2018**, *140*, 1423-1427.
171. Zhu, Y.; Shao, P.; Hu, L.; Sun, C.; Li, J.; Feng, X.; Wang, B., Construction of Interlayer Conjugated Links in 2D Covalent Organic Frameworks via Topological Polymerization. *J. Am. Chem. Soc.* **2021**, *143*, 7897-7902.
172. Lin, Y.; Lu, Q.; Song, F.; Yu, L.; Mechler, A. K.; Schlögl, R.; Heumann, S., Oxygen Evolution Reaction at Carbon Edge Sites: Investigation of Activity Evolution and Structure–Function Relationships with Polycyclic Aromatic Hydrocarbons. *Angew. Chem. Int. Ed.* **2019**, *58*, 8917-8921.
173. Bansal, D.; Cardenas-Morcoso, D.; Boscher, N., Conjugated porphyrin polymer films with nickel single sites for the electrocatalytic oxygen evolution reaction. *J. Mater. Chem. A* **2023**, *11*, 5188-5198.
174. Gopalakrishnan, M.; Mohamad, A. A.; Nguyen, M. T.; Yonezawa, T.; Qin, J.; Thamyongkit, P.; Somwangthanaroj, A.; Kheawhom, S., Recent advances in oxygen electrocatalysts based on tunable structural polymers. *Mater. Today Chem.* **2022**, *23*, 100632.
175. Wang, S.; Zhang, L.; Xia, Z.; Roy, A.; Chang, D. W.; Baek, J.-B.; Dai, L., BCN Graphene as Efficient Metal-Free Electrocatalyst for the Oxygen Reduction Reaction. *Angew. Chem. Int. Ed.* **2012**, *51*, 4209-4212.

Reference

176. Wu, P.; Du, P.; Zhang, H.; Cai, C., Graphyne As a Promising Metal-Free Electrocatalyst for Oxygen Reduction Reactions in Acidic Fuel Cells: A DFT Study. *J. Phys. Chem. C* **2012**, *116*, 20472-20479.
177. Wang, D.-W.; Su, D., Heterogeneous nanocarbon materials for oxygen reduction reaction. *Energy Environ. Sci.* 2014, *7*, 576-591.
178. Yu, G.; Lyu, L.; Zhang, F.; Yan, D.; Cao, W.; Hu, C., Theoretical and experimental evidence for rGO-4-PPNc as a metal-free Fenton-like catalyst by tuning the electron distribution. *RSC Adv.* **2018**, *8*, 3312-3320.
179. Li, L.; Hu, C.; Zhang, L.; Yu, G.; Lyu, L.; Li, F.; Jiang, N., Framework Cu-doped boron nitride nanobelts with enhanced internal electric field for effective Fenton-like removal of organic pollutants. *J. Mater. Chem. A* **2019**, *7*, 6946-6956.
180. Jia, H.; Sun, Z.; Jiang, D.; Du, P., Covalent Cobalt Porphyrin Framework on Multiwalled Carbon Nanotubes for Efficient Water Oxidation at Low Overpotential. *Chem. Mater.* **2015**, *27*, 4586-4593.
181. Huang, H.; Li, F.; Zhang, Y.; Chen, Y., Two-dimensional graphdiyne analogue Co-coordinated porphyrin covalent organic framework nanosheets as a stable electrocatalyst for the oxygen evolution reaction. *J. Mater. Chem. A* **2019**, *7*, 5575-5582.
182. Liu, Y.; Yan, X.; Li, T.; Zhang, W.-D.; Fu, Q.-T.; Lu, H.-S.; Wang, X.; Gu, Z.-G., Three-dimensional porphyrin-based covalent organic frameworks with tetrahedral building blocks for single-site catalysis. *New J. Chem.* **2019**, *43*, 16907-16914.
183. Cai, G.; Zeng, L.; He, L.; Sun, S.; Tong, Y.; Zhang, J., Imine Gels Based on Ferrocene and Porphyrin and Their Electrocatalytic Property. *Chem. - Asian J.* **2020**, *15*, 1963-1969.
184. Gao, Z.; Yu, Z.; Huang, Y.; He, X.; Su, X.; Xiao, L.; Yu, Y.; Huang, X.; Luo, F., Flexible and robust bimetallic covalent organic frameworks for the reversible switching of electrocatalytic oxygen evolution activity. *J. Mater. Chem. A* **2020**, *8*, 5907-5912.
185. Wang, X.; Sun, L.; Zhou, W.; Yang, L.; Ren, G.; Wu, H.; Deng, W.-Q., Iron

Reference

single-atom catalysts confined in covalent organic frameworks for efficient oxygen evolution reaction. *Cell Rep. Phys. Sci.* **2022**, *3*, 100804.

186. Zhang, T.; Zhang, G.; Chen, L., 2D Conjugated Covalent Organic Frameworks: Defined Synthesis and Tailor-Made Functions. *Acc. Chem. Res.* **2022**, *55*, 795-808.

187. Yue, Y.; Li, H.; Chen, H.; Huang, N., Piperazine-Linked Covalent Organic Frameworks with High Electrical Conductivity. *J. Am. Chem. Soc.* **2022**, *144*, 2873-2878.

188. Guo, C.; Zhou, J.; Chen, Y.; Zhuang, H.; Li, Q.; Li, J.; Tian, X.; Zhang, Y.; Yao, X.; Chen, Y.; Li, S. L.; Lan, Y. Q., Synergistic Manipulation of Hydrogen Evolution and Zinc Ion Flux in Metal-Covalent Organic Frameworks for Dendrite-free Zn-based Aqueous Batteries. *Angew. Chem. Int. Ed.* **2022**, *61*, e202210871.

189. Zhang, L.; Zhou, Y.; Jia, M.; He, Y.; Hu, W.; Liu, Q.; Li, J.; Xu, X.; Wang, C.; Carlsson, A.; Lazar, S.; Meingast, A.; Ma, Y.; Xu, J.; Wen, W.; Liu, Z.; Cheng, J.; Deng, H., Covalent Organic Framework for Efficient Two-Photon Absorption. *Matter* **2020**, *2*, 1049-1063.

190. Guo, X.; Mao, T.; Wang, Z.; Cheng, P.; Chen, Y.; Ma, S.; Zhang, Z., Fabrication of Photoresponsive Crystalline Artificial Muscles Based on PEGylated Covalent Organic Framework Membranes. *ACS Cent. Sci.* **2020**, *6*, 787-794.

191. Liu, M.; Chen, Y.-J.; Huang, X.; Dong, L.-Z.; Lu, M.; Guo, C.; Yuan, D.; Chen, Y.; Xu, G.; Li, S.-L.; Lan, Y.-Q., Porphyrin-Based COF 2D Materials: Variable Modification of Sensing Performances by Post-Metallization. *Angew. Chem. Int. Ed.* **2022**, *61*, e202115308.

192. Zhang, X.; Zhang, Z.; Li, H.; Gao, R.; Xiao, M.; Zhu, J.; Feng, M.; Chen, Z., Insight Into Heterogeneous Electrocatalyst Design Understanding for the Reduction of Carbon Dioxide. *Adv. Funct. Mater.* **2022**, *12*, 2201461.

193. Qin, H.; Wang, Y.; Wang, B.; Duan, X.; Lei, H.; Zhang, X.; Zheng, H.; Zhang, W.; Cao, R., Cobalt porphyrins supported on carbon nanotubes as model

Reference

- catalysts of metal-N4/C sites for oxygen electrocatalysis. *J. Energy Chem.* **2021**, *53*, 77-81.
194. Cichocka, M. O.; Liang, Z.; Feng, D.; Back, S.; Siahrostami, S.; Wang, X.; Samperisi, L.; Sun, Y.; Xu, H.; Hedin, N.; Zheng, H.; Zou, X.; Zhou, H.-C.; Huang, Z., A Porphyrinic Zirconium Metal–Organic Framework for Oxygen Reduction Reaction: Tailoring the Spacing between Active-Sites through Chain-Based Inorganic Building Units. *J. Am. Chem. Soc.* **2020**, *142*, 15386-15395.
195. Zhao, C.-X.; Li, B.-Q.; Liu, J.-N.; Huang, J.-Q.; Zhang, Q., Transition metal coordinated framework porphyrin for electrocatalytic oxygen reduction. *Chin. Chem. Lett.* **2019**, *30*, 911-914.
196. He, T.; Yang, C.; Chen, Y.; Huang, N.; Duan, S.; Zhang, Z.; Hu, W.; Jiang, D., Bottom-Up Interfacial Design of Covalent Organic Frameworks for Highly Efficient and Selective Electrocatalysis of CO₂. *Adv. Mater.* **2022**, *34*, 2205186.
197. An, S.; Lu, C.; Xu, Q.; Lian, C.; Peng, C.; Hu, J.; Zhuang, X.; Liu, H., Constructing Catalytic Crown Ether-Based Covalent Organic Frameworks for Electroreduction of CO₂. *ACS Energy Lett.* **2021**, *6*, 3496-3502.
198. Zhai, L.; Yang, S.; Lu, C.; Cui, C.-X.; Xu, Q.; Liu, J.; Yang, X.; Meng, X.; Lu, S.; Zhuang, X.; Zeng, G.; Jiang, Z., CoN₅ Sites Constructed by Anchoring Co Porphyrins on Vinylene-Linked Covalent Organic Frameworks for Electroreduction of Carbon Dioxide. *Small* **2022**, *18*, 2200736.
199. Zhu, H.-J.; Lu, M.; Wang, Y.-R.; Yao, S.-J.; Zhang, M.; Kan, Y.-H.; Liu, J.; Chen, Y.; Li, S.-L.; Lan, Y.-Q., Efficient electron transmission in covalent organic framework nanosheets for highly active electrocatalytic carbon dioxide reduction. *Nat. Commun.* **2020**, *11*, 497.
200. Li, N.; Si, D.-H.; Wu, Q.-j.; Wu, Q.; Huang, Y.-B.; Cao, R., Boosting Electrocatalytic CO₂ Reduction with Conjugated Bimetallic Co/Zn Polyphthalocyanine Frameworks. *CCS Chem.* **2022**, *5*, 1130-1143.
201. Wu, Q. J.; Si, D. H.; Wu, Q.; Dong, Y. L.; Cao, R.; Huang, Y. B., Boosting Electroreduction of CO₂ over Cationic Covalent Organic Frameworks: Hydrogen Bonding Effects of Halogen Ions. *Angew. Chem. Int. Ed.* **2023**, *62*,

e202215687.

202. Han, B.; Ding, X.; Yu, B.; Wu, H.; Zhou, W.; Liu, W.; Wei, C.; Chen, B.; Qi, D.; Wang, H.; Wang, K.; Chen, Y.; Chen, B.; Jiang, J., Two-Dimensional Covalent Organic Frameworks with Cobalt(II)-Phthalocyanine Sites for Efficient Electrocatalytic Carbon Dioxide Reduction. *J. Am. Chem. Soc.* **2021**, *143*, 7104-7113.

203. Liang, Z.; Wang, H.-Y.; Zheng, H.; Zhang, W.; Cao, R., Porphyrin-based frameworks for oxygen electrocatalysis and catalytic reduction of carbon dioxide. *Chem. Soc. Rev.* **2021**, *50*, 2540-2581.

204. Yan, X.; Lyu, S.; Xu, X.-Q.; Chen, W.; Shang, P.; Yang, Z.; Zhang, G.; Chen, W.; Wang, Y.; Chen, L., Superhydrophilic 2D Covalent Organic Frameworks as Broadband Absorbers for Efficient Solar Steam Generation. *Angew. Chem. Int. Ed.* **2022**, *61*, e202201900.

205. Zou, L.; Sa, R.; Zhong, H.; Lv, H.; Wang, X.; Wang, R., Photoelectron Transfer Mediated by the Interfacial Electron Effects for Boosting Visible-Light-Driven CO₂ Reduction. *ACS Catal.* **2022**, *12*, 3550-3557.

206. Wu, Q.-J.; Liang, J.; Huang, Y.-B.; Cao, R., Thermo-, Electro-, and Photocatalytic CO₂ Conversion to Value-Added Products over Porous Metal/Covalent Organic Frameworks. *Acc. Chem. Res.* **2022**, *55*, 2978-2997.

207. Tian, X.; Huang, X.; Shi, J.-W.; Zhou, J.; Guo, C.; Wang, R.; Wang, Y.-R.; Lu, M.; Li, Q.; Chen, Y.; Li, S.-L.; Lan, Y.-Q., Implanting Built-In Electric Field in Heterometallic Phthalocyanine Covalent Organic Frameworks for Light-Assisted CO₂ Electroreduction. *CCS Chem.* **2023**, 1-10.

208. Geng, Q.; Wang, H.; Wang, J.; Hong, J.; Sun, W.; Wu, Y.; Wang, Y., Boosting the Capacity of Aqueous Li-Ion Capacitors via Pinpoint Surgery in Nanocoral-Like Covalent Organic Frameworks. *Small Methods* **2022**, *6*, 2200314.

209. Shang, Y.; Ding, Y.; Zhang, P.; Wang, M.; Jia, Y.; Xu, Y.; Li, Y.; Fan, K.; Sun, L., Pyrrolic N or pyridinic N: The active center of N-doped carbon for CO₂ reduction. *Chin. J. Catal.* **2022**, *43*, 2405-2413.

Reference

210. Lu, C.; Yang, J.; Wei, S.; Bi, S.; Xia, Y.; Chen, M.; Hou, Y.; Qiu, M.; Yuan, C.; Su, Y.; Zhang, F.; Liang, H.; Zhuang, X., Atomic Ni Anchored Covalent Triazine Framework as High Efficient Electrocatalyst for Carbon Dioxide Conversion. *Adv. Funct. Mater.* **2019**, *29*, 1806884.
211. Yuan, J.; Chen, S.; Zhang, Y.; Li, R.; Zhang, J.; Peng, T., Structural Regulation of Coupled Phthalocyanine–Porphyrin Covalent Organic Frameworks to Highly Active and Selective Electrocatalytic CO₂ Reduction. *Adv. Mater.* **2022**, *34*, 2203139.
212. Voiry, D.; Chhowalla, M.; Gogotsi, Y.; Kotov, N. A.; Li, Y.; Penner, R. M.; Schaak, R. E.; Weiss, P. S., Best Practices for Reporting Electrocatalytic Performance of Nanomaterials. *ACS Nano* **2018**, *12*, 9635-9638.
213. Cao, C.; Ma, D.-D.; Jia, J.; Xu, Q.; Wu, X.-T.; Zhu, Q.-L., Divergent Paths, Same Goal: A Pair-Electrosynthesis Tactic for Cost-Efficient and Exclusive Formate Production by Metal–Organic-Framework-Derived 2D Electrocatalysts. *Adv. Mater.* **2021**, *33*, 2008631.
214. McCrory, C. C. L.; Jung, S.; Peters, J. C.; Jaramillo, T. F., Benchmarking Heterogeneous Electrocatalysts for the Oxygen Evolution Reaction. *J. Am. Chem. Soc.* **2013**, *135*, 16977-16987.
215. Ning, G.-H.; Chen, Z.; Gao, Q.; Tang, W.; Chen, Z.; Liu, C.; Tian, B.; Li, X.; Loh, K. P., Salicylideneanilines-Based Covalent Organic Frameworks as Chemoselective Molecular Sieves. *J. Am. Chem. Soc.* **2017**, *139*, 8897-8904.
216. El-Kaderi, H. M.; Hunt, J. R.; Mendoza-Cortés, J. L.; Côté, A. P.; Taylor, R. E.; O'Keeffe, M.; Yaghi, O. M., Designed Synthesis of 3D Covalent Organic Frameworks. *Science* **2007**, *316*, 268-272.
217. Fang, Q.; Gu, S.; Zheng, J.; Zhuang, Z.; Qiu, S.; Yan, Y., 3D Microporous Base-Functionalized Covalent Organic Frameworks for Size-Selective Catalysis. *Angew. Chem. Int. Ed.* **2014**, *53*, 2878-2882.
218. Yang, Z.; Liu, J.; Li, Y.; Zhang, G.; Xing, G.; Chen, L., Arylamine-Linked 2D Covalent Organic Frameworks for Efficient Pseudocapacitive Energy Storage. *Angew. Chem. Int. Ed.* **2021**, *60*, 20754-20759.

Reference

219. He, C.; Si, D. H.; Huang, Y. B.; Cao, R., A CO₂-Masked Carbene Functionalized Covalent Organic Framework for Highly Efficient Carbon Dioxide Conversion. *Angew. Chem. Int. Ed.* **2022**, *61*, e202207478.
220. Wang, Y.-R.; Ding, H.-M.; Sun, S.-N.; Shi, J.-w.; Yang, Y. L.; Li, Q.; Chen, Y.; Li, S.-L.; Lan, Y.-Q., Light, Heat and Electricity Integrated Energy Conversion System: Photothermal-Assisted Co-Electrolysis of CO₂ and Methanol. *Angew. Chem. Int. Ed.* **2022**, *61*, e202212162.
221. Mi, Z.; Yang, P.; Wang, R.; Unruangsri, J.; Yang, W.; Wang, C.; Guo, J., Stable Radical Cation-Containing Covalent Organic Frameworks Exhibiting Remarkable Structure-Enhanced Photothermal Conversion. *J. Am. Chem. Soc.* **2019**, *141*, 14433-14442.
222. Kalmutzki, M. J.; Diercks, C. S.; Yaghi, O. M., Metal–Organic Frameworks for Water Harvesting from Air. *Adv. Mater.* **2018**, *30*, 1704304.
223. Song, Y.; Zhang, J.-J.; Dou, Y.; Zhu, Z.; Su, J.; Huang, L.; Guo, W.; Cao, X.; Cheng, L.; Zhu, Z.; Zhang, Z.; Zhong, X.; Yang, D.; Wang, Z.; Tang, B. Z.; Yakobson, B. I.; Ye, R., Atomically Thin, Ionic–Covalent Organic Nanosheets for Stable, High-Performance Carbon Dioxide Electroreduction. *Adv. Mater.* **2022**, *34*, 2110496.

Outputs during the period of PhD

- [1] **M. Liu**, S. Liu, Q. Xu, Q. Miao, S. Yang, S. Hanson, G. Chen, J. He, Z. Jiang, G. Zeng, Dual atomic catalysts from COF-derived carbon for CO₂RR by Suppressing HER through Synergistic Effects. *Carbon Energy* **2023**, 1-12. doi:10.1002/cey2.300. **(Prof. Jun He as corresponding author)**
- [2] **M. Liu**, X. Zhao, S. Yang, X. Yang, X. Li, G. Z. Chen, J. He, Q. Xu and G. Zeng, Modulating Density of Catalytic Sites in Multiple-component Covalent Organic Frameworks for Electrocatalytic Carbon Dioxide Reduction. *ACS Appl. Mater. Interfaces* **2023**, *15*, 44384–44393. **(Prof. Jun He as corresponding author)**
- [3] **M. Liu**, Y. Fu, S. Bi, S. Yang, X. Yang, X. Li, G. Z. Chen, J. He, Q. Xu, G. Zeng, Dimensionally-controlled interlayer spaces of covalent organic frameworks for the oxygen evolution reaction. *Chem. Eng. J.* **2023**, 147682. DOI: 10.1016/j.cej.2023.147682. **(Prof. Jun He as corresponding author)**
- [4] **M. Liu**, S. Yang, Y. Fu, X. Yang, X. Li, G. Z. Chen, J. He, Q. Xu and G. Zeng, Ladder Type Covalent Organic Frameworks Constructed with Natural Units for the Oxygen and Carbon Dioxide Reduction Reactions. *Chem. Eng. J.* **2024**, accepted **(Prof. Jun He as corresponding author)**
- [5] **M. Liu**, Q. Xu, Q. Miao, S. Yang, P. Wu, G. Liu, J. He, C. Yu, G. Zeng, Atomic Co-N₄ and Co nanoparticles confined in COF@ZIF-67 derived core-shell carbon frameworks: Bifunctional non-precious metal catalysts toward ORR and HER *J. Mater. Chem. A* **2022**, *10*, 228-233. **(Cooperation between SARI and UNNC)**
- [6] **M. Liu**, S. Yang, S. Liu, Q. Miao, X. Yang, X. Li, Q. Xu, G. Zeng, Construction of Atomic Metal-N₂ Sites by Interlayers of Covalent Organic Frameworks for Electrochemical H₂O₂ Synthesis. *Small* **2022**, 2204757. **(Cooperation between SARI and UNNC)**

- [7] **M. Liu**, S. Liu, C.-X. Cui, Q. Miao, Y. He, X. Li, Q. Xu, G. Zeng, Construction of Catalytic Covalent Organic Frameworks with Redox-Active Sites for the Oxygen Reduction and the Oxygen Evolution Reaction. *Angew. Chem. Int. Ed.* **2022**, e202213522. **(Cooperation between SARI and UNNC)**
- [8] **M. Liu**, S. Yang, X. Yang, C.-X. Cui, G. Liu, X. Li, J. He, G. Z. Chen, Q. Xu, G. Zeng, *Nat. Commun.* **2023**, *14*, 3800. **(Cooperation between SARI and UNNC)**
- [9] **M. Liu**, S. Yang, Y. Fu, X. Yang, X. Li, G. Z. Chen, J. He, Q. Xu and G. Zeng, Construction of Multi-Component Covalent Organic Frameworks for the Carbon Dioxide Reduction Reaction. *Angew. Chem. Int. Ed* **2024**, e202401750. **(Cooperation between SARI and UNNC)**
- [10] **M. Liu**, H. -Y. Kong, S. Bi, X. Ding, G. Chen, J. He, Q. Xu, G. Zeng, Noninterpenetrated Three-dimensional Covalent Organic Framework with dia Topology for Au Ions Capture. *Adv. Funct. Mater.* **2023**, 2302637. **(Cooperation between SARI and UNNC)**
- [11] **M. Liu**, D. Jiang, Y. Fu, G.-Z. Chen, S. Bi, X. Ding, J. He, B.-H. Han, Q. Xu, G. Zeng, Modulating Skeletons of Covalent Organic Framework for High-Efficiency Gold Recovery. *Angew. Chem. Int. Ed.* **2023**, e202317015. DOI: 10.1002/anie.202317015. **(Cooperation between SARI and UNNC)**
- [12] S. Liu, **M. Liu**, X. Li, S. Yang, Q. Miao, Q. Xu, G. Zeng, Metal Organic Polymers with Dual Catalytic Sites for Oxygen Reduction and Oxygen Evolution Reaction. *Carbon Energy* **2022**, 1-11. doi:10.1002/cey2.303. **(co-first author, Cooperation between SARI and UNNC)**
- [13] Z. Duan, **M. Liu**, X. Li, S. Yang, S. Liu, Q. Xu, G. Zeng, Integrating multifunctional catalytic sites in COF@ZIF-67 derived carbon for the HER and ORR. *Chem. Commun.* **2022**, DOI: 10.1039/D2CC05433G. **(co-first author, Cooperation between SARI and UNNC)**
- [14] M. Zhou, **M. Liu**, Q. Miao, H. Shui, Q. Xu, Synergetic Pt Atoms and Nanoparticles Anchored in Standing Carbon-Derived from Covalent Organic Frameworks for Catalyzing ORR. *Adv. Mater. Interfaces* **2022**, *9*, 2201263.

Acknowledgement

I am filled with profound gratitude and appreciation for all those who have contributed to my journey. Completing my academic pursuits in 2024 has marked a significant milestone, but I understand that learning is a lifelong endeavour. I am genuinely grateful for the guidance and support from my supervisors, friends, and family. Throughout my dedicated pursuit of a doctoral degree, each day of my intense and captivating scientific research life has brought me abundant knowledge and valuable experiences. Through the continuous exploration and study of science, I have gained insights into the remarkable advancements and vastness of scientific endeavours in the ever-evolving relationship between humanity and nature. Moreover, I have realized that despite resource scarcity, a group of researchers always strive to contribute to our planet. I have also grown to understand the importance of approaching science and life with diligence and seriousness. Reflecting upon my progress over these years, I realize that every step forward was made possible by the care and assistance of those around me. I want to express my most profound respect and gratitude to them. I extend my heartfelt appreciation to Prof. Jun He, Prof. Gaofeng Zeng and Prof. Qing Xu, Prof. George Zheng Chen, and Prof. Svenja Hanson for their guidance throughout my research journey. Through their help and encouragement, I have learned the importance of approaching scientific research earnestly, cultivating a passion for exploring the unknown, and persistently solving problems. In addition, I also thanks for their invaluable contribution to my understanding and exploration of covalent organic frameworks, electrochemistry, energy conversion, and ion adsorption. Through their teachings, I have acquired knowledge in these fields and mastered the intricacies of experimental details, as well as the art of effectively communicating scientific research. Furthermore, I am grateful for the assistance

Acknowledgement

provided by my laboratory peers, including Dr. Shuai Yang, Guojuan Liu, Dian Gong, Xiubei Yang, Xuewen Li, Sijia Liu, Qiyang Miao, Shuang Zheng, and Zhuangyan Guo. Their collaboration, support, and camaraderie have been instrumental in my growth as a researcher. Last, I would like to express my heartfelt appreciation to Xingyue Zhao and my family for their unwavering support. Their encouragement during adversity has been uplifting and motivated me to continue striving for excellence. In conclusion, I am deeply grateful to every one of you who has shaped my academic and personal journey. Your guidance, support, and encouragement have been invaluable, and I am honoured to have had the opportunity to work with and learn from such remarkable individuals. As I embark on the next chapter of my life, I carry with me the lessons and experiences gained during these years, and I am confident that the knowledge and values instilled in me will continue to guide my path.